Bioinspired Microphysiological Systems for *in vitro* Elucidation of Prostate Tumorigenic Progression and Application in Pre-clinical Therapeutic Evaluation

by

Nicole Lee Habbit

A dissertation submitted to the Graduate Faculty of
Auburn University
in partial fulfillment of the
requirements for the Degree of
Doctor of Philosophy

Auburn, Alabama
December 10, 2022

Keywords: Tissue Engineered Cancer Model, Tumor Microenvironment, PEG-fibrinogen Biomaterial, Cancer Stromal Interaction, Organ-on-a-chip, Pre-clinical Drug Testing

Approved by

Elizabeth A. Lipke, Chair, Mary and John H. Sanders Professor of Chemical Engineering
Robert D. Arnold, Professor of Drug Discovery and Development
Allan E. David, John W. Brown Associate Professor of Chemical Engineering
Virginia A. Davis, Dr. Daniel F. and Josephine Breeden Professor of Chemical Engineering

Abstract

Contrary to conventional belief, prostate cancer tumors are not merely uniform clusters of cancerous cells that undergo uncontrollable growth and migrate indiscriminately throughout the body. Instead, the prostatic tumor microenvironment is a highly intricate network of cancer and other tumor-supporting cell types that is characterized by a high degree of spatial and temporal heterogeneity in cell populations, tissue microarchitecture, vascularization, and therapeutic sensitivity. Despite this complexity, the traditional anti-cancer therapeutic development pipeline relies heavily on drastically oversimplified pre-clinical cancer models to predict drug safety and efficacy in patients. Consequently, nearly 97% of oncology therapeutic candidates fail during clinical trials, while many targetable mechanisms and biomarkers of tumorigenic progression are left undiscovered.

To improve clinical translation in prostate cancer, this dissertation amalgamates an improved understanding of tumor pathophysiology with advances in biomaterial design and tissue engineering techniques to create bioinspired microphysiological systems that more accurately mimic patient disease *in vitro*. Chapter 1 elucidates tumorigenic progression and reviews both current therapeutic development processes and tools employed in the cancer tissue engineering field. Chapter 2 examines the pathophysiological tumor tissue stiffness range and introduces a mechanically tunable engineered prostate cancer tissue model to illuminate the role of matrix stiffness in prostate cancer. Chapter 3 expands the engineered prostate cancer tissue model to investigate the impact of varied cancer to stromal cell populations on aggressive versus indolent prostate cancer progression. Clinical relevancy is subsequently probed through a transcriptomic

comparison to patient data. Finally, Chapter 4 reports the development of a microfluidic prostate tumor-on-a-chip platform that augments the engineered prostate cancer tissue model by incorporating dynamic flow conditions, additional tumor cell types, observation of cell migration, and differential drug exposure. To demonstrate the future utility of the prostate tumor-on-a-chip platform in anti-cancer therapeutic development, liposomal and solid nanoparticle drug delivery systems are evaluated on-chip. Finally, commentary on the recommended future directions for microphysiological system advancement and improved clinical translation in prostate cancer is provided.

Acknowledgments

I first sincerely thank Dr. Elizabeth A. Lipke for her guidance and mentorship throughout the duration of my doctoral studies, as well as for her unending dedication toward comprehensive preparation for my future career goals. I also thank my committee members, Dr. Robert D. Arnold, Dr. Allan E. David, and Dr. Virginia A. Davis, as well as my university reader, Dr. Michael W. Greene, for their support and commitment toward my academic and research development. I again thank Dr. Robert D. Arnold, Dr. Allan E. David, and Dr. Michael W. Greene, in addition to Dr. Balabhaskar Prabhakarpandian, Dr. Peter R. Panizzi, Dr. Yuan Tian, Dr. Tareq B. Anani, and Dr. Taraswi Mitra Ghosh, for their collaborative assistance. I also thank the Auburn University Department of Chemical Engineering faculty and staff for their assistance.

I sincerely thank current and former members of the Lipke Lab including Dr. Yuan Tian, Mohammadjafar Hashemi, B. Justin Harvell, Shireen Singh, Mayra Páez, Benjamin Anbiah, Dr. Ferdous Finklea, Dr. Morgan Ellis, Dr. Iman Hassani, and Dr. Jessica Larsen for their support and friendship. I also thank my talented undergraduate researchers, Joshita Suresh, Luke Anderson, Peter Abraham, Megan Davies, Trey Sims, and Grace Hester for their immense work ethic and friendship; this dissertation work would not have been possible without their contributions.

I sincerely thank my graduate student family (particularly Dr. Sumaiya Islam, Dr. David Young, Dr. Zahra Karimi, Phillip Martin, Steve Montgomery, Katie Lawson, Delaney Clouse, Mackenzie Woods, Ali Bradford, B. Justin Harvell, Jacob Faulkner, Loyal Murphy, Mercedes Haley, Jazmine Torres, Alex Summers, Matthew Garnett, Ati Alimirzaei, and Austin Evers) for their constant friendship and for truly making Auburn

my home. I also thank my Auburn Community Church (particularly Trinity Hutchins and Kathleen Anderson) and West Auburn Baptist Church community groups for their unending support outside of the academic environment. I sincerely thank my service puppies-in-training, Archie and Luna, for their constant companionship. Lastly but most importantly, I thank my parents, Robert and Kelli Habbit, as well as my brother, Bobby Habbit, and my entire extended family for their unending love, support, and encouragement throughout every day of my life. I would not be who I am without you.

Psalm 115:1

Table of Contents

List of Tables

List of Figures

List of Abbreviations

^{1}H NMR	Proton Nuclear Magnetic Resonance
2D	Two-Dimensional
3D	Three-Dimensional
ADPC	Androgen Dependent Prostate Cancer
ADT	Androgen Deprivation Therapy
ANOVA	Analysis of Variance
APMA	4-Aminophenylmercuric Acetate
B2M	Anti-Human Beta-2-Microglobulin Antibody Clone
BC	before Christ
BCA	Bicinchoninic Acid Assay
BPH	Benign Prostatic Hyperplasia
BSA	Bovine Serum Albumin
CA	Chitosan Alginate
$CaCl_2$	Calcium Chloride
CAFs	Cancer-Associated Fibroblasts
CAT	Catalog Number
CCD	Charge-coupled Device
cDNA	Complementary Deoxyribonucleic Acid
Chol	Cholesterol
CK20	Anti-Keratin 20 D9Z1Z XP® Antibody Clone
CO_2	Carbon dioxide

CPM	Counts Per Million
CRC	Colorectal Cancer
CRPC	Castration Resistant Prostate Cancer
CRPC-ne	Neuroendocrine Variant of CRPC
CT	Computed Tomography
CTP	Central Tumor Port
CY5HQ	Cyanine 5
DAPI	4’,6-Diamidino-2-Phenylindole
DEG	Differentially Expressed Gene
DiI	Tetramethylindocarbocyanine Perchlorate
DMEM	Dulbecco’s Modified Eagle’s Medium
DMSO	Dimethyl Sulfoxide
DNA	Deoxyribonucleic Acid
DNAse	Deoxyribonuclease I
DSPC	Distearoylphsphatidylcholine
DSPE	1,2-Distearoyl-sn-glycero-3phosphorylethanolamine
ECM	Extracellular Matrix
EDHM	Enhanced Darkfield Hyperspectral Microscopy
EGM-2	Endothelial Cell Growth Medium-2 Bulletkit
Em	Emission
EMT	Epithelial-Mesenchymal Transition
EPCaT	Engineered Prostate Cancer Tissue

EPR	Enhanced Permeability and Retention Effect
Ex	Excitation
F-12K	Kaighn's Modification of Ham's F-12K Medium
FBS	Fetal Bovine Serum
FDA	US Food & Drug Administration
FDR	False Discovery Rate
FGF-2	Fibroblast Growth Factor-2
FITC	Fluorescein Isothiocyanate
Foxp3	Foxp3 Fixation and Permeabilization Solution
FRET	Fluorogenic Resonance Energy Transfer
G1X	Group 1 Mice
G2X	Group 2 Mice
GEMMs	Genetically Engineered Mouse Models
GFOGER	Gly-Phe-hydroxyproline-Gly-Glu-Arg peptide
GFP	Green Fluorescent Protein
GO	Gene Ontology
GSEA	Gene Set Enrichment Analysis
H&E	Hematoxylin and Eosin
H2Db	Anti-Mouse MHC Class I H-2 Db Antibody Clone
H33342	bisBenzimide Hoechst 33342 Fluorochrome
HA	Glycosaminoglycan Hyaluronic Acid
HBSS	Hank's Balanced Salt Solution

HPC	High-Perfusion Chip
hTERT	Human Telomerase Reverse Transcriptase
HTS	High Throughput Screening
HUVECs	Human Umbilical Vein Endothelial Cells
IACUC	Institutional Animal Care and Use Committee
IKVAV	Ile-Lys-Val-Ala-Val peptide
IND	Investigational New Drug
Ki67	Anti-Ki67 Antibody Clone
LED	Light Emitting Diode
LPC	Low-Perfusion Chip
Luc	Luciferase
LUTs	Look-up Tables
MDACC	MD Anderson Cancer Center
MHC	Major Histocompatibility Complex
MMP	Matrix Metalloproteinase
MPS	Microphysiological System
MSigDB	Molecular Signature Database
$MSIgG_1$	Mouse IgG_1 Isotype Control
$MSIgG_{2a}$	Mouse IgG_{2a} Isotype Control
MSOT	Multispectral Optoacoustic Tomography
NaCl	Sodium Chloride
NCI	National Cancer Institute

NDA	New Drug Application
NDDs	Nano-sized Drug Delivery System
NES	Normalized Enrichment Score
nHA	Nanohydroxyapatite
NK	Natural Killer
NVP	1-vinyl-2-pyrrolidinone
PA	Polyacrylamide
PBLs	Peripheral Blood Lymphocytes
PBS	Phosphate Buffered Saline
PCa	Prostate Cancer
PCL	Poly(ε-caprolactone)
PDMS	Poly(dimethyl siloxane)
PDX	Patient-Derived Xenograft
PEG	Poly(ethylene glycol)
PEGDA	Poly(ethylene glycol)-diacrylate
Pen-Strep	Penicillin-Streptomycin
PF	Poly(ethylene glycol)-fibrinogen
PF+1%PEGDA	PF with 1% (w/v) excess PEGDA
PF+2%PEGDA	PF with 2% (w/v) excess PEGDA
PF+3%PEGDA	PF with 3% (w/v) excess PEGDA
PFA	Paraformaldehyde
PGA	Poly(glycolic acid)

PHS	Public Health Service
PLA	Poly(lactic acid)
PTC	Primary Tumor Chamber
QC	Quality Control
RADA	Arg-Ala-Asp-Ala peptide
RBIgG	Rabbit IgG Isotype Control
Red-FLuc	Red Shifted Firefly Luciferase
RFU	Relative Fluorescence Units
RGD	Arg-Gly-Asp peptide
RIN	RNA Integrity Number
RNA	Ribonucleic Acid
RNAseq	RNA Sequencing
ROI	Region of Interest
ROUT	Robust Regression and Outlier Removal
RPMI	Roswell Park Memorial Institute
SAM	Spectral Angle Mapper
SD	Standard Deviation
SHG	Second Harmonic Generation
SPION	Superparamagnetic Iron Oxide Nanoparticle
STAR	Spliced Transcripts Alignment to a Reference
TAMs	Tumor-Associated Macrophages
TCEP-HCl	Tris (2-carboxyethyl) Phosphine Hydrochloride

TCGA	The Cancer Genome Atlas
TCGA-PRAD	TCGA Prostate Adenocarcinoma Project Database
TE-7	Anti-Fibroblast Antibody Clone
TEOA	Triethanolamine
TME	Tumor Microenvironment
TRIS-HCl	TRIS Hydrochloride
TRITC	Tetramethylrhodamine
US	United States
UV	Ultraviolet
VDA	Vascular Disrupting Agent
VEGF	Vascular Endothelial Growth Factor
VWF	Von Willebrand Factor

Introduction to Cancer and Microphysiological Systems

While the term cancer, translated from *carcinos*, was first introduced in 400 BC by the ancient Greek physician Hippocrates, tumorigenic growths in the human body have been perpetually chronicled since the dawn of recorded history. The first known descriptions of cancerous masses were found in an Egyptian trauma surgery textbook, the *Edwin Smith Surgical Papyrus*, written in 3000 BC, in which the script states, "There is no treatment" for the tumors (American Cancer Society, 2018). Ancient techniques to combat both malignant and benign growths were comprised of cauterization and primitive surgical removal of the affected tissue. Tumor recurrence was often noted, and many physicians and scientists alike concluded that cancer could not be cured, a mindset that translated well into the 20th century. Throughout the roughly 5,000 years since the initial documentation of cancer, modern medicine has evolved to generate advanced diagnostic and therapeutic methodologies, however, a cure for the disease has yet to be discovered.

According to the National Cancer Institute (NCI), approximately 39.5% of Americans will be diagnosed with cancer during his or her lifetime; furthermore, the global incidence of cancer is projected to increase to 29.5 million new cases diagnosed annually by the year 2040 (National Cancer Institute, 2020). Beyond affecting numerous lives, cancer also presents as an immense societal burden with an annual global economic cost of US $1.16 trillion, which is projected to increase by 70% within the next two decades (International Agency for Research on Cancer, 2014). Therefore, it has become increasingly critical that highly effective anti-cancer therapeutics are expeditiously developed and made clinically available.

Although often referred to as a singular disease, cancer encompasses a wide range of pathophysiological disorders in which at least one genetically mutant cell divides uncontrollably, resulting in tumorigenesis (Vogelstein and Kinzler, 2004). A myriad of factors, entitled the hallmarks of cancer, have been found to enable tumorigenic progression. They have been defined as sustaining proliferative signaling, evading growth suppressors, resisting cell death, enabling replicative immortality, inducing angiogenesis, activating invasion and metastasis, reprogramming energy metabolism, and evading immune destruction (Hanahan and Weinberg, 2000, Hanahan and Weinberg, 2011). The combinatorial effect of these hallmarks results in an extremely heterogeneous pathological profile that is characterized by both genotypic and phenotypic inter- and intratumoral variations (Burrell et al., 2013). It additionally initiates a cascade of highly complex cellular and molecular pathways which aid in the formation of and operate within the native tumor microenvironment (TME) (Burrell et al., 2013, Whiteside, 2008).

The field of tissue engineering has emerged to implement chemical and biomedical engineering principles in the combination of novel biomaterials with cells and bioactive factors to construct functional *in vitro* microphysiological systems (MPS) (National Institute of Biomedical Imaging and Bioengineering, 2018, Roth, 2021). Through intentional design choices, the bioinspired microphysiological systems introduced in this dissertation are each engineered to integrate several key characteristics of tumor pathophysiology, thereby providing a more rigorous platform for future application in mechanistic disease progression studies and clinically translatable pharmacological testing. *This section has been adapted from previous thesis work (Habbit, 2018).*

Chapter 1. Background

1.1 The Anti-cancer Therapeutic Development Pathway

Bringing a new pharmaceutical drug to the market is a tremendously lengthy process during which the therapeutic is subjected to a myriad of investigations to determine its safety and efficacy. It is currently estimated that, on average, it takes between 10-15 years and approximately US $800 million to US $1 billion to successfully research and develop one new therapeutic (Pharmaceutical Research and Manufacturers of America, 2007). Upon discovery, the development pathway begins with the pre-clinical research phase which serves to investigate the pharmacological profile and acute toxicity of the drug and its metabolites both *in vitro* and in at least two animal species *in vivo* (US Food & Drug Administration, 2018). If the therapeutic is found to be reasonably safe during this stage, an Investigational New Drug (IND) application can be filed with the US Food & Drug Administration (FDA) to begin clinical research.

Clinical trials are then conducted in four major phases with each geared towards answering a specific question about the safety and efficacy of the experimental agent *in vivo*. Phase I aims to investigate drug behavior and interaction in the diseased human body while determining the appropriate dosage to maximize treatment potential and limit side effects to an acceptable level (US Food & Drug Administration, 2018). Phase II then implements the dose found to be safest and most effective during Phase I in a larger number of participants to closely monitor how well the therapeutic achieves the goal of the treatment, as well as investigate rare side effects (US Food & Drug Administration, 2018). Phase III further augments the Phase II findings by monitoring efficacy in a much larger

patient population over a longer treatment period to examine both the desired and undesired long-term effects of the therapeutic. Furthermore, Phase III trials serve to determine how the experimental agent compares to the current standard treatment in terms of both safety and efficacy (US Food & Drug Administration, 2018). Upon successful completion of Phase III, a New Drug Application (NDA) is filed with the FDA to acquire approval for general use in patients with the disease for which it was tested. Finally, Phase IV serves to continuously monitor the FDA-approved therapeutic throughout its lifetime on the market to ensure it is still appropriately safe and efficacious to continue to be administered to patients (US Food & Drug Administration, 2018). Moreover, Phase IV considers factors such as treatment cost and patient quality of life that are not investigated during Phases I through III.

1.2 The Critical Need for Pathophysiologically Relevant *in vitro* Tumor Models

The compound probability of progressing from Phase I trials to FDA Approval for all drug development programs combined is only 9.6%, with the largest failure occurring at the progression from Phase II to Phase III (Biotechnology Innovation Organization, 2016). Oncology drug development programs had an outsized, detrimental effect on the overall clinical trials success rate with only 5.1% of experimental drugs being successfully approved between 2006 and 2015 (Biotechnology Innovation Organization, 2016). Recent estimates exposed even more dire circumstances than previously understood, in which only 3.4% of oncology drugs acquired FDA approval between 2000 and 2015 (Wong et al., 2018). Regardless of the precise percentage of failure, this poor clinical translation leads to the conclusion that current pre-clinical therapeutic testing platforms are not nearly rigorous enough to accurately predict therapeutic behavior in the human body.

In vitro, pre-clinical studies are conventionally performed on two-dimensional (2D) cell sheets or three-dimensional (3D) multicellular aggregate testing platforms. While these methods provide some insight into cell-therapeutic interactions, they are severely limited in their physiological relevancy and ability to model tumorigenic progression. 2D cell sheet cultures do not recapitulate important 3D cell-cell interactions formed in tumors *in vivo*, resulting in severe morphological and phenotypical deviations (Breslin and O'Driscoll, 2016, Myungjin Lee et al., 2013). Cancer cells cultured in 2D have been found to present diversified receptor proteins and drug transporters, in addition to decreased metabolizing enzyme activity, leading to lower innate resistance to anti-cancer therapeutics (Breslin and O'Driscoll, 2016). Furthermore, 2D cell sheet tissues also fail to recapitulate the limited molecular transport and subsequent differential drug distribution gradient found in tumors *in vivo* (Chauhan et al., 2011, Minchinton and Tannock, 2006). As a result, agents administered to 2D tissue cultures experience a near-infinite residence time during which they can initiate a therapeutic effect on each cell present in the culture, thus leading to a vast overestimation of their clinical capabilities (Das et al., 2015, Imamura et al., 2015).

Multicellular aggregates, or tumor spheroids, have emerged to address the dimensionality limitations of 2D cell sheets by culturing clumps of cancer cells in 3D formation, thus allowing biochemical gradients to form across the mass. Many fabrication methods have been reported including cell suspension spinner flasks, liquid-overlay, hanging-droplet, non-adherent microwell, and microfluidic techniques (Katt et al., 2016). Fundamentally, each of these methods preferentially initiate cell-cell interaction by suppressing cell-substrate interaction, thus inducing cellular aggregation. While tumor cell aggregates have the ability to express thickness-dependent genotypic and phenotypic

cellular variations and can be used in high-throughput screening (HTS), they are limited by poor structural control, high batch-to-batch variability, and difficulty in employing multiple or non-aggregating cell types (Mehta et al., 2012, Katt et al., 2016). Therefore, 3D tumor spheroids offer little more clinical relevancy than 2D cell sheets.

In vivo, pre-clinical studies employ animal models to provide the necessary drug safety and efficacy data needed for translation from bench to bedside. Furthermore, animal models provide a platform to study the events of tumorigenic progression from normal to invasive neoplastic tissue. Murine species, or rodents, are used most often and can be genetically engineered to develop *de novo* tumors or to modulate and humanize their immune response. Each mouse strain presents its own advantages and disadvantages in terms of its ability to serve as a pre-clinical oncology model. For example, immunocompetent syngeneic mice or genetically engineered mouse models (GEMMs) provide the ability to model a complete TME representative of the studied tumor with comprehensive stroma and murine immunity, however, experimental compounds must be cross-reactive for both humans and mice as the tumor will be comprised of only murine cells (Denayer et al., 2014, Kersten et al., 2017). Meanwhile, human-derived xenografts on immunodeficient mice allow analysis of human tumor response to administered therapeutics, however, they are unable to fully capture the intact human immune factor and complex tumor milieu (Denayer et al., 2014).

Several additional challenges face all murine model studies, regardless of mouse strain. These include costly animal maintenance, slow tumor development, complicated orthotopic implantation, dissimilar metabolic processes, limited accessibility for imaging and analysis, and most notably, poor predictive value (Denayer et al., 2014, Singh et al.,

2016). As a result, *in vivo* pre-clinical models fail to preferentially select efficacious, clinically translatable therapeutics, and thus cannot successfully bridge the gap between 2D *in vitro* and human studies. To begin to address some limitations of both *in vitro* and *in vivo* pre-clinical testing platforms, it is imperative that 3D engineered tumor tissue models be developed and implemented in the therapeutic development process.

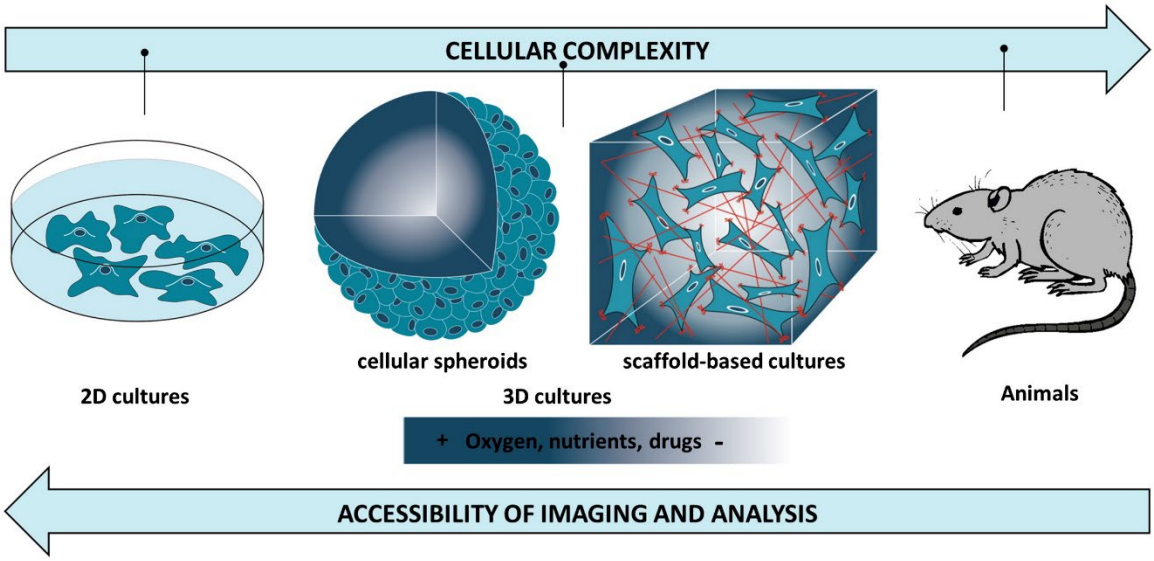

Figure 1: Current pre-clinical cancer models.

Advancements in tissue engineering techniques have enabled the development of in vitro cancer models that boast increased complexity and pathophysiological mimicry over traditional 2D or 3D aggregate culture systems, while maintaining a high level of accessibility for imaging and analysis (Reprinted with permission from Alemany-Ribes et al., 2014).

1.3 Tumorigenic Progression and the Native Tumor Microenvironment

The native TME is a multifarious network characterized by spatial and temporal heterogeneities and is found to contain genetically and phenotypically variable tumor, stromal, vascular endothelial, and immune cells embedded within the ECM (Junttila and de Sauvage, 2013, Dingli et al., 2009). Tumorigenic progression, and thereby formation of the TME, is initiated as a result of the uncontrollable division of a singular or small group of genetically mutant cell(s). Mutations are often thought to occur in a proto-oncogene, tumor-suppression gene, or stability gene, which result in stimulation of cellular division, prevention of apoptotic processes, and inability to mitigate detrimental genetic alterations, respectively (Vogelstein and Kinzler, 2004).

While a tumor can be originated from a single mutation, not all tumor cells within the TME are genotypically and phenotypically similar. Intratumoral, or subclonal, heterogeneity often arises as a result of spatial variations within the TME, which are derived from immediate cell population, biochemical gradients, and microarchitectural structure (Liu et al., 2018a, Burrell et al., 2013, Dingli et al., 2009). Tumor cells are found to adapt to changes in their immediate milieu and as a result, phenotypically express features that ensure their survival (Burrell et al., 2013, Balani et al., 2017).

As the tumor cells proliferate and commence the neoplastic process, they begin to recruit stromal cells, attract infiltrates of inflammatory cells, and initiate angiogenesis, or the formation of new blood vessels (Whiteside, 2008). Once entrapped within the TME, each of these cell types tend to deviate from their normal physiological roles and are coerced to promote tumorigenic progression (Whiteside, 2008, Yang, 2017). For example, tumor-associated macrophages (TAMs) are found to secrete pro-tumorigenic proteases,

cytokines, and growth factors; similarly, cancer-associated fibroblasts (CAFs) secrete ECM proteins and basement membrane components, while also suppressing immune response and supporting angiogenesis (Quail and Joyce, 2013).

As cells embedded within the TME proliferate to form cell-cell junctions and construct the ECM, several biophysical characteristics emerge within the tumor mass such as increased ECM stiffness, high interstitial pressure, and incomplete leaky vascularization (Cairns et al., 2006, Yang, 2017). These, in turn, induce biochemical gradients of pH, oxygen and nutrients, and metabolic waste, which most often lead to acidosis and hypoxia (Yang, 2017, Justus et al., 2013). As a result, distinct zones develop within the 3D tissue in which cellular behavior varies drastically.

Tumor cells at the core of the mass experience a highly acidic environment with little to no oxygen or nutrients and increased accumulation of metabolic waste; therefore, the tissue becomes necrotic (Lyssiotis and Kimmelman, 2017, Milotti et al., 2012). Conversely, tumor and stromal cells at the periphery of the mass are subjected to a highly vascularized environment and are thus tremendously proliferative and prone to metastasize (Lyssiotis and Kimmelman, 2017, Quail and Joyce, 2013, Milotti et al., 2012). Cells found at the midpoint of the mass, between the necrotic core and proliferative periphery, exist in a quiescent state in which they remain alive, however, do not actively divide (Milotti et al., 2012).

Metastasis, or the development of secondary tumor growths in tissues and organs beyond the point of origination, is the phenomenon that most directly results in cancer patient mortality (Budczies et al., 2015). It begins when primary tumor cells invade through the basement membrane and intravasate into the vascular system (Martin et al., 2013).

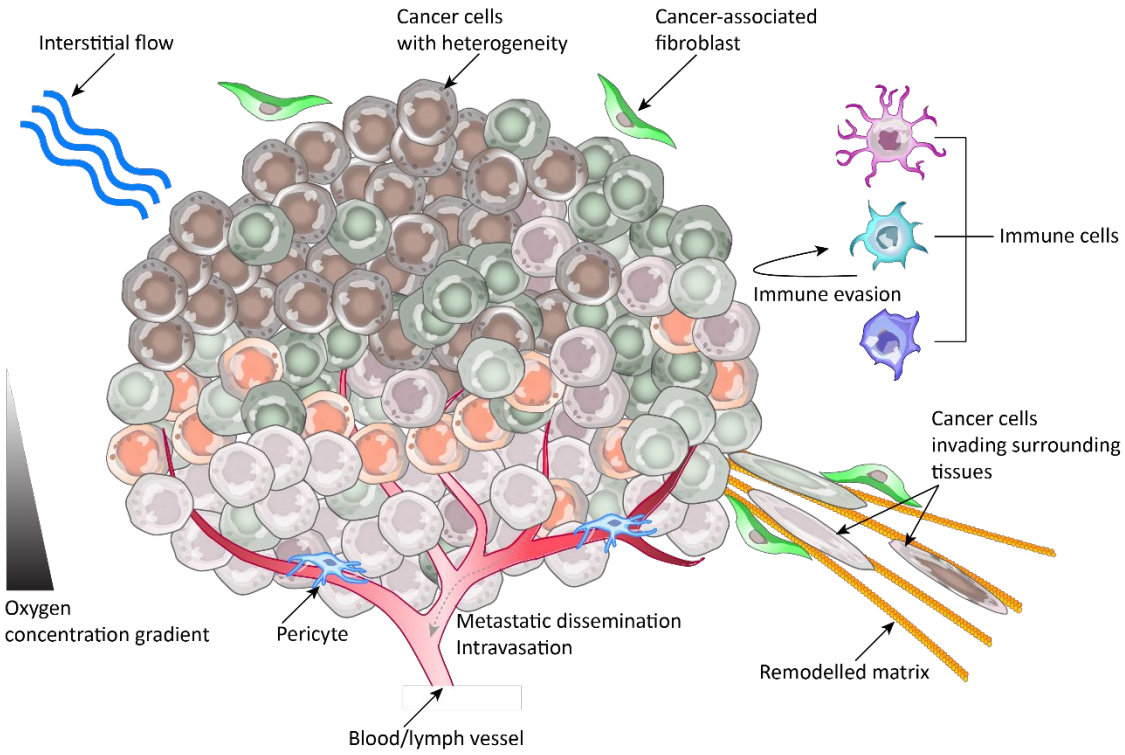

Figure 2: The complex pathophysiology of the native tumor microenvironment.

The native TME encompasses numerous spatial and temporal heterogeneities that ultimately result in well-defined inter- and intratumoral variability. Tumors in vivo exhibit non-uniform vascularization, induced oxygen and nutrient gradients, immune evasion, high interstitial pressure, and invasion and metastatic dissemination of cancer and stromal cell types (Reprinted with permission from Kim et al., 2019).

From there, the tumor cell can circulate throughout the body until it preferentially extravasates at a distal location based on the tissue or organ milieu.

Increasing evidence has demonstrated that tumor metastasis is likely enabled via the epithelial-mesenchymal transition (EMT), during which polarized epithelial cells assume a mesenchymal phenotype and thus, acquire migratory and invasive properties (Kalluri and Weinberg, 2009, Heerboth et al., 2015). Factors such as vascular structure, blood flow, tissue stiffness, and the presence of metastasis-initiating cells all contribute to the preferential metastatic pattern of circulating tumor cells (Lam et al., 2014, Quail and Joyce, 2013, Budczies et al., 2015, Baccelli et al., 2013, Polzer and Klein, 2013). Collectively, the TME is a highly intricate network that directly contributes to the complex pathophysiology of cancer. Therefore, it is imperative to accurately recapitulate as many characteristics of the TME as possible when engineering a biomimetic *in vitro* cancer microphysiological system for use in anti-cancer therapeutic testing.

1.4 Cell Sources for Cancer Tissue Engineering

As previously defined, cancer tissue engineering aims to combine novel biomaterials with cells and bioactive factors to produce functional tumor tissues. Cancer cells, as well as occasionally other supporting cell types, are employed in the model and are primarily derived from two sources: commercially available immortalized cell lines and patient-derived cells.

1.4.1 Immortalized Cell Lines

Human-derived cancer cell lines are the most widely used cell source employed in the investigation of cancer biology and anti-cancer therapeutic testing. Cell lines are originated from a patient and are immortalized to acquire the ability to avoid replicative

senescence and undergo unlimited divisions *in vitro*. The immortalization process can be performed via numerous methods of genetic manipulation; for example, the introduction of an exogenous human telomerase reverse transcriptase (hTERT) complementary deoxyribonucleic acid (cDNA) sequence encoding the catalytic subunit of telomerase can prevent the shortening of telomeres during the replication process, thus immortalizing the cell (Lee et al., 2004). Cell lines directly derived from tumors, however, innately demonstrate an infinite lifespan *in vitro*, signifying that tumor cells *in vivo* evade telomere attrition and subsequently, replicative senescence, which contributes to their high proliferative capacity (Jha et al., 1998).

The use of cell lines in cancer tissue engineering boasts numerous advantages such as an unlimited supply of a pure cell population, ability to yield reproducible results, and cost-effective culture (Kaur and Dufour, 2012). However, this in turn, introduces a set of limitations to their clinical relevancy. Cell lines at early passage numbers are genetically homogeneous, however, with serially increasing passages, cells may begin to express genotypic and phenotypic variations within a singular culture (Kaur and Dufour, 2012). Additionally, cell lines certainly do not incorporate the full range of cells found in tumors *in vivo*; moreover, the cancerous cells present often demonstrate poor correlation when compared back to tumor primary cells due to prolonged 2D culture *in vitro* (Kaur and Dufour, 2012, Sharma et al., 2010, Gillet et al., 2013). This significantly impacts their native function and response to external stimuli, and thus detracts from their ability to serve as a clinically relevant, predictive therapeutic testing platform.

1.4.2 Patient-derived Cells

To fully recapitulate both the genotypic and phenotypic variations of the myriad of cell types found in tumors *in vivo*, patient-derived cells must be employed. These cells originate from a current patient and are typically expanded in a mouse model prior to their implementation in cancer research efforts. To begin, tumor tissue samples are excised from the human patient and either dissociated to collect the cells (termed primary cells or primary cell lines) or immediately grafted as a solid mass into the flank of immunocompromised mice (Damhofer et al., 2015, Jang et al., 2017, Cheung et al., 2016, Mattern et al., 1988). This process, termed a patient-derived xenograft (PDX), is typically repeated multiple times to examine changes in the cell population and phenotypic expression after each regraftment, as well as to develop a bank of cells for future experimentation (Cheung et al., 2016, Damhofer et al., 2015).

Primary and PDX cells are found to more closely resemble the inter- and intratumoral cellular heterogeneity of the native TME than do immortalized cell lines (Choi et al., 2014). Important factors such as microarchitecture and gene expression profiles have been shown to be well preserved in PDX models (Daniel et al., 2009, Zhang et al., 2013, Lin et al., 2014). Furthermore, when grafted into humanized mouse models, these cells provide important insight into cancer biology and tumorigenic progression *in vivo* (Choi et al., 2014, Siolas and Hannon, 2013).

While patient-derived cell sources overcome many limitations of immortalized cell lines, inherent impediments are unavoidable. Most notably, primary and PDX cells are extremely unstable and will express major deviations from the original tumor upon serial passaging (Choi et al., 2014). Additionally, due to their propagation in host animals, a

significant portion of the PDX cell population is non-human, thus significantly affecting cell-cell interactions and targeting strategies. Finally, patient-derived cell sources are extremely limited, involve complex techniques, and require immense time and monetary investments throughout the duration of their use (Choi et al., 2014).

1.5 Biomaterials for Cancer Tissue Engineering

Recent advances in biomaterial synthesis and characterization have revolutionized the cancer tissue engineering field by introducing precise control over the biochemical and biophysical cellular microenvironment, thus overcoming the limitations of 2D cell sheets and providing critical physiological context. As previously discussed, 2D cell culture does not accurately recapitulate the microarchitecture of the native TME, and as a result, induces both genotypic and phenotypic aberrations *in vitro*. By equipping the cells with a 3D biomaterial scaffold, crucial cell-cell and signaling interactions are facilitated, resulting in the presentation of native tumor-mimetic morphology, gene and protein expression, and reactivity to anti-cancer therapeutics (Liu and Vunjak-Novakovic, 2016, Gill and West, 2014, Alemany-Ribes and Semino, 2014, Duval et al., 2017). Biomaterials in cancer tissue engineering can be classified in three key categories: natural, synthetic, and hybrid, and are preferentially chosen based upon the specific microenvironmental cues required by the application (Liu and Vunjak-Novakovic, 2016).

1.5.1 Natural Biomaterials

Natural biomaterials are typically derived from plant or animal sources, and as a result, have the ability to more accurately recapitulate native ECM structure and stiffness, as well as cell-matrix interactions. Collagen, Matrigel, glycosaminoglycan hyaluronic acid (HA), and decellularized human tissue ECM are most frequently used in cancer tissue

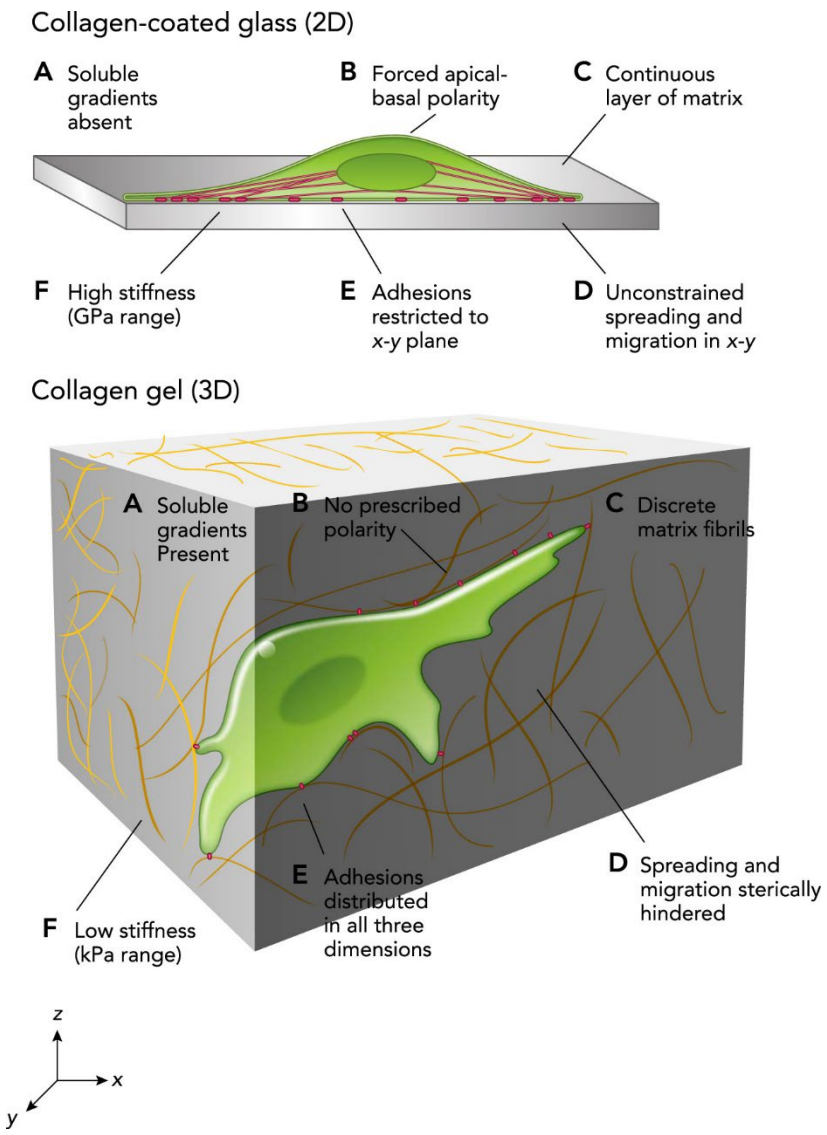

Figure 3: Biophysical advantages of three-dimensional versus two-dimensional cell culture methods.

The implementation of 3D engineered matrix scaffolds in cell culture introduces important biophysical cues at a cellular level, and thus yields more physiologically relevant cell behavior and morphology in vitro (Reprinted with permission from Duval et al., 2017).

engineering, and offer an ample presence of ligands for cell adhesion, as well as cell-mediated matrix degradation sites (Gill and West, 2014). Furthermore, due to the often fibrillar network of natural biomaterials, they are excellent candidates for the investigation of cellular migration and cancer cell metastasis (Gurski et al., 2012, Yu and Machesky, 2012, Provenzano et al., 2008). This in turn, however, introduces a set of limitations including batch to batch variation, limited culture time due to scaffold remodeling, very limited control over the matrix and its mechano-architectural properties, and loss of biochemical functionality upon additional physical crosslinking (Gill and West, 2014, Alemany-Ribes and Semino, 2014).

1.5.2 Synthetic Biomaterials

Conversely, synthetic biomaterials feature heightened control over the matrix complexity, as well as tunable physical physiognomies such as stiffness, pore size, and crosslinking density (Liu and Vunjak-Novakovic, 2016). Common polymers include polyacrylamide (PA), poly(ε-caprolactone) (PCL), poly(lactic acid) (PLA), poly(glycolic acid) (PGA), and poly(ethylene-glycol) (PEG), with each introducing unique advantages and disadvantages to the model. For example, PA is cytotoxic in 3D culture yet presents an immense range of tunable substrate mechanics; similarly, the polyesters (PCL, PLA, PGA, etc.) are non-cytotoxic, however, require an additional porogen processing step to ensure appropriate pore size for cell encapsulation and culture medium diffusion (Weigel et al., 2006, Gill and West, 2014, Caliari and Burdick, 2016, Alemany-Ribes and Semino, 2014). Altogether, most synthetic biomaterials also exhibit restricted bioactivity and rely on non-specific protein adsorption from culture medium to support cell adhesion and proliferation; furthermore, while the degradation of the synthetic matrices is well-

characterized and predictable, it is unable to be cell-mediated (Gill and West, 2014). As such, encapsulated cells cannot temporally remodel their microenvironment as they migrate and proliferate through the polymer matrix.

1.5.3 Hybrid Biomaterials

Many limitations of both natural and synthetic biomaterials can be alleviated through supplemental engineering efforts to adjust the biophysical and biochemical characteristics of the substrate. These hybrid, or biosynthetic, materials are often crosslinkable, boast precise control over the scaffold and its mechano-architectural properties, as well as ensure the presence of bioactive components to augment the biomimicry of the model and promote appropriate tumor cell behavior *in vitro*. For example, synthetic polymers can be improved through the intercalation of integrin-binding cell adhesion sites, such as an Arg-Gly-Asp (RGD) tripeptide, or cell-mediated degradation sites, such as a matrix metalloproteinase (MMP) hexapeptide substrate linked with the amino acid blocks, Arg-Ala-Asp-Ala (RADA) (Chau et al., 2008, Ruoslahti, 1996). Conversely, novel natural biomaterial-derived matrices can be fabricated the through the functionalization and acrylation of bioactive hydrogels, such as HA, to permit increased crosslinking ability (Xu et al., 2012, Park et al., 2017). Similarly, denatured fibrinogen fragments can be PEGylated utilizing poly(ethylene glycol)-diacrylate (PEGDA), thus resulting in a photocrosslinkable hybrid matrix featuring both cell adhesion and cell-mediated degradation sites (Almany and Seliktar, 2005).

Overall, the incorporation of biocompatible materials in 3D cancer cell culture augments the ability of the *in vitro* model to mimic key characteristics of the native TME. Most notably, hybrid biomaterials boast the ability to amalgamate the biomimetic features

of natural biomaterials required for appropriate cellular function with the tunability and reproducibility of synthetic biomaterials; thus, demonstrating immense potential for scalable production and increasing the likelihood of implementation in the drug development process.

This chapter has been adapted from previous thesis work (Habbit, 2018).

Chapter 2. Tunable Engineered Prostate Cancer Tissues for *in vitro* Recapitulation of Heterogeneous *in vivo* Prostate Tumor Stiffness

2.1 Abstract

This chapter reports the establishment and characterization of a three-dimensional *in vitro*, coculture engineered prostate cancer tissue (EPCaT) disease model based upon and informed by a characterization of *in vivo* prostate cancer (PCa) xenograft tumor stiffness. In prostate cancer, tissue stiffness is known to impact changes in gene and protein expression, alter therapeutic response, and be positively correlated with an aggressive clinical presentation. To inform an appropriate stiffness range for the *in vitro* model, PC-3 prostate tumor xenografts were established. Tissue stiffness ranged from 95 to 6,750 Pa. Notably, xenograft cell seeding density significantly impacted tumor stiffness; a two-fold increase in the number of seeded cells not only widened the tissue stiffness range throughout the tumor, but also resulted in significant spatial heterogeneity. To fabricate the *in vitro* EPCaT model, PC-3 castration-resistant prostate cancer cells were co-encapsulated with BJ-5ta fibroblasts within a poly(ethylene glycol)-fibrinogen matrix augmented with excess poly(ethylene glycol)-diacrylate to modulate the matrix mechanical properties. Encapsulated cells temporally remodeled their *in vitro* microenvironment and enrichment of gene sets associated with tumorigenic progression was observed in response to increased matrix stiffness. Through variation of matrix composition and culture duration, EPCaTs were tuned to mimic the wide range of biomechanical cues provided to PCa cells *in vivo*; collectively, a range of 50 to 10,000 Pa was achievable. Markedly, this also encompasses published clinical PCa stiffness data. Overall, this study serves to introduce the bioinspired,

tunable EPCaT model and provide the foundation for future PCa progression and drug development studies.

2.2 Introduction

Prostate cancer (PCa) currently represents 10.6% of all new cancer cases in the United States; due to advances in early detection, 76% are localized to the prostate at the time of diagnosis, however, 13% have invaded regional lymphatic vessels and 6% exhibit distant metastases (National Cancer Institute). Notably, the five-year relative survival rate drops from 100% in localized cases to 30.2% in patients who present with metastatic lesions (National Cancer Institute). As neoplastic epithelial cells proliferate at the primary tumor site, they begin to incorporate and even alter the phenotype transition of stromal cell types, such as macrophages and fibroblasts; clinically in PCa, the epithelial to stromal cell ratio varies drastically and stromal content can range from 2 – 100% (Boufaied et al., 2019). Often, these cells deviate from their normal physiological roles to promote localized tumorigenesis and provide the toolset necessary for cancer cell invasion and metastasis, thus driving poor clinical prognoses (Whiteside, 2008, Kalluri, 2016). This intricate tumor microenvironment (TME) is heterogeneous and characterized by spatial disparities in the incidence of phenomena such as fibroblast-mediated extracellular matrix (ECM) remodeling and angio- and lymphangiogenic development; this culminates in the development of distinct biochemical and biophysical gradients across the tumor mass and drives heterogeneity in both cancer cell behavior and tumor tissue stiffness (Oudin and Weaver, 2016, Malandrino et al., 2018, Emon et al., 2018, Levental et al., 2009).

Tumor stiffness has been previously found to induce changes away from original tumor cell lineage, lead to variations in gene expression and intracellular signaling

pathways, and initiate epithelial-mesenchymal transition (EMT), thus regulating cell migration (Kalli and Stylianopoulos, 2018, Handorf et al., 2015, Wei and Yang, 2016, Emon et al., 2018, Wei et al., 2015, Matte et al., 2019, Seo et al., 2015, Leight et al., 2017, Aw Yong et al., 2017, Alonso-Nocelo et al., 2018). Furthermore, strong correlations have been found to exist between both two-dimensional (2D) and three-dimensional (3D) cell culture platform stiffness and acquired chemoresistance and varied drug response *in vitro* (Lam et al., 2014, Langhans, 2018, Deville and Cordes, 2019, Leight et al., 2017). Therefore, to accurately recapitulate the TME and more closely mimic patient tumor behavior, *in vitro* cancer models must not only support cancer and stromal cell-cell interactions, but also provide pathophysiologically relevant biomechanical cues via the inclusion of a matrix of similar stiffness to native tumors. In recent years, a number of 3D *in vitro* models of other solid cancer types with tunable matrix stiffnesses have been reported (Shen et al., 2014, Chwalek et al., 2014, Fisher et al., 2015, Jabbari et al., 2015, Yang et al., 2013, Cavo et al., 2016, Pradhan et al., 2017b); once established, studies employing these models expounded upon and validated the significant impact of biophysical cues on key tumorigenic aspects such as aggressiveness, stemness, vascularization, and invasion. Frequently, however, a correlation to the pathogenic stiffness ranges observed in tumors *in vivo* was not provided. Markedly, a 3D *in vitro* PCa model that employs a tunable matrix stiffness and introduces an ability to mimic the range of specific biomechanical phenomena within the site-of-origin or soft-tissue metastatic TME has yet to be reported at all, despite numerous reviews expressing the critical need for such a platform (Kalli and Stylianopoulos, 2018, Gkretsi and Stylianopoulos, 2018, Malandrino et al., 2018, Chim and Mikos, 2018).

This study reports a first of its kind *in vivo – in vitro* prostate tumor tissue stiffness comparison and introduces a tunable poly(ethylene glycol)-fibrinogen (PF) based *in vitro* 3D engineered prostate cancer tissue (EPCaT) platform that is based upon and informed by a characterization of *in vivo* PCa xenograft tumor stiffness. The EPCaT model is enzymatically cleavable and thus supports cell-mediated remodeling of the 3D matrix. Furthermore, it is functionalized to mimic the biomechanical cues provided to PCa cells *in vivo* via matrix modulation with the addition of 1%, 2%, and 3% (w/v) excess poly(ethylene glycol)-diacrylate (PEGDA). The addition of excess PEGDA to the PF polymer precursor solution in amounts ranging from 0-3% (w/v) has been previously reported to significantly increase the Young's modulus of acellular hydrogels and direct phenotypic and behavioral changes among encapsulated cell populations (Pradhan et al., 2017b, Peyton et al., 2008, Dikovsky et al., 2006). Within the EPCaT model, the biophysical cues are further augmented by the presence of matrix-remodeling fibroblast cells; notably, the fibroblasts also provide more physiologically relevant biochemical cues via direct interaction with the PCa cells (Levesque and Nelson, 2018, Blom et al., 2019). Consequential changes in encapsulated cell behavior and gene expression due to modulation of the EPCaT matrix composition are monitored and reported. Furthermore, the impact of initial cell seeding number on the resultant microarchitecture of PC-3 tumor xenografts is elucidated. Overall, these findings can be utilized to evaluate the ability of the established PF-based EPCaT model to more accurately recapitulate several key characteristics of the *in vivo* prostate cancer TME; additionally, this work provides a foundation for future application of the EPCaT model in drug testing and disease modeling studies.

2.3 Materials and Methods

All chemicals were acquired from Sigma-Aldrich (St. Louis, MO) unless stated otherwise.

2.3.1 PEGDA Synthesis and Characterization

PEGDA was synthesized according to established protocols (Pradhan et al., 2014, DeLong et al., 2005). 10kDA molecular weight PEG was reacted with acryloyl chloride (1:4 molar ratio) in anhydrous dichloromethane with triethylamine (1:2 molar ratio) under argon overnight at 25 ºC. The resultant PEGDA was purified through phase separation with 2M potassium carbonate. The organic phase, containing PEGDA, was dried using anhydrous magnesium sulfate and subsequently filtered. Finally, the synthesized PEGDA was precipitated using diethyl ether, again filtered, and dried overnight under vacuum at 25 ºC. ^{1}H NMR was performed to characterize the degree of acrylation achieved during synthesis. PEGDA was stored at -20 ºC.

2.3.2 PF Synthesis and Characterization

PF was synthesized according to an established protocol (Almany and Seliktar, 2005). Bovine fibrinogen was dissolved in an 8M urea solution in 10mM phosphate buffered saline (PBS) at a final concentration of 7 mg/mL. Tris (2-carboxyethyl) Phosphine Hydrochloride (TCEP-HCl) was added to the solution at a TCEP to fibrinogen cysteine molar ratio of 1.5:1. The final solution pH was adjusted to 8.0. Synthesized PEGDA was also dissolved and subsequently centrifuged in an 8M urea in 10mM PBS buffer solution at a final concentration of 280 mg/mL. The PEGDA solution was slowly added to the fibrinogen solution, and the consequent reaction was allowed to proceed under dark conditions for 3 hours at 25 ºC. The reaction was stopped by adding an equal volume of the urea-PBS buffer solution and precipitated through the addition of acetone at a 4:1

volumetric ratio of acetone to reaction solution. The precipitate product was separated from the liquid phase via centrifugation, weighed, and re-dissolved in the urea-PBS buffer at a final concentration of 2.6 mL buffer per gram of precipitate. The product solution was then dialyzed against 1L sterile PBS three times over a period of 24 hours under dark conditions at 4 ºC. The final PF product was aliquoted into sterile microcentrifuge tubes and stored at -80 ºC. A standard Pierce™ BCA Protein Assay Kit (Thermo Fisher Scientific, Rockford, IL) was utilized to characterize the protein concentration of the synthesized PF; PF with protein concentrations ranging from 10 – 12 mg/mL was used for all experiments performed herein.

2.3.3 Cell Culture and Maintenance

PC-3 cells (ATCC, Manassas, VA) were cultured in F-12K culture media (Corning, Corning, NY) supplemented with 10% (v/v) fetal bovine serum (FBS) (Atlanta Biologicals, Flowery Branch, GA) and 1% (v/v) Pen-Strep (GE Healthcare Bio-Sciences, Pittsburgh, PA). BJ-5ta normal human foreskin hTERT immortalized fibroblasts were acquired from ATCC (Manassas, VA) and were cultured in 4 parts of DMEM (Lonza, Walkersville, MD) containing 4 mM L-glutamine, 4.5 g/L glucose and 1.5 g/L sodium bicarbonate, and 1 part of Medium 199 (Lonza, Walkersville, MD) supplemented with 0.01 mg/mL hygromycin B (MilliporeSigma, Burlington, MA), and 10% (v/v) FBS. All cells were maintained within plasma-treated polystyrene tissue-culture flasks stored in a humidified atmosphere with 5% CO_2 and a constant temperature of 37 ºC; culture media was renewed twice weekly. Cells adherently cultured in 2D were enzymatically dissociated from the tissue-culture flask surface in preparation for passaging or 3D culture using 0.25% trypsin/2.21mM EDTA (Corning, Corning, NY).

2.3.4 Prostate Tumor Xenograft Sample Preparation

Human PC-3 tumor xenografts were established in partially immunocompromised, athymic NCr nude (nu/nu) mice obtained from Taconic Farms, Inc., (Germantown, NY). Mice were maintained in pathogen-free cages in a light and temperature-controlled isolated room and provided standard rodent chow and water *ad libitum* during the study. All studies were performed under protocols that were approved by the Institutional Animal Care and Use Committee (IACUC) and in compliance with the U.S. Public Health Service (PHS) Policy on Humane Care and Use of Laboratory Animals, updated 2015. Tumor xenografts were established by injection of 200 μL of a 1:1 (v/v) suspension of human PC-3 cells in serum-free media with ice-cold sterile Matrigel (Corning, Tewksbury, MA) subcutaneously into the left rear flank of NCr mice (approximately 25 grams in weight and 8 weeks of age). The impact of seeding density on tumor properties was determined via injection of cell suspension containing either: 1 x 10^6 cells (Group 1X) or 2 x 10^6 cells (Group 2X). Note, the total injection volume and volume of Matrigel were not changed. Tumor growth was measured weekly by palpating the tumor mass and measuring the dimensions with digital calipers to estimate the volume, as described previously (Kang et al., 2015). In brief, tumor ellipsoid volume was estimated by the product of the largest dimension and (smallest dimension)^2 × Pi/2. Tumors were surgically excised from the host animals at diverse volumes that ranged from approximately 300 to 1,500 mm^3 to ensure adequate intertumoral heterogeneity was assessed in regard to the native mechanical stiffness of the tumor tissue. It is important to note that xenograft sample sets are named alphabetically according to the tumor size at excision (e.g. the smallest tumor of Group 1X is named 1X-A). Upon excision, tumors were sliced into approximately 1 mm thick

sections and labeled as core, midpoint, or periphery, depending on their original geometric location within the tumor mass. A 3 mm diameter biopsy punch was then used to yield disc-shaped samples that mimic the geometry of the EPCaTs. A total of five Group 1X and ten Group 2X tumors were harvested; each tumor was sectioned to yield up to three samples from each of the three geometric locations, depending on the original tumor size. *In vivo* prostate tumor tissue samples were placed in PBS and immediately analyzed using the MicroSquisher apparatus (CellScale, Waterloo, ON, CA).

2.3.5 Multispectral Optoacoustic Tomography

MSOT imaging was performed using the *InVision 256-TF* and *ViewMSOT* v3.6.0.119 (iThera Medical GmbH, Munich, GE), as previously reported (Brannen et al., 2018). Mice were anesthetized with constant 1–3% isoflurane and medical-grade oxygen supply throughout the imaging procedure. Scans were performed using a 0.5 mm slice separation spanning the entire tumor region for each mouse at excitation lights of 715, 730, 760, 800, and 850 nm. Photo-acoustic signals from oxygenated and deoxygenated hemoglobin were spectrally un-mixed from the overall photo-acoustic signal using built-in reference spectra.

2.3.6 Cell Encapsulation in PF Hydrogels with Excess PEGDA

EPCaTs were formed in cylindrical shaped poly(dimethyl siloxane) (PDMS) molds, which were prefabricated for use in the encapsulation process. Briefly, PDMS sheets were constructed using the SYLGARD 184 Elastomer Kit (Thermo Fisher Scientific, Rockford, IL) and shaped with a 3 mm diameter biopsy punch. PDMS molds were firmly adhered to the bottom of a 6-well polystyrene plasma treated tissue-culture plate to prevent leakage of the cell-laden hydrogel precursor solution. The hydrogel

precursor solution was prepared by adding 1.5% (v/v) Triethanolamine (TEOA), 37 mM 1-vinyl-2-pyrrolidinone (NVP), and 0.1 mM Eosin Y to the synthesized PF in solution with PBS. With the aim of modulating the mechanical stiffness of the EPCaTs, excess synthesized PEGDA at a concentration of 250 mg/mL in solution with 1X PBS was added to the hydrogel precursor solution at volumetric ratios of 96:4 (1% w/v), 92:8 (2% w/v), and 88:12 (3% w/v). To encapsulate cells within the hydrogel scaffold, cancer and stromal cells maintained in 2D tissue-culture flasks were enzymatically dissociated from the flask surface as previously stated, counted using a hemocytometer with 0.4% Trypan Blue (Lonza, Walkersville, MD), and resuspended in the hydrogel precursor solution at a concentration of 20 x 10^6 cells/mL at a ratio of 5:1 PC-3 cancer cells to BJ-5ta fibroblasts. It is important to again note that while the stromal content of native PCa varies substantially (Boufaied et al., 2019), the epithelial to stromal cell ratios in the normal prostate and in benign prostatic hyperplasia (BPH) are 1:2 and 1:5, respectively (Shapiro et al., 1992). As such, the 5:1 cancer cell to fibroblast cell ratio employed in this study was chosen as a starting point opposite the normal and BPH conditions. A volume of 10 μL of the cell-laden hydrogel precursor solution was pipetted into each PDMS mold well and photocrosslinked via visible light exposure (light intensity: 203 mW/cm^2) for 2 minutes. Upon crosslinking completion, the PDMS mold was carefully peeled back from the well plate surface, thus leaving behind disc-shaped, EPCaTs. Appropriate culture media was added to the well plate, which was finally stored in a humidified atmosphere with 5% CO_2 and a constant temperature of 37 ºC; culture media was renewed twice weekly. Encapsulation was performed on Day 0 of EPCaT culture; all Day 1 time points evaluated

herein were assessed approximately 24 hours post-encapsulation and thus, some cell-derived impacts on the microenvironment are expected on Day 1.

2.3.7 Image Acquisition and Analysis

Phase contrast images of the EPCaTs were acquired at several levels of magnification (2X, 10X, 20X) using an inverted Nikon Eclipse Ti microscope fitted with an Andor Luca S camera on culture Days 1, 8, 15, 22, and 29 post-encapsulation. The resultant images were analyzed utilizing ImageJ software, version 1.52c, to quantify both whole hydrogel tissue and individual cell colony area and roundness by drawing regions of interest (ROI) around the desired structures.

2.3.8 Cell Viability Investigation

Encapsulated cell viability was assessed via fluorescent microscopy through the visualization and quantification of both live and dead cells within the EPCaTs. Using the LIVE/DEAD™ (Invitrogen, Carlsbad, CA) mammalian cell cytotoxicity kit, live cells were positively labeled with green-fluorescent Calcein-AM, indicating intracellular esterase activity and an intact plasma membrane. Simultaneously, dead cells were positively labeled with red-fluorescent Ethidium Homodimer-1, indicating the loss of plasma membrane integrity. The H33342 fluorochrome (MilliporeSigma, Burlington, MA) was also used to positively label DNA within all cellular nuclei. It is important to note that the photoinitiator utilized during the encapsulation process auto-fluoresces on the same wavelength as the Calcein-AM live cell stain and thus can interfere with image analysis. EPCaTs were incubated in the LIVE/DEAD/H33342 stain on Days 1 and 15 post-encapsulation for 30 minutes at 25 ºC, washed with PBS, and imaged utilizing confocal microscopy (Nikon AI Confocal Scanning Laser Microscope). The DEAD stain was visualized via the TRITC

filter, the LIVE stain was visualized via the FITC filter, and the H33342 stain was visualized via the DAPI filter. The resultant z-stack images were analyzed with ImageJ software and cellular viability was quantified by manually counting the live and dead cells in each slice of the z-stack.

2.3.9 Immunostaining and Fluorescence Microscopy

The 3D cell morphology and population distribution of cancer and stromal cells within the EPCaTs was visualized by immunostaining and confocal fluorescent microscopy on Days 1 and 15. Alexa Fluor™ 568 Phalloidin (Thermo Fisher Scientific, Rockford, IL) at a 1:200 dilution in PBS was used to positively label F-actin filaments. H33342 at a 1:200 dilution in PBS was used to positively label intranuclear DNA. Finally, a Zenon™ Alexa Fluor™ 647 Mouse IgG_1 Labeling Kit (Thermo Fisher Scientific, Rockford, IL) was employed with the anti-fibroblast monoclonal antibody clone TE-7 (MilliporeSigma, Burlington, MA) at a 1:100 dilution to positively label fibroblasts. In preparation for staining, EPCaTs were washed in PBS and fixed overnight at 4 ºC with 4% paraformaldehyde (PFA) (Electron Microscopy Sciences, Hatfield, PA). Encapsulated cells were permeabilized with 0.5% Triton-X for 30 minutes and subsequently blocked via incubation in 0.2 μm filtered blocking buffer (10% FBS and 0.5% bovine serum albumin (BSA) in PBS) for 1 hour at 25 ºC. EPCaTs were then labeled in a Phalloidin/Zenon™ Alexa Fluor™ 647-TE-7 staining solution for a minimum of 1 hour at 25 ºC, rinsed with PBS, again labeled in a H33342 staining solution for a minimum of 1 hour at 25 ºC, and finally rinsed with PBS. Immunostained EPCaTs were mounted on glass coverslips and imaged utilizing confocal microscopy (Nikon AI Confocal Scanning Laser Microscope). The phalloidin stain was visualized via the TRITC filter, the H33342 stain was visualized

via the DAPI filter, and finally the Zenon™ Alexa Fluor™ 647-TE-7 stain was visualized via the cyanine-5 (CY5HQ) filter. Fluorescent images were analyzed utilizing ImageJ software and ROI were drawn to quantify the area, circularity, aspect ratio, and feret diameter of each of the cell colonies throughout the z-stacks; calculated values were then exported to Microsoft Excel.

2.3.10 Tissue Stiffness Quantification

The mechanical stiffness of the EPCaTs on Days 1, 15, and 22 post-encapsulation and the *in vivo* prostate tumor tissues post-excision were quantified via parallel plate compression testing under physiological conditions through the use of a MicroSquisher (CellScale, Waterloo, ON, CA) apparatus according to manufacturer instructions. *In vitro* and *in vivo* samples were loaded onto a stage at the front of a fluid bath test chamber filled with PBS and held at 37 ºC. A 558.8 μm diameter tungsten wire microcantilever beam fitted with a compression platen was affixed to the vertical piezo motor driven actuator at a 90º angle and positioned at the top of the sample. Tissues were compressed to a minimum 15% deformation at a maximum compression rate of 10 μm/s for three cycles. Cycle to cycle and sample to sample variability for acellular PF hydrogels is illustrated in Figure 4 to demonstrate MicroSquisher measurement reproducibility when there is no cell-derived heterogeneity between samples. The force applied to the sample was calculated via deflection of the employed microcantilever beam; tissue displacement was tracked with the MicroSquisher system camera and analyzed utilizing ImageJ software. Force versus displacement data was gathered and exported to a custom Microsoft Excel macro to create

a compressive stress (σ) versus strain (ε) curve; the linear portion slope of which yielded the Young's modulus of the sample. All tissue samples were tested in triplicate.

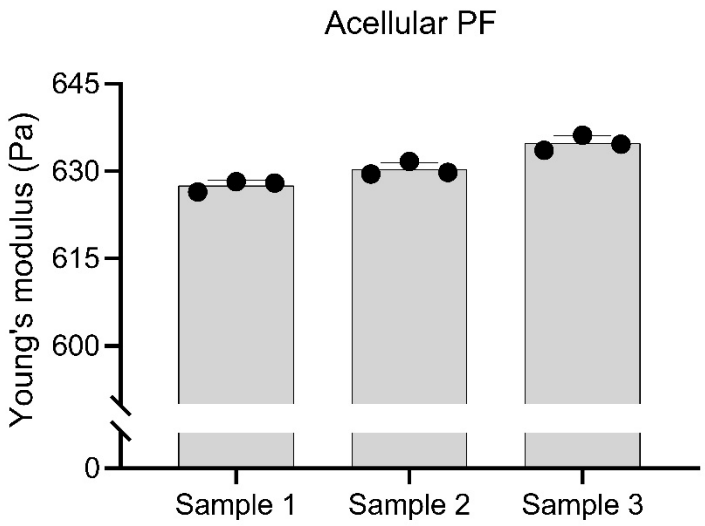

Figure 4: The Young's modulus of acellular PF hydrogels is highly reproducible when there are no cell-derived effects on matrix integrity.

Hydrogel stiffness was measured using the MicroSquisher apparatus via three compression cycles; each data point above represents one cycle (n = 3 cycles per each of three acellular hydrogel samples).

2.3.11 Acellular EPCaT Degradation

The enzymatic degradation profiles of PF, PF+1%PEGDA, PF+2%PEGDA, and PF+3% PEGDA EPCaTs were assessed according to a published protocol (Pradhan et al., 2017b). Briefly, acellular hydrogels of each matrix composition were crosslinked and permitted to swell in PBS until equilibrium was reached. The hydrogels were then incubated in a 1 mg/mL collagenase type 2 (Worthington, LakeWood, NJ) solution. Leveraging the green autofluorescence of the EosinY photoinitiator, fluorescent images

were taken at 15 minute intervals for up to 150 minutes. The resultant images were analyzed using ImageJ to quantify temporal changes in area by drawing ROI around the edge of the hydrogels. All samples were tested in triplicate.

2.3.12 Immunohistochemistry

To visualize *in vitro* EPCaT microanatomy, immunohistochemical staining was performed. EPCaTs of each matrix composition were fixed in 70% ethanol with 0.1% (w/v) EosinY to help visualize the tissues. Next, fixed EPCaTs were paraffin-embedded, sectioned, and stained using hematoxylin and eosin (H&E). An Aperio CS2 scanner (Leica Biosystems, Buffalo Grove, IL) was employed to image the stained tissues at 40X magnification and Aperio ImageScope software (Ver. 12.4.0.5043) was used to visualize the digital images.

2.3.13 Next-generation RNA sequencing

RNAseq was performed similar to an established protocol (Mitra et al., 2020). Briefly, high-quality total RNA from EPCaTs ($n \geq 2$ EPCaTs per matrix composition) and 2D co-cultured PC-3 and BJ-5ta cells ($n > 1 \times 10^6$ 2D cells, seeded at a cancer to fibroblast cell ratio of 5:1) was extracted using QIAshredder and an RNeasy kit (QIAGEN, Germantown, MD) according to the manufacturer protocol. RNA concentration and integrity were evaluated using a 2100 Bioanalyzer Instrument (Agilent, Santa Clara, CA) and the Nanodrop-8000 (ThermoFisher Scientific, Rockford, IL). An RNA integrity number (RIN) greater than nine was achieved for all samples. RNAseq libraries were constructed using a TruSeq RNA Sample Preparation kit v2 (Illumina, Inc., San Diego, CA) and RNA sequencing was performed on a HiSeq 2000 (Illumina, Inc., San Diego, CA). The FastQC tool was employed in a quality control (QC) check on the RNAseq raw

reads. Finally, processed RNAseq reads were mapped to the human genome using the Spliced Transcripts Alignment to a Reference (STAR) aligner tool. It is important to note that Day 15 PF, PF+2%PEGDA and PF+3%PEGDA EPCaTs were selected for transcriptomic analysis as it was anticipated the resultant comparisons would reveal the most interesting variations in gene expression.

2.3.14 Bioinformatics Analysis

Differential gene expression analysis was performed on CPM-normalized read counts using a multi-model approach based on limma trend through an empirical Bayes method for gene expression estimation. Genes with $p \leq 0.05$ and Log_2(Fold Change) $\geq \pm 1.5$ were considered differentially expressed. Gene set enrichment analysis (GSEA) was performed using the clusterProfiler R package (Yu et al., 2012) and the Molecular Signature Database (MSigDB) Hallmark gene sets (Liberzon et al., 2015). Normalized enrichment scores (NES) and the false discovery rate (FDR) q-value are reported. Gene ontology (GO) biological process over-representation analysis was also performed using the clusterProfiler R package; the GOSemSim (Yu et al., 2010, Yu, 2020) and rrvgo (Sayols, 2020) packages were additionally employed to eliminate redundant GO terms and to generate tree maps to illustrate a two-level hierarchy of GO terms, respectively. Finally, Euler diagrams were constructed using the eulerr web application (Larsson, 2020).

2.3.15 Statistical Methods

GraphPad Prism 8.0 (GraphPad Software, San Diego, CA) was employed for statistical analysis and figure preparation. Outliers were removed using the robust regression and outlier removal (ROUT) method with coefficient Q = 1% and the distribution normality and equality of variance were checked. T-tests were performed to

compare the means of two groups, while one- or two-way ANOVA in conjunction with the Tukey *post hoc* test was performed to compare the means of more than two groups. In the event of non-normal distribution, the Kruskal-Wallis and Dunn's multiple comparisons *post hoc* test was alternatively performed to compare the means of more than two groups. Finally, linear regression analysis was used to determine rates of increase or decrease. A p value of ≤ 0.05 was considered statistically significant unless otherwise stated. Statistical significance is denoted by the following symbol and letter designations: ns indicates no statistical significance, * indicates statistical significance with $p \leq 0.05$, ** indicates statistical significance with $p \leq 0.01$, and **** indicates statistical significance with $p \leq 0.0001$; data that do not share a letter designation (e.g. A versus B or C versus DE) are significantly different with $p \leq 0.05$. Error bars indicate standard deviation unless otherwise indicated.

2.4 Results

In vivo and *in vitro* experiments were performed in parallel; results from each are first presented individually and then subsequently combined in a unique *in vivo* versus *in vitro* prostate tumor comparison.

2.4.1 *PCa tumor xenografts exhibit significant inter- and intratumor spatial heterogeneity in tissue stiffness and vascular microarchitecture*

To generate prostate tumor xenografts for application in an *in vivo – in vitro* tissue microarchitecture study, PC-3 cells suspended in Matrigel were subcutaneously injected into the rear flank of partially immunocompromised, athymic nude NCr mice in two groups. Group 1X tumors were seeded with 1 x 10^6 PC-3 cells; Group 2X tumors were seeded with 2 x 10^6 PC-3 cells. The resultant tumors from each group were surgically

excised at sizes ranging from approximately 300 to 1,500 mm^3 to ensure adequate intertumoral heterogeneity. Table 1 provides information regarding the time from implantation to excision and the final tumor volume for both Group 1X and Group 2X PC-3 tumors.

Table 1: Group 1X and Group 2X PC-3 xenograft tumor data.

Group	Mouse	Tumor Growth Duration (days)	Final Tumor Volume (mm^3)
1X	A	54	361
1X	B	54	598
1X	C	54	643
1X	D	54	708
1X	E	54	1430
2X	A	54	306
2X	B	33	360
2X	C	69	392
2X	D	33	393
2X	E	33	416
2X	F	69	432
2X	G	54	441
2X	H	54	651
2X	I	69	819
2X	J	69	927

Upon excision, the PC-3 tumors were sectioned into 1 mm thick slices and biopsied using a 3 mm punch to yield samples from the geometric core, midpoint, and periphery, similar in geometry to the EPCaTs (Fig. 5). It is important to note that the geometric core reported here does not necessarily correlate to a necrotic core within the tumor mass in all cases; rather samples were collected from a variety of locations to establish adequate representation of the intratumoral spatial heterogeneity observed *in vivo*.

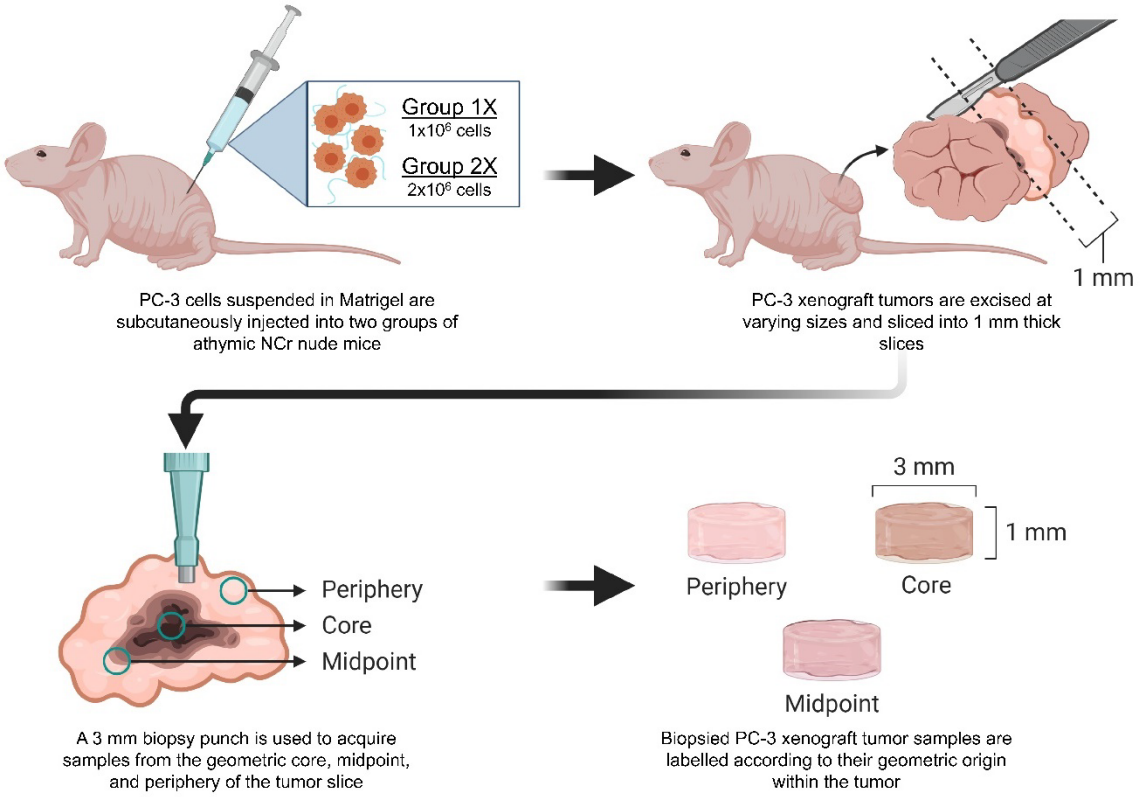

Figure 5: PC-3 xenograft tumors were sectioned and biopsied to generate tissue samples originating from the geometric core, midpoint, and periphery of the malignant mass.

Group 1X and Group 2X *in vivo* PC-3 tumor samples originating from the geometric core, midpoint, and periphery of the xenograft tumors were subjected to parallel plate compression testing to elucidate the stiffness range via Young's modulus quantification. Depending on tumor size, approximately three samples from each core, midpoint, and periphery were analyzed per tumor (n = nine) with three measurements performed per sample. The Group 1X core, midpoint, and periphery regions ranged in stiffness from approximately 95 – 2,000 Pa, 350 – 3,500 Pa, and 100 – 3,300 Pa, respectively (Fig. 6A,F). Conversely, the Group 2X core, midpoint, and periphery regions ranged from approximately 400 – 3,200 Pa, 250 – 4,500 Pa, and 650 – 6,750 Pa, respectively (Fig. 6C,F). It is important to note that both Group 1X and Group 2X tumors are arranged according to the size at excision in Figure 6(A,C); tumor volume increases from left to right within each geometric region, however, a clear trend in stiffness relative to tumor size was not initially observed for either group. The 1X-C tumor core sample data showed inconsistencies in parallel plate compression test recordings and was thus eliminated to ensure overall data integrity; consequently, the 1X-C sample was moved to the end of the Group 1X tumor set in Figure 6A. The 2X-C tumor presented visually distinct regions of heterogeneous vascularization; six samples in total (two from each core, midpoint, and periphery) were collected from both the bloody and non-bloody regions of the tumor to provide context for the role of heterogeneous tumor vascularization in tissue stiffness.

Size binning was performed to better elucidate the relationship between tumor size and the Young's modulus of the tumor tissue; the Group 1X and Group 2X tumor size classifications presented below were chosen based upon the number of mice in the group

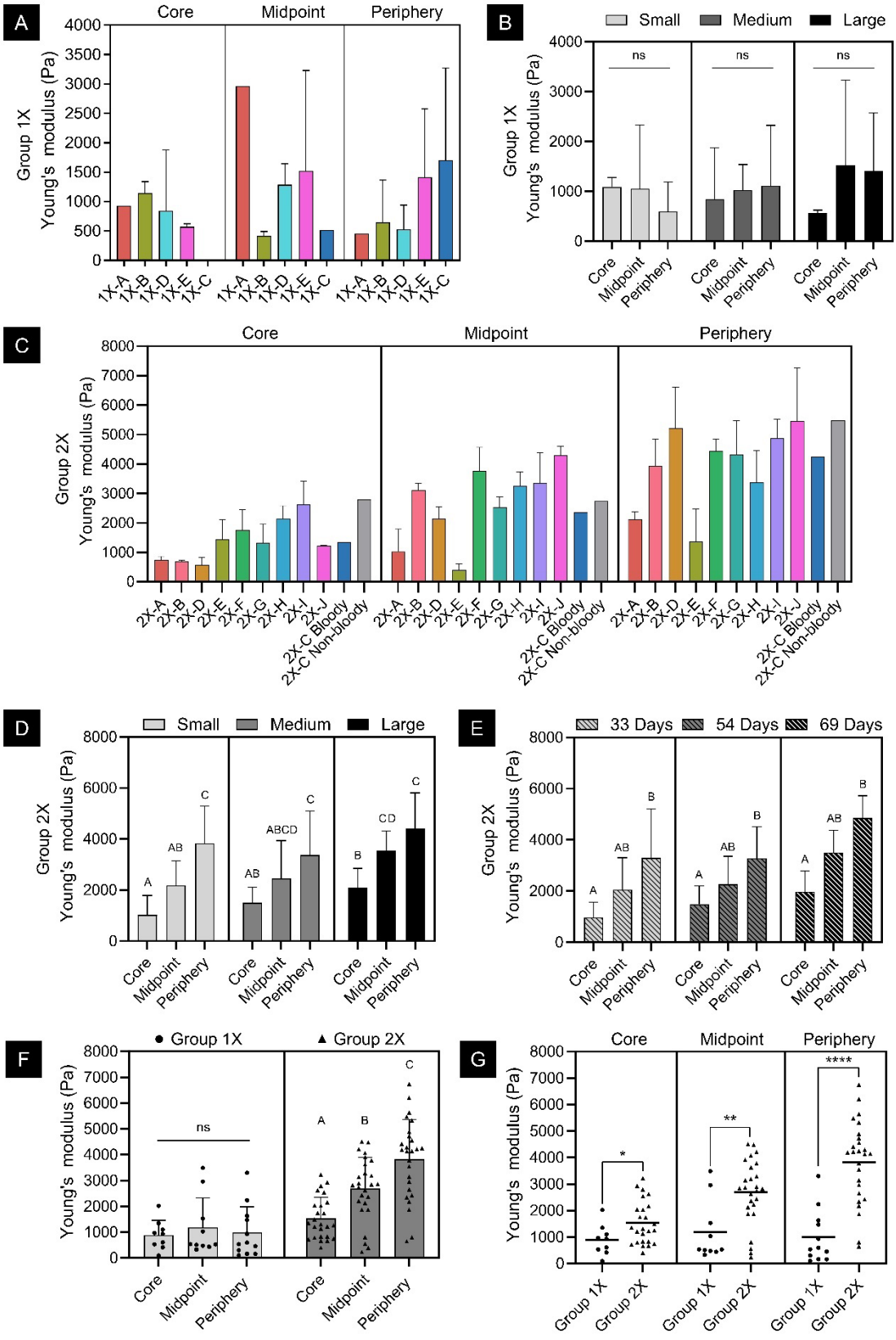

Figure 6: PC-3 tumor xenograft tissue stiffness varied throughout the tumor mass and was significantly dependent on the number of cells used in tumor seeding.

Figure 6 caption continued: A) Young's moduli of Group 1X tumors (organized left to right from smallest to largest tumor, n = 3). B) Binning of Group 1X tumors by size (per geometric region: small n = 6, medium n = 9, large, n = 3). C) Young's moduli of Group 2X tumors (organized left to right from smallest to largest tumor, n = 3). D) Binning of Group 2X tumors by size (per geometric region: small n = 12, medium n = 9, large n = 9). E) Binning of Group 2X tumors by growth duration (per geometric region: 33 days n = 9, 54 days n = 9, 69 days n = 12). F,G) Combined Young's moduli of all Group 1X and Group 2X tumors at each geometric region (per geometric region: Group 1X n = 15, Group 2X n = 33).

and the distribution of tumor sizes. Group 1X tumors were binned into small, medium, and large classifications; small tumors were designated to be less than 600 mm^3 (1X-A and 1X-B), medium tumors ranged between 600 and 800 mm^3 (1X-C and 1X-D), and finally large tumors were greater than 800 mm^3 (1X-E). No significant difference in tumor tissue stiffness was found when comparing geometric locations within a single tumor size classification or the same geometric regions of different tumor size classifications (Fig. 6B). Group 2X tumors were also binned in to small, medium, and large classifications in which small tumors were defined as less than 400 mm^3 (2X-A, 2X-B, 2X-C, and 2X-D), medium tumors ranged between 400 and 600 mm^3 (2X-E, 2X-F, and 2X-G), and finally large tumors were greater than 600 mm^3 (2X-H, 2X-I, and 2X-J). Notably, the Group 2X tumor periphery region presented a significantly larger average Young's modulus as compared to the core region for all three size classifications; the periphery region was also significantly stiffer than the midpoint region in small Group 2X tumors only (Fig. 6D,

$p \leq 0.05$). Furthermore, the core and midpoint regions of large Group 2X tumors were significantly stiffer than the core and midpoint regions of small Group 2X tumors (Fig. 6D, $p \leq 0.05$); the periphery regions did not vary significantly between size classifications.

In addition to tumor size at excision, the duration of *in vivo* tumor growth, *i.e.,* time of seeding injection to excision, was also hypothesized to impact the resultant tissue stiffness; in support of this, Group 2X tumors were excised in three groups at 33 days, 54 days, and 69 days post-tumor seeding (Group 1X tumors all experienced the same growth duration). Interestingly, regardless of the time between tumor xenograft seeding and excision, the tumor core, midpoint, and periphery regions each exhibited similar Young's moduli (Fig. 6E). Importantly, the Group 2X periphery region was significantly stiffer than the core region for all three growth durations, similar to the size binning investigation discussed above (Fig. 6E, $p \leq 0.05$).

Overall, Group 1X and Group 2X tumors exhibited both intertumoral (between multiple tumors) and intratumoral (within a single tumor) heterogeneity in stiffness; variations in tissue stiffness were found between regions of a single tumor, between similar regions of different tumors, and between different regions of different tumors (Fig. 6). This is evidenced by the wide range of average Young's modulus values, as well as the large standard deviations (Fig. 6A,C). Notably, when all Group 2X average Young's modulus values were combined by tumor region, a significant increase in tumor tissue stiffness was observed to follow a spatial progression from the geometric core, to the midpoint, to the periphery; no significant difference was noted between regions of Group 1X tumors (Fig. 6F, $p \leq 0.05$). Furthermore, Group 2X tumors presented significantly higher average Young's moduli at each of the three geometric regions relative to Group 1X tumors

(Fig. 6G, $p \leq 0.05$). In order to recapitulate *in vitro* the entire stiffness range observed *in vivo* for both Group 1X and Group 2X tumors, and thereby provide EPCaT-encapsulated cells with differential, pathophysiologically relevant biomechanical cues, these results demonstrate the necessity of employing a biomaterial with widely tunable matrix properties.

Two subcutaneous PC-3 xenograft tumors from Group 2X were also non-invasively visualized by whole-body photoacoustic imaging using the MSOT imager to examine the distribution of vasculature within the tumors, which may contribute to the noted spatial heterogeneity in tumor stiffness. Results are shown in both Figure 7 and Figure 8. MSOT imaging showed vasculature signal consistent with the presence of oxygenated and deoxygenated hemoglobin near the periphery of the tumor (Fig. 7); the vasculature signal is enriched nearest the skin and is appreciable at an axial depth of 77 – 79 mm where mouse 2X-F is shown with embedded tumor nodules wrapped in oxygenated hemoglobin signal. A different presentation is noted for mouse 2X-C (Fig. 8), wherein the animal exhibited a pronounced signal accumulation not only at the tumor periphery nearest the skin, but also a marked vascular signal within one of the upper tumor nodules. As previously mentioned, after tumor excision following mouse 2X-C euthanasia, the 2X-C tumor presented with distinct regions of bloody and non-bloody tissue sections. This area of enriched vasculature is appreciable at an axial depth of 67 – 71 mm. The MSOT data indicates that the area is not consistent with a necrotic core as both arteries and veins are still discernable in the photoacoustic image.

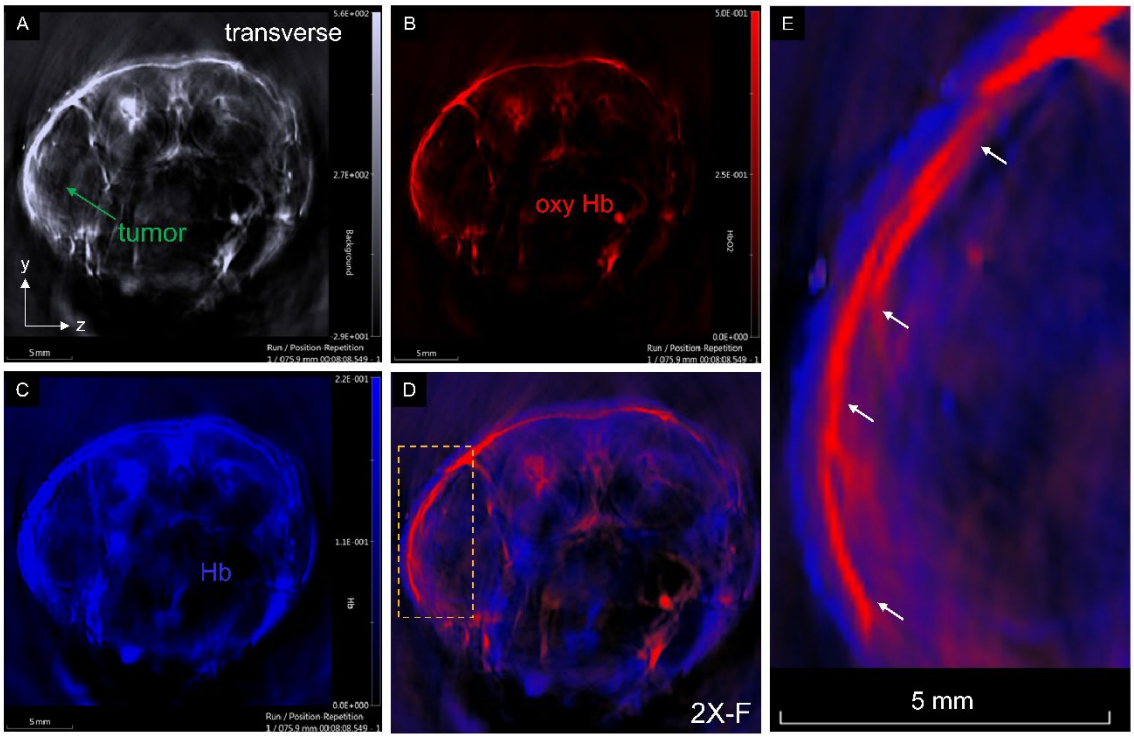

Figure 7: Multispectral optoacoustic tomographic image of a subcutaneous PC-3 tumor xenograft illustrates intratumoral spatial heterogeneity in vascularization that may contribute to the differential stiffness observed.

Representative MSOT images for corresponding channels are shown for a transverse slice. Panels correspond to: A) total photoacoustic channel, B) oxygenated hemoglobin, C) deoxygenated hemoglobin, and D,E) combined channels. Panel E is a magnified view of the yellow dashed box in panel D. Arrows point to enriched vasculature signal near the skin of the host animal.

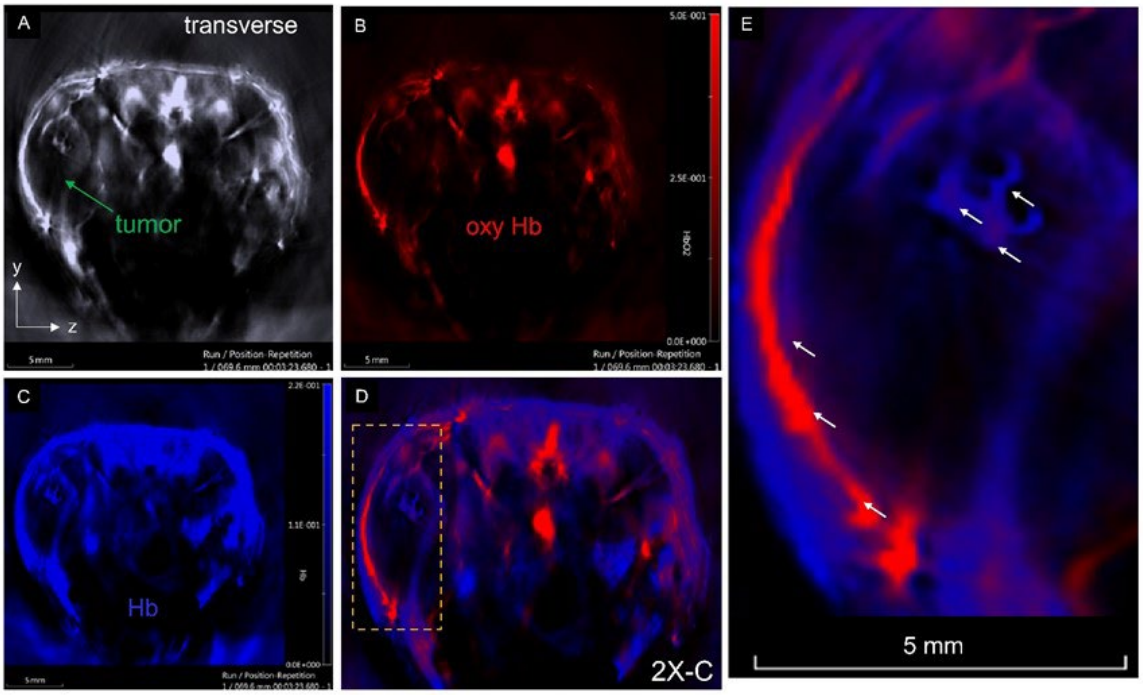

Figure 8: Multispectral optoacoustic tomographic imaging of the 2X-C subcutaneous PC-3 tumor xenograft illustrates intratumoral spatial heterogeneity in vascularization and provides context for the bloody and non-bloody regions observed upon excision.

Representative MSOT images for corresponding channels are shown for a transverse slice. Panels correspond to: A) total photoacoustic channel, B) oxygenated hemoglobin, C) deoxygenated hemoglobin, and D,E) combined channels. Panel E is a magnified view of the yellow dashed box in panel D. Arrows point to enriched vasculature signal near the skin of the host animal.

2.4.2 *PCa cells and fibroblasts remain viable throughout long-term in vitro coculture in varying 3D matrix stiffnesses*

In order to modulate the matrix-dependent biomechanical cues provided to PCa cells in 3D *in vitro* culture, the EPCaT model was fabricated by encapsulating the PC-3 prostate cancer cell line in coculture with BJ-5ta fibroblasts within PF-based hydrogels augmented with 0%, 1%, 2%, and 3% (w/v) excess PEGDA (Fig. 9A). PC-3 and BJ-5ta cells were mixed at a 5:1 cancer cell to fibroblast ratio, encapsulated at a concentration of 20 x 10^6 cells/mL, and cultured in PC-3 culture media *in vitro* for up to 29 days. PC-3 and BJ-5ta cells survived the encapsulation process and maintained high viability throughout long-term *in vitro* coculture regardless of the modulated matrix composition. EPCaTs demonstrated greater than 95% viability (Fig. 9B-G, n = three EPCaTs per condition) on Day 1 post-encapsulation in each of the four PF matrix compositions (representative Day 1 image shown in Fig. 9C; live cells are visualized in green and dead cells are visualized in red). After 15 days of *in vitro* culture, EPCaTs maintained greater than 90% viability (n = three EPCaTs per condition), again with no significant difference between matrix compositions (Fig.9 D-G). Live cells were uniformly distributed throughout the biomaterial matrix and no locational variations in viability were noted.

2.4.3 *Encapsulated cells temporally remodel and colonize within the PF-based EPCaT matrices*

As a result of PF being a natural-synthetic hybrid biomaterial, encapsulated cells can enzymatically degrade the fibrinogen backbone over time in order to remodel and migrate within the provided matrix, thus resulting in EPCaT spatial heterogeneity. To investigate the impact of modulated matrix stiffness on temporal cell colonization and cell-

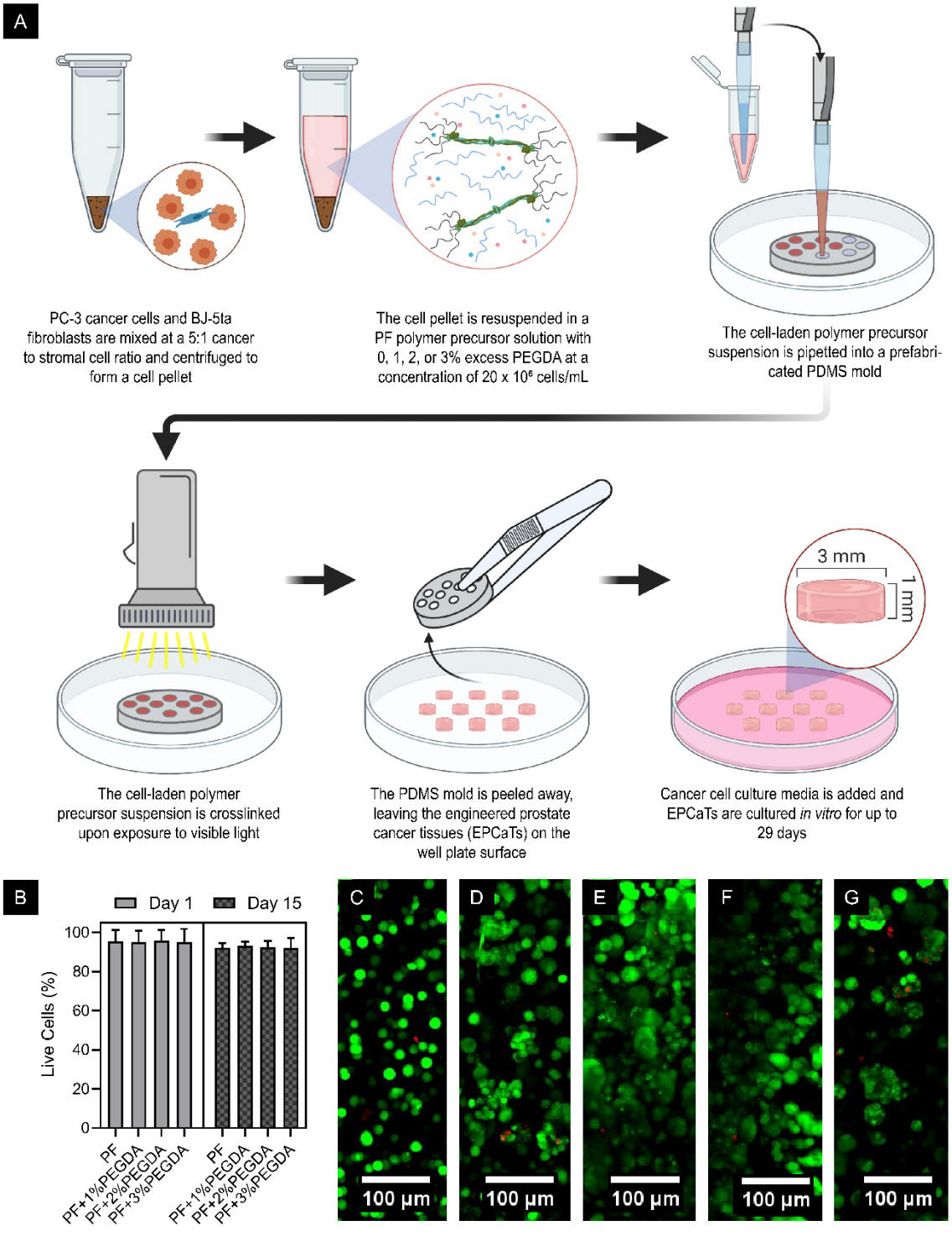

Figure 9: EPCaTs survived the encapsulation process and remained viable over time.

Figure 9 caption continued: A) Fabrication of EPCaTs. B) Quantification of encapsulated cell viability (n = 3). C-G) 10X confocal microscopy viability assay images; live cells are visualized in green and dead cells are visualized in red. C) Representative EPCaT on Day 1. D) PF EPCaT on Day 15. E) PF+1%PEGDA on Day 15. F) PF+2%PEGDA on Day 15. G) PF+3%PEGDA on Day 15 (scale bars = 100 μm).

mediated PF matrix remodeling, multi-magnification phase contrast imaging was performed. Substantial differences were observed in overall EPCaT structure and cell colonization over long-term *in vitro* culture (Fig. 10A-D), relative to Day 1 post-encapsulation (Fig. 10G). Increased colonization was observed around the edge of PF (Fig. 10A) and PF+1%PEGDA (Fig. 10B) tissues, as compared to PF+2%PEGDA (Fig. 10C) and PF+3%PEGDA (Fig. 10D); furthermore, PF EPCaTs exhibited substantial matrix remodeling and loss of structural integrity around the edge of the tissue (Fig. 10A). These composition-mediated differences in matrix remodeling, particlularly around the edge of the EPCaTs, were also appreciable in H&E stained EPCaT sections (Fig. 11); in general, less remodeling and matrix degradation was observed with increasing percentage of excess PEGDA. PF, PF+1%PEGDA, and PF+3%PEGDA tissues all significantly increased in area between Days 8 and 15 post-encapsulation, whereas PF+2%PEGDA tissue size remained constant throughout long-term culture (Fig. 10E, n = ten EPCaTs per condition, $p \leq 0.05$). A linear regression of temporal EPCaT growth revealed that PF and PF+1%PEGDA EPCaTs exhibited a significantly increased growth rate compared to PF+2%PEGDA EPCaTs (Fig. 10F, $p \leq 0.05$); the PF+3%PEGDA tissue growth rate did not vary significantly in comparison to all other matrix compositions.

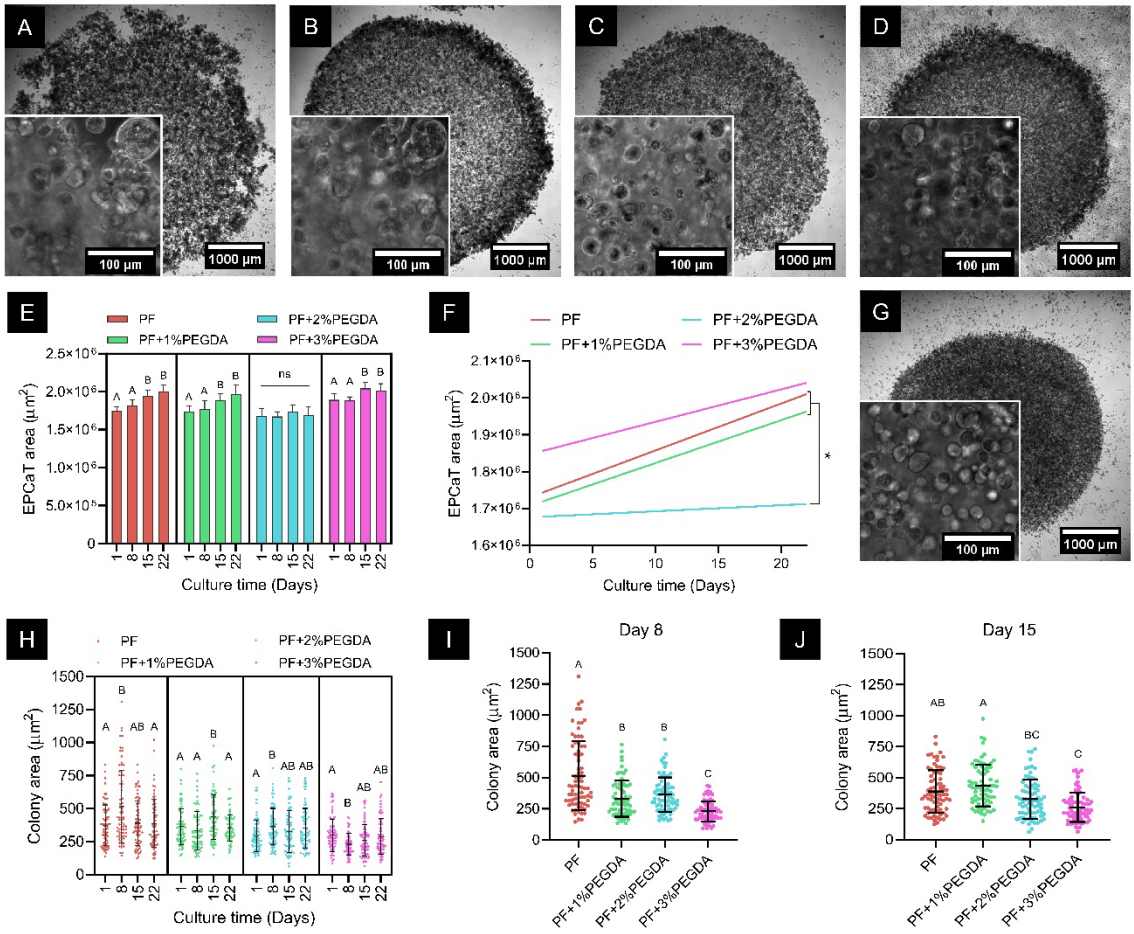

Figure 10: Cells temporally remodeled and colonized within the EPCaT matrix.

A-D,G) 2X phase contrast images of EPCaTs on Day 29 with 20X image inlays on Day 22. A) PF. B) PF+1%PEGDA. C) PF+2%PEGDA. D) PF+3%PEGDA. G) Representative Day 1 sample. E) Temporal changes in EPCaT area (n = 10 EPCaTs each per timepoint). F) Linear regression of temporal EPCaT growth. H-J) Quantification of encapsulated cell colony area (n = 75 colonies each per timepoint).

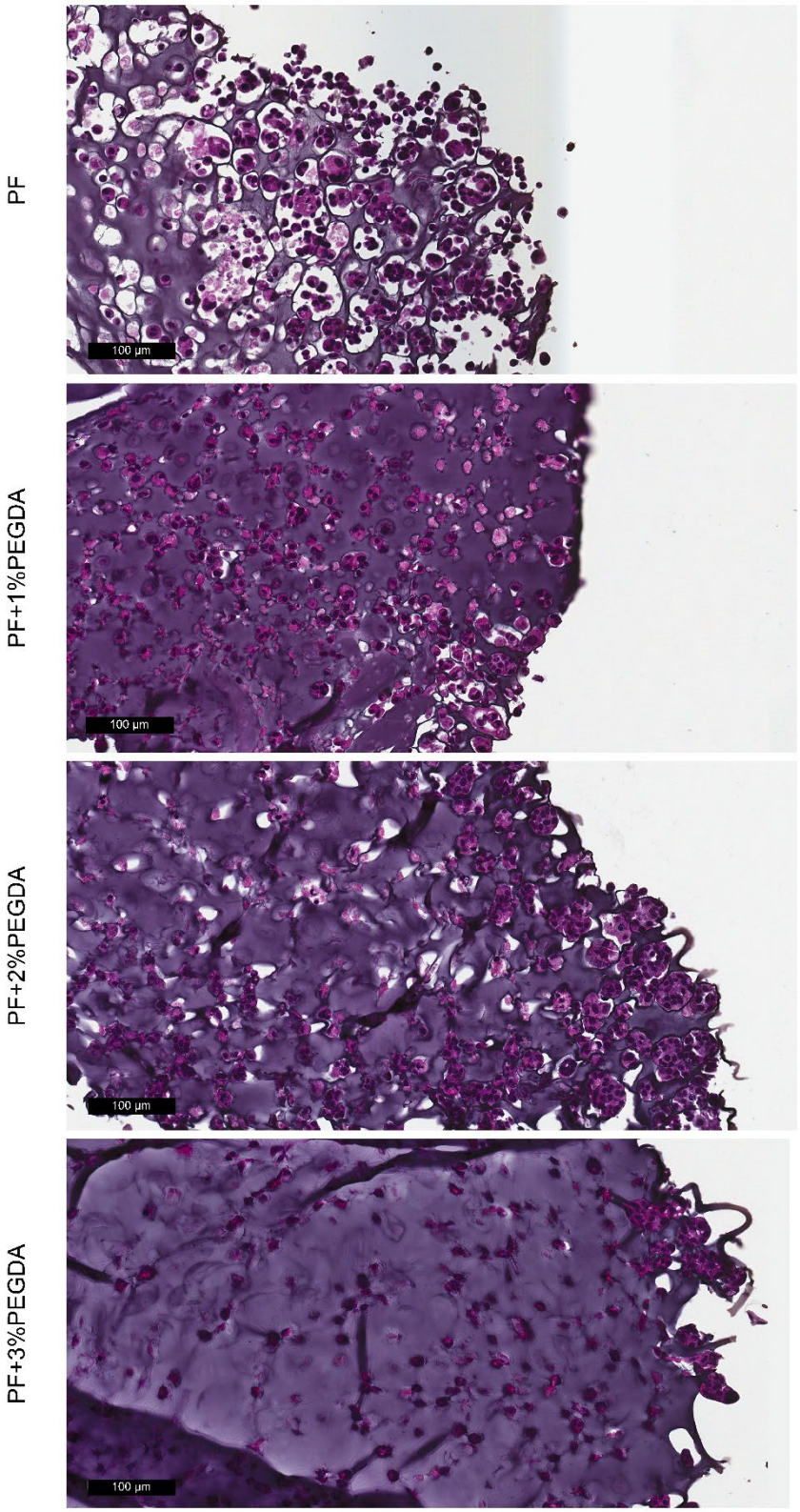

Figure 11: H&E stained sections of EPCaTs on Day 15 post-encapsulation.

Figure 11 caption continued: Stained sections illustrate matrix composition-dependent heterogeneity in degradation and colonization at the edge of the tissue (scale bars = 100 μm).

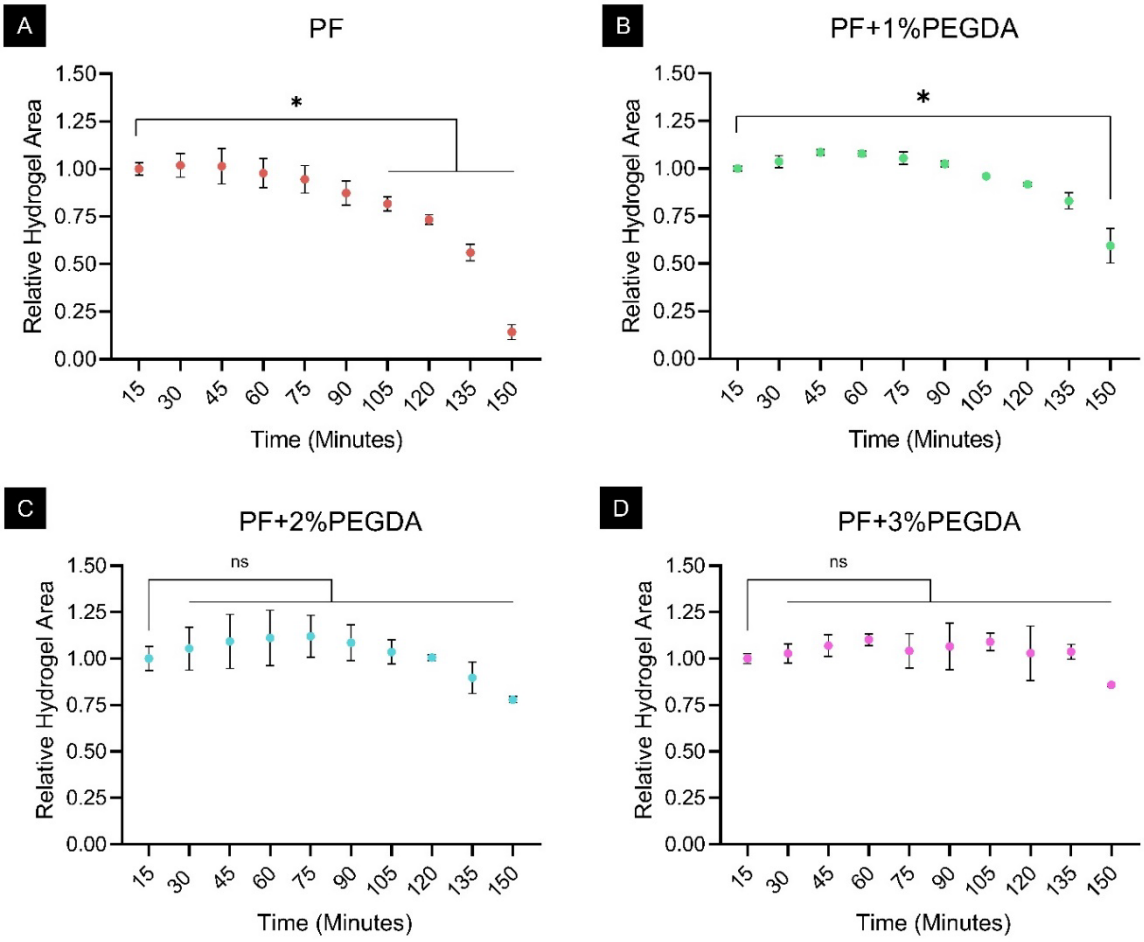

Figure 12: Degradation profiles of acellular hydrogels.

PF hydrogels underwent complete enzyme-mediated degradation; however, the addition of excess synthetic PEGDA within the hydrogel matrices inhibited disassembly of PF+1%PEGDA, PF+2%PEGDA, and PF+3%PEGDA hydrogels (n = 3 hydrogels per matrix composition).

Degradation behavior analysis revealed that EPCaTs do not swell during the degradation process (Fig. 12); therefore, the temporal tissue growth observed in PF and PF+1%PEGDA EPCaTs is likely a result of cell proliferation and ECM deposition around the edge of the tissues.

As expected, variations in PC-3 and BJ-5ta cell colonization were noted throughout 22 days of *in vitro* culture (Fig. 10H, n = 75 colonies measured per condition). PF EPCaTs exhibited the widest range of colony sizes varying from approximately 140 – 830 μm^2 on Day 1, 150 – 1,310 μm^2 on Day 8, 130 – 840 μm^2 on Day 15, and 120 – 1,020 μm^2 on Day 22; a significant increase in average colony size occurred on Day 8 post-encapsulation (Fig. 10H, $p \leq 0.05$). PF+1%PEGDA EPCaT colonies ranged in size from approximately 150 – 800 μm^2 on Day 1, 140 – 770 μm^2 on Day 8, 150 – 980 μm^2 on Day 15, and 160 – 650 μm^2 on Day 22; a significantly larger average colony size was observed on Day 15 relative to all other time points (Fig. 10H, $p \leq 0.05$). PF+2%PEGDA EPCaT colonies ranged in size from approximately 140 – 660 μm^2 on Day 1, 160 – 800 μm^2 on Day 8, 60 – 740 μm^2 on Day 15, and 140 – 730 μm^2 on Day 22; a significant increase in average colony size was observed on Day 8, as compared to Day 1 (Fig. 10H, $p \leq 0.05$). Finally, PF+3%PEGDA EPCaTs exhibited the most narrow range of colony sizes with colonies measured between approximately 90 – 610 μm^2 on Day 1, 100 – 440 μm^2 on Day 8, 60 – 560 μm^2 on Day 15, and 100 – 700 μm^2 on Day 22; a significant decrease in average colony size was observed between Days 1 and 8 post-encapsulation, however, the average colony size showed an increasing trend between Day 8 and Day 22 (Fig. 10H, $p \leq 0.05$). Overall, as expected, increasing the percentage of excess PEGDA within the matrix resulted in a significantly decreased average EPCaT colony size, as well as a narrower range of colony

sizes present within the tissue (Fig. 10I,J, $p \leq 0.05$), probably as a result of the reduced number of fibrinogen molecules available for matrix remodeling.

2.4.4 *EPCaTs demonstrate spatial heterogeneity in cell morphology*

As previously mentioned in section 2.4.3, EPCaT spatial heterogeneity was observed throughout long-term *in vitro* coculture, particularly in PF and PF+1%PEGDA tissues. To better characterize this and also elucidate variations in encapsulated cell morphology within the EPCaT matrix in response to the modulation of mechanical properties, immunostaining and confocal microscopy studies were performed at three regions of the EPCaTs (center, middle, and edge) on Day 15 post-encapsulation (Fig. 13A). Cytoskeleton F-actin filaments are visualized in red, intranuclear double stranded DNA is visualized in blue, and fibroblasts are marked by TE-7 in green to distinguish between cell types.

PC-3 prostate cancer cell colonies and BJ-5ta fibroblasts were distributed throughout the EPCaTs; however, matrix composition-dependent variations in colony size and shape and cell morphology were noted. PF tissues exhibited uniformly shaped cell colonies throughout the EPCaT, with larger colonies at the center and middle of the tissue compared to the edge; conversely, PF+1%PEGDA EPCaTs demonstrated larger and more elongated colonies at the middle and edge of the tissue (Fig. 13 E-G, $p \leq 0.05$). No significant spatial variation was observed in colony circularity or aspect ratio in either PF+2%PEGDA or PF+3%PEGDA EPCaTs; however, PF+3%PEGDA EPCaTs exhibited larger colonies at the middle and edge of the tissue, as compared to the center (Fig. 13E-G, $p \leq 0.05$). When all spatial locations of analysis were grouped together, PF+3%PEGDA EPCaTs presented significantly more circular colonies than

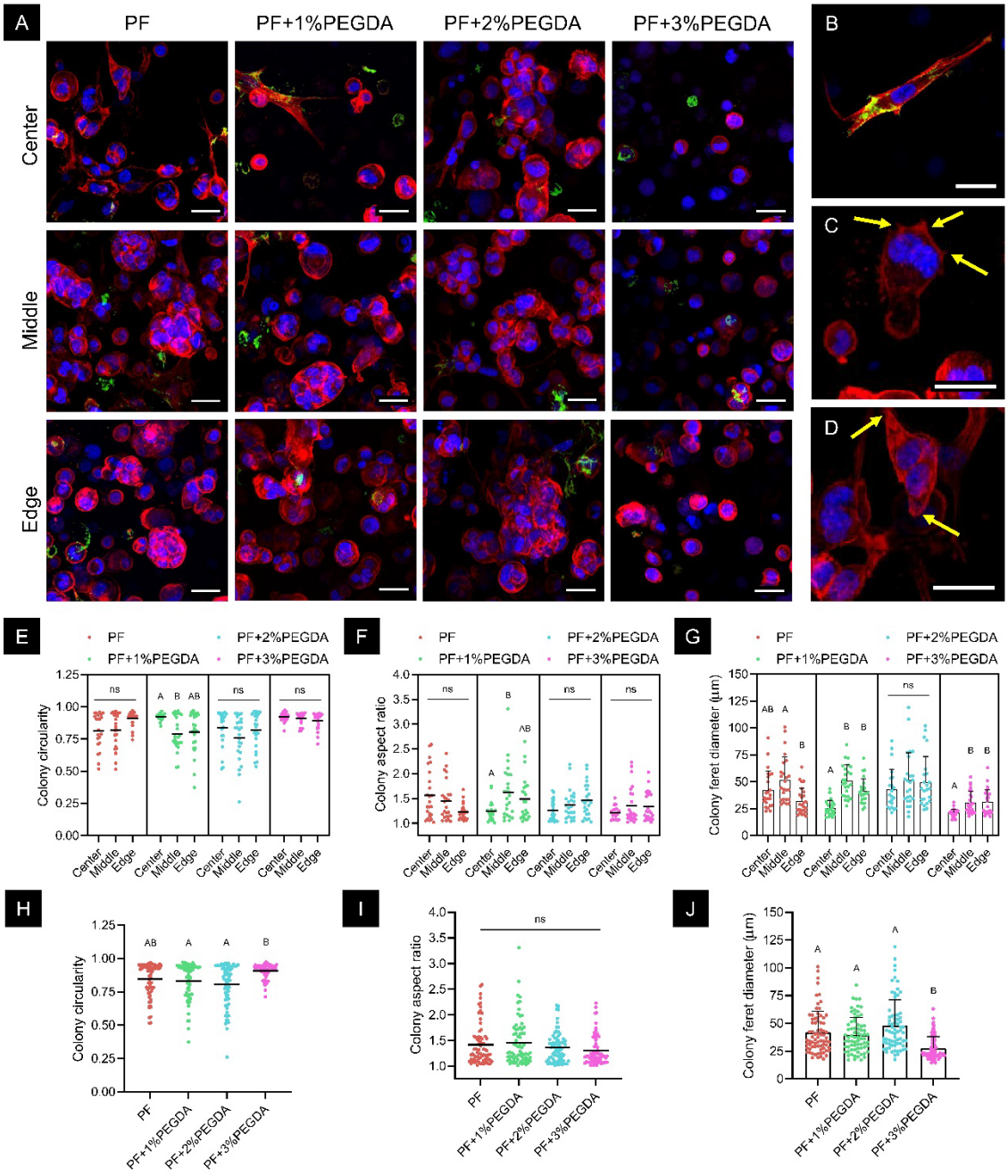

Figure 13: Encapsulated cells displayed appropriate pathophysiological morphology and exhibited spatial heterogeneity across the EPCaT.

Figure 13 caption continued: A) 20X confocal microscopy immunostaining images of Day 15 EPCaTs at three locations; F-actin filaments are visualized in red, nuclei are visualized in blue, and fibroblasts are marked in green (scale bars = 30 μm). B) Representative image of fibroblast elongation (PF+3%PEGDA EPCaT, scale bar = 30 μm). C,D) Representative images of extended cell protrusions; yellow arrows indicate f-actin assemblies that appear to resemble C) leading edge lamellipodia with filopodia extensions and D) invadopodia morphologies (C represents a PF+1%PEGDA EPCaT, D represents a PF EPCaT, scale bars = 30 μm). E) Quantification of colony circularity (n = 25 colonies per location). F) Quantification of colony aspect ratio (n = 25 colonies per location). G) Quantification of colony feret diameter (n = 25 colonies per location). H) Combined quantification of colony circularity at all three EPCaT locations (n = 75 colonies per condition). I) Combined quantification of colony aspect ratio at all three EPCaT locations (n = 75 colonies per condition). J) Combined quantification of colony feret diameter at all three EPCaT locations (n = 75 colonies per condition).

PF+1%PEGDA and PF+2%PEGDA tissues (Fig. 13H, $p \leq 0.05$); however, the grouped colony aspect ratio did not significantly vary between PF matrix compositions (Fig. 13I, $p \leq 0.05$). PF+3%PEGDA EPCaTs presented the smallest cell colonies, evidenced by a significantly smaller colony feret diameter in comparison to all three other PF matrix compositions (Fig. 13J, $p \leq 0.05$). In general, the PF+3%PEGDA matrix yielded more uniform, small, circular cell colonies, which is indicative of relatively decreased

colonization throughout the tissue. Decreased f-actin filament presence was also noted in comparison to the other EPCaT matrix compositions.

Notably, fibroblast elongation (Fig. 13A,B) was observed within the EPCaT platform, suggesting that encapsulated cells can maintain physiological phenotypes. F-actin assemblies also illustrated single-cell morphologies with extended cell protrusions (Fig. 13C,D). Finally, cancer-fibroblast cell-cell interactions were visible in all four matrix compositions (Fig. 13A).

2.4.5 *Addition of excess PEGDA significantly stiffens the EPCaT matrix*

As previously reported, the addition of 1%, 2%, and 3% (w/v) excess PEGDA to acellular PF hydrogels resulted in a significantly higher Young's modulus (Pradhan et al., 2017b, Peyton et al., 2008, Dikovsky et al., 2006). To ensure this trend also occurred in the presence of PC-3 prostate cancer cells and BJ-5ta fibroblasts, as well as to evaluate the effects of long-term coculture on matrix stiffness, EPCaTs were subjected to parallel plate compression testing (three measurements taken and averaged per EPCaT, n = six EPCaTs per matrix composition per timepoint). Increasing amounts of excess PEGDA were proven to significantly stiffen the Young's modulus of modulated EPCaT matrices, as compared to PF EPCaTs (Fig. 14A, $p \leq 0.05$). Day 1 stiffness values for all four matrix compositions ranged from approximately 230 – 10,000 Pa, Day 15 values ranged from 50 – 3,130 Pa, and Day 22 values ranged from 50 – 4,130 Pa (Fig. 14B). The Young's modulus was found to significantly decrease with increasing culture time in PF, PF+1%PEGDA, and PF+3%PEGDA EPCaTs. PF EPCaTs exhibited a significant decrease in mechanical stiffness on Day 15 and the total stiffness range achievable by modulating culture duration was approximately 50 – 870 Pa (Fig. 14B). PF+1%PEGDA EPCaTs also exhibited a

significant decrease in mechanical stiffness on Day 15; however, the total achievable stiffness range was higher between approximately 260 – 1,360 Pa (Fig. 14B, $p \leq 0.05$). The addition of 2% excess PEGDA did not yield significant differences in stiffness over time, though a slight decreasing trend was noted, and exhibited an achievable stiffness range of approximately 600 – 3,830 Pa (Fig. 14B). Finally, PF+3%PEGDA EPCaTs presented both the highest achievable Young's modulus and the largest stiffness range of approximately 530 – 10,000 Pa (Fig. 14B, $p \leq 0.05$). The stiffness of PF+3%PEGDA EPCaTs also significantly decreased between Days 1 and 15 of *in vitro* culture. Overall, PC-3 and BJ-5ta coculture EPCaTs can be tuned to exhibit mechanical stiffnesses between 50 – 10,000 Pa through modulations of polymer matrix composition and culture duration.

2.4.6 *EPCaTs successfully mimic the entire in vivo tumor stiffness range*

Notably, PC-3 and BJ-5ta coculture EPCaTs were successful in fully recapitulating the entire stiffness range quantified from both Group 1X and Group 2X PC-3 murine xenograft tumors through modulations in both the PF matrix composition and culture duration. In total, considering stiffness measurements from all three geometric locations, Group 1X tumors ranged from approximately 95 – 3,500 Pa and Group 2X tumors ranged from approximately 230 – 6,750 Pa (Fig. 14C). In comparison, considering all culture duration time points, EPCaTs ranged from approximately 50 – 870 Pa, 260 – 1,360 Pa, 600 – 3,830 Pa, and 530 – 10,000 Pa for PF, PF+1%PEGDA, PF+2%PEGDA, and PF+3%PEGDA matrices, respectively (Fig. 14C, measurements for each culture time point are represented by different colors). Statistical analysis revealed no significant difference between Group 1X tumors and either PF or PF+1%PEGDA EPCaTs or between Group 2X tumors and either PF+2%PEGDA or PF+3%PEGDA (Fig. 14D, $p \leq 0.05$). Therefore, the

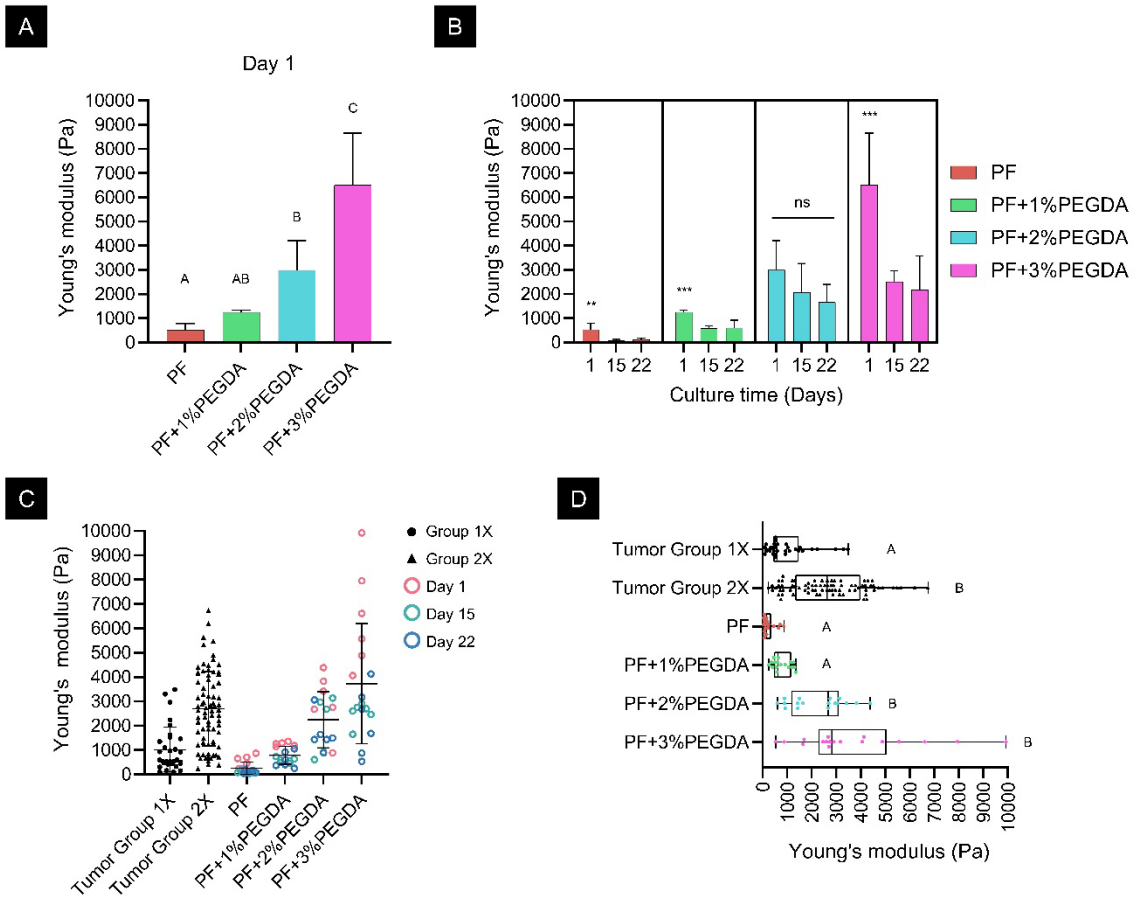

Figure 14: EPCaTs successfully recapitulated *in vitro* the full stiffness range of *in vivo* Group 1X and Group 2X PCa tumors.

A) Quantification of EPCaT Young's moduli on Day 1 (n = 6). B) Quantification of temporal changes in EPCaT Young's moduli (n = 6). C,D) In vivo and in vitro tissue stiffness comparison; box and whisker plots in panel D indicate the data range and median for all timepoints measured. (Group 1X n = 45, Group 2X n = 99, PF, PF+1%PEGDA, PF+2%PEGDA, and PF+3%PEGDA n = 18).

EPCaT platform has been established as a tunable model that introduces the ability to preferentially select the biomechanical cues provided to PCa or other supporting cell types *in vitro* based on the specific *in vivo* tumor microenvironment that is desired to be recapitulated.

2.4.7 *Modulating EPCaT stiffness induces differential gene expression and enrichment of tumorigenic gene sets*

Bulk transcriptomic analyses successfully isolated and characterized EPCaT matrix stiffness-derived changes in differential gene expression both between EPCaTs, as well as between EPCaTs and a 2D coculture of PC-3 and BJ-5ta cells. As expected, many significant differentially expressed genes (DEGs) were found between each EPCaT matrix composition and the 2D PCa-fibroblast cell coculture. When considering all genes that were differentially expressed in one or more of the EPCaT versus 2D comparisons, the PF versus 2D DEG profile was significantly more diverse and contained more DEGs than the PF+2%PEGDA or PF+3%PEGDA versus 2D comparisons (Fig. 15, $p \leq 0.05$). In total, the PF EPCaTs expressed 1,199 DEGs, 502 of which were unique (Fig.16). The PF+2%PEGDA and PF+3%PEGDA EPCaTs expressed 801 and 805 total DEGs, respectively; however, 49 of the PF+2%PEGDA DEGs were unique whereas 109 DEGs were unique to PF+3%PEGDA EPCaTs (Fig. 16). Notably, 537 genes were found to be differentially expressed in all three EPCaT matrix compositions (Fig. 16).

Stiffness-dependent variations in biological processes, interpreted from the differential gene expression quantified between 3D and 2D culture, were elucidated through hallmark gene set enrichment analysis (Fig. 17A). Bubble plots were used to simultaneously illustrate the normalized enrichment score (bubble size, positive

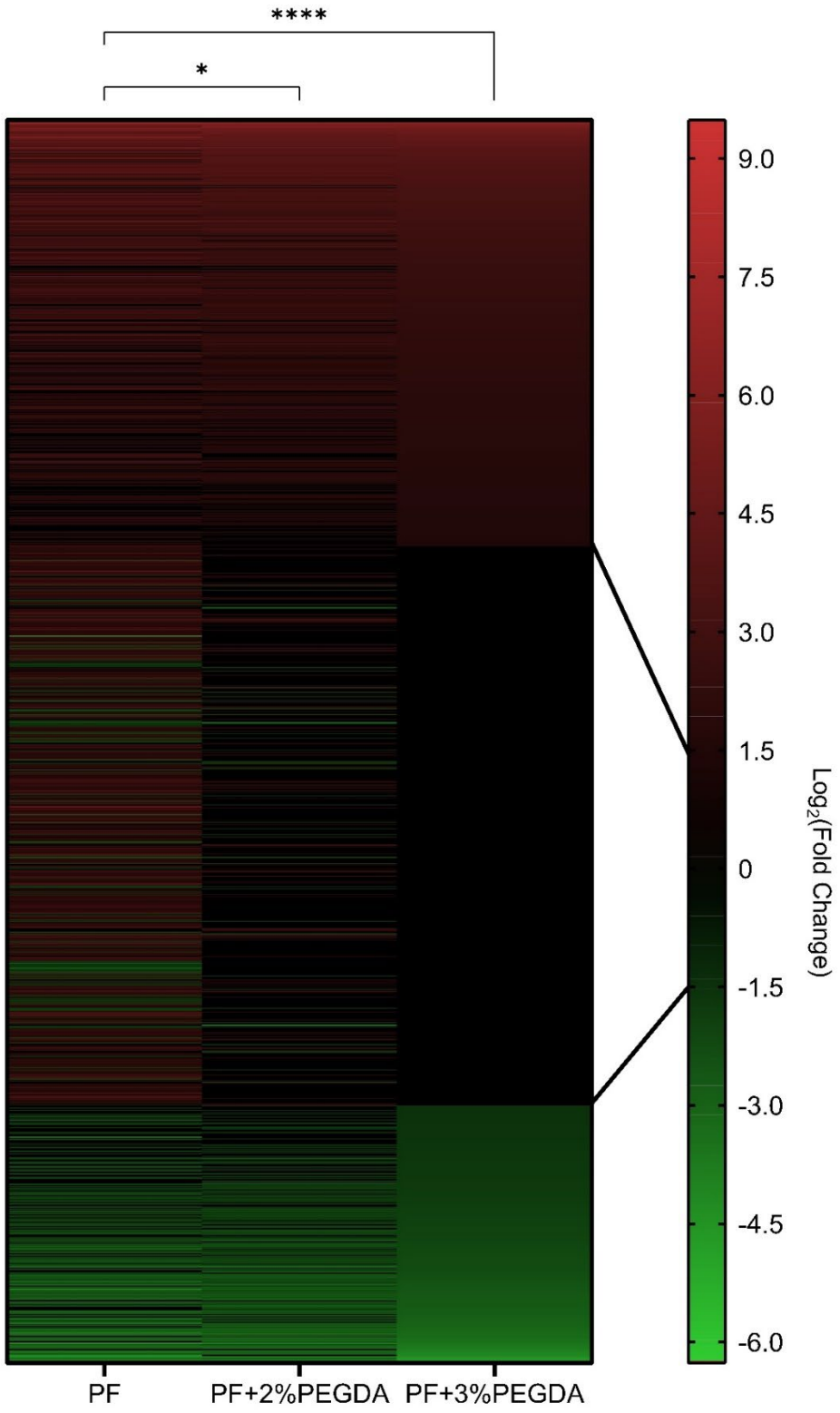

Figure 15: Heatmap of all significant DEGs occurring in at least one EPCaT composition, as compared to a 2D PCa-fibroblast coculture.

Figure 15 caption continued: It is important to note that DEGs with Log_2(Fold Change) < ± 1.5 were not regarded as significant and are illustrated here in black (RNA isolated from n > 2 EPCaTs or 1 x 10^6 2D cells per condition).

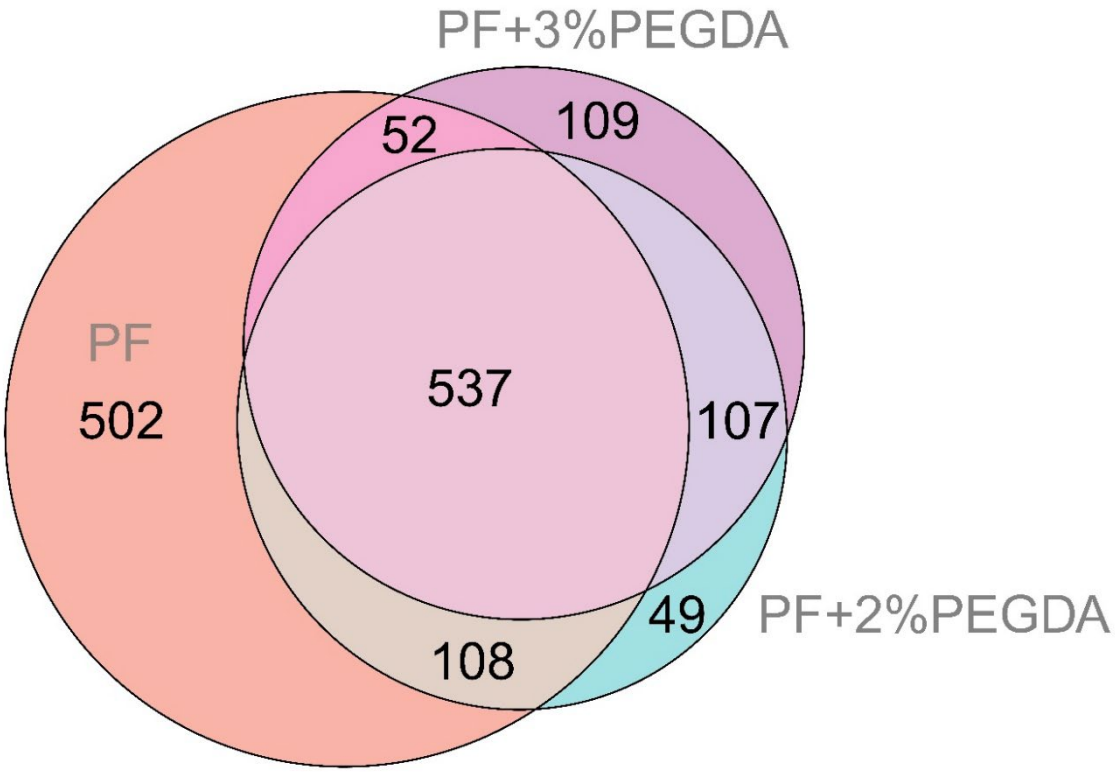

Figure 16: Euler diagram illustrating the number of shared versus unique DEGs for each EPCaT matrix composition, relative to 2D PCa-fibroblast coculture.

enrichment is demarcated by a plus sign) and the false discovery rate (bubble color). Many gene sets were similarly enriched across all three EPCaT matrix compositions relative to 2D coculture; these include positive enrichment of glycolysis and negative enrichment in the epithelial to mesenchymal transition (EMT), genes downregulated in response to ultra-violet (UV) radiation, unfolded protein response, genes regulated by MYCv2, and TNFA signaling via NFKB. Interestingly, PF and PF+2%PEGDA EPCaTs exhibited positive enrichment of gene sets associated with proliferation processes such as mitotic spindle assembly, G2M checkpoint, and targets of E2F transcription factors. Conversely, PF+2%PEGDA and PF+3%PEGDA EPCaTs demonstrated positive enrichment of genes upregulated in response to hypoxia and genes downregulated in response to KRAS activation. PF EPCaTs were the only 3D sample to result in differential enrichment of immune gene sets and yielded negative enrichment in inflammatory response, complement system, and coagulation. Finally, PF+3%PEGDA EPCaTs showed unique positive enrichment of genes upregulated through activation of the mTORC1 complex, as well as those upregulated in response to KRAS activation.

Enriched gene ontologies provided further insight into the biological meaning of the EPCaT versus 2D differential gene expression and were illustrated using tree maps in which the size of a box represents the enrichment score and related ontologies with the same parent term are grouped by color. Interestingly, the PF versus 2D DEG comparison yielded enriched ontologies related to cell division including chromosome segregation, meiotic cell cycle process, organelle fission, DNA replication, and mitotic cell cycle process (Fig. 18). PF+2%EPCaTs demonstrated enrichment in several processes linked to tumorigenesis including angiogenesis, cell motility, response to hypoxia, extracellular

structure organization, cell adhesion, chromosome segregation, and locomotion (Fig. 19). PF+3%EPCaTs exhibited similarly enriched ontologies as the PF+2%EPCaTs; however, enrichment of glycolytic process, NAD and NADH metabolic processes, nucleotide phosphorylation, and system process was also observed (Fig. 20). Specific DEGs responsible for the enrichment of either hallmark gene sets or gene ontologies are visualized in Figure 17B; those found to overlap between GSEA and GO analysis are visualized in Figure 21. Volcano plots were additionally employed to more clearly illustrate the differential expression of individual genes in Figures 22 through 24 (DEGs with $p \leq 0.05$ and Log_2(Fold Change) $\geq \pm 1.5$ are shown in red and DEGs with $p \leq 0.05$ and Log_2(Fold Change) $< \pm 1.5$ are shown in green).

,

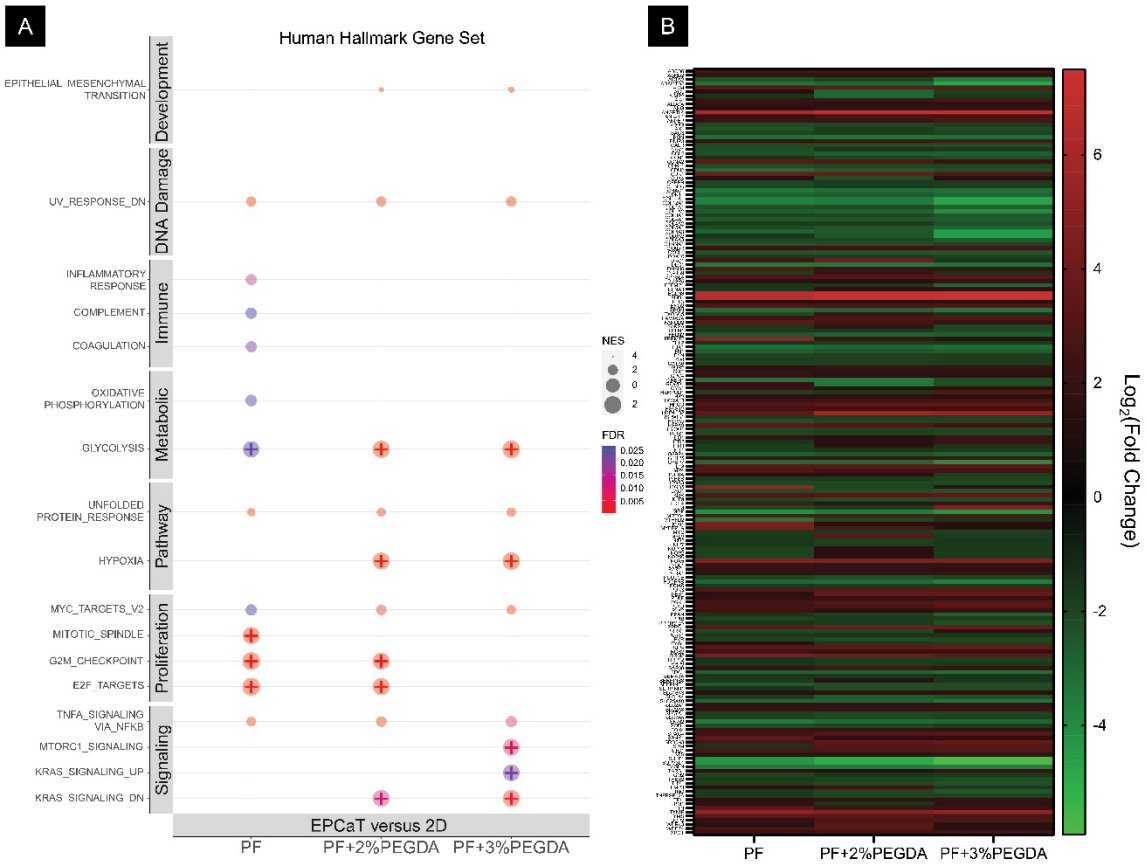

Figure 17: EPCaT matrix composition significantly impacted differential gene expression versus a 2D PCa-fibroblast coculture and yielded stiffness-dependent enrichment of hallmark gene sets and gene ontologies.

A) Bubble plot of EPCaT versus 2D cancer-fibroblast coculture GSEA using hallmark gene sets (bubble size indicates NES, bubble color indicates FDR, positive enrichment is demarcated by a plus sign). B) Heatmap of DEGs responsible for hallmark gene set or gene ontology enrichment (RNA isolated from n > 2 EPCaTs or 1 x 10^6 2D cells per condition).

Figure 18: Tree map representing gene ontology enrichment between PF EPCaTs and 2D PCa-fibroblast coculture.

Figure 19: Tree map representing gene ontology enrichment between PF+2%PEGDA EPCaTs and 2D PCa-fibroblast coculture.

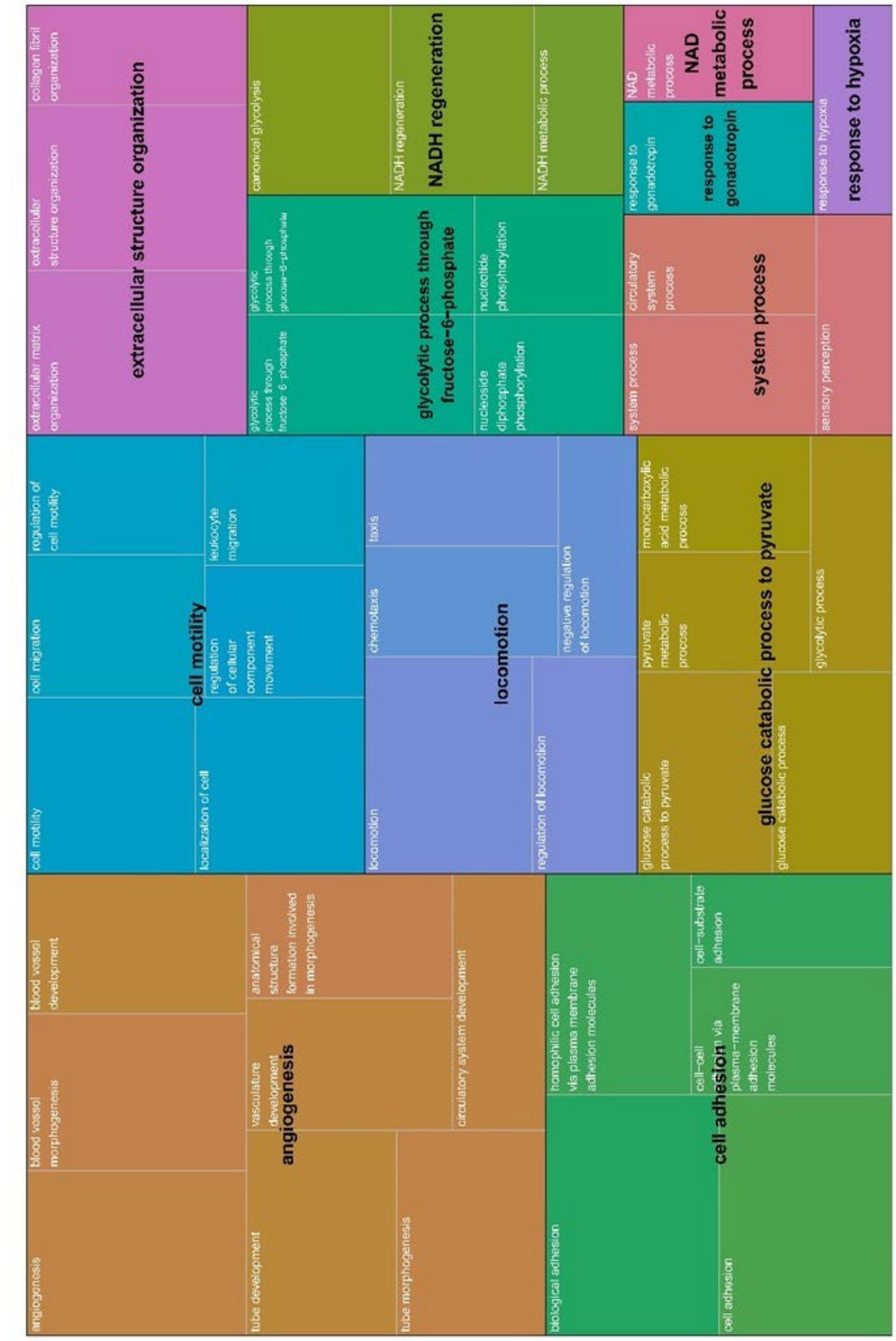

Figure 20: Tree map representing gene ontology enrichment between PF+3%PEGDA EPCaTs and 2D PCa-fibroblast coculture.

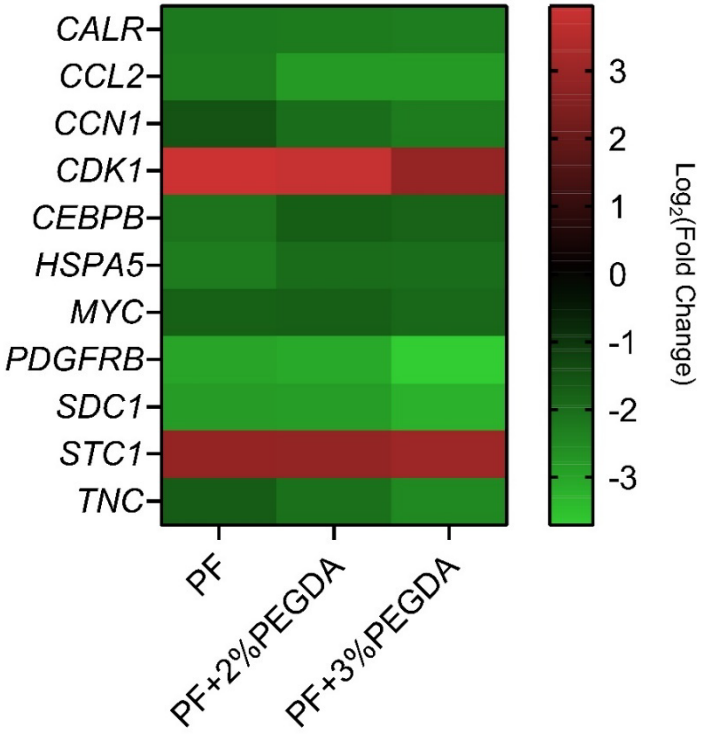

Figure 21: Heatmap illustrating the differential expression of individual genes found to be responsible for both the enrichment of hallmark gene sets and the enrichment of gene ontologies between EPCaTs and a 2D PCa-fibroblast coculture.

(RNA isolated from n > 2 EPCaTs or 1 x 10^6 2D cells per condition).

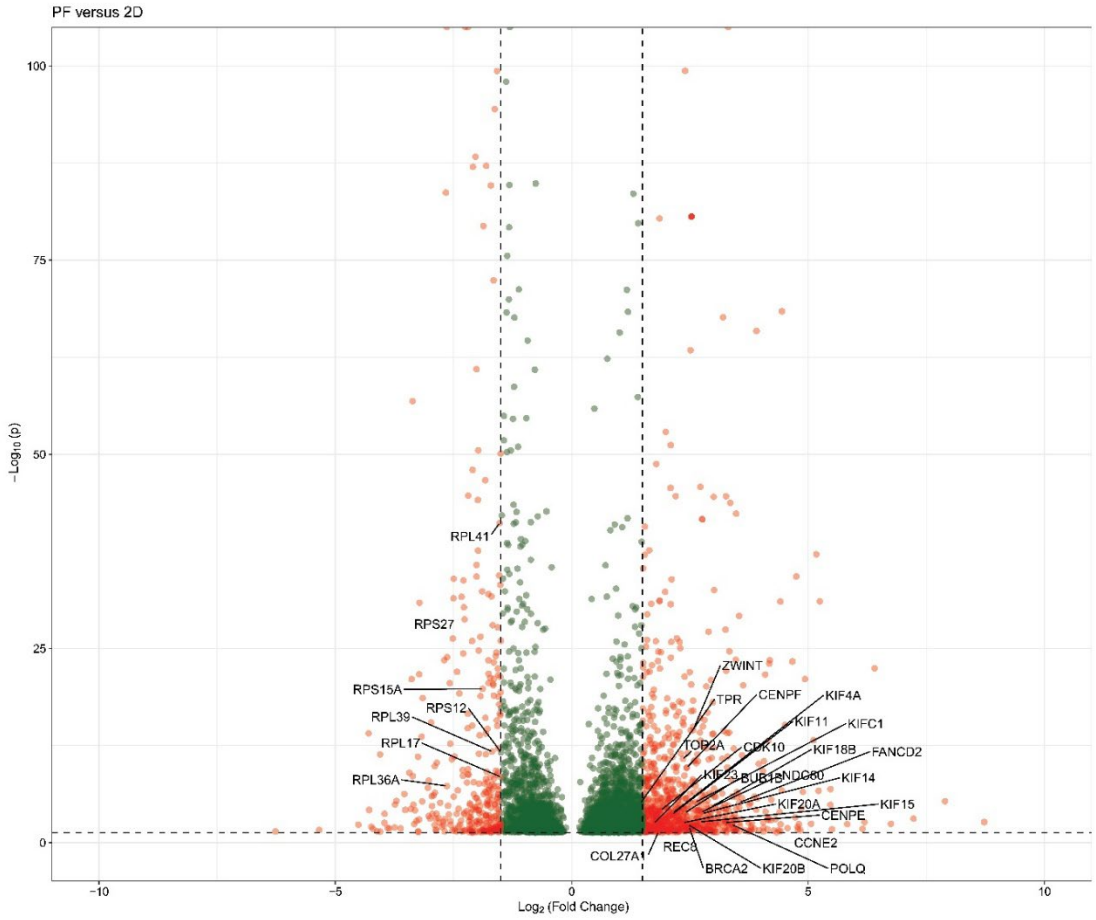

Figure 22: Volcano plot of DEGs between PF EPCaTs versus 2D.

Genes involved in GO enrichment are labeled (DEGs with $p \leq 0.05$ and Log_2(Fold Change) $\geq \pm 1.5$ are shown in red and DEGs with $p \leq 0.05$ and Log_2(Fold Change) $< \pm 1.5$ are shown in green).

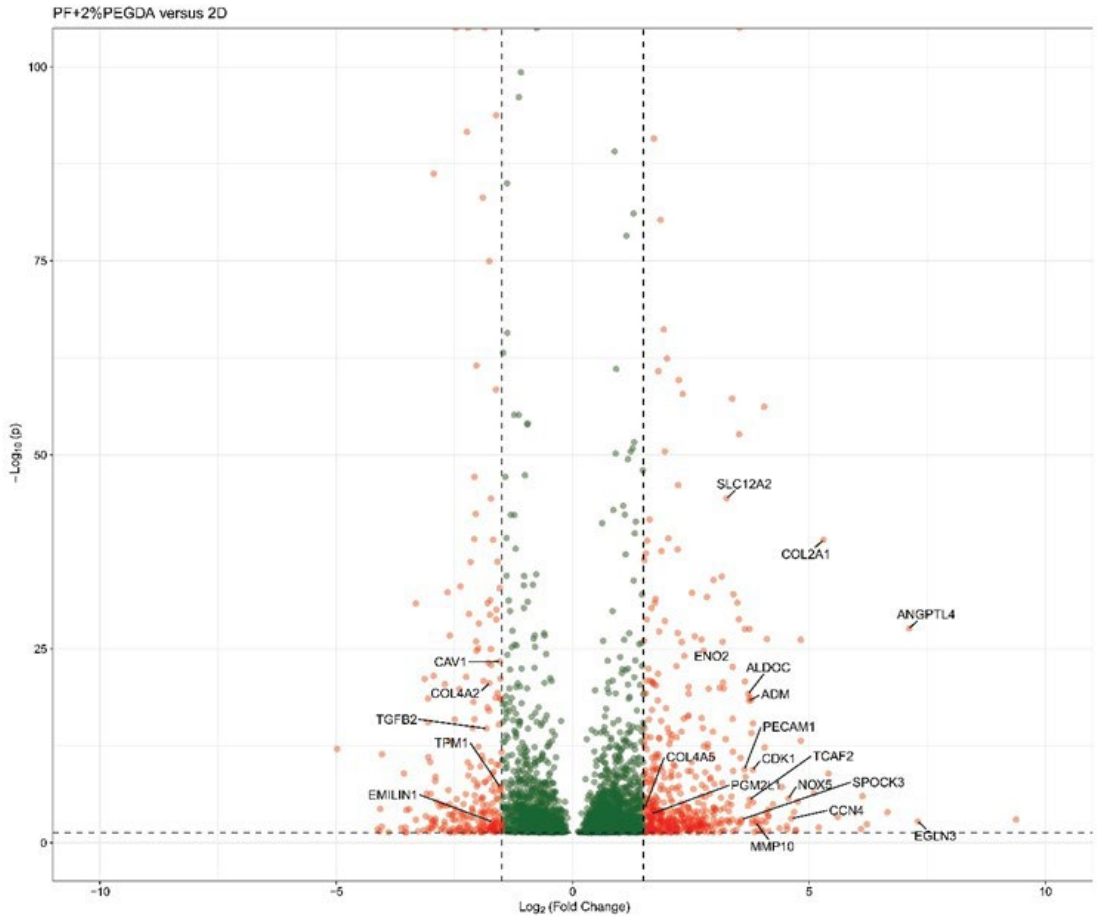

Figure 23: Volcano plot of DEGs between PF+2%PEGDA EPCaTs versus 2D.

Genes involved in GO enrichment are labeled (DEGs with $p \leq 0.05$ and Log_2(Fold Change) $\geq \pm 1.5$ are shown in red and DEGs with $p \leq 0.05$ and Log_2(Fold Change) $< \pm 1.5$ are shown in green).

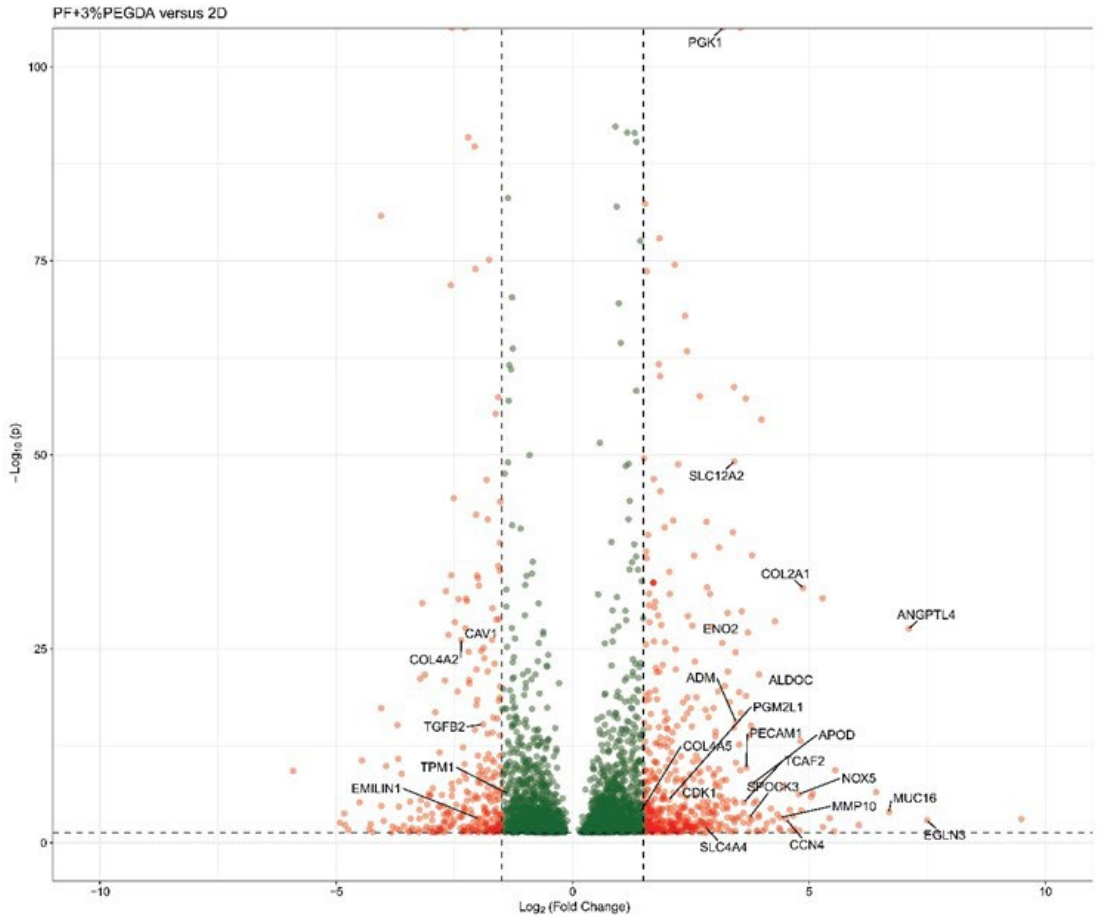

Figure 24: Volcano plot of DEGs between PF+3%PEGDA EPCaTs versus 2D.

Genes involved in GO enrichment are labeled (DEGs with $p \leq 0.05$ and Log_2(Fold Change) $\geq \pm 1.5$ are shown in red and DEGs with $p \leq 0.05$ and Log_2(Fold Change) $< \pm 1.5$ are shown in green).

Differential gene expression in PF+2%PEGDA and PF+3%PEGDA samples, relative to PF, built upon and provided context for the EPCaT comparisons presented here thus far. Interestingly, GSEA using the hallmark gene sets yielded similar enrichment profiles for PF+2%PEGDA and PF+3%PEGDA (Fig. 25A). Positive enrichment was noted in the EMT, adipogenesis, immune complement and coagulation, genes encoding proteins involved in oxidative phosphorylation and the metabolism of fatty acids, cholesterol homeostasis, genes upregulated in response to hypoxia, and genes upregulated through activation of the mTORC1 complex. Negative enrichment was observed in proliferation gene sets including mitotic spindle assembly, G2M checkpoint, and targets of E2F transcription factors. The PF+2%PEGDA versus PF comparison yielded two unique enrichment results: positive enrichment of glycolysis and positive enrichment of genes regulated by MYCv1. When directly comparing PF+3%PEGDA to PF+2%PEGDA EPCaTs, only negative enrichment in the mitotic spindle assembly, G2M checkpoint, and targets of E2F transcription factors gene sets was found (Fig. 25A). Interestingly, deeper investigation into the biological meaning of significant DEGs revealed that neither the PF+2%PEGDA versus PF nor the PF+3%PEGDA versus PF+2%PEGDA comparisons resulted in significantly enriched gene ontologies. Many enriched ontologies were elucidated in PF+3%PEGDA EPCaTs relative to PF; however, interestingly, all revolved around proliferative biological processes, including cell cycle, chromosome segregation, microtubule-based process, nuclear division, and cell division (Fig. 26). Most interestingly, in response to a stiffer environment, enrichment was observed in genes responsible for meiotic cell cycle processes in addition to mitotic cell cycle processes. Individual genes involved in the enriched hallmark gene sets and ontologies are visualized by the Figure 25B

volcano plot, as well as in Figures 27 and 28. Volcano plots for other EPCaT comparisons are included in Figures 29 and 30.

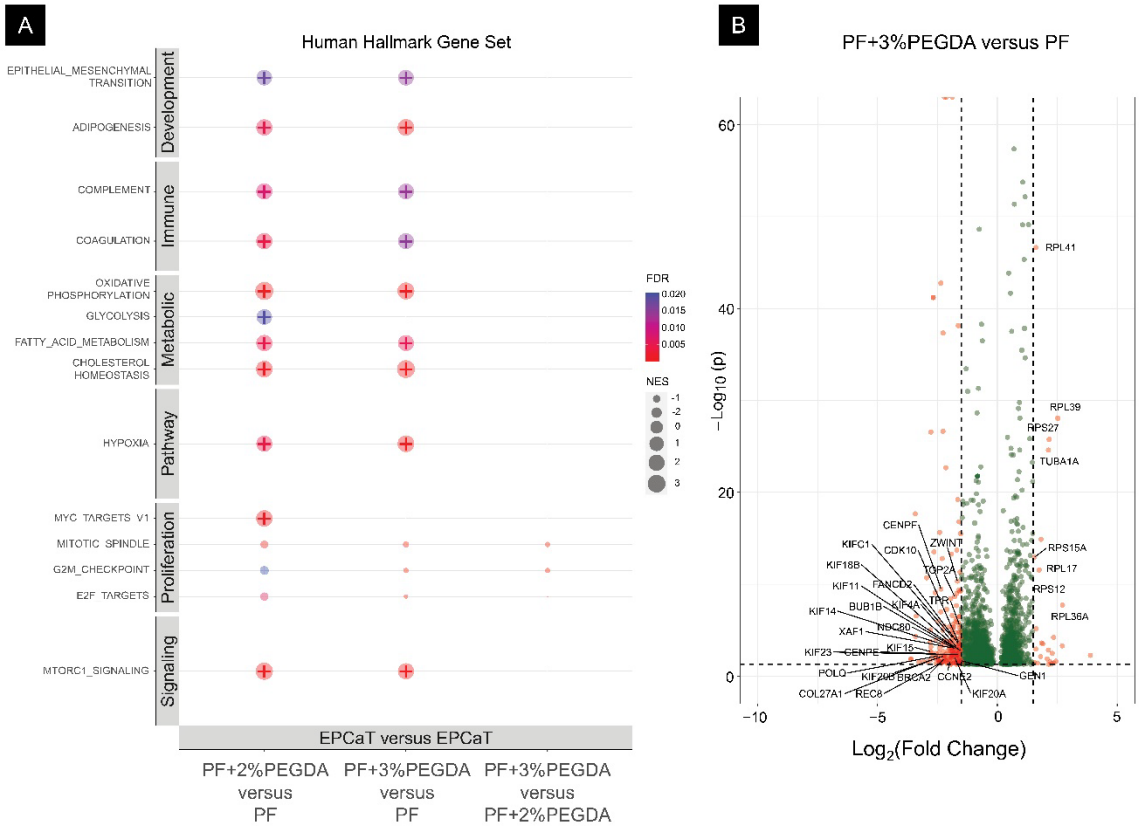

Figure 25: A stiffened EPCaT matrix resulted in differential gene expression and yielded stiffness-dependent enrichment of hallmark gene sets and gene ontologies.

A) Bubble plot of EPCaT versus EPCaT GSEA using hallmark gene sets (bubble size indicates NES, bubble color indicates FDR, positive enrichment is demarcated by a plus sign). B) Volcano plot of significant DEGs from the PF+3%PEGDA versus PF comparison; genes involved in hallmark gene set and GO enrichment are labeled ($p \leq 0.05$ and Log_2(Fold Change) $\geq \pm 1.5$ are shown in red and DEGs with $p \leq 0.05$ and Log_2(Fold Change) $< \pm 1.5$ are shown in green).

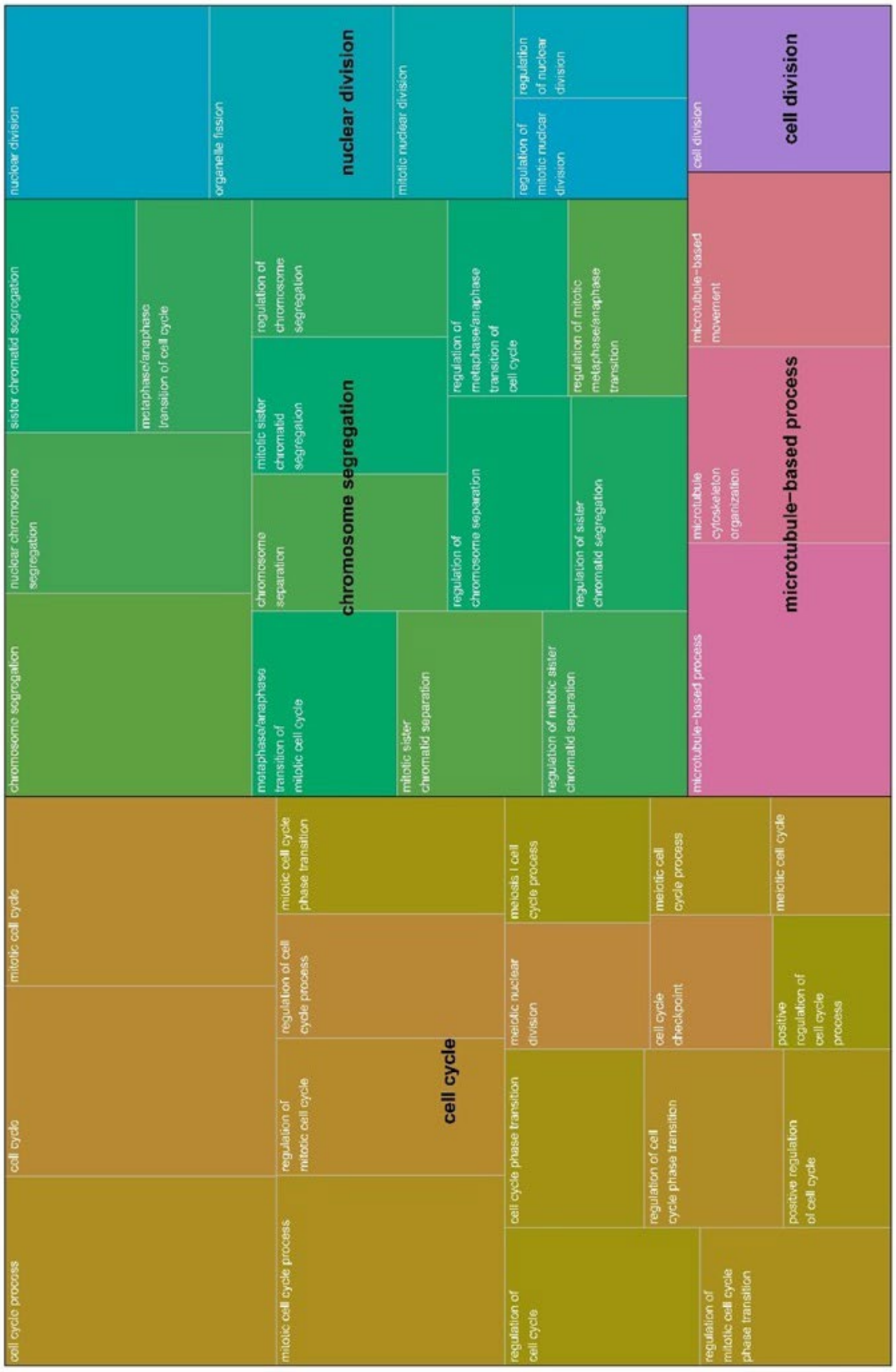

Figure 26: Tree map representing gene ontology enrichment between PF+3%PEGDA EPCaTs and PF EPCaTs.

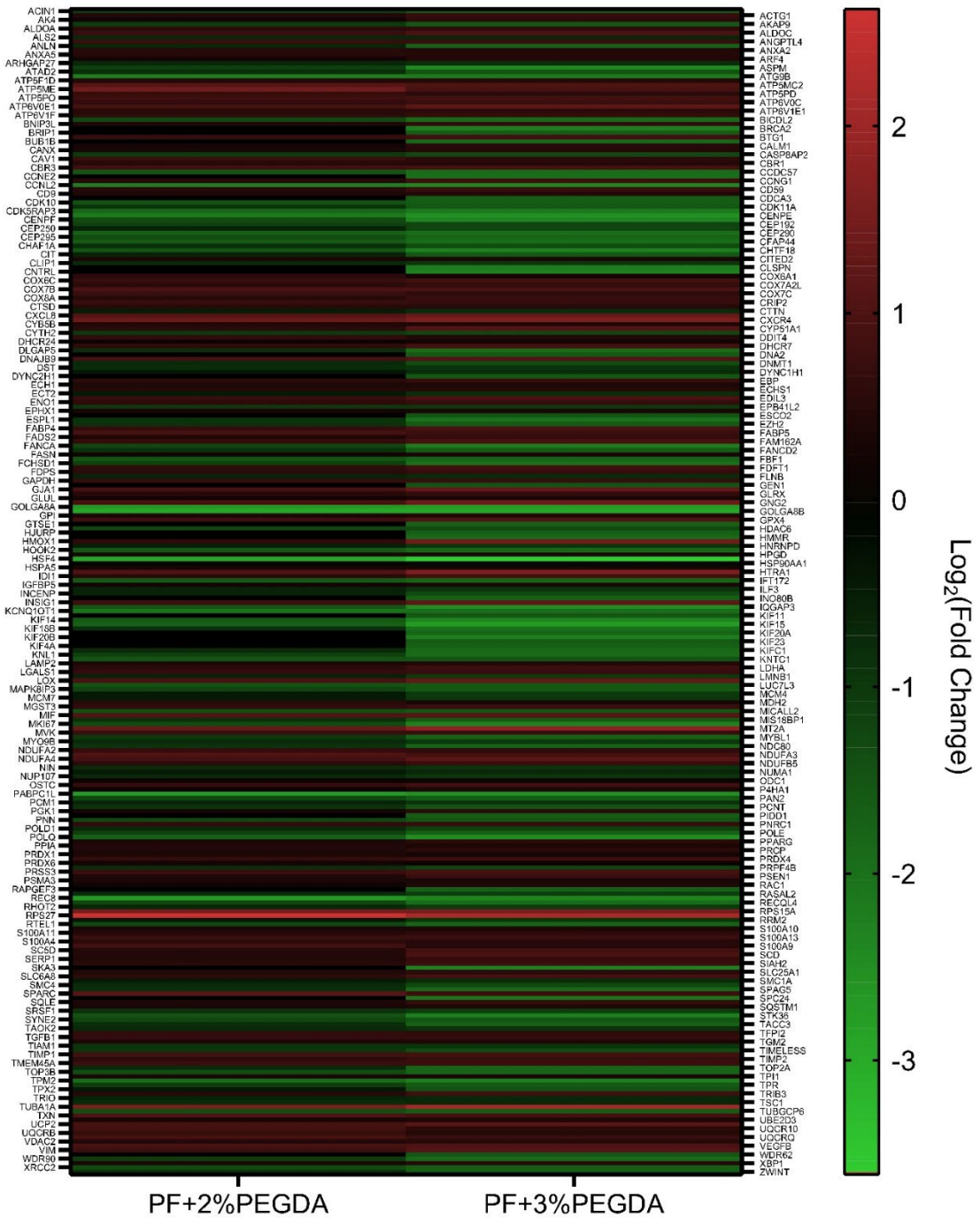

Figure 27: Heatmap illustrating the differential expression of individual genes found to be responsible for the enrichment of hallmark gene sets or gene ontologies in PF+2%PEGDA and PF+3%PEGDA EPCaTs, as compared to PF EPCaTs.

(RNA isolated from n > 2 EPCaTs).

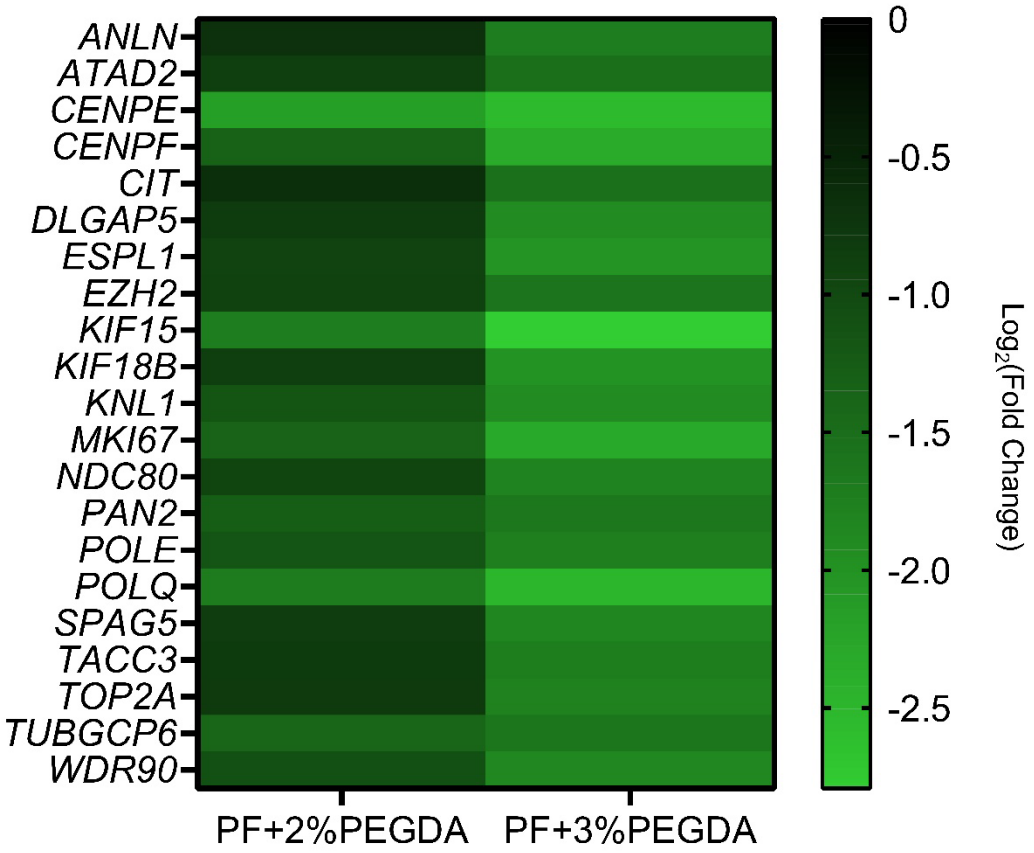

Figure 28: Heatmap illustrating the differential expression of individual genes found to be responsible for both the enrichment of hallmark gene sets and the enrichment of gene ontologies between either PF+2%PEGDA or PF+3%PEGDA EPCaTs versus PF EPCaTs.

(RNA isolated from n > 2 EPCaTs).

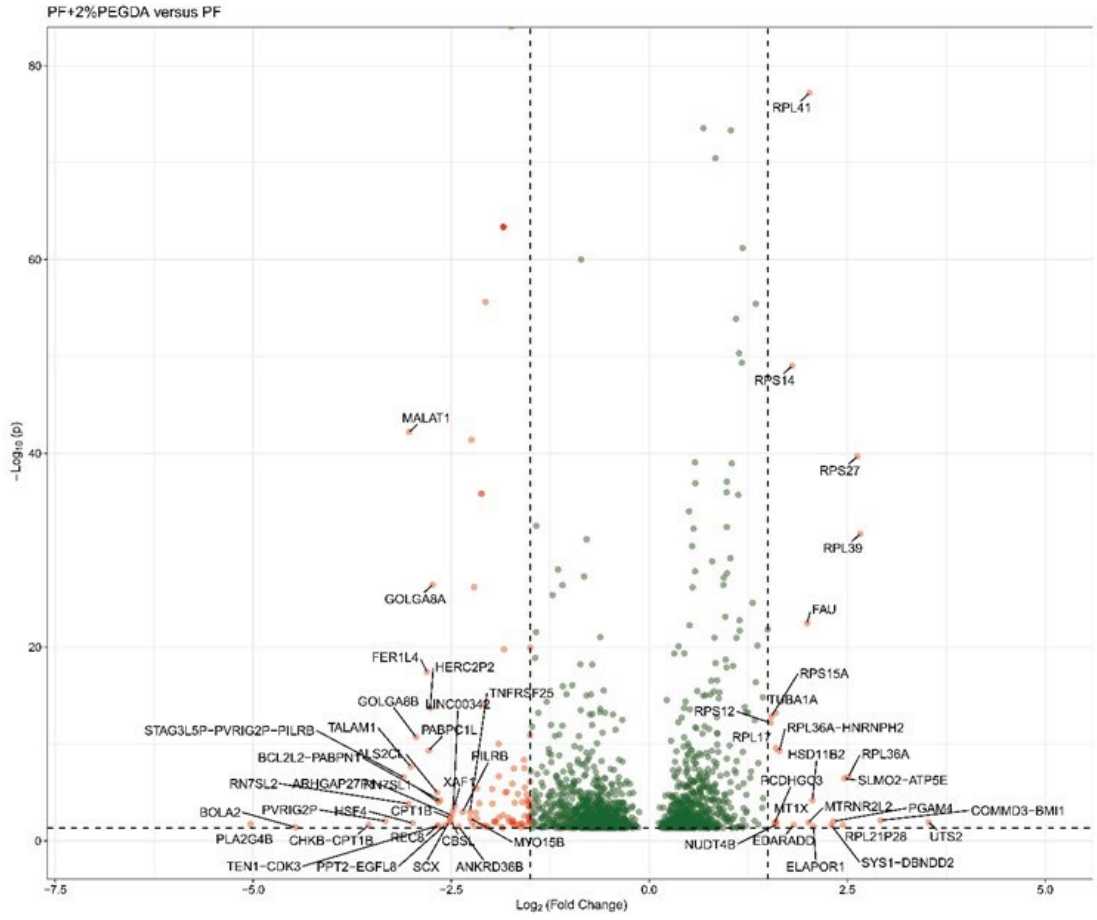

Figure 29: Volcano plot of DEGs between PF+2%PEGDA versus PF EPCaTs.

Genes are labeled based upon fold change cut-off values (DEGs with $p \leq 0.05$ and Log_2(Fold Change) $\geq \pm 1.5$ are shown in red and DEGs with $p \leq 0.05$ and Log_2(Fold Change) $< \pm 1.5$ are shown in green).

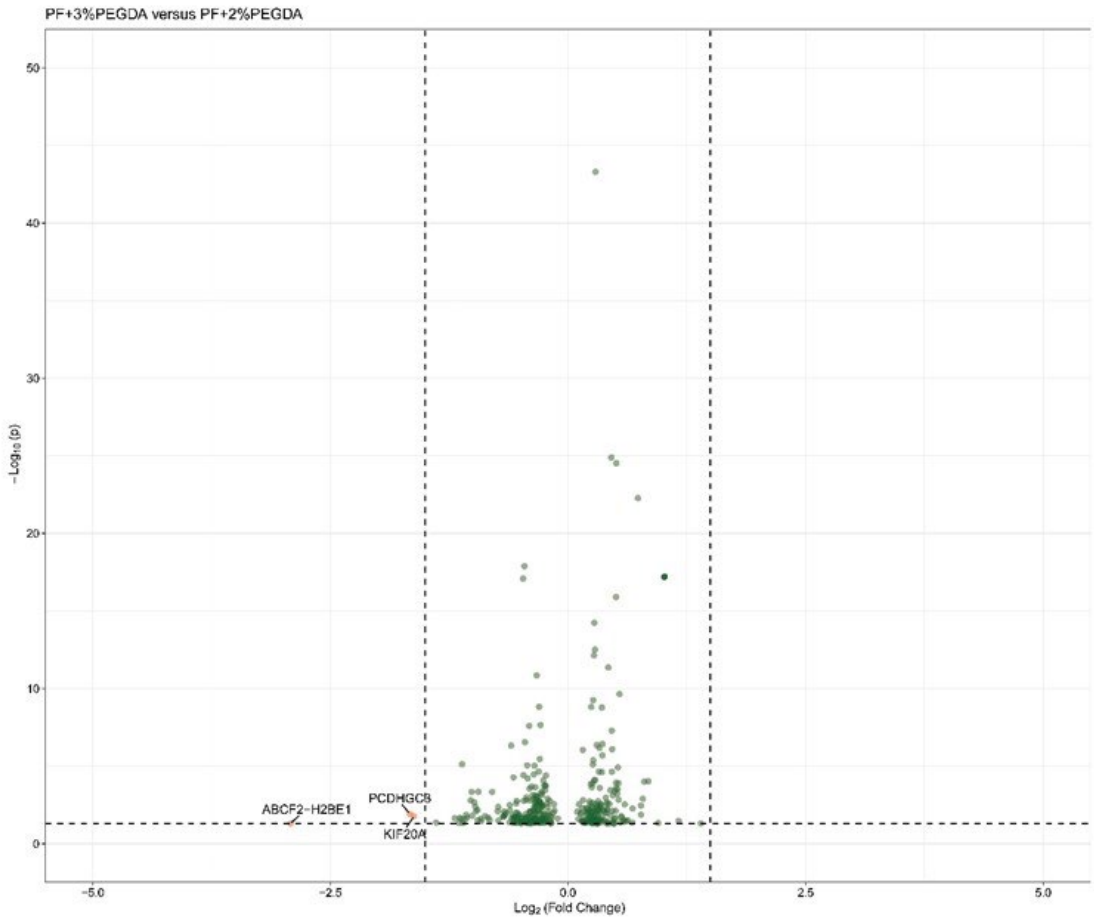

Figure 30: Volcano plot of DEGs between PF+3%PEGDA versus PF+2%PEGDA EPCaTs.

Genes are labeled based upon fold change cut-off values (DEGs with $p \leq 0.05$ and $Log_2(Fold\ Change) \geq \pm 1.5$ are shown in red and DEGs with $p \leq 0.05$ and $Log_2(Fold\ Change) < \pm 1.5$ are shown in green).

2.5 Discussion

The development of *in vitro* cancer models that accurately mimic key features of native tumors is critical to addressing current clinical challenges; such models boast significant potential for application in both translatable drug development and disease progression studies (Kim et al., 2019). Here, an *in vitro* 3D engineered prostate cancer tissue model, fabricated with a tunable matrix to recapitulate *in vivo* biomechanical cues provided to tumor cells, was established. *In vivo* prostate tumor stiffness was quantified and both inter- and intratumoral stiffness heterogeneity was observed. Most often, the peripheral region of the tumors was found to be more stiff than the geometric core and midpoint regions, which has been observed clinically in other types of adenocarcinomas (Pratt et al., 2020). Notably, the number of prostate cancer cells used in tumor seeding significantly impacted both regional and overall tumor tissue stiffnesses; Group 1X tumors seeded with 1 x 10^6 PC-3 cells were significantly less stiff than Group 2X tumors seeded with 2 x 10^6 PC-3 cells at all geometric locations. Surprisingly, the impacts of tumor size at excision and growth duration in the host animal were not as substantial. MSOT imaging clearly indicated the presence of vasculature surrounding growing clusters located both around and inside the Group 2X PC-3 xenograft tumors. As the enriched vasculature signal was roughly concentrated around the periphery of the tumor, it can be speculated that those enriched regions correlate with the highest rates of tumor growth and stiffness measurements collected per tumor. It is hypothesized this may be a result of increased cellular density at collagen-enriched regions of increased vasculature as a direct or indirect result of increased nutritional supply and waste elimination in those regions.

Through the use of a natural-synthetic hybrid biomaterial, PF, EPCaTs not only supported cell-matrix interactions, but also fostered long-term, direct coculture of both cancer and stromal cell types with high maintained viability. Tight control over matrix mechanical properties and the ability to recapitulate the full range of observed *in vivo* tumor stiffnesses were achieved through augmentation with varying amounts of excess PEGDA. Overall, the encapsulated prostate cancer and fibroblast cells exhibited key features of a pathophysiologically relevant phenotype on a both a cellular and whole-tissue level. Interestingly, extended cell protrusions were observed in all matrix stiffnesses; morphologically-speaking, these protrusions appear to resemble physical features of cells in the preliminary stages of migration, such as leading edge lamellipodia formation, filapodia extensions, and the development of invadopodia. This suggests the EPCaT platform may enable future investigations of important tumorigenic phenomena such as cell migration and invasion. Substantial, spatially heterogeneous cell colonization was observed in all matrix compositions, likely resulting from encapsulated cell proliferation within the engineered microenvironment; notably, larger colonies and enrichment of cell proliferation were found in EPCaTs comprised of less stiff matrices. PF and PF+1%PEGDA EPCaTs also demonstrated the greatest degree of cell-mediated matrix remodeling and whole tissue growth. Over time, PF EPCaTs lost structural integrity and exhibited smaller cancer cell colonies at the edge of the tissue, as compared to both early timepoints and other regions of the EPCaT, which suggests that larger cancer cell colonies may have degraded the PF and migrated out between Days 1 and 15 of coculture. PF+1%PEGDA EPCaTs yielded significant spatial heterogeneity in cancer cell morphology in that cells became more elongated with respect to a spatial progression from

the center to the edge of the tissue. This phenomena may be indicative of a more migratory phenotype in response to the increased matrix stiffness. Conversely, PF+2%PEGDA EPCaTs were spatially uniform and did not significantly degrade or demonstrate tissue area growth over time, likely due to the increased synthetic fraction of the EPCaT matrix which limits cell-mediated remodeling. While this trend was expected to continue with the addition of 3% excess PEGDA, a significant temporal decrease in the Young's modulus, similar to PF and PF+1%PEGDA EPCaTs, was observed. Interestingly, matrix degradation did not continue beyond Young's moduli similar to that of the PF+2%PEGDA EPCaTs. It is hypothesized that this initial degradation, as well as the temporal EPCaT growth and spatial heterogeneity in colony size, could be due to a more aggressive cancer cell phenotype in response to a significantly stiffer matrix. When compared to the *in vivo* prostate tumor samples, the EPCaTs successfully recapitulated the stiffness range quantified from all geometric locations of both Group 1X and Group 2X xenograft tumors; PF and PF+1%PEGDA EPCaTs were most similar to the softer Group 1X tumors whereas PF+2%PEGDA and PF+3%PEGDA EPCaTs were most similar to the stiffer Group 2X tumors. Thus, the biomechanical cues provided to EPCaT encapsulated cells were also found to be pathophysiologically relevant in all four matrix compositions.

Bulk transcriptomic analyses afforded the opportunity to elucidate EPCaT matrix stiffness-derived changes in differential gene expression, first against a field-standard 2D coculture of PCa and fibroblast cells and then against other EPCaTs of different matrix compositions. Considering gene set enrichment and gene ontology analyses together, an increased EPCaT matrix stiffness was most often associated with: 1) positive enrichment of gene sets known to be associated with tumorigenesis (EMT, hypoxia, immune

complement, migration, angiogenesis, etc.), 2) plasticity in cell metabolism (glycolysis versus oxidative phosphorylation, fatty acid metabolism), 3) activation of the mTOR signaling pathway, 4) negative enrichment of gene sets associated with cell proliferation, and 5) variation in cell cycle processes, particularly those associated with chromosomal segregation. Notably, several of the hallmark gene sets enriched in response to a stiffened EPCaT matrix were also reported to be enriched in tumor-adjacent normal tissues isolated from patients deemed to be high-risk for PCa progression; these include positive enrichment of the EMT and oxidative phosphorylation, as well as negative enrichment of targets of E2F transcription factors (Zhou et al., 2021).

Interestingly, very few differences in gene expression were found between the PF+2%PEGDA and PF+3%PEGDA EPCaTs, although each exhibited differences in EPCaT growth and degradation; however, when considering the matrix stiffness on Day 15 (the timepoint at which samples were used for RNA isolation), there are no significant differences between the PF+2%PEGDA or PF+3%PEGDA matrix-provided biomechanical cues. It is hypothesized that by Day 15 of *in vitro* culture, encapsulated cells have established their microenvironment and, therefore, initial matrix stiffness-driven changes in gene expression are no longer detectable. It is likely that transcriptomic analyses performed on Days 1 or 8 post-encapsulation would yield a different set of DEGs which could warrant a more in-depth future investigation.

In future studies employing the EPCaT platform, matrix composition selection should be based in part on the goals of the study; whereas the addition of 3% excess PEGDA was necessary to mimic the most stiff peripheral regions of PCa xenograft tumors, it also limited cell migration, colonization, and matrix remodeling to the greatest extent.

Conversely, PF EPCaTs (without excess PEGDA) were substantially remodeled by encapsulated cells and supported significant PCa cell colonization and migration; however, the biomechanical cues were more similar to those of the soft *in vivo* tumor core region. Thus, an optimal EPCaT matrix composition is not recommended for future studies, but rather consideration of which tumor microenvironmental properties are most appropriate on an application-by-application basis is encouraged.

Previous studies have investigated the impact of 2D (Moazzem Hossain et al., 2014, Prauzner-Bechcicki et al., 2015) and 3D (Sieh et al., 2012, Bäcker et al., 2016, Tam et al., 2020, Xu et al., 2019) culture platform stiffness on prostate cancer cell behavior and have provided important insight into potential, application-dependent *in vitro* PCa model parameters necessary for accurate recapitulation of the prostate TME. Each of the reported 3D models employed varying methods of manipulating the scaffold or matrix-provided biomechanical cues experienced by the PCa cells and were mimetic of varying pathophysiological environments. Tam et al. and Xu et al. each employed a scaffold overlay 3D cell culture method and modulated the stiffness of the scaffold via material concentration changes; the former aimed to mimic a soft tissue microenvironment using hyaluronic acid (HA) hydrogels and reported a stiffness range of approximately 250 to 3,100 Pa (Tam et al., 2020) whereas the latter aimed to mimic the metastatic bone microenvironment using porous chitosan-alginate (CA) and reported bulk stiffnesses of approximately 2 kPa, 12 kPa, and 42 kPa for each of their three CA scaffold compositions (Xu et al., 2019). Backer et al. investigated a number of approaches to modulate the physical properties of their LNCaP overlay cryogel scaffold, including modifying the PEGDA crosslinker concentration, resulting in an achievable modulus of approximately

10, 40, or 65 kPa (Bäcker et al., 2016). Using a similar method, Sieh et al. modulated the stiffness of their matrix metalloproteinase (MMP)-sensitive PEG-based hydrogels via augmentation with PEG at contents of 1.5%, 2%, and 2.5% resulting in a modulus range of 0.8 to 10 kPa (Sieh et al., 2012). Notably, the mechanical stiffness values reported by each of these monoculture studies when employing similar augmentations of the synthetic PEG-based fraction of the 3D tissue are similar to the values presented here. Sieh et al. noted a decreased ability of PCa cells to colonize and proliferate in a 2.5% PEG content hydrogel matrix in comparison to less stiff matrices, similar to the behavior observed in the PF+3%PEGDA EPCaTs; however, here it was found that encapsulated cells are able to remain viable in the EPCaT model and do temporally remodel the matrix. Interestingly, Sieh et al. also reported no significant changes in the overall 2% matrix stiffness over four weeks of culture, which is in stark contrast to the observations outlined herein. This discrepancy in findings is attributed to two key design features of the EPCaTs. First, the more aggressive PC-3 cell line at an initial concentration of 20 x 10^6 cells/mL is employed herein, whereas Sieh et al. employ the more indolent LNCaP cell line at a concentration of 3.5 x 10^5 cells/mL when forming their engineered tissues. Second and most importantly, the EPCaT model includes direct coculture of PCa cells with matrix-remodeling fibroblasts. Fibroblasts typically contribute to an increased matrix stiffness (Alkasalias et al., 2018, Kesselman et al., 2013); however, here the PCa-fibroblast coculture appears to significantly expedite degradation of the EPCaT PF matrix. To further understand the potential mechanisms leading to these unexpected results, additional studies investigating both the impact of cancer to stromal ratio and differences between androgen-dependent versus castration-resistant PCa within the coculture EPCaT platform will be undertaken.

As the importance of the role tissue stiffness plays in cancer progression has become more widely accepted (Deville and Cordes, 2019, Kraning-Rush and Reinhart-King, 2012), many groups have aimed to characterize the mechanical properties of the native prostate gland under both normal and cancer conditions. Transrectal shear wave elastography has been employed to assess the Young's modulus of the entire prostate gland *in situ* for several patient cohorts (Anbarasan et al., 2021), as well as in a murine xenograft model using DU-145 PCa cells (Wang et al., 2017). Shear wave elastography of PCa tumor xenografts yielded whole tumor Young's moduli ranging from 22 to 57 kPa depending on tumor size and implantation time (Wang et al., 2017). Patient studies reported a wide range of minimum, maximum, and average Young's moduli for both malignant and benign prostate gland lesions with reported cut off values to distinguish between healthy and cancerous tissue ranging from 28.5 to 82.6 kPa (Anbarasan et al., 2021). When considering these studies, it is important to note that the overall prostate gland stiffness reported can be influenced by other phenomena, such as benign prostatic hyperplasia, fibrosis, inflammation or calcification; furthermore, the actual impact of malignant growth can be limited depending on the size of the prostate and the size of the cancerous region, as well as its location within the prostate (Correas et al., 2013, Ji et al., 2019). Interestingly, positive correlations were found between prostate stiffness and both the Gleason score and the serum prostate specific antigen (PSA) level of the patient, thus indicating that a higher stiffness is linked to a higher PCa risk and increased aggressiveness (Ji et al., 2019, Correas et al., 2014). Employing a method more similar to that reported here, Hoyt et al. performed mechanical characterization of seventeen patient prostate tissue samples post-radical prostatectomy and reported a Young's modulus of 3.8 ± 1.8 kPa for normal prostate tissue

and a significantly stiffer Young's modulus of 7.8 ± 3.3 kPa for cancerous prostate tissue at a frequency of 0.1 Hz (Hoyt et al., 2008). These values are within the reported range of gland and other soft tissue stiffnesses (approximately 0.1 to 10 kPa) (Levental et al., 2007) and are similar to the quantification of PC-3 xenograft stiffness presented herein. Notably, the EPCaT model can be tuned to mimic both the normal and cancerous native biomechanical cues found in literature (Fig. 31).

While the 3D engineered prostate cancer tissues present several advantages as an *in vitro* model, both design limitations and gaps in characterization of the EPCaTs do exist. Whereas the stiffness of the EPCaTs has been shown to mimic that of murine xenograft and patient PCa tumors from literature, characterization of the ECM composition has not been investigated and will be the focus of future research. Although native PCa tumors are laminin and collagen-rich (Stewart et al., 2004), fibrinogen was chosen as the natural component of the engineered matrix as it has been previously established for use in other engineered cancer tissue models (Pradhan et al., 2017a, Pradhan et al., 2017b), has been implicated in tumor migration and malignant transformation (Zhang and Long, 2017, Simpson-Haidaris and Rybarczyk, 2001), does not contain many inherent growth factors, and introduces the opportunity to investigate cell-secreted ECM. Nonetheless, it may be likely that the matrix-provided biochemical cues are not similar to that of native prostate tumors and future investigation of the impact of EPCaT matrix composition is warranted.

Next, here a normal human fibroblast cell line in coculture with PCa cells was employed due to the physiological role of fibroblasts in ECM remodeling, thus providing the opportunity to more closely mimic the native TME. As the stromal content of native PCa varies substantially (Boufaied et al., 2019), and with the knowledge that normal

prostate and benign prostatic hyperplasia exhibit approximately a 1:2 and 1:5 epithelial to stromal cell ratio, respectively (Shapiro et al., 1992), a 5:1 cancer cell to fibroblast ratio was chosen as a starting point. With this ratio, significantly more aggressive PCa cell behavior and accelerated matrix degradation was observed in coculture EPCaTs as compared to monoculture EPCaTs. However, the impact of varying the cancer to fibroblast cell ratio, the specific mechanisms driving this behavior, and the impact of including prostate cancer-associated fibroblasts in place of the normal fibroblasts employed herein should be investigated further in future studies.

Finally, there are inherent differences in the cellular content of native tissue and engineered models. Native tissue is mostly comprised of cells with interspersing ECM throughout, whereas most *in vitro* tissue models employ interspersed cells throughout an engineered matrix at a much lower cell density. The EPCaT model is encapsulated at 20×10^6 cells/mL, which is substantially higher than most other engineered prostate cancer models in the literature (Sieh et al., 2012, Tam et al., 2020, Xu et al., 2019); however, the EPCaTs still do not replicate the cell to ECM ratio of native tissue. While the PF-based, cell-laden matrix has been tuned to mimic the bulk mechanical properties of both PC-3 xenograft and published clinical prostate tumor stiffness data, a direct comparison of the cell-derived contribution to overall tissue stiffness between the EPCaT model and native tumor tissue cannot be made. It is also important to note that the subcutaneous PC-3 tumor xenograft model also differs from clinical PCa tumors with respect to cellular content and pathophysiological complexity. The long-term goal is to understand how mechanical properties influence drug delivery and disease progression; although subcutaneous PC-3 xenograft tumors are not the most pathophysiologically relevant *in vivo* prostate cancer

model, they are widely used in drug screening and disease modeling studies. Therefore, it is important to not only characterize these tumors, but also have the ability to mimic them in an *in vitro* setting.

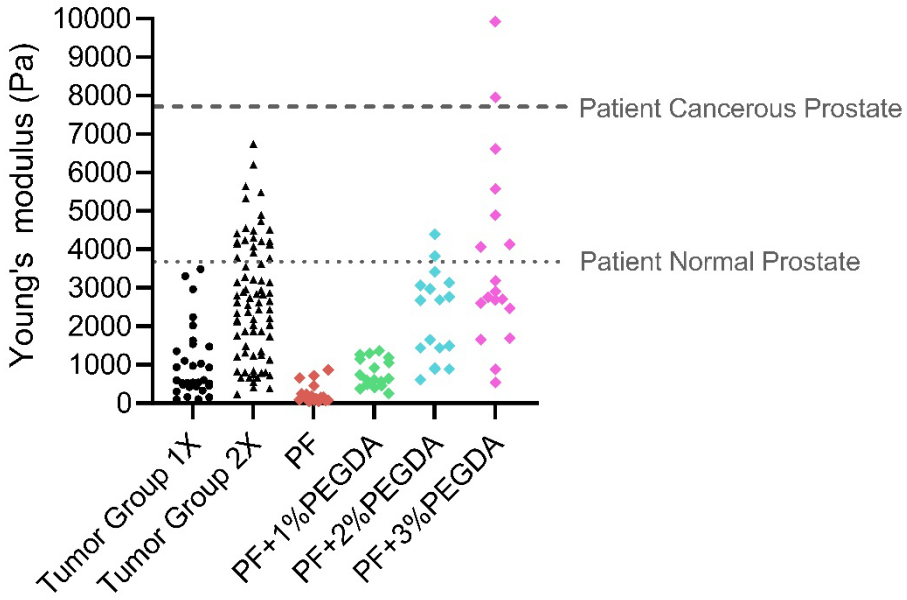

Figure 31: The achievable range of EPCaT stiffness encompassed published clinical data for patient normal and cancerous prostate tissue stiffness.

2.6 Conclusions

In this study, the tissue stiffness range present in PCa tumor xenografts was characterized and a tunable, 3D engineered prostate cancer tissue model was developed for a first of its kind *in vivo – in vitro* comparison. PCa xenograft tumor stiffness was found to be highly dependent on initial cell seeding concentration and both inter- and intratumoral heterogeneity in tissue stiffness and microarchitecture was observed, including spatial disparities in tumor vascularization which appeared to correlate to subsequent disparities in tumor stiffness. The EPCaT model was designed to support both tumor-mimetic cell-matrix and cell-cell interactions through long-term direct coculture of multiple tumor cell types within a natural-synthetic hybrid biomaterial, PF. Within the EPCaT model, PCa and fibroblast cells were viable, temporally remodeled their microenvironment, and exhibited matrix stiffness-driven changes in differential gene expression and gene set enrichment. Most notably, through augmentation with excess PEGDA, the *in vitro* biomechanical cues were successfully modulated to recapitulate those experienced by cells *in vivo* in both PCa tumor xenografts and patient tumors. In conclusion, this work introduces and characterizes the EPCaT platform as an *in vitro* tool for supporting biomimetic cell-cell and cell-matrix interactions, thus serving as the foundation for a number of future PCa disease modeling and drug development studies.

This chapter has been previously published in Acta Biomaterialia (Habbit et al., 2022a).

Chapter 3. Ratiometric Inclusion of Fibroblasts Promotes both Castration-resistant and Androgen-dependent Tumorigenic Progression in Engineered Prostate Cancer Tissues

3.1 Abstract

The complex prostate tumor microenvironment (TME) is governed by a dynamic cohort of cancer, stromal, and immune cell populations; notably, the tumor-supporting cell cadre often abandon traditional physiological roles and enable tumorigenic phenomena, such as invasion and metastasis. Fibroblasts, in particular, have been linked to the exacerbation of prostate cancer (PCa); however, our ability to define the mechanisms by which fibroblasts elevate disease state and drive poor clinical outcomes is currently hindered by the lack of a TME-mimetic *in vitro* model of PCa-fibroblast interaction. This study aims to develop and characterize a three-dimensional engineered prostate cancer tissue (EPCaT) model comprised of neuroendocrine-variant, castration-resistant (CRPC-ne) or androgen-dependent (ADPC) PCa cells in direct coculture with normal fibroblasts within a bioinspired poly(ethylene glycol)-fibrinogen (PF) matrix. By specifically isolating this important cell-cell interaction, the EPCaT model introduces the ability to reverse engineer coculture-driven mechanisms responsible for PCa progression at a whole tissue, cellular, and transcriptomic level.

To investigate the role of fibroblasts in CRPC-ne EPCaTs, PC-3 cells were encapsulated both in monoculture and in coculture with BJ-5ta fibroblasts at cancer to stromal cell ratios of 5:1, 1:1, and 1:5. To examine fibroblast impact on ADPC in relation to CRPC-ne, LNCaP cancer cells were also encapsulated within a PF matrix, both in

monoculture and coculture with BJ-5ta fibroblasts at a 5:1 cancer to stromal ratio. Temporal changes in encapsulated cell behavior, cell populations, and EPCaT matrix stiffness were monitored. In addition, bulk transcriptomic changes in gene expression resulting from PCa-fibroblast interaction in both CRPC-ne and ADPC EPCaTs were assessed. To probe clinical significance, normal and primary tumor tissue transcriptomic data was acquired from the Cancer Genome Atlas (TCGA). Differential gene expression, gene ontology, and hallmark gene set enrichment analyses were performed.

When formed using both cancer cells and fibroblasts, all coculture CRPC-ne EPCaTs demonstrated significant cell-mediated remodeling of the PF matrix and increased percentages of proliferative cells. Interestingly, PC-3 5:1 EPCaTs demonstrated this behavior to a much greater degree than other ratios while simultaneously maintaining the original cancer to fibroblast cell ratio throughout long-term *in vitro* culture. In comparison to the monoculture condition, LNCaP 5:1 EPCaTs also yielded a higher number of proliferative cells and temporal degradation of the PF matrix. Bulk transcriptomic analyses revealed that both CRPC-ne and ADPC fibroblast coculture resulted in significant enrichment of genes defining important tumorigenic processes, including the epithelial to mesenchymal transition, inflammatory response, and extracellular matrix (ECM) organization. ADPC coculture EPCaTs also uniquely demonstrated enrichment in angiogenesis, epithelial cell proliferation, complement system activation, and cell-substrate adhesion and migration, suggesting that fibroblasts may play a role in elevating indolent disease to a more aggressive state. Finally, a comparison to the TCGA PCa patient cohort revealed similar hallmark gene set enrichment between the EPCaT models and the patient primary tumor transcriptome, as compared to patient normal tumor adjacent tissue.

In total, the findings of this study suggest that 1) cell-cell interactions between prostate cancer cells and a small number of fibroblasts promote increased aggression, proliferation, and significant remodeling of the supporting matrix, 2) fibroblasts may play an elevated role in more indolent PCa disease states and participate in the transition from ADPC to CRPC, and 3) the EPCaT system demonstrates potential as a TME-mimetic tool in future therapeutic target identification and drug testing studies.

3.2 Introduction

Prostate cancer (PCa) represented 14.1% of all new male cancer cases worldwide in 2020 and was responsible for over 375,000 deaths, rendering it the second most common cancer and the fifth leading cause of cancer-related death in men (Sung et al., 2021). Approximately 20% of PCa cases have spread beyond the primary site at diagnosis and, unfortunately, patients who present with distant metastases are faced with a 5-year relative survival rate of only 30.2% (National Cancer Institute). Currently, there are no curative therapies for advanced metastatic PCa, and most men develop serial resistance to hormone therapies resulting in a more aggressive disease state, known as castration-resistant prostate cancer (CRPC), which is substantially more difficult to treat. Simultaneously, more men diagnosed with localized PCa are choosing active surveillance over surgical intervention via radical prostatectomy (Mahal et al., 2019). In order to interrupt PCa advancement both in low-grade tumors during the active surveillance period and in higher-grade tumors, particularly those that have metastasized or have developed hormone therapy resistance, we must better understand the tumor microenvironmental phenomena that actuate disease progression. As such, there exists a critical need to develop and characterize tumor microenvironment (TME) mimetic, *in vitro* models of PCa that can then be used to

elucidate and evaluate the targeting of molecular mechanisms driving PCa invasion and metastasis, as well as illuminate the switch from androgen-dependent prostate cancer (ADPC) to CRPC and how it exacerbates disease aggression.

The complex prostate TME is comprised of a variety of supporting cell types that stimulate tumorigenic progression. Fibroblasts in particular have been implicated in PCa progression and are abundant at both the site of origin and soft tissue metastases; clinically, the epithelial cancer cell to stromal cell ratio in PCa tends to deviate from the normal prostate epithelial cell to stromal cell ratio of 1:2 (Shapiro et al., 1992) and can vary drastically between patients with stromal content ranging from 2 – 100% (Boufaied et al., 2019). Fibroblasts are thought to not only provide the toolset necessary for PCa cell intravasation, but also circulate alongside cancer cells and prime metastatic sites for tumor growth (Ortiz-Otero et al., 2020, Bonollo et al., 2020). Our understanding of the precise mechanisms by which they contribute to overall PCa progression, however, is relatively underdeveloped in comparison to other solid cancer types. In recent years, several *in vitro* prostate cancer-fibroblast coculture models have been reported (Eder et al., 2016, Iacopino et al., 2012, Ortiz-Otero et al., 2020, Ojalill et al., 2018, Ojalill et al., 2020, Neuwirt et al., 2020, Ishii et al., 2021, Åkerfelt et al., 2015, Richards et al., 2019, Yu et al., 2021); these studies contributed fundamental information to the field regarding the role of fibroblasts in PCa cell dissemination, enhancing the survival of circulating PCa cells, inhibiting epithelial cell proliferation, and recruiting immune cell types, as well as their impact on drug response. However, each of these studies employ either traditional two-dimensional (2D) cell culture, three-dimensional (3D) self-aggregated spheroidal cell culture, or 3D culture techniques involving sandwiching sheets of cells between polymerized natural

biomaterials. As previously reviewed (Kim et al., 2019, Kapałczyńska et al., 2018), these techniques induce inherent limitations to the pathophysiological relevance of the model by failing to facilitate key cell-cell and cell-matrix interactions observed in the native TME. Animal models of PCa-fibroblast interaction have also been reported (Thalmann et al., 2010, Linxweiler et al., 2020, Ippolito et al., 2019); however, they are often unable to appropriately facilitate the investigation of human cancer-stromal interactions as the host-provided stromal cadre overwhelms human stromal cell growth. Markedly, a matrix-inclusive *in vitro* model of PCa-fibroblast interaction, that is mimetic of both the site-of-origin and soft tissue metastases, is currently lacking from our PCa therapeutic development toolkit.

This chapter reports an *in vitro* 3D engineered prostate cancer tissue (EPCaT) model comprised of either CRPC or ADPC prostate cancer cell lines in direct coculture with fibroblasts within a bioinspired (Habbit et al., 2022a), enzymatically cleavable poly(ethylene glycol)-fibrinogen (PF) matrix. To simultaneously model a highly aggressive, neuroendocrine variant of metastatic CRPC (CRPC-ne) and investigate the impact of cancer cell to fibroblast cell ratio on PCa cell behavior, PC-3 prostate cancer cells were encapsulated in monoculture and in coculture with BJ-5ta normal fibroblasts at cancer to stromal cell ratios of 5:1, 1:1, and 1:5. Building upon these findings, LNCaP prostate cancer cells were encapsulated in monoculture and coculture with BJ-5ta normal fibroblasts at a 5:1 cancer to stromal cell ratio to model ADPC and provide insight into the role of fibroblasts in the ADPC to CRPC switch. Overall, by specifically isolating the PCa-fibroblast cell-cell interaction within a controlled environment, the ability to reverse engineer cellular dynamics driving cancer progression in both CRPC and ADPC at a whole

tissue, cellular, and transcriptomic level is introduced, while the potential utility of the *in vitro* EPCaT model in the identification of molecular therapeutic targets and other future drug testing applications is simultaneously explored.

3.3 Materials and Methods

All chemicals were acquired from Sigma-Aldrich (St. Louis, MO) unless stated otherwise.

3.3.1 PEGDA Synthesis and Characterization

Poly(ethylene glycol)-diacrylate (PEGDA) was synthesized in-house according to an established protocol (DeLong et al., 2005). Briefly, 10 kDa molecular weight poly(ethylene glycol) (PEG) was reacted with acryloyl chloride at a 1:4 molar ratio in anhydrous dichloromethane with triethylamine at a 1:2 molar ratio; the reaction was allowed to proceed overnight at 25 ºC. Phase separation with 2M potassium carbonate was then employed to purify the resultant PEGDA; the organic phase, containing PEGDA, was dried using anhydrous magnesium sulfate and subsequently filtered. The PEGDA was precipitated using diethyl ether, filtered again, and finally dried overnight under vacuum at 25 ºC. Synthesized PEGDA was stored at -20 ºC and ^{1}H NMR was performed to characterize the degree of acrylation achieved during synthesis; PEGDA with greater than 99% acrylation was employed in this study.

3.3.2 PF Synthesis and Characterization

PF was synthesized in-house according to a previously reported protocol (Almany and Seliktar, 2005, Habbit et al., 2022a). Briefly, bovine fibrinogen was dissolved to a final concentration of 7 mg/mL in an 8M urea in 10mM phosphate buffered saline (PBS) solution. Synthesized PEGDA was also dissolved in an 8M urea-PBS buffer solution at a final concentration of 280 mg/mL; vortex and centrifugation at 2,500 RPM for 3 minutes

were employed to clear the solution. Tris (2-carboxyethyl) Phosphine Hydrochloride (TCEP-HCl) was added to the fibrinogen solution at a 1.5:1 molar ratio to the fibrinogen cysteines; subsequently, the pH of the solution was adjusted to 8.0. Next, the PEGDA solution was slowly combined with the fibrinogen solution; the consequent reaction progressed under dark conditions at 25 ºC. After 3 hours, the reaction was stopped via the addition of an equal volume of urea-PBS buffer solution and the reaction product was then precipitated by adding acetone at a 4:1 volumetric ratio to the reaction solution. The precipitate was centrifuged out of the liquid phase and re-dissolved in urea-PBS to a final concentration of 2.6 mL buffer per gram of precipitate. The PF product was dialyzed against sterile PBS for 24 hours at 4 ºC under dark conditions before being collected and stored at -80 ºC for future use. The PF protein concentration was quantified through the use of a Pierce™ BCA Protein Assay Kit (Thermo Fisher Scientific, Rockford, IL); all experiments performed in this study employed PF with protein concentrations between 10 – 12 mg/mL.

3.3.3 Cell Culture and Maintenance

All cells employed in this study were acquired from ATCC (Manassas, VA). PC-3 cells were cultured in F-12K culture media (Corning, Corning, NY) supplemented with 10% (v/v) fetal bovine serum (FBS) (Atlanta Biologicals, Flowery Branch, GA) and 1% (v/v) Pen-Strep (GE Healthcare Bio-Sciences, Pittsburgh, PA). LNCaP cells were cultured in Roswell Park Memorial Institute (RPMI) 1640 culture media (Thermo Fisher Scientific, Rockford, IL) supplemented with 10% FBS and 1% Pen-Strep. BJ-5ta normal fibroblasts were cultured in 4 parts of Dulbecco's Modified Eagle's Medium (DMEM) (Lonza, Walkersville, MD) containing 4 mM L-glutamine, 4.5 g/L glucose and 1.5 g/L sodium

bicarbonate, and 1 part of Medium 199 (Lonza, Walkersville, MD) supplemented with 0.01 mg/mL hygromycin B (MilliporeSigma, Burlington, MA), and 10% FBS. All cells were maintained in a humidified atmosphere with 5% carbon dioxide (CO_2) at a constant temperature of 37 ºC. The appropriate cell culture media was replenished at least twice weekly. To prepare for passaging or 3D culture, adherent cells were enzymatically dissociated from the plasma-treated tissue-culture flask surface using 0.25% trypsin/2.21 mM EDTA (Corning, Corning, NY).

3.3.4 Encapsulation of 3D CRPC-ne Engineered Prostate Cancer Tissues

3D EPCaTs were formed within prefabricated, cylindrical shaped poly(dimethyl siloxane) (PDMS) molds as previously described (Habbit et al., 2022a). In brief, PDMS sheets were produced utilizing the SYLGARD 184 Elastomer Kit (Thermo Fisher Scientific, Rockford, IL); encapsulation wells were shaped utilizing a biopsy punch (3 mm diameter). Immediately prior to beginning the cell encapsulation process, the PDMS molds were placed at the bottom of a 6-well plasma-treated tissue-culture plate. Simultaneously, the PF hydrogel precursor solution was prepared by augmenting the synthesized PF-PBS solution with 37 mM 1-vinyl-2-pyrrolidinone (NVP), 1.5% (v/v) triethanolamine (TEOA), and 0.1 mM Eosin Y; the precursor solution was kept under dark conditions at 25 ºC prior to mixing with cells.

To prepare for encapsulation of CRPC-ne EPCaTs, PC-3 prostate cancer and BJ-5ta fibroblast cells were enzymatically dissociated from the tissue-culture flask surface using 0.25% trypsin/2.21 mM EDTA (Corning, Corning, NY). The cells were then manually counted utilizing a hemocytometer with 0.4% Trypan Blue (Lonza, Walkersville, MD) and resuspended in PF at a concentration of 20 x 10^6 cells/mL precursor solution. Cancer to

fibroblast cell ratios of 5:1, 1:1, and 1:5 were prepared, in addition to monocultures of each cell type. A 10 μL volume of the cell-laden PF precursor solution was pipetted into each PDMS encapsulation well and subsequently photocrosslinked via visible light exposure (light intensity: 203 mW/cm^2). After two minutes, the PDMS mold was peeled away from the well plate surface, thus leaving behind disc-shaped EPCaTs. Finally, culture media was added, and the well plate was stored in a humidified atmosphere with 5% CO_2 and a constant temperature of 37 ºC for up to 29 days; culture media was renewed at least twice weekly. It is important to note that: 1) after investigating several cancer-fibroblast culture media blends (as described below), cancer cell-specific culture media was chosen for all coculture EPCaTs and 2) the day of encapsulation is considered to be Day 0 of EPCaT culture; it then follows that some cell-driven changes in the EPCaT microenvironment are expected on Day 1 as this time point was evaluated approximately 24 hours post-encapsulation.

3.3.5 Encapsulation of ADPC Engineered Prostate Cancer Tissues

ADPC EPCaTs were fabricated in a similar method to CRPC-ne EPCaTs; however, building upon the results from the CRPC-ne study, a LNCaP cancer cell to BJ-5ta fibroblast cell ratio of 5:1 was the sole coculture condition investigated. Both LNCaP and BJ-5ta monoculture EPCaTs were also fabricated for comparison.

3.3.6 Cell Viability Investigation

Visualization of live and dead cells within the EPCaTs, as well as quantification of viable populations, were performed using confocal fluorescent microscopy (Nikon AI Confocal Scanning Laser Microscope). The LIVE/DEAD™ (Invitrogen, Carlsbad, CA) mammalian cell cytotoxicity kit positively labeled live cells with green-fluorescent

Calcein-AM and dead cells with red-fluorescent Ethidium homodimer-1. The bisBenzimide Hoechst 33342 (H33342) (MilliporeSigma, Burlington, MA) fluorochrome was simultaneously employed to positively label intranuclear deoxyribonucleic acid (DNA). Briefly, on Days 1 and 15 post-encapsulation, EPCaTs or 2D cell cultures were washed with PBS, incubated in the LIVE/DEAD/H33342 stain for 30 minutes at 25 ºC, again washed with PBS, and finally imaged via confocal microscopy. The consequent z-stack images were analyzed in ImageJ software (version 1.52c, NIH) and viable populations were quantified by manually counting the number of live cells, dead cells, and nuclei in each slice of the z-stack.

3.3.7 Phase Contrast Image Acquisition and Analysis

EPCaTs were imaged weekly for up to 29 days using an inverted Nikon Eclipse Ti microscope fitted with an Andor Luca S camera. Phase-contrast images were analyzed with ImageJ software (version 1.52c, NIH). Whole tissue and cell colony characteristics were quantified by drawing a region of interest (ROI) around the physical feature; the resultant measurements were then exported to Microsoft Excel for further analysis.

3.3.8 Immunostaining and Fluorescence Microscopy

To simultaneously elucidate the distribution of both cancer and stromal cell types within the 3D EPCaT model and monitor coculture-driven changes in cell morphology, immunostaining and confocal fluorescent microscopy were performed. F-actin filaments were visualized by Alexa Fluor™ 568 Phalloidin staining (1:200 dilution in PBS; Thermo Fisher Scientific, Rockford, IL) and intranuclear DNA was visualized by H33342 staining (1:200 dilution in PBS). To distinguish cell types, the anti-fibroblast monoclonal antibody clone TE-7 (1:100 dilution in PBS; MilliporeSigma, Burlington, MA) was coupled with

the Zenon™ Alexa Fluor™ 647 Mouse IgG_1 Labeling Kit (Thermo Fisher Scientific, Rockford, IL). Prior to staining, EPCaTs underwent a PBS wash, overnight fixation at 4 ºC in 4% paraformaldehyde (PFA) (Electron Microscopy Sciences, Hatfield, PA), permeabilization in 0.5% Triton-X for 30 minutes, and blocking via an hour-long incubation in 0.2 μm filtered blocking buffer (10% FBS and 0.5% bovine serum albumin (BSA) in PBS) at 25 ºC. EPCaTs were then serially labeled with a Phalloidin/Zenon™ Alexa Fluor™ 647-TE-7 staining solution followed by a H33342 staining solution; EPCaTs were incubated in each of these staining solutions for a minimum of 1 hour at 25 ºC and washing steps were performed after each stain. Upon completion of the immunostaining process, EPCaTs were imaged via confocal microscopy (Nikon AI Confocal Scanning Laser Microscope). ImageJ software was employed for analysis; similar to above, ROI were manually drawn around cells and cell colonies to quantify the area, circularity, aspect ratio, and feret diameter. Calculated values were subsequently exported to Microsoft Excel for further analysis.

3.3.9 Flow Cytometry

Flow cytometry was performed to quantify cell populations within the EPCaTs on Days 1 and 15 post-encapsulation. Zombie Green™ (BioLegend, San Diego, CA) was utilized to positively label dead cells and cell debris. The Zenon™ Alexa Fluor™ 647 Mouse IgG_1 Labeling Kit and anti-fibroblast antibody clone TE-7 at a 1:100 dilution were utilized to positively label all BJ-5ta fibroblast cells; no TE-7 cross-labeling of either PC-3 or LNCaP cells was observed (Fig. 32). The Zenon™ Alexa Fluor™ 647 Rabbit IgG Labeling Kit (Thermo Fisher Scientific, Rockford, IL) was utilized with the Anti-Ki67

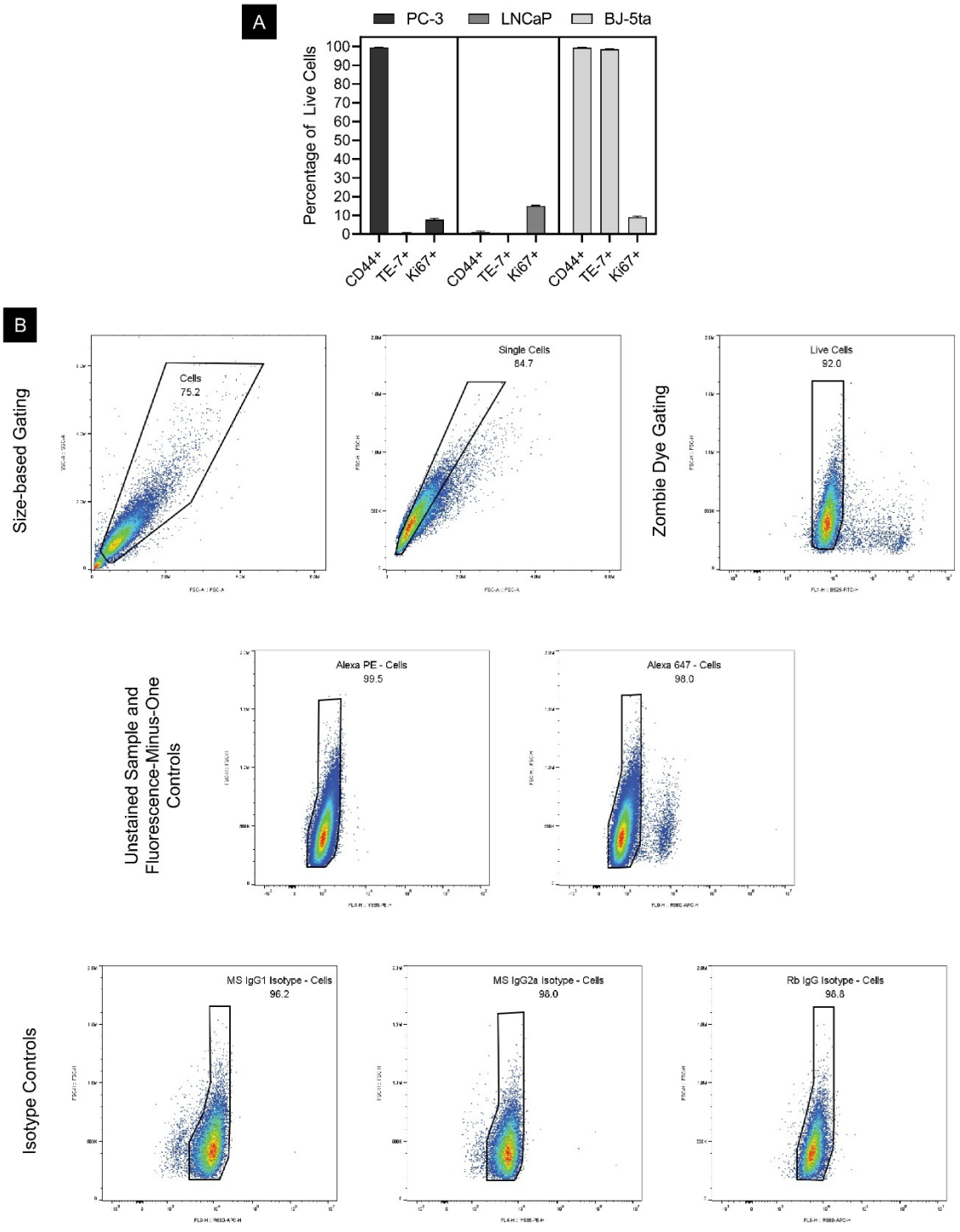

Figure 32: Flow cytometry monoculture controls for each immunomarker used and gating strategies employed throughout analysis.

(Abcam, Cambridge, MA) antibody at a 1:2000 dilution to positively label all proliferative cells. Lastly, the Zenon™ R-Phycoerythrin Mouse IgG_{2a} Labeling Kit (Thermo Fisher Scientific, Rockford, IL) was employed with the Anti-CD44 (Bio-Techne Corporation, Minneapolis, MN) antibody to monitor changes in CD44 expression. Positive and negative controls were performed utilizing PC-3, LNCaP, and BJ-5ta monoculture EPCaTs and fluorescence minus one (FMO) gating. Additionally, isotype controls were performed utilizing the antibody Mouse IgG_1 Isotype Control ($MSIgG_1$) (Thermo Fisher Scientific, Rockford, IL) with the Zenon™ Alexa Fluor™ 647 Mouse IgG_1 Labeling Kit, the antibody Rabbit IgG Isotype Control (RbIgG) (Thermo Fisher Scientific, Rockford, IL) at a 1:1000 dilution with the Zenon™ Alexa Fluor™ 647 Rabbit IgG Labeling Kit, and the antibody Mouse IgG_{2a} Isotype Control ($MSIgG_{2a}$) at a 1:500 dilution with the Zenon™ R-Phycoerythrin Mouse IgG_{2a} Labeling Kit. Unstained single cell suspensions were also analyzed to monitor cell auto-fluorescence as well as to gate auto-fluorescence from the Eosin Y photoinitiator used in the PF photocrosslinking procedure.

EPCaTs were dissociated at 37 ºC utilizing collagenase type IV (Worthington Biochemical Corporation, Newark, NJ) at a concentration of 1 mg/mL in PBS for 30 minutes, or until completely dissociated. Forced pipetting was also used to aid the degradation of the PF matrix. The cell suspension solution was centrifuged at 300g for 5 minutes with the brake off and resuspended in Accumax (Innovative Cell Technologies, Inc., San Diego, CA) for 15 minutes to yield single cells. Cells were re-centrifuged, washed with PBS, centrifuged again, and resuspended in Zombie Green™ at a 1:1000 dilution in PBS and incubated at 4 ºC in the dark for 30 minutes. Cells were washed with 0.2 μm filtered blocking buffer (10% FBS and 0.5% BSA in PBS), centrifuged, resuspended in

blocking buffer, and incubated for 30 minutes at 4 ºC in the dark. The Zenon™ R-Phycoerythrin-CD44 or Zenon™ R-Phycoerythrin-MSIgG$_{2a}$ extracellular staining solution was subsequently added and followed by another 30-minute incubation at 4 ºC in the dark. Next, eBioscience™ Foxp3 Fixation/Permeabilization (Foxp3) (Invitrogen, Carlsbad, CA) working solution was added and samples were incubated at 4 ºC under dark conditions overnight. The following day, samples were centrifuged, washed with 1X permeabilization buffer (Invitrogen, Carlsbad, CA), resuspended in FACS buffer (10% FBS and 1% BSA in 1X permeabilization buffer), and allowed to incubate in the dark at 25 °C for 30 minutes. Either the Zenon™ Alexa Fluor™ 647-TE-7, Zenon™ Alexa Fluor™ 647-Ki67, Zenon™ Alexa Fluor™ 647-MSIgG$_1$, or Zenon™ Alexa Fluor™ 647-RBIgG intracellular staining solution was subsequently added and followed by another 30-minute incubation at 4 ºC in the dark. Stained cells were washed with blocking buffer twice, resuspended in blocking buffer at a concentration of approximately 1 x 10^6 cells/mL, and finally passed through a 40 µm Flowmi™ Cell Strainer filter.

The stained cell population was quantified utilizing a CytoFLEX (Beckman-Coulter, Indianapolis, IN) flow cytometer according to manufacturer instructions. The analysis was stopped after the incidence of 30,000 events within gating that excluded positively labeled Zombie Green™ cells (dead cells), as well as size-excluded small debris and PF particles. Results were analyzed and event gating was performed utilizing FlowJo (FlowJo, LLC, Ashland, OR) software. The gating strategies employed in this study are illustrated in Figure 32.

3.3.10 Engineered Tissue Stiffness Quantification

The EPCaT matrix mechanical stiffness was measured on days 1, 15, and 22 of *in vitro* coculture using a MicroSquisher parallel plate compression tester (CellScale, Waterloo, ON, CA) under physiological conditions. Briefly, EPCaTs were loaded onto the MicroSquisher stage within a PBS-filled fluid bath test chamber; a compression platen was fitted onto a microcantilever beam (tungsten wire with a diameter of 558.8 μm) and positioned at the top of the sample. A maximum compression rate of 10 μm/s and a minimum deformation of 15% were used for all parallel plate compression testing runs in this study. Each sample was cyclically compressed three times and the resultant Young's moduli (calculated from a compressive stress (σ) versus strain (ε) curve created from force versus displacement data recorded by the MicroSquisher) were averaged together to yield one stiffness value per EPCaT. All EPCaT conditions were tested in triplicate for each separately prepared batch.

3.3.11 Investigation of Cancer-fibroblast Cell Culture Media Blends

In order to determine an appropriate culture media for the coculture EPCaT model, several investigations were performed, including 2D cell viability, 3D EPCaT flow cytometry, and 3D EPCaT matrix parallel plate compression testing. First, PC-3 and BJ-5ta cells were individually seeded into a 24-well plate and cultured in five different cancer-fibroblast media blends; these include 100% PC-3 media, 75% PC-3 media/25% BJ-5ta media, 50% PC-3 media/50% BJ-5ta media, 25% PC-3 media/75% BJ-5ta media, and 100% BJ-5ta media. After 48 hours of *in vitro* culture, a LIVE/DEAD/H33342 stain (as described above) was added directly to the well plate and fluorescent images were taken using an inverted Nikon Eclipse Ti microscope fitted with an Andor Luca S camera.

Resultant viability images were exported to ImageJ software (version 1.52c, NIH) for further analysis.

Next, EPCaTs were fabricated as described above and cultured in 100% PC-3 media or a 50/50 blend of PC-3 and BJ-5ta media. Flow cytometry was performed as described above on Days 1, 15, and 29 post-encapsulation, utilizing the TE-7 anti-fibroblast antibody to positively label the fibroblast cell population. It is important to note that the Accuri™ C6 (BD Biosciences, Franklin Lakes, NJ) personal flow cytometer and CFlow® analysis software were employed in this media blend investigation; as such, slight differences in the reported cell populations are to be expected between this investigation and the main study. Quantification of EPCaT mechanical stiffness was also performed on Days 1, 8, 15, 22, and 29 post-encapsulation, as described above. Once again, it is important to note that this media blend investigation employed a separately synthesized batch of PF than is used in the main study; the initial EPCaT stiffness is dependent, in part, on the fibrinogen concentration of each PF batch, which differed between the main study and this investigation. In both the flow cytometry and parallel plate compression investigations, EPCaTs cultured in a 50/50 blend of PC-3 and BJ-5ta media were compared to EPCaTs cultured in 100% PC-3 media at each time point.

3.3.12 Immunohistochemistry

Hematoxylin and eosin (H&E) and Masson's Trichrome immunohistochemistry staining strategies were employed to visualize the EPCaT microanatomy. Prior to staining, EPCaTs were fixed in 70% ethanol with 0.1% (w/v) Eosin Y to aid in the visualization of the engineered tissues; fixed EPCaTs were subsequently embedded in paraffin, sectioned, and stained. An Aperio CS2 Scanner (Leica Biosystems, Buffalo Grove, IL) was used to

image the stained EPCaT sections at 40X magnification. Finally, Aperio ImageScope software (version 12.4.0.5043) was employed to visualize and process the digital images.

3.3.13 Next-generation RNA Sequencing

Bulk RNAseq was performed based upon an established protocol (Mitra et al., 2020). Briefly, total RNA was extracted from CRPC-ne and ADPC EPCaTs using QIAshredder and a RNeasy kit (QIAGEN, Germantown, MD) ($n \geq 3$ pooled EPCaTs per matrix composition). A 2100 Bioanalyzer Instrument (Agilent, Santa Clara, CA) and the Nanodrop-8000 (Thermo Fisher Scientific, Rockford, IL) were subsequently employed to measure RNA concentration and integrity. All samples reported in this study demonstrated an RNA integrity number (RIN) greater than nine. A TruSeq RNA Sample Preparation kit v2 (Illumina, Inc., San Diego, CA) was selected to construct RNAseq libraries, and sequencing was performed on a HiSeq 2000 (Illumina, Inc., San Diego, CA). Raw RNAseq reads were normalized using Partek Flow data analysis software and quality control (QC) checked utilizing the FastQC tool. Lastly, the Spliced Transcripts Alignment to a Reference (STAR) aligner tool was employed to map the processed RNAseq reads to the human genome.

3.3.14 Bioinformatics Analysis

Analysis of differentially expressed genes (DEGs) was performed on counts per million (CPM)-normalized read counts through the use of a multi-model approach based on limma trend through an empirical Bayes method for gene expression estimation. Genes with $p \leq 0.05$ and Log_2(Fold Change) $\geq \pm 1.5$ were considered differentially expressed. Gene set enrichment analysis (GSEA) was performed using the clusterProfiler R package (Yu et al., 2012) to report the normalized enrichment scores (NES) and false discovery rate

adjusted q-values (FDR) for the 50 Molecular Signature Database (MSigDB) Hallmark gene sets (Liberzon et al., 2015). The clusterProfiler R package was also employed in gene ontology (GO) biological process over-representation analysis; redundant GO terms were eliminated and two-level hierarchy tree map illustrations were generated using the GOSemSim (Yu et al., 2010, Yu, 2020) and rrvgo (Sayols, 2020) packages. Finally, Euler diagrams were constructed using the Eulerr web application (Larsson, 2020) and Venn diagrams were constructed using the InteractiVenn web application (Heberle et al., 2015).

3.3.15 Comparison to the Cancer Genome Atlas

Transcriptomic profiles of CRPC-ne and ADPC EPCaTs were compared to patient expression through the use of the National Cancer Institute Genomic Data Commons Cancer Genome Atlas Prostate Adenocarcinoma (TCGA-PRAD) project database. Primary solid tumor data from 498 prostate adenocarcinoma patients was available and used in this study; 52 of these patient cases also provided solid tissue normal data. The *TCGAbiolinks* (Colaprico et al., 2015) R package was employed to acquire HT-Seq gene counts, which were subsequently merged with EPCaT data by Ensembl gene ID's. The *DeSeq2* (Love et al., 2014) R package was employed to calculate differentially expressed genes between EPCaTs, patient primary solid tumor tissue, and tumor-adjacent solid tissue normal. Genes with $p \leq 0.05$ and Log_2(Fold Change) $\geq \pm 1.5$ were considered differentially expressed. GSEA and GO downstream analyses were additionally performed as described above.

3.3.16 Statistical Methods

GraphPad Prism 8.0 (GraphPad Software, San Diego, CA) was selected for both statistical analysis and figure preparation. First, data set outliers were eliminated using the robust regression and outlier removal (ROUT) method with coefficient Q = 1%; data

distribution normality and equality of variance were subsequently checked. T-tests were performed to compare the means of two groups, while one- or two-way ANOVA and the Tukey *post hoc* test were performed to compare the means of more than two groups. The Kruskal-Wallis and Dunn's multiple comparisons *post hoc* tests were alternatively performed for data sets comparing the means of more than two groups with non-normal distribution. Finally, rates of increase or decrease were determined via linear regression analysis. Overall, $p \leq 0.05$ was considered statistically significant unless otherwise stated and error bars indicate standard deviation unless otherwise indicated. Throughout this chapter, statistical significance is denoted by the following symbol and letter designations: ns indicates no statistical significance, * indicates statistical significance with $p \leq 0.05$, ** indicates statistical significance with $p \leq 0.01$, and **** indicates statistical significance with $p \leq 0.0001$; data that do not share a letter designation (e.g. D versus E or A versus BC) are significantly different with $p \leq 0.05$.

3.4 Results

Findings from the ratiometric investigation of fibroblast impact on EPCaTs comprised of a highly aggressive, neuroendocrine variant of castration-resistant prostate cancer are presented here first. Building upon these results, findings from a secondary EPCaT coculture study employing a more indolent, androgen-dependent variant of prostate cancer are reported. Finally, these investigations culminate in a CRPC-ne versus ADPC coculture comparison with an outlook on clinical relevancy. The overarching study design is illustrated in Figure 33.

3.4.1 *CRPC-ne EPCaTs are initially fabricated with varying prostate cancer cell to fibroblast ratios*

To investigate CRPC-ne-fibroblast cell-cell interactions within a three-dimensional, biomechanically-relevant (Habbit et al., 2022a) engineered microenvironment, PC-3 cancer cells and BJ-5ta fibroblasts were encapsulated in PF at a concentration of 20 x 10^6 cells/mL both individually in monoculture and in coculture at cancer to fibroblast cell ratios of 5:1, 1:1 and 1:5 (Fig. 33A). Regardless of initial cell population ratio, greater than 95% of cells survived the encapsulation process (n = three EPCaTs from separately prepared batches per condition, $p \leq 0.05$); similarly high viability (> 96%, n = three EPCaTs from separately prepared batches per condition, $p \leq 0.05$) was maintained over 15 days of *in vitro* coculture in cancer cell-specific media (Fig. 33B,C). Cells were distributed homogenously throughout the PF matrix and no spatial variation in viability was observed (Fig. 33B; live cells are visualized in green and dead cells in red). Importantly, additional viability and tissue characterization studies examined the impact of modulating the *in vitro* culture media to include various percentages of cancer-specific and fibroblast-specific medium; no significant impacts on 2D cell viability or 3D EPCaT behavior were observed (Fig. 34, $p \leq 0.05$).

3.4.2 *Encapsulated cells temporally colonize within the CRPC-ne EPCaT PF-based matrix*

Importantly, the engineered PF matrix is enzymatically cleavable due to the natural-synthetic hybrid structure of the biomaterial; as such, encapsulated cancer and fibroblast cells have the opportunity to migrate within and remodel their microenvironment throughout long-term *in vitro* culture. Multi-magnification phase contrast imaging

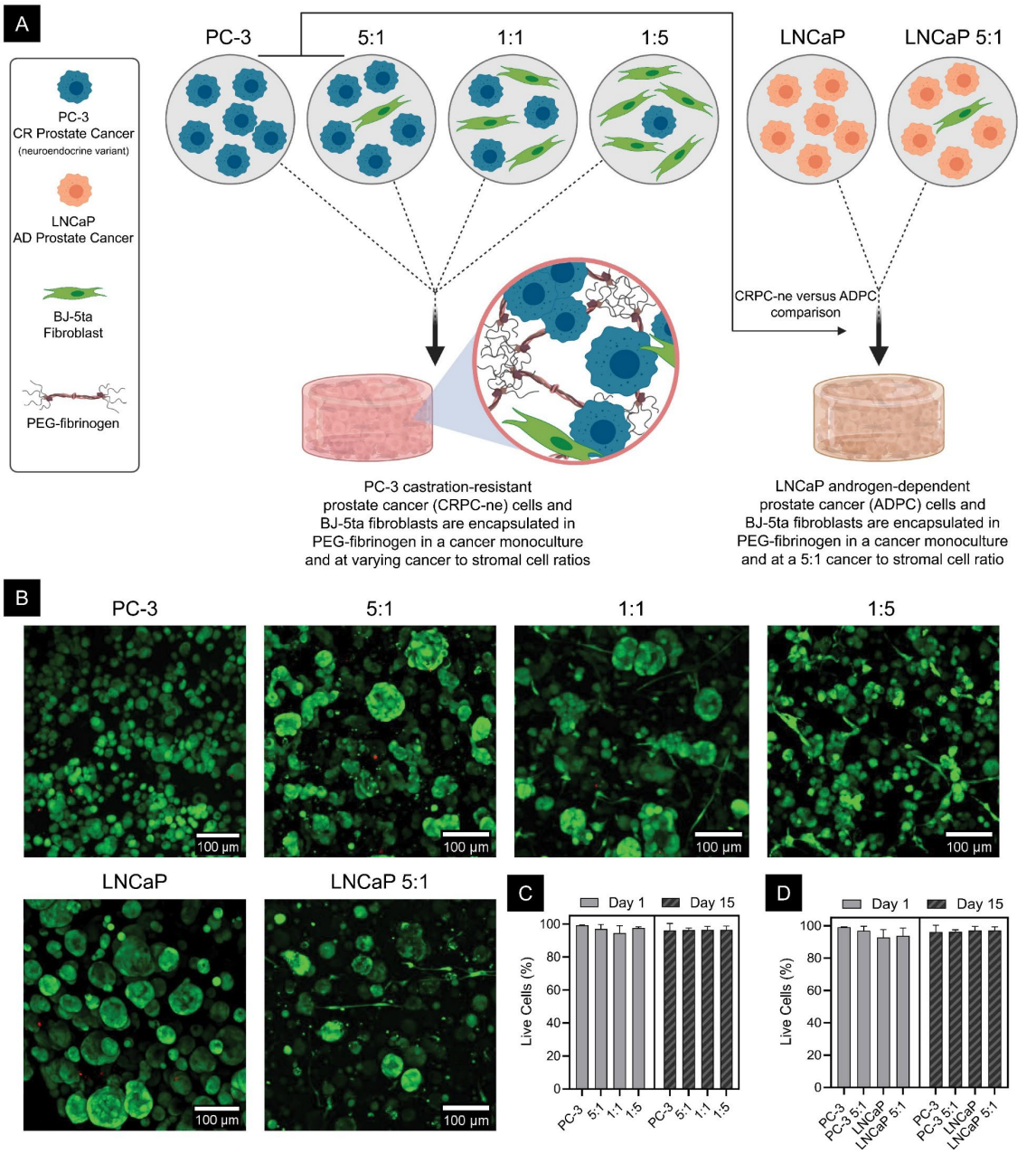

Figure 33: Prostate cancer cells of varying disease stages were successfully encapsulated with high viability in direct coculture with fibroblasts at varying cancer to stromal cell ratios.

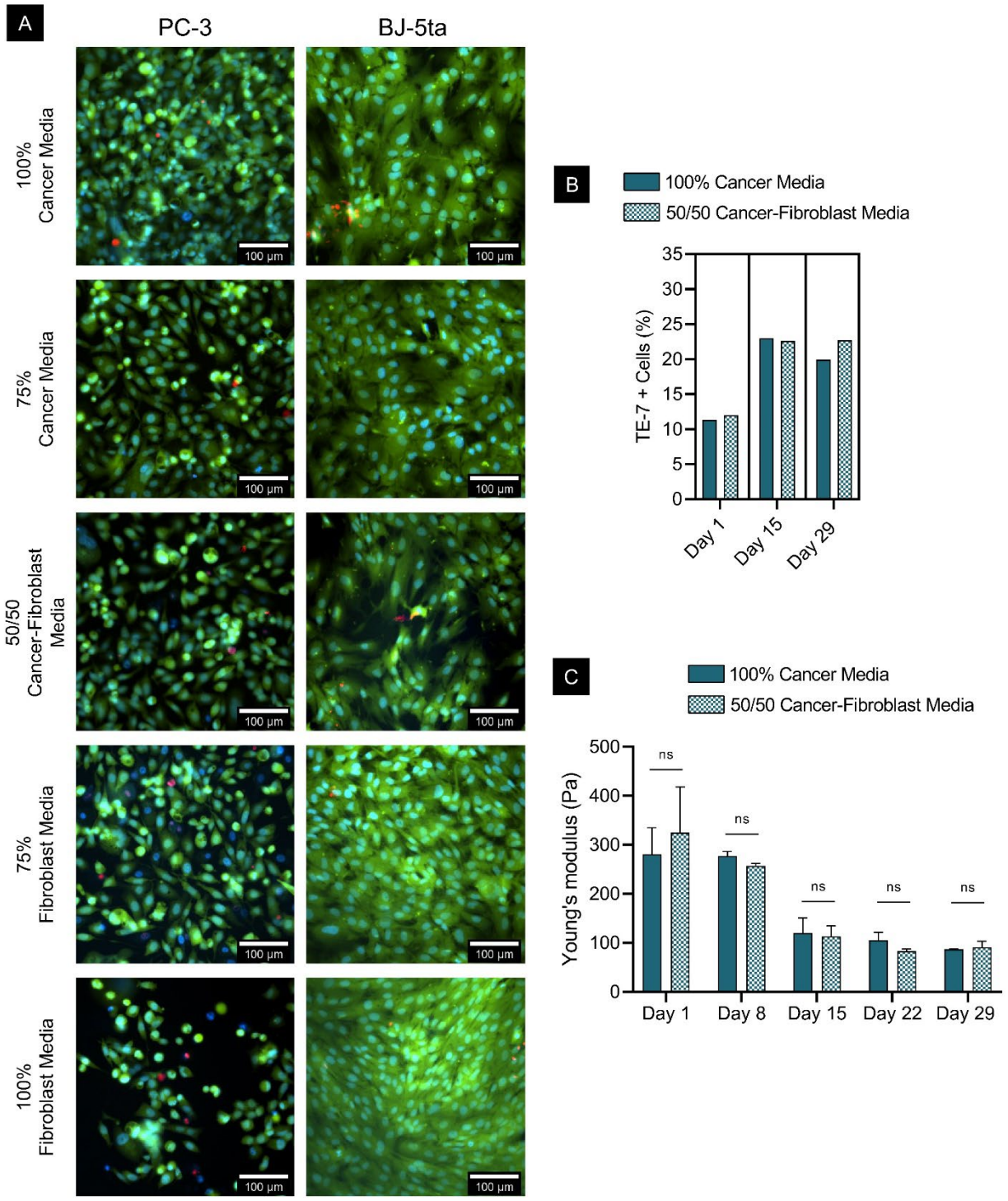

Figure 34: Fibroblasts remained viable when cultured in cancer-cell specific media and no significant differences in EPCaT cell populations or matrix stiffness were observed when a blended media was used.

Figure 33 caption continued: A) Experimental design for our ratiometric investigation of fibroblast impact on CRPC-ne, as well as our CRPC-ne versus ADPC coculture comparison. B) 10X confocal microscopy viability assay images on Day 15 post-encapsulation; live cells are visualized in green and dead cells are visualized in red. C) Quantification of CRPC-ne coculture EPCaT cell viability on Days 1 and 15 post-encapsulation (n = 3 EPCaTs per condition per time point). D) Quantification of CRPC-ne and ADPC EPCaT cell viability on Days 1 and 15 post-encapsulation (n = 3 EPCaTs per condition per time point).

Figure 34 caption continued: A) 2D PC-3 and BJ-5ta cells remain viable in a range of culture media blends. Some differences in cell density were noted. B) PC-3 5:1 EPCaTs cultured in 100% cancer media and a 50/50 cancer-fibroblast media blend yielded similar cell populations throughout long-term culture (it is important to note that this study was performed using a different flow cytometer and less rigorous analysis software than the main flow cytometry investigation reported in Figure 39 and as such, differences in reported cell populations are expected). C) PC-3 5:1 EPCaTs exhibited similar matrix stiffnesses when cultured in 100% cancer media and a 50/50 cancer-fibroblast media blend throughout long-term culture (it is important to note that this study was performed using a separate batch of PF than that used in the main study and as such, differences in initial EPCaT stiffness are expected).

(Fig. 35A-D) revealed significant, cell ratio-driven differences in tissue and cell colony growth. Substantial colonization was appreciable around the EPCaT edge in all ratios tested (as evidenced by the dark ring surrounding tissues in Figure 35A-D); notably, this phenomena was uniquely coupled with severe PF matrix degradation and colony outgrowth in the 5:1 coculture EPCaTs (Fig. 35B). H&E and Masson's Trichrome immunohistochemistry staining also clearly demonstrated this unique remodeling of the CRPC-ne EPCaT-provided matrix and is shown in Figure 36. Linear regression of total CRPC-ne EPCaT area revealed that both PC-3 monoculture and 5:1 coculture EPCaTs exhibited significant temporal tissue growth over 29 days of *in vitro* culture; conversely, 1:1 and 1:5 coculture EPCaTs remained uniformly sized (Fig. 35E, n = ten EPCaTs, $p \leq 0.05$). Furthermore, all CRPC-ne EPCaTs maintained their original shape, irrespective of encapsulated cell population or culture duration, and presented mean roundness values greater than 0.9 for all time points (Fig. 35F, n = ten EPCaTs, $p \leq 0.05$).

A wide range of cell colony sizes within the CRPC-ne EPCaTs was observed for each prostate cancer to fibroblast ratio and across all time points (Fig. 35G-I, n = 75 colonies per EPCaT condition per time point). PC-3 monoculture EPCaT colonies ranged in cross-sectional area from approximately 200 to 1,150 μm^2 on Day 1, 100 to 1,000 μm^2 on Day 15, and 200 to 1,000 μm^2 on Day 29. The 5:1 coculture EPCaT colonies ranged from 50 to 900 μm^2 on Day 1, 100 to 950 μm^2 on Day 15, and 50 to 1,100 μm^2 on Day 29. The 1:1 coculture EPCaT colonies exhibited a relatively narrower distribution, ranging from 100 to 500 μm^2 on Day 1 and from 100 to 700 μm^2 on both Days 15 and 29. Similarly, 1:5 coculture EPCaT colonies ranged in area from 100 to 600 μm^2 on both Days 1 and 15 and from 50 to 800 μm^2 on Day 29. The mean colony area of PC-3 monoculture and 5:1

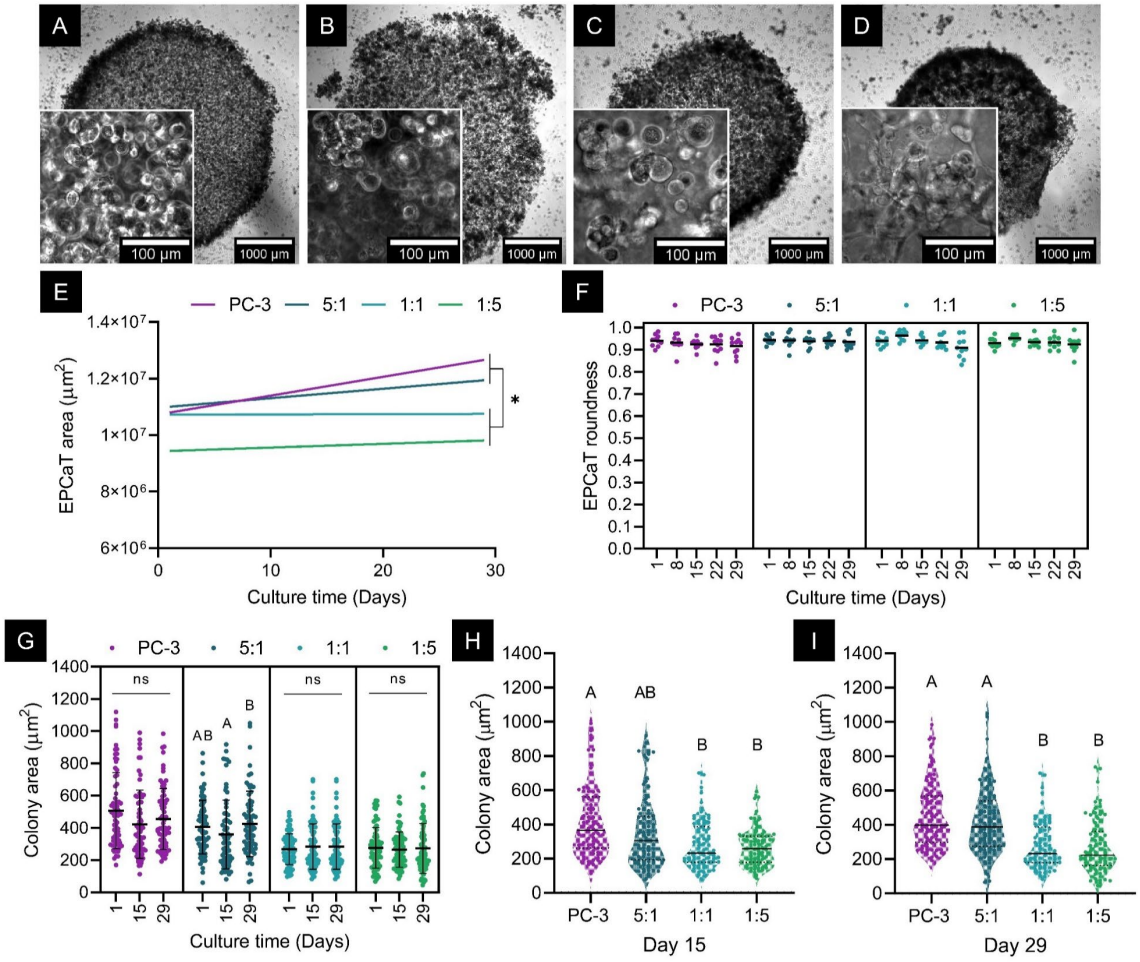

Figure 35: Encapsulated PC-3 and BJ-5ta cells remodeled and colonized within the provided CRPC-ne EPCaT matrix throughout long-term *in vitro* coculture; ratiometric variations in EPCaT growth and cell colonization were observed.

A-D) 2X phase contrast images of CRPC-ne EPCaTs with 20X phase contrast image inlays on Day 29. A) PC-3 EPCaT. B) 5:1 EPCaT. C) 1:1 EPCaT. D) 1:5 EPCaT. E) Linear regression of temporal EPCaT growth (n = 10 EPCaTs per condition per time point). F) Quantification of temporal changes in whole-tissue morphology (n = 10 EPCaTs per condition per time point). G-I) Quantification of encapsulated cell colony cross-sectional area (n = 75 colonies per condition per time point).

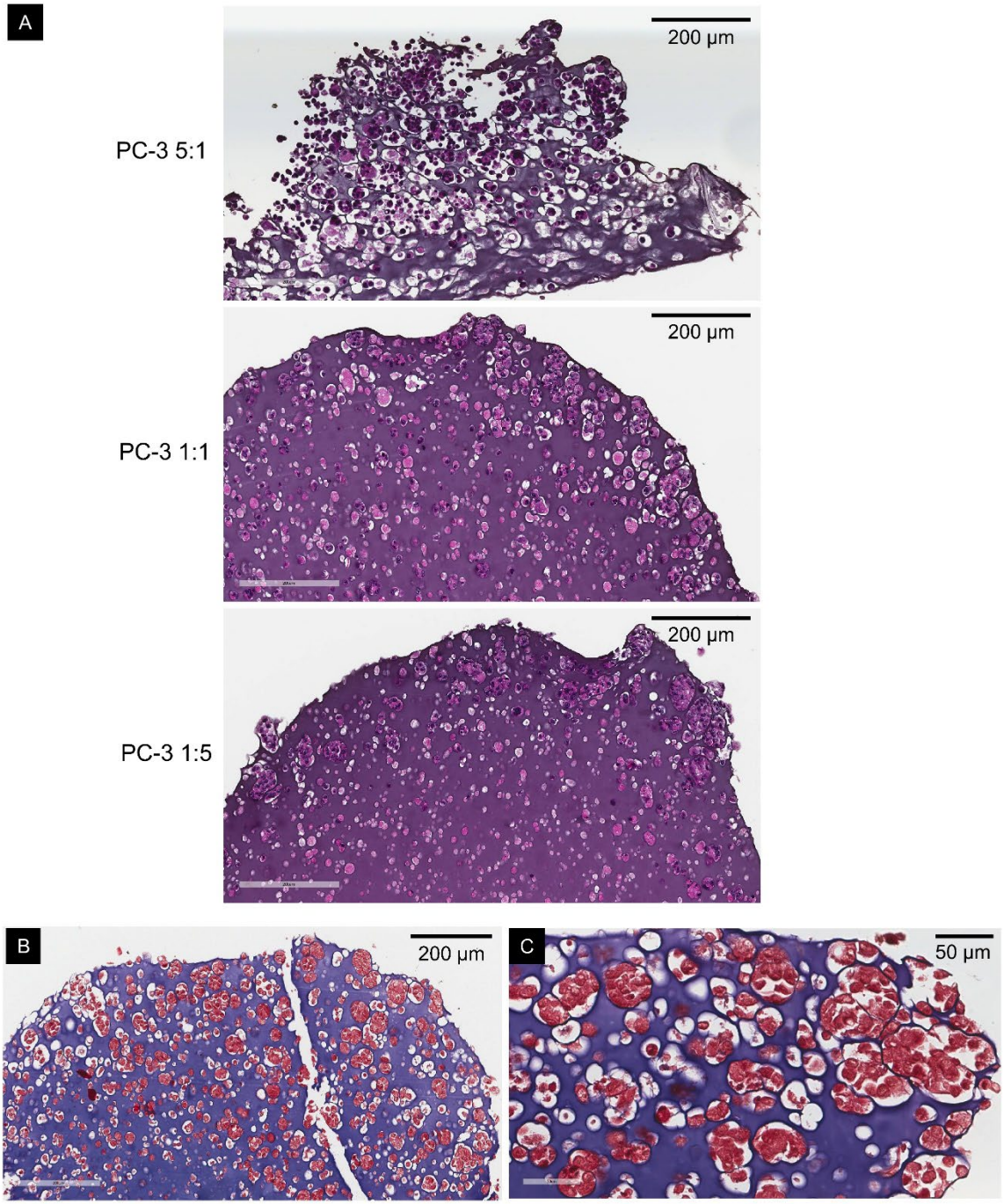

Figure 36: Immunohistochemical staining of varied cancer-stromal ratio EPCaTs.

A) H&E staining reveals substantially more severe matrix degradation in PC-3 5:1 EPCaTs, as compared to PC-3 1:1 and PC-3 1:5 EPCaTs on Day 15 post-encapsulation. B,C) Masson's trichrome staining reveals little to no ECM production in PC-3 1:1 EPCaTs on Day 15.

coculture EPCaTs was larger than that of 1:1 and 1:5 coculture EPCaTs on Day 1, likely due to the inherent difference in cell size between PC-3 and BJ-5ta cells (Fig. 35G, n = 75 colonies per EPCaT condition, $p \leq 0.05$). On Day 15, however, the mean colony area of 5:1 EPCaTs slightly decreased, resulting in no significant difference between coculture conditions (Fig. 35H, n = 75 colonies per EPCaT condition, $p \leq 0.05$). Then between Days 15 and 29 the 5:1 EPCaT colonies significantly increased in size, once again rendering the mean colony area significantly larger than other coculture conditions on Day 29. Whereas the PC-3 monoculture EPCaT maximum colony size remained constant over time, the maximum colony size increased temporally for all three coculture EPCaT conditions. As previously mentioned, the 5:1 coculture EPCaTs were the only condition to exhibit a significant temporal increase in mean colony area (Fig. 35G, n = 75 colonies per time point, $p \leq 0.05$). Furthermore, the 5:1 coculture EPCaT phase-contrast images also revealed an apparent substantial loss of structural integrity and outgrowth of cell colonies around the edge of the tissue (Fig. 35B); this phenomenon was not observed in monoculture or in the other coculture CRPC-ne EPCaT conditions which had higher ratios of fibroblasts per prostate cancer cell.

3.4.3 *Encapsulated PCa cells exhibit ratiometric heterogeneity in cell colony morphology*

Ratiometric, fibroblast coculture-driven heterogeneity in encapsulated cell morphology was detected by immunostaining and confocal microscopy performed on Day 15 post-encapsulation. Spatial uniformity in both PC-3 and BJ-5ta cell distribution was observed across CRPC-ne EPCaTs of all three ratios investigated (Fig. 37A). Cancer-fibroblast cell-cell interactions are visible in all coculture EPCaTs, whereas the formation

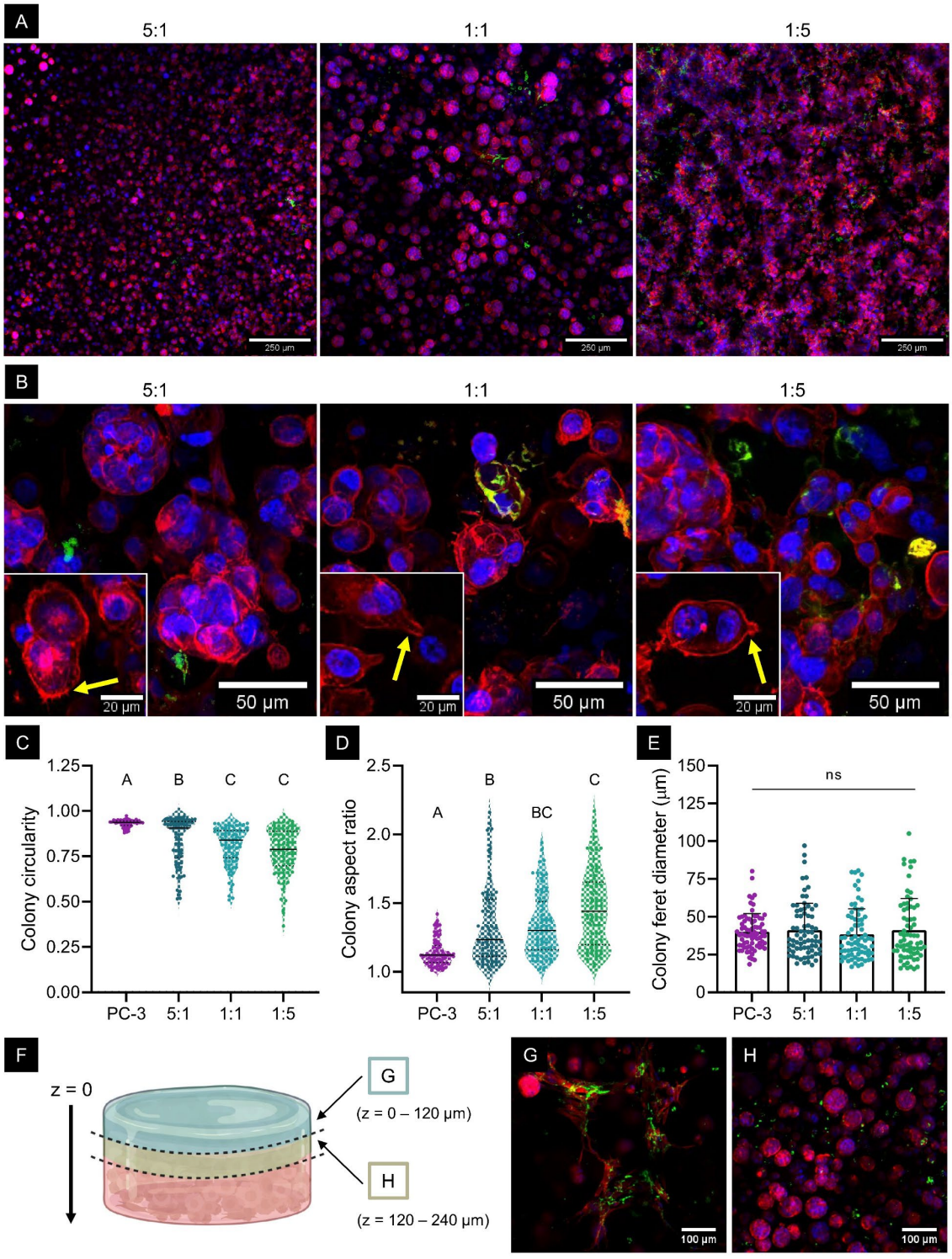

Figure 37: Substantial cancer-fibroblast cell-cell interactions, as well as ratiometric differences in cell colony morphology, were observed within CRPC-ne coculture EPCaTs on Day 15.

Figure 37 caption continued: A) 10X confocal microscopy images of immunostained CRPC-ne EPCaTs. B) 20X confocal microscopy images of immunostained CRPC-ne EPCaTs with inlays highlighting cancer cell protrusions (yellow arrows) that resemble preliminary features of a motile phenotype. C-E) Quantification of cell colony circularity, aspect ratio, and feret diameter (n = 75 colonies per condition). F-H) Illustration and corresponding confocal microscopy images of z-directional heterogeneity in EPCaT-encapsulated cell morphology (G,H are representative images from a 1:1 CRPC-ne EPCaT). All confocal microscopy images included in this figure illustrate f-actin filaments in red, cell nuclei in blue, and fibroblast cells in green.

of elongated fibroblast networks is first appreciable in the 1:1 EPCaTs and well-formed in the 1:5 EPCaTs (Fig. 37A). Rounded single cancer cells and cancer cell colonies are also observed in all coculture EPCaTs (Fig. 37A,B). Focusing on f-actin structures at higher magnification, morphological features of cancer cell protrusions are evident which may indicate cell motility (Fig. 37B, indicated by yellow arrows).

With an increasing fraction of fibroblast cells, there was a significant loss of colony circularity based on image quantification (Fig. 37C, n = 75 colonies per EPCaT condition, $p \leq 0.05$, a value of one is indicative of being perfectly circular). PC-3 monoculture EPCaT colonies exhibited a mean circularity of approximately 0.93 and ranged between 0.88 and 0.97. The 5:1 EPCaT colonies were significantly less circular with a mean circularity of approximately 0.84 and spanned a larger range of 0.52 to 0.97. Both the 1:1 and 1:5 EPCaT colonies exhibited a significantly lower mean circularity than either the monoculture or 5:1 EPCaTs with values of 0.81 and 0.77, respectively. The 1:1 EPCaT colony circularity

ranged between 0.51 to 0.94 and 1:5 EPCaT colony circularity ranged between 0.37 to 0.94.

As expected, increased cell and colony elongation with fibroblast coculture was indicated by aspect ratio quantification, particularly in CRPC-ne EPCaTs with a higher ratio of fibroblast cells (Fig. 37D, n = 75 colonies per EPCaT condition, $p \leq 0.05$). PC-3 monoculture EPCaT colonies had a mean aspect ratio of 1.14 and an overall range of 1.01 to 1.42. Comparatively, the 5:1 EPCaT colonies were significantly more elongated with a mean aspect ratio of 1.35 and exhibited the largest range spanning from 1.02 to 2.16. Despite exhibiting a significantly larger mean aspect ratio than the 5:1 EPCaTs (mean aspect ratio = 1.46), the 1:5 EPCaT colonies were found to have a similar range of 1.04 to 2.17. The 1:1 EPCaT mean colony aspect ratio was not significantly different than either of the other coculture conditions (mean aspect ratio = 1.35) and spanned a smaller range of 1.02 to 1.94.

Interestingly, there were no ratiometric differences in cell colony feret diameter, regardless of the initial EPCaT cell population (Fig. 37E, n = 75 colonies per EPCaT condition, $p \leq 0.05$, feret diameter represents the longest distance between any two points along the ROI boundary). PC-3 monoculture, 5:1, 1:1, and 1:5 EPCaTs exhibited mean colony feret diameters of 40.1 μm, 41.2 μm, 38.5 μm, and 41.2 μm, respectively. The overall colony feret diameter ranges were also similar between conditions; PC-3 monoculture EPCaT colonies ranged in feret diameter from 18.6 μm to 80.2 μm, 5:1 EPCaT colonies ranged from 18.0 μm to 97.0 μm, 1:1 EPCaT colonies ranged from 16.9 μm to 80.6 μm, and finally, 1:5 EPCaT colonies ranged from 15.4 μm to 105 μm. When this result is considered in tandem with the findings that circularity decreases and elongation

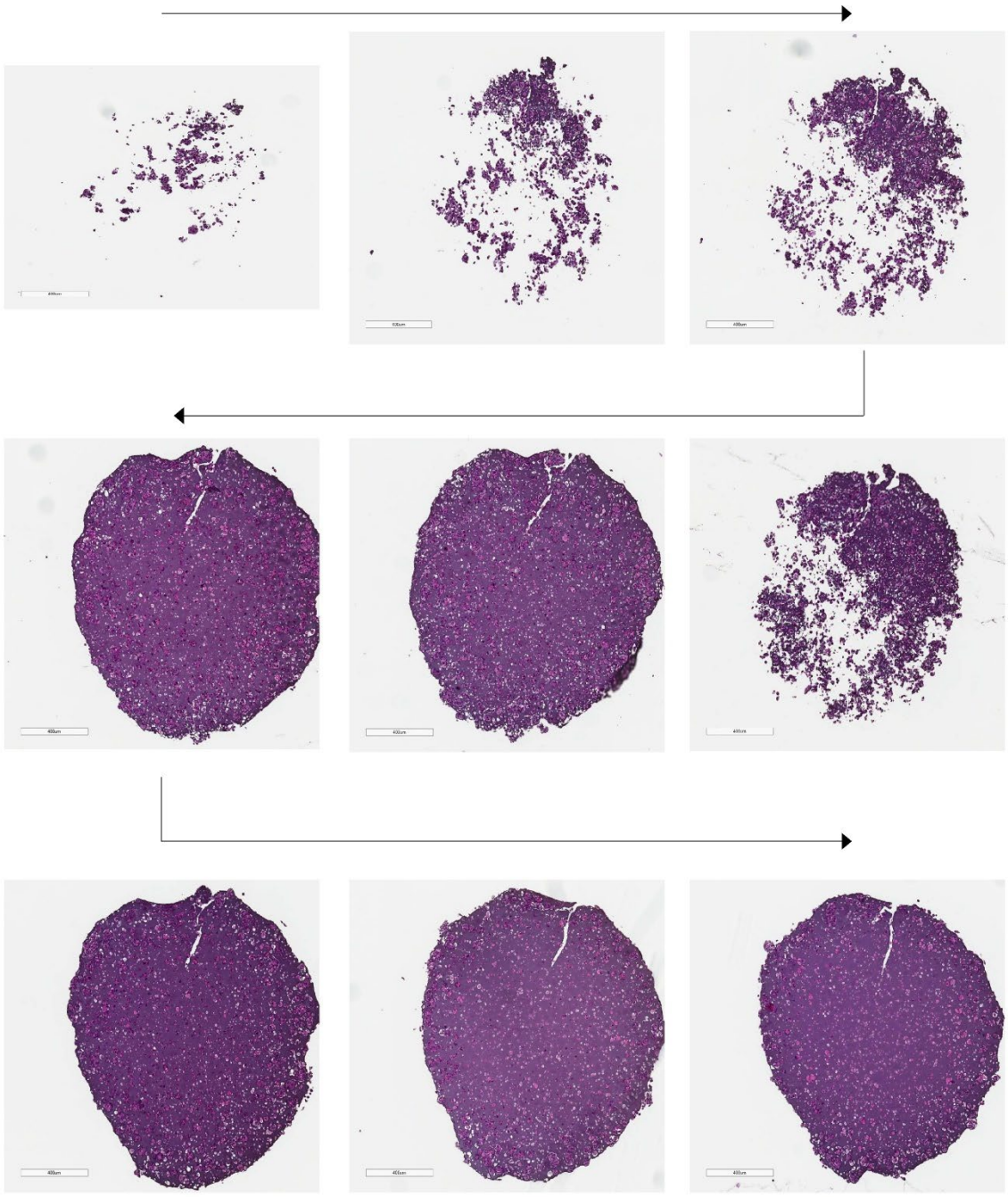

Figure 38: A progression of H&E stained slices of a PC-3 1:5 EPCaT on Day 15 illustrates cell colony growth outside the provided PF matrix.

Top left image represents the top of the EPCaT, bottom right image represents the middle of the EPCaT; colonization is observed at the center of the EPCaT in multiple tissue slices.

increases with an increasing ratio of fibroblasts in the cell population, it can be inferred that colony area must then decrease with an increasing ratio of fibroblasts. This outcome aligns with the previous quantification of colony area presented in Figure 35H.

While no spatial heterogeneity in cell type distribution or morphology was observed between the EPCaT center, midpoint, or edge geometric locations, some morphological variation was observed in the z-direction (Fig. 37F-H). More fibroblast elongation was noted at the top and bottom surfaces of all coculture EPCaTs (Fig. 37G), as compared to the internal matrix where rounded cell colonies are more prevalent (Fig. 37H). Z-directional differences in EPCaT structure are also observed in sequential H&E stained histological sections (Fig. 38).

3.4.4 *CRPC-ne EPCaT cell population ratios change temporally and exhibit a fibroblast-driven increase in proliferation*

Temporal changes in encapsulated cancer cell and fibroblast populations throughout long-term *in vitro* culture, as well as a fibroblast-driven increase in proliferative cell populations, were identified by flow cytometric analysis of enzymatically dissociated EPCaTs. The initial coculture EPCaT PC-3 cancer cell to fibroblast cell ratios of 5:1, 1:1 and 1:5 were confirmed on Day 1 post-encapsulation (Fig. 39A,B, n = two separately prepared batches of 15 EPCaTs per condition per time point, error bars indicate data range). Approximately 16.0% of the total dissociated 5:1 EPCaT cell population was positive for the fibroblast immunomarker, TE-7. The 1:1 and 1:5 EPCaT cell populations yielded approximately 48.5% and 79.6% TE-7+ cells, respectively. Notably, over 15 days of *in vitro* coculture, the 5:1 EPCaT cancer and fibroblast cell population percentages did not substantially change (13.5% TE-7+); thus, preserving the initial approximate cancer to

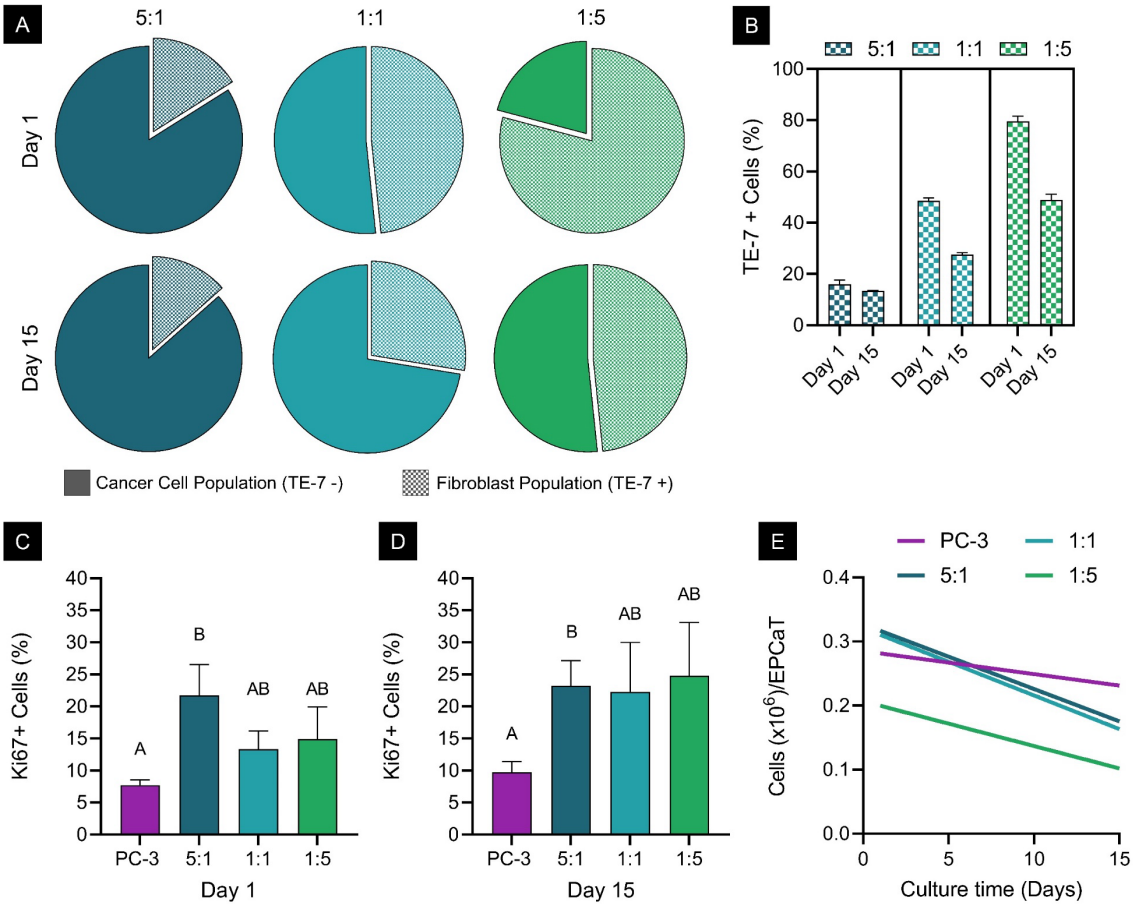

Figure 39: Fibroblast-coculture resulted in increased cell proliferation in CRPC-ne EPCaTs, particularly when encapsulated at a 5:1 cancer to fibroblast cell ratio; temporal changes in cell populations were also observed in EPCaTs fabricated with an equal or higher number of fibroblast cells than prostate cancer cells.

A) Pie charts illustrating temporal changes in EPCaT cell populations. B) Corresponding quantification of the fibroblast (TE-7+) cell populations (n = 2 separately prepared batches of 15 EPCaTs per condition per time point, error bars indicate data range). C) Quantification of proliferative (Ki67+) cell populations on Day 1 (n = 3 separately prepared batches of 15 EPCaTs per condition). D) Quantification of proliferative (Ki67+) cell populations on Day 15 (n = 3 separately prepared batches of 15 EPCaTs per condition). E) Quantification of total cell count per EPCaT (n = 3 batches of 15 EPCaTs per condition per time point).

fibroblast cell ratio of 5:1 (Fig. 39A,B, n = two separately prepared batches of 15 EPCaTs per condition per time point, error bars indicate data range). In both the 1:1 and 1:5 EPCaTs there was an approximate 40% decrease in the percentage of TE-7+ cells by Day 15 post-encapsulation, yielding 27.7% and 48.9% fibroblasts, respectively (Fig. 39A,B, n = two separately prepared batches of 15 EPCaTs per condition per time point, error bars indicate data range).

Notably, on Day 1 post-encapsulation, the 5:1 coculture EPCaT cell population had already begun to display a more proliferative phenotype than the monoculture PC-3 EPCaT population. Upon EPCaT dissociation, significantly more cells from the 5:1 EPCaTs were immunolabeled positively by Ki67 (21.7%), as compared to only 7.7% in the PC-3 monoculture condition (Fig. 39C, n = three separately prepared batches of 15 EPCaTs per condition per time point, $p \leq 0.05$). Markedly, incorporating a higher initial ratio of fibroblasts did not result in an additional increase in the percentage of Ki67+ cells; instead, the 1:1 and 1:5 coculture EPCaTs had 13.3% and 14.9% Ki67+ cells, respectively, which was not significantly different from either the PC-3 monoculture or 5:1 coculture EPCaTs (Fig. 39C, n = three separately prepared batches of 15 EPCaTs per condition per time point, $p \leq 0.05$). After 15 days of coculture, the 5:1 coculture EPCaT cell population continued to maintain a more proliferative phenotype than the PC-3 monoculture EPCaT population with a significantly higher percentage of Ki67+ cells (23.2% in comparison to 9.8%, respectively) (Fig. 39D, n = three separately prepared batches of 15 EPCaTs per condition per time point, $p \leq 0.05$). The 1:1 and 1:5 coculture EPCaT dissociated cell populations exhibited a significant increase in the percentage of proliferative cells between Days 1 and 15 post-encapsulation; 1:1 EPCaTs yielded 22.3% Ki67+ cells and 1:5 EPCaTs yielded

24.8% Ki67+ cells on Day 15 (Fig. 39D, n = three separately prepared batches of 15 EPCaTs per condition per time point, $p \leq 0.05$), which was similar to the percentage for the 5:1 EPCaTs on Day 15.

To better understand these temporal and coculture-driven changes in encapsulated cell populations, the total number of live cells collected per CRPC-ne EPCaT after tissue dissociation was monitored at each time point. Linear regression revealed an overall decreasing trend in the number of live cells per coculture EPCaT with increasing *in vitro* culture time, whereas the PC-3 monoculture EPCaT cell counts appeared more stable (Fig. 39E, n = three separately prepared EPCaT batches, where the value for each batch was based on the average of 15 EPCaTs per condition per time point, $p \leq 0.05$).

3.4.5 *Fibroblast coculture drives rapid decline in CRPC-ne EPCaT mechanical properties*

Directly coculturing CRPC-ne cells with fibroblasts resulted in a significant decrease in EPCaT mechanical stiffness throughout long-term *in vitro* culture, as quantified by parallel plate compression testing. On Day 1 post-encapsulation, all CRPC-ne EPCaTs exhibited a similar stiffness regardless of initial cancer cell to fibroblast ratio; the mean Young's modulus values of PC-3 monoculture, 5:1, 1:1, and 1:5 EPCaTs on Day 1 were 730 Pa, 750 Pa, 830 Pa, and 1070 Pa, respectively (Fig. 40A, n = three EPCaTs per condition with 3 measurements averaged per EPCaT). Interestingly, the initial tissue to tissue variability between EPCaTs of the same cellular composition followed an increasing trend when a larger population of fibroblasts was present.

PC-3 monoculture EPCaTs maintained a constant stiffness over 22 days of *in vitro* culture; Young's moduli were 730 Pa, 610 Pa, and 720 Pa on Days 1, 15, and 22,

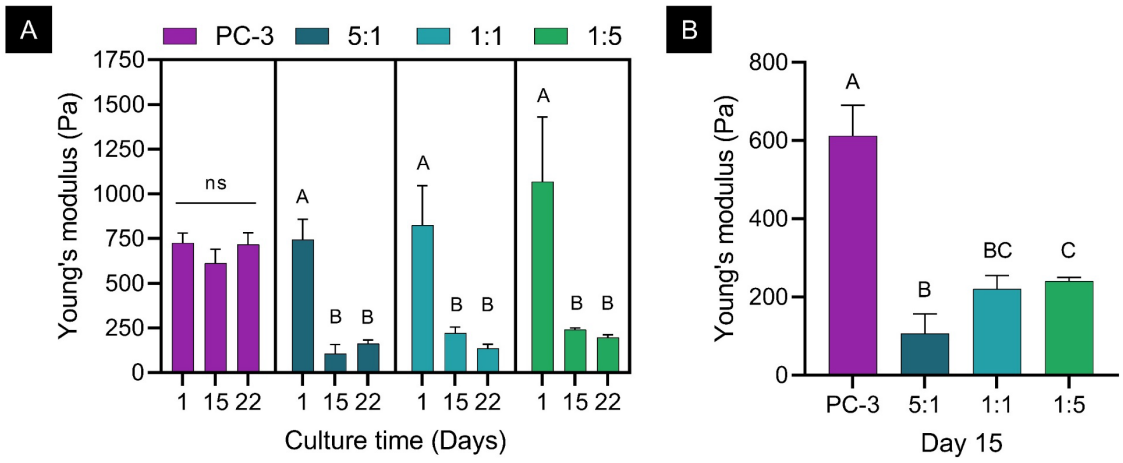

Figure 40: Fibroblast coculture resulted in a rapid, significant decrease in the CRPC-ne EPCaT matrix mechanical stiffness.

A) Temporal quantification of the CRPC-ne EPCaT Young's modulus (n = 3 EPCaTs per condition per time point with three measurements averaged per EPCaT). B) Quantification of the CRPC-ne EPCaT Young's modulus on Day 15 illustrating more severe degradation in the 5:1 condition than other coculture ratios (n = 3 EPCaTs per condition per time point with 3 measurements averaged per EPCaT).

respectively (Fig. 40A, n = three EPCaTs per condition per time point with three measurements averaged per EPCaT). Surprisingly, the inclusion of fibroblasts resulted in significant temporal degradation of the EPCaT matrix by Day 15, as evidenced by significantly lower Young's moduli for all coculture EPCaTs. The 5:1 EPCaT mechanical stiffness plummeted from 750 Pa on Day 1 to 110 Pa on Day 15; no significant changes were found between Day 15 and Day 22, the latter of which exhibited a final average Young's modulus of 160 Pa (Fig. 40A, n = three EPCaTs per condition per time point with three measurements averaged per EPCaT, $p \leq 0.05$). The 1:1 EPCaTs exhibited Young's moduli of 220 Pa and 140 Pa on Days 15 and 22, respectively; this also signified a

significant decrease from the Day 1 modulus of 830 Pa (Fig. 40A, n = three EPCaTs per condition per time point with three measurements averaged per EPCaT, $p \leq 0.05$). The 1:5 EPCaTs exhibited similar Young's moduli to the 1:1 coculture condition at each time point measured; Young's modulus values of 1070 Pa, 240 Pa, and 200 Pa were quantified on Days 1, 15, and 22, respectively (Fig. 40A, n = three EPCaTs per condition per time point with three measurements averaged per EPCaT, $p \leq 0.05$).

Although all three fibroblast coculture ratios tested within the CRPC-ne EPCaT platform demonstrated a significant decrease in PF matrix stiffness by Day 15, the relationship between EPCaT stiffness and percentage of fibroblast did not follow a linear trend. Inclusion of a small percentage of fibroblasts resulted in the greatest decrease in EPCaT mechanical properties; the stiffness of the 5:1 EPCaTs (fabricated with the highest percentage of cancer cells and lowest percentage of fibroblasts) was the lowest and the stiffness of the PC-3 monoculture EPCaTs was the highest, with 1:1 and 1:5 EPCaTs having stiffnesses in between. Specifically, the 5:1 EPCaT Young's modulus on Day 15 was only 110 Pa, which was approximately half that of the 1:1 EPCaTs (220 Pa) and was significantly lower than the 1:5 EPCaTs (240 Pa) (Fig. 40B, n = three EPCaTs per condition with three measurements averaged per EPCaT, $p \leq 0.05$).

3.4.6 *Inclusion of fibroblasts in ADPC EPCaTs promotes more aggressive PCa cell behavior*

To investigate ADPC-fibroblast interactions within the three-dimensional EPCaT model and elucidate fibroblast-mediated differences between ADPC and CRPC-ne, LNCaP prostate cancer cells were encapsulated in monoculture and in coculture with BJ-5ta fibroblasts (Fig. 33A). A 5:1 cancer to fibroblast cell ratio was chosen based on this

ratio having had the most interesting fibroblast coculture-driven changes in CRPC-ne EPCaTs. LNCaP and BJ-5ta cells survived the encapsulation process with greater than 93% viability on Day 1 post-encapsulation (Fig. 33B,D, n = three EPCaTs from separately prepared batches per condition). High viability was maintained throughout long-term *in vitro* coculture; on Day 15 post-encapsulation, greater than 97% of cells (n = three EPCaTs from separately prepared batches per condition) were viable in both ADPC EPCaT conditions (Fig. 33B,D). Similar to CRPC-ne EPCaTs, ADPC EPCaT cells were also distributed homogenously throughout the PF matrix and no spatial variation in viability was observed (Fig. 33B; live cells are visualized in green and dead cells are visualized in red). Furthermore, no significant differences in viability were observed either between ADPC monoculture versus coculture EPCaTs, or between ADPC EPCaTs versus CRPC-ne EPCaTs (Fig. 33D).

Multi-magnification phase-contrast imaging revealed significant differences in EPCaT growth and cell colonization resulting from long-term *in vitro* coculture with fibroblasts (Fig. 41A-C). Whereas LNCaP EPCaTs did not grow with increasing culture duration, linear regression of the total EPCaT area revealed that LNCaP 5:1 EPCaTs underwent significant temporal growth (n = ten EPCaTs per condition per time point, $p \leq 0.05$), similar to the more aggressive PC-3 monoculture and PC-3 5:1 EPCaTs (Fig. 41B). Simultaneously, LNCaP monoculture EPCaT colonies grew significantly larger over time (n = 75 colonies per condition per time point, $p \leq 0.05$) and the maximum colony sizes on Days 15 and 29 were substantially larger than those observed in any other ADPC or CRPC-ne EPCaT condition (Fig. 41C). As reported in the ratiometric CRPC-ne EPCaT study results above, PC-3 monoculture EPCaT colonies ranged in cross-sectional area

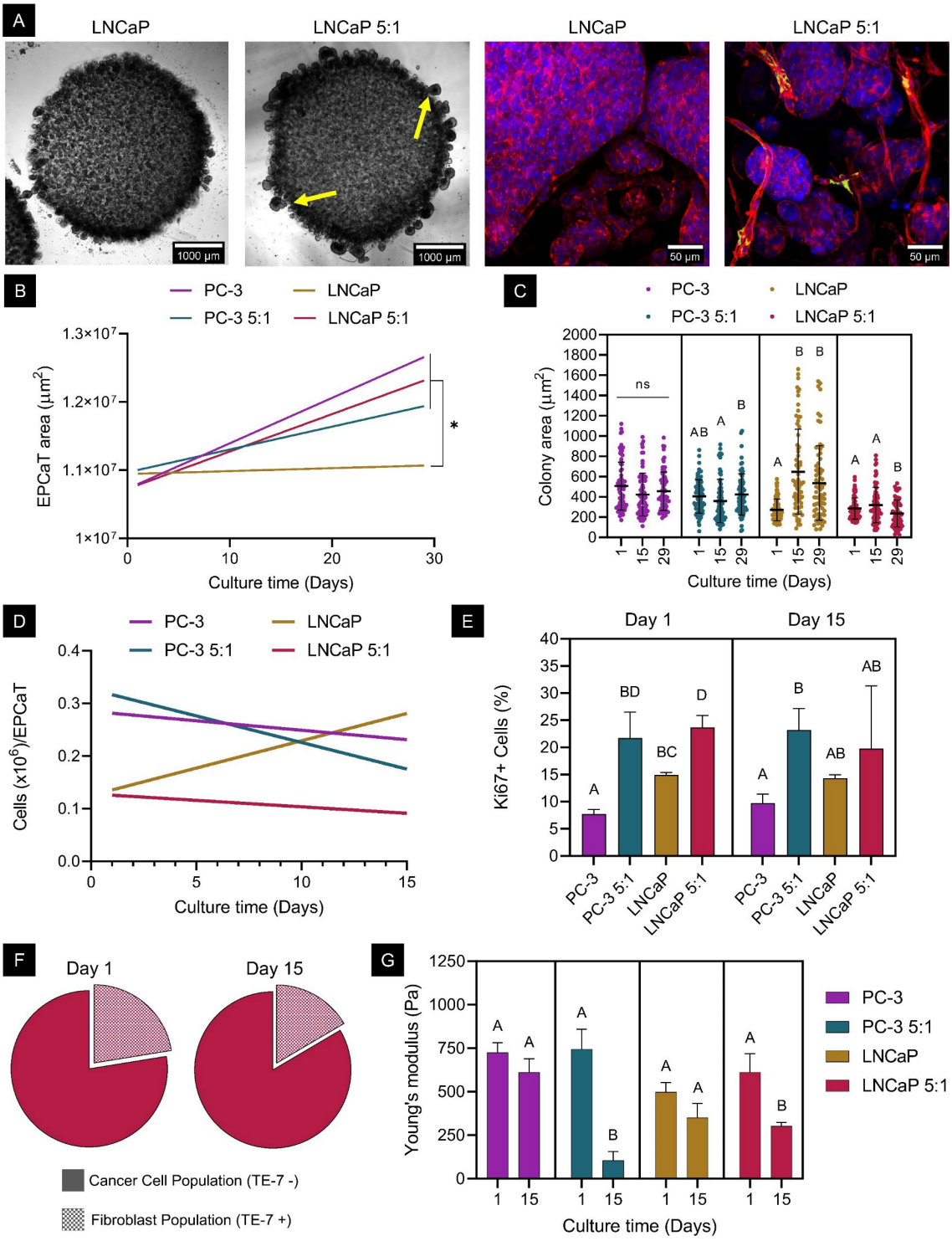

Figure 41: The inclusion of fibroblasts in ADPC EPCaTs increased cancer cell aggression, resulting in behavior more similar to the CRPC-ne condition.

Figure 41 caption continued: A) 2X phase contrast images of ADPC EPCaTs on Day 29 (yellow arrows indicate LNCaP 5:1 colonies that broke apart from the originating tissue) and 20X confocal microscopy images of immunostained ADPC EPCaTs (f-actin filaments, cell nuclei, and fibroblast cells are visualized in red, blue, and green, respectively). B) Linear regression of temporal EPCaT growth (n = 10 EPCaTs per condition per time point). C) Quantification of cell colony cross-sectional area (n = 75 colonies per condition per time point). D) Quantification of total cell count per EPCaT (n = 3 separately prepared batches of 15 EPCaTs per condition per time point). E) Quantification of proliferative (Ki67+) cell populations (n = 3 separately prepared batches of 15 EPCaTs per time point per condition). F) Pie charts illustrating temporal changes in EPCaT cell populations (n = 2 separately prepared batches of 15 EPCaTs per condition per time point). G) Temporal quantification of CRPC-ne and ADPC Young's modulus (n = 3 EPCaTs per condition per time point with three measurements averaged per EPCaT).

from approximately 200 to 1,150 μm^2 on Day 1, 100 to 1,000 μm^2 on Day 15, and 200 to 1,000 μm^2 on Day 29. PC-3 5:1 coculture EPCaT colonies ranged from 50 to 900 μm^2 on Day 1, 100 to 950 μm^2 on Day 15, and 50 to 1,100 μm^2 on Day 29. LNCaP monoculture EPCaT colonies ranged from 120 to 580 μm^2 on Day 1, 89 to 1,700 μm^2 on Day 15 and 79 to 1,500 μm^2 on Day 29. Finally, LNCaP 5:1 coculture EPCaT colonies ranged from 140 to 600 μm^2 on Day 1, 70 to 810 μm^2 on Day 15, and 25 to 530 μm^2 on Day 29.

This disparity between LNCaP and LNCaP 5:1 EPCaT colony size was also apparent through immunostaining and fluorescence microscopy (Fig. 41A); at the same geometric location within the EPCaTs, LNCaP colonies appeared much larger than LNCaP 5:1 colonies. Fibroblast elongation and substantial ADPC cancer-fibroblast cell-

cell interaction was also observed in LNCaP 5:1 EPCaTs (Fig. 41A). Throughout long-term *in vitro* culture, colonies located around the edge of LNCaP 5:1 EPCaTs grew larger while simultaneously remodeling the PF matrix enough to break apart from the original tissue and release into the surrounding culture media. This phenomenon was unique to the ADPC-fibroblast coculture condition and was evident in both phase contrast and fluorescence microscopy of the LNCaP 5:1 EPCaTs. Examples of colonies close to the breakaway point, but still attached to the originating EPCaT, are marked by yellow arrows in Figure 41A.

To better understand temporal changes in the total cell content and cell populations of ADPC EPCaTs, flow cytometry was employed. Cell counts following dissociation of the engineered tissues revealed an overall increasing trend in the number of cells within LNCaP EPCaTs over time (Fig. 41D, n = three separately prepared batches of 15 EPCaTs per condition per time point). Conversely, LNCaP 5:1 EPCaTs appeared to undergo a decrease in total cell number over time; once again, this is similar to what was found for the more aggressive CRPC-ne EPCaTs (Fig. 41D, n = three separately prepared EPCaT batches, where the value for each batch was based on the average of 15 EPCaTs per condition per time point).

As previously shown in Figure 39D, the PC-3 5:1 EPCaTs yielded a more proliferative phenotype than PC-3 monoculture EPCaTs after only one day of coculture (21.7% versus 7.7% Ki67+), as well as after fifteen days of coculture (23.2% versus 9.8% Ki67+) (n = three separately prepared batches of 15 EPCaTs per condition per time point, $p \leq 0.05$). Notably, a similar fibroblast-driven increase in proliferative populations was also observed in the ADPC coculture EPCaTs. On Day 1, LNCaP 5:1 EPCaTs had already

begun to exhibit a significantly higher percentage of Ki67+ cells (23.7%) than LNCaP monoculture EPCaTs (14.9%) time point (Fig. 41E, n = three separately prepared batches of 15 EPCaTs per condition per time point, $p \leq 0.05$). This trend continued throughout long-term *in vitro* culture; on Day 15, 14.4% of the LNCaP EPCaT cell population was Ki67+, whereas 19.7% of the LNCaP 5:1 EPCaT was Ki67+ (Fig. 41E, n = three separately prepared batches of 15 EPCaTs per condition per time point). Interestingly, the 5:1 cancer cell to fibroblast ratio was also preserved over 15 days of coculture in the ADPC condition, similar to the CRPC-ne findings presented in Figure 39A,B. On Day 15, LNCaP 5:1 EPCaTs yielded 16.5% TE-7+ fibroblast cells (Fig. 41F, n = two separately prepared batches of 15 EPCaTs).

A temporal, fibroblast-driven decline in ADPC EPCaT mechanical properties was evident through parallel plate compression testing. LNCaP monoculture EPCaTs did not exhibit significant changes in tissue stiffness between Days 1 and 15 of *in vitro* culture; the average Young's modulus on Days 1 and 15 was 500 Pa and 350 Pa, respectively (Fig. 41G, n = three EPCaTs per condition per time point with three measurements averaged per EPCaT, $p \leq 0.05$). Conversely, ADPC-fibroblast coculture resulted in a significant decrease in the Young's modulus of LNCaP 5:1 EPCaTs by Day 15 post-encapsulation. Day 1 LNCaP 5:1 EPCaTs exhibited a Young's modulus of 610 Pa, whereas Day 15 LNCaP 5:1 EPCaTs exhibited a Young's modulus of 300 Pa (n = three EPCaTs per condition per time point with three measurements averaged per EPCaT, $p \leq 0.05$). Once again, this finding is indicative of fibroblast-driven changes in ADPC EPCaT behavior that follows trends observed in the more aggressive CRPC-ne EPCaTs.

3.4.7 *Fibroblast coculture enriches tumorigenic hallmark gene sets in CRPC-ne and ADPC EPCaTs*

Bulk analysis of the ADPC and CRPC-ne EPCaT transcriptomes successfully identified fibroblast-driven differential gene expression between monoculture and coculture tissues after 15 days of *in vitro* coculture. Interestingly, only eleven total significant DEGs were found between PC-3 5:1 and PC-3 EPCaTs (all DEGs were upregulated), whereas 82 significant DEGs were found between LNCaP 5:1 and LNCaP EPCaTs (67 DEGs were upregulated and 15 were downregulated) (Fig. 42A,D-E, $p \leq 0.05$ and Log_2(Fold Change) $\geq \pm$ 1.5). Only four DEGs overlapped between the ADPC and CRPC-ne conditions; these included *EMILIN1, COL6A3, CTSK*, and *IGFBP7* (Fig. 42A). To understand the clinical significance of the fibroblast-driven DEGs in both ADPC and CRPC-ne EPCaTs, differentially expressed genes between the TCGA-PRAD primary solid tumor tissue versus solid tissue normal were also investigated. In total, 1,079 genes were differentially expressed between patient tumor and normal tissue (Fig. 42B, $p \leq 0.05$ and Log_2(Fold Change) $\geq \pm$ 1.5); eight of these overlapped with the LNCaP 5:1 versus LNCaP DEGs (*OR51E2, FLNC, CRABP2, PTGS1, FRMD6, SLC22A10, HPN-AS1,* and *SNHG19*) and one overlapped with the PC-3 5:1 versus PC-3 DEGs (*AKR1B1)*. No DEGs were commonly found in all three comparisons.

Hallmark gene set enrichment analysis provided more detailed insight into the impact of fibroblasts on ADPC and CRPC-ne biological processes and is visualized by a bubble plot in Figure 42C; the bubble size indicates the normalized enrichment score (positive enrichment is demarcated by a plus sign) and the bubble color indicates the false discovery rate. As expected from the differential gene expression results, the inclusion of

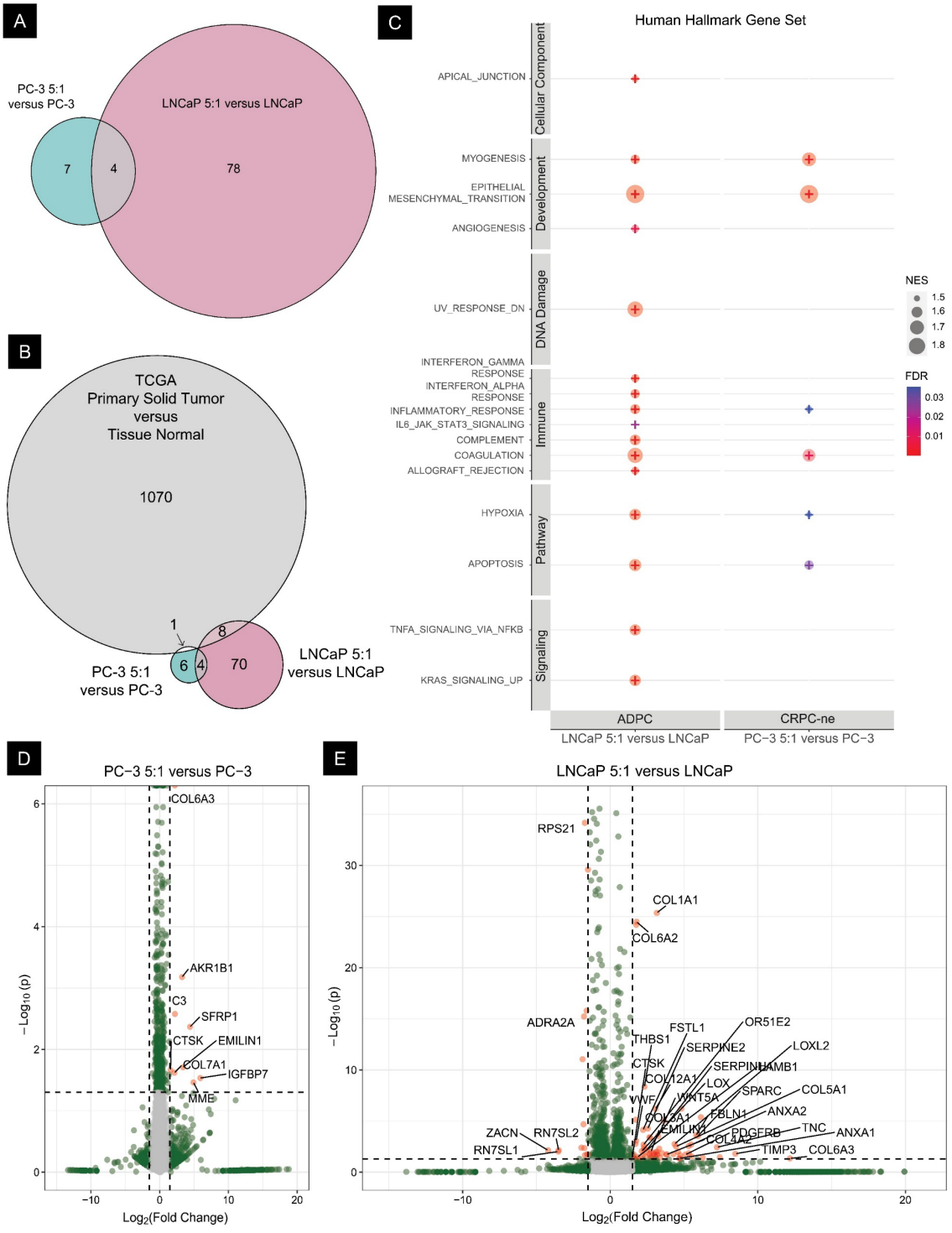

Figure 42: Fibroblast-driven differential gene expression in coculture CRPC-ne and ADPC EPCaTs resulted in significant enrichment of several hallmark gene sets known to be involved in tumorigenesis.

Figure 42 caption continued: Fibroblasts were additionally observed to have a larger impact on the ADPC transcriptome, indicating they may play an elevated role in less aggressive disease states. A) Euler diagram illustrating the number of unique and shared DEGs between CRPC-ne and ADPC coculture EPCaTs, as compared to monoculture conditions. B) Euler diagram illustrating the number of unique and shared fibroblast-driven DEGs between coculture and monoculture EPCaTs that are also differentially expressed between the TCGA patient primary tumor and normal tissue. C) Bubble plot illustrating GSEA results from EPCaT coculture versus monoculture comparisons (bubble size indicates NES, bubble color indicates FDR, positive enrichment is demarcated by a plus sign). D,E) Volcano plots of significant DEGs from the EPCaT coculture versus monoculture comparisons; genes involved in GO enrichment are labeled ($p \leq 0.05$ and $Log_2(Fold\ Change) \geq \pm 1.5$ are shown in red and DEGs with $p > 0.05$ and $Log_2(Fold\ Change) < \pm 1.5$ are shown in green).

fibroblasts had a larger impact on the ADPC condition than the CRPC-ne condition. Notably, however, those hallmark gene sets found to be positively enriched in response to CRPC-ne-fibroblast coculture are important in tumorigenic progression and include the epithelial to mesenchymal transition, myogenesis, inflammatory response, coagulation, hypoxia, and apoptosis (Fig. 42C). Each of these were also found to be positively enriched in the ADPC coculture; moreover, positive enrichment was also noted in genes encoding apical junction structures, angiogenesis, genes downregulated in response to ultraviolet (UV) radiation, interferon gamma and alpha response, IL-6/JAK/STAT3 signaling, the immune complement system, allograft rejection, TNFα signaling via NF-κβ, and genes

upregulated by KRAS activation. The specific genes per each EPCaT condition that are responsible for hallmark gene set enrichment are delineated in Table 2; those genes also found to drive enrichment in patient tumors are shown in red.

Gene ontology enrichment further elucidated the biological implications of the fibroblast-driven differential gene expression in ADPC and CRPC-ne EPCaTs; enriched ontologies were visualized through the use of treemaps in which box size indicates the enrichment score and related ontologies with the same parent term are clustered by color. In comparison to PC-3 monoculture EPCaTs, PC-3 5:1 EPCaTs demonstrated enrichment of ontologies including extracellular matrix organization, regulation of angiogenesis, and collagen and hormone metabolic processes, among others (Fig. 43). Similar to GSEA findings, the LNCaP 5:1 versus LNCaP monoculture ADPC EPCaT comparison resulted in a substantially higher number of enriched ontologies than the CRPC-ne comparison. Examples of fibroblast-driven enriched ontologies in ADPC include extracellular matrix organization, angiogenesis, epithelial cell proliferation, response to wounding, and cell-substrate adhesion (Fig. 44). Specific DEGs responsible for both ADPC and CRPC-ne hallmark gene set enrichment and gene ontology enrichment are visualized using volcano plots in which DEGs with $p \leq 0.05$ and Log_2(Fold Change) $\geq \pm 1.5$ are shown in red and DEGs with $p \leq 0.05$ and Log_2(Fold Change) $< \pm 1.5$ are shown in green (Fig. 42D,E).

3.4.8 *EPCaTs recapitulate key aspects of PCa patient primary tumor hallmark gene set enrichment*

To further elucidate the clinical significance of the ADPC and CRPC-ne EPCaT models, differential gene expression was individually evaluated for LNCaP EPCaTs,

Table 2: Top 10 core enrichment genes contributing to the GSEA results shown in Figure 42.

Those found to be top 10 core enrichment genes in both the TCGA primary solid tumor versus tissue normal comparison and the EPCaT coculture versus EPCaT monoculture comparisons are shown in red.

Hallmark Gene Set	Top 10 Core Enrichment Genes		
	LNCaP 5:1 versus LNCaP	PC-3 5:1 versus PC-3	TCGA Primary Solid Tumor versus Tissue Normal
APICAL_JUNCTION	*MMP2, TNFRSF11B, CDH11, RAC2, LAYN, SLIT2, ACTG2, FYB1, VCAN, SYK*		*EGFR, ARHGEF6, PTEN, DSC1, ACTN4, NECTIN1, CERCAM, LAMA3, ADAM23, SIRPA*
MYOGENESIS	*CDH13, LAMA2, PPP1R3C, FHL1, SSPN, PTGIS, SGCD, COL15A1, GJA5, COL6A3*	*AEBP1, BDKRB2, COL15A1, PTGIS, PPP1R3C, MYOM2, IGFBP7, CDH13, COL6A3, FABP3*	*TPD52L1, BHLHE40, TNNC1, COL6A2, LAMA2, CACNA1H, COL4A2, GSN, CHRNB1, MYH3*
EPITHELIAL_MESENCHYMAL_TRANSITION	*MMP2, COL1A2, LUM, GJA1, DCN, IGFBP4, SERPINE1, ANPEP, TIMP1, MXRA5*	*TIMP3, MMP2, MXRA5, THY1, COL5A3, GAS1, ACTA2, NTM, COL11A1, COL1A2*	*PTX3, GPC1, VCAN, GADD45B, SFRP1, CDH6, PLOD2, FBLN5, SNTB1, SPARC*
ANGIOGENESIS	*LUM, TIMP1, KCNJ8, CXCL6, VCAN, COL3A1, S100A4, FSTL1*		
UV_RESPONSE_DN	*COL1A2, GJA1, SERPINE1, CAV1, FBLN5, EFEMP1, DAB2, LPAR1, ITGB3, F3*		*NR1D2, FYN, ATXN1, FBLN5, PIK3CD, RXRA, MAPK14, PRKAR2B, CDC42BPA, LDLR*
INTERFERON_GAMMA_RESPONSE	*SERPING1, OAS2, CFH, CASP1, SSPN, XAF1, NMI, GBP4, CCL2, CCL5*		
INTERFERON_ALPHA_RESPONSE	*CASP1, NMI, GBP4, CXCL10, IL7, RTP4, SAMD9L, IFI44L, BST2, IFITM1*		
INFLAMMATORY_RESPONSE	*SERPINE1, TIMP1, LPAR1, IL7R, ITGB3, MSR1, EREG, F3, INHBA, HAS2*	*PTGIR, BDKRB1, TACR1, CCL2, CXCL10, SLC1A2, CXCR6, CSF3, GP1BA, MSR1*	*NFKBIA, NMI, HIF1A, BDKRB1, SLC31A1, CALCRL, PTPRE, ATP2A2, IL4R, IRAK2*
IL6_JAK_STAT3_SIGNALING	*ITGB3, ITGA4, CXCL10, IL7, IL1R2, CXCL1, CD44, CCR1, A2M, PDGFC*		
COMPLEMENT	*SERPINE1, TIMP1, SERPING1, CDH13, F3, CFH, C3, CASP1, TFPI2, SERPINB2*		*CTSH, CTSS, PLSCR1, CASP10, PIK3CA, ANG, IRF2, FYN, ERAP2, PPP2CB*
COAGULATION	*MMP2, SERPINE1, TIMP1, MMP1, SERPING1, MMP3, F2RL2, ITGB3, F3, CFH*	*TIMP3, MMP2, A2M, VWF, MMP3, F2RL2, C3, GP1BA, MMP11, HPN*	*ISCU, SPARC, MAFF, HTRA1, TMPRSS6, PRSS23, DUSP6, TF, USP11, F8*
ALLOGRAFT_REJECTION	*TIMP1, EREG, INHBA, CCL2, CCL5, STAT4, FYB1, IL7, CD79A, CCR1*		
HYPOXIA	*DCN, SERPINE1, CAV1, CAVIN3, PPP1R3C, F3, BGN, PLAC8, CSRP2, TPBG*	*CAVIN1, CAVIN3, HEXA, PPP1R3C, BGN, TGFBI, SLC2A3, DCN, FOS, LARGE1*	*HK1, ILVBL, GPC1, RBPJ, UGP2, ERRFI1, SULT2B1, NFIL3, ZFP36, CCN2*
APOPTOSIS	*MMP2, LUM, DCN, CAV1, TIMP1, HGF, EREG, CASP1, DPYD, PLPPR4, BGN, CD44*	*TIMP3, MMP2, BGN, PDGFRB, LUM, PLPPR4, DCN, HGF, IL1A, CD14*	*PPP2R5B, CCNA1, GSR, HGF, TIMP1, BCL10, BIRC3, CD44, EBP, PEA15*
TNFA_SIGNALING_VIA_NFKB	*SERPINE1, IL7R, F3, INHBA, PLAU, SERPINB2, CCL2, CCL5, TNFRSF9, CXCL10*		*TANK, B4GALT1, NFKBIA, SNN, CD83, SQSTM1, PTX3, IFIT2, GADD45B, PTPRE*
KRAS_SIGNALING_UP	*PRRX1, IL7R, EREG, CFH, GNG11, INHBA, PLAU, GYPC, KCNN4, ADGRL4*		*BTBD3, SATB1, IGFBP3, PIGR, PLEK2, IL1B, DUSP6, MMD, PPP1R15A, EPHB2*

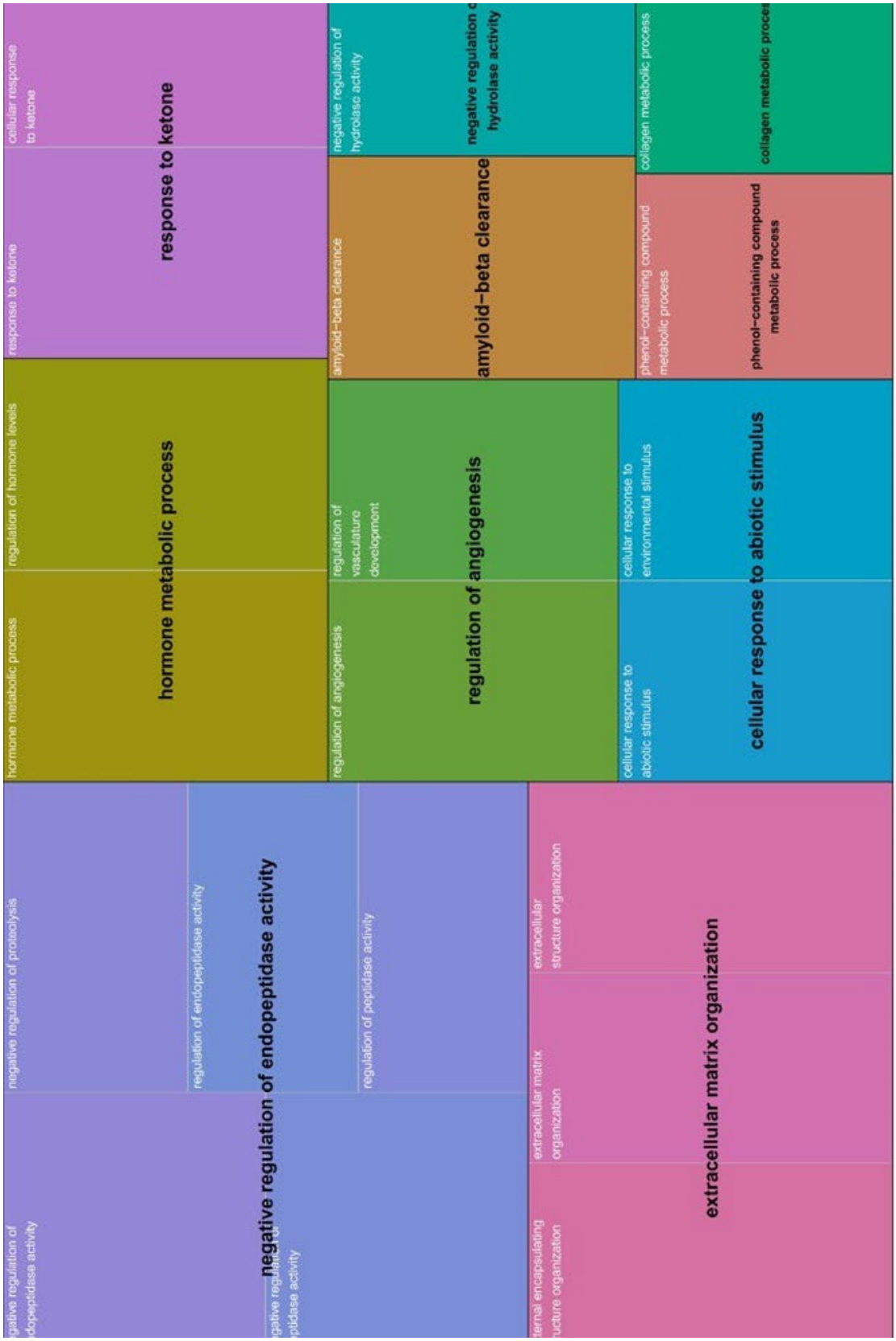

Figure 43: Tree map illustrating gene ontology over-representation analysis of PC-3 5:1 versus PC-3 EPCaTs.

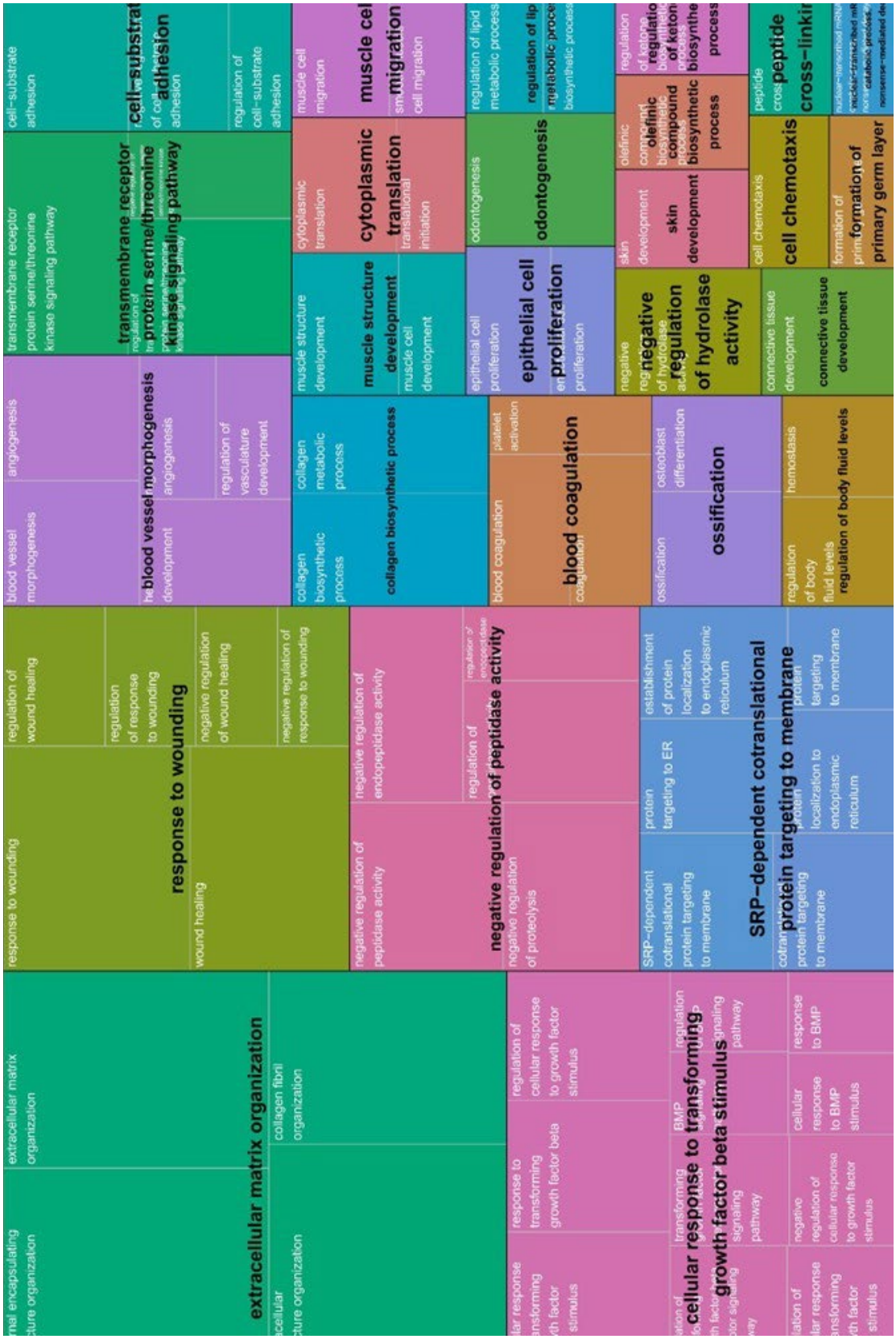

Figure 44: Tree map illustrating gene ontology over-representation analysis of LNCaP 5:1 versus LNCaP EPCaTs.

LNCaP 5:1 EPCaTs, PC-3 EPCaTs, PC-3 5:1 EPCaTs, and the TCGA-PRAD primary solid tumor tissue, each against the TCGA-PRAD solid tissue normal dataset. Again, genes with $p \leq 0.05$ and Log_2(Fold Change) $\geq \pm 1.5$ were considered significantly differentially expressed. In total, whereas 1,079 DEGs were quantified between patient tumor versus normal tissue, LNCaP EPCaTs expressed 5,502 DEGs, LNCaP 5:1 EPCaTs expressed 4,796 DEGs, PC-3 EPCaTs expressed 5,081 DEGs, and PC-3 5:1 EPCaTs expressed 5,120 DEGs (Fig. 45A). Of the total number of DEGs, LNCaP EPCaTs, LNCaP 5:1 EPCaTs, PC-3 EPCaTs, PC-3 5:1 EPCaTs, and the patient tumor tissue each exhibited 719, 270, 321, 374, and 447 unique DEGs, respectively (Fig. 45A). Interestingly, 192 DEGs were commonly found in all EPCaT conditions, as well as in the patient tumor tissue (Fig. 45A). Of those 192 DEGs, no significant differences in expression were observed amongst EPCaT conditions; however, the patient tumor differential gene expression demonstrated significantly less severe upregulation and downregulation than the *in vitro* EPCaT conditions (Fig. 45B).

Evaluation of hallmark gene set enrichment in relation to patient normal tissue revealed that both the ADPC and CRPC-ne EPCaTs recapitulated several key characteristics of the patient tumor tissue enrichment. Once again, bubble plots were employed to illustrate these results, where the bubble size indicates the normalized enrichment score (positive enrichment is demarcated by a plus sign) and the bubble color indicates the false discovery rate. Common normalized enrichment scores among all EPCaTs and the patient tumor tissue included negative enrichment of genes encoding apical junction structures, myogenesis, the epithelial to mesenchymal transition, inflammatory response, immune complement system and coagulation, apoptosis, genes up-

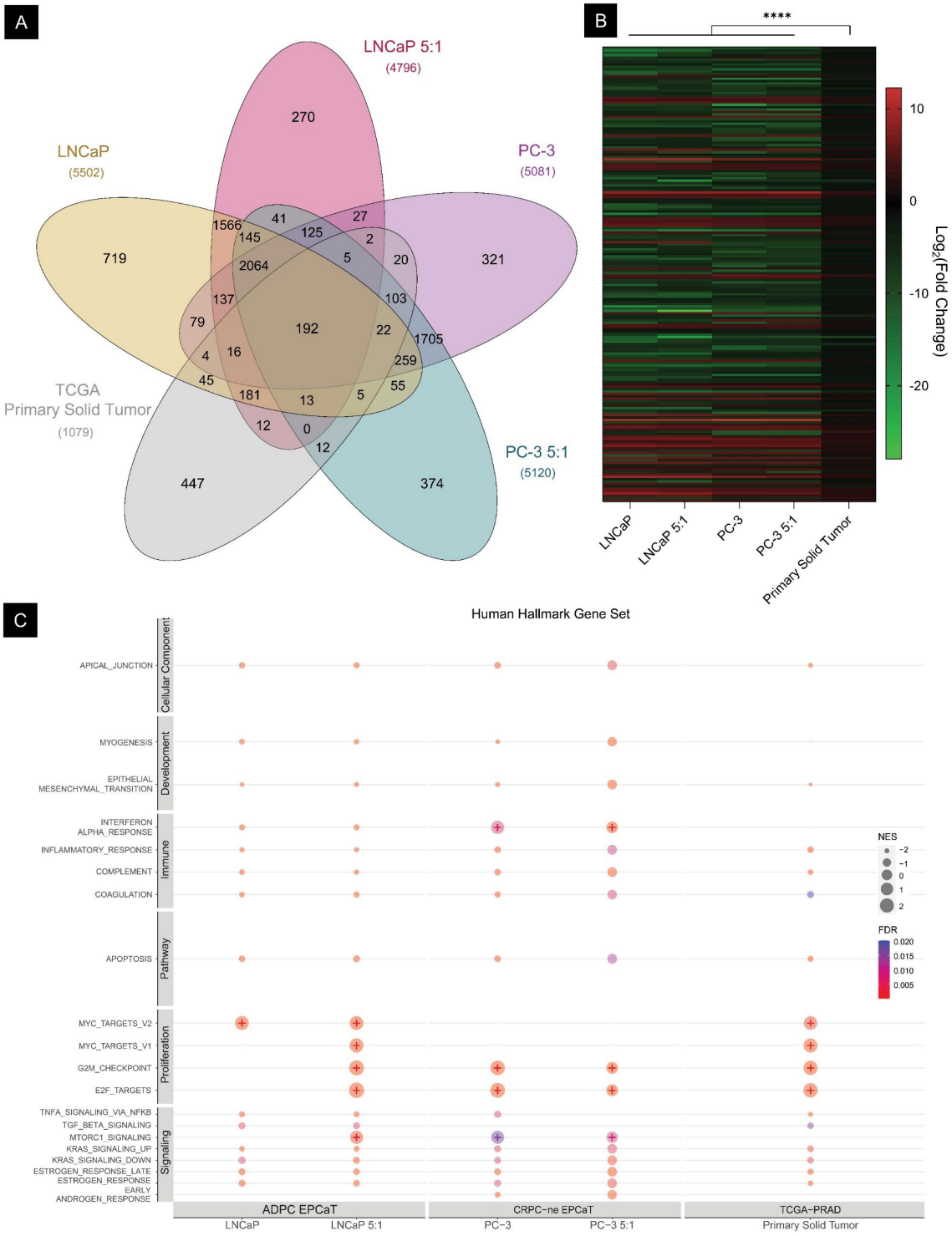

Figure 45: CRPC-ne and ADPC EPCaTs exhibited similar hallmark gene set enrichment to the TCGA patient primary tumor cohort, as compared to the TCGA patient tissue normal dataset.

Figure 45 caption continued: A) Venn diagram illustrating the number of unique and shared DEGs between CRPC-ne and ADPEC EPCaTs and the TCGA patient primary tumor cohort. B) Heatmap indicating differential expression of the 192 common DEGs expressed by all EPCaT conditions and the TCGA patient primary tumor cohort. C) Bubble plot illustrating GSEA results for EPCaTs and the TCGA patient primary tumor cohort from individual comparisons to the TCGA patient tissue normal dataset (bubble size indicates NES, bubble color indicates FDR, positive enrichment is demarcated by a plus sign).

and down-regulated in response to KRAS activation, and genes defining early and late response to estrogen (Fig. 45C). Interestingly, the LNCaP 5:1 EPCaT enrichment was more similar to the CRPC-ne enrichment signatures than the LNCaP enrichment signature for several proliferation and signaling hallmark gene sets including genes involved in the G2M checkpoint, targets of E2F transcription factors, and MTORC1 signaling (Fig. 45C). Overall, the LNCaP 5:1 EPCaTs exhibited the most similar hallmark gene set enrichment to the patient tumor tissue. It is also important to note that negative enrichment of the genes defining androgen response was appropriately observed in both CRPC-ne EPCaTs but not in the ADPC or patient tumor tissue conditions. The specific genes responsible for EPCaT and patient primary tumor hallmark gene set enrichment are delineated in Table 3; those genes commonly found to be responsible for enrichment in both *in vitro* and clinical conditions are shown in red.

Table 3: Top 5 core enrichment genes contributing to the GSEA results shown in Figure 45.

Those found to be top 5 core enrichment genes in both the TCGA primary solid tumor versus tissue normal comparison and the EPCaT versus TCGA tissue normal comparisons are shown in red.

Hallmark Gene Set	Top 5 Core Enrichment Genes				
	LNCaP	LNCaP 5:1	PC-3	PC-3 5:1	TCGA Primary Solid Tumor
APICAL_JUNCTION	IRS1, KCNH2, CALB2, PCDH1, CADM2	KCNH2, VASP, GNAI2, CERCAM, AMIGO2	COL17A1, MAP3K20, NEGR1, SDC3, AMIGO1, PTEN	CLDN11, BAIAP2, MMP2, AMIGO1, MAP3K20, PTEN	EGFR, ARHGEF6, PTEN, DSC1, ACTN4
MYOGENESIS	DENND2B, CHRNA1, SOD3, LARGE1, GADD45B	SOD3, DENND2B, SORBS3, SH3BGR, LARGE1	DTNA, GADD45B, SCHIP1, CDKN1A, SVIL	TNNT2, MRAS, ITGB5, APOD, COL3A1	TPD52L1, BHLHE40, TNNC1, COL6A2, LAMA2
EPITHELIAL_MESENCHYMAL_TRANSITION	TNFAIP3, EFEMP2, TPM1, ECM1, FERMT2	TPM4, GREM1, LRRC15, GPC1, LOXL1	SPOCK1, HTRA1, THBS1, TNFAIP3, SPARC	COL12A1, TNFAIP3, THY1, SPARC, SCG2	PTX3, GPC1, VCAN, GADD45B, SFRP1
ANGIOGENESIS	APP, TNFRSF21, PDGFA, FGFR1, JAG1	FGFR1, LUM, S100A4, COL3A1, JAG1			
INTERFERON_ALPHA_RESPONSE	IFIH1, SELL, IFI44, IFITM3, HERC6	ELF1, SAMD9, HLA-C, IFIT2, CD47	ISG15, IFI30, IRF9, OASL, IFI44L	ISG15, IFI30, IRF9, OASL, IFI44L	
INFLAMMATORY_RESPONSE	ITGA5, IRF1, TNFSF15, TLR3, IL15RA	DCBLD2, GP1BA, SLC4A4, SELL, MSR1	PTPRE, NDP, CXCL11, GABBR1, CCL20	CDKN1A, OLR1, SLC7A2, IL6, TNFRSF1B	NFKBIA, NMI, HIF1A, BDKRB1, SLC31A1
COMPLEMENT	ANG, CTSB, KYNU, LRP1, CD59	RHOG, CASP7, CDH13, CTSB, CASP9	CTSH, TNFAIP3, OLR1, CTSL, ZEB1		CTSH, CTSS, PLSCR1, CASP10, PIK3CA
COAGULATION	ANG, CTSB, LRP1, ITGA2, CTSK	CTSB, CASP9, FURIN, GP1BA, MAFF	CTSH, HTRA1, THBS1, SPARC, OLR1	APOA1, ANXA1, ACOX2, S100A1, CTSH	ISCU, SPARC, MAFF, HTRA1, TMPRSS6
APOPTOSIS	NEDD9, BIRC3, LMNA, APP, DNAJC3	EBP, RARA, BIRC3, APP, SAT1	CASP9, BIRC3, CASP7, TXNIP, SOD2	DNM1L, CASP7, SOD2, ANXA1, RNASEL	PPP2R5B, CCNA1, GSR, HGF, TIMP1
MYC_TARGETS_V2	PLK1, IPO4, PPAN, HK2, PLK4	PLK1, IPO4, PPAN, HK2, PLK4			SLC19A1, PLK1, PPAN, SRM, NOP16
MYC_TARGETS_V1		EIF4A1, U2AF1, CCNA2, CDC45, CDC20			CDC20, CDC45, CCNA2, NME1, IMPDH2
G2M_CHECKPOINT		PBK, MYBL2, NEK2, POLQ, HMMR	MYBL2, BIRC5, CDKN3, CENPA, PBK	MYBL2, BIRC5, CDKN3, PBK, EXO1	MYBL2, BIRC5, CENPA, TROAP, UBE2C
E2F_TARGETS		RRM2, KIF18B, MYBL2, DLGAP5, DIAPH3	CDKN2A, KIF18B, MYBL2, RRM2, DLGAP5	KIF18B, MYBL2, CDKN2A, DLGAP5, RRM2	MYBL2, KIF18B, BIRC5, KIF4A, CENPM
TNFA_SIGNALING_VIA_NFKB	NFKBIA, TRIP10, NFE2L2, IL6ST, BCL3	LITAF, IFIT2, NFE2L2, PLAUR, BIRC3	EFNA1, B4GALT1, PLK2, TSC22D1, CD83		TANK, B4GALT1, NFKBIA, SNN, CD83
TGF_BETA_SIGNALING	BCAR3, MAP3K7, KLF10, SKIL, RAB31	TGIF1, KLF10, MAP3K7, BMPR1A, SERPINE1			LTBP2, TGFBR1, BMPR2, MAP3K7, BMPR1A
MTORC1_SIGNALING		XBP1, RRM2, DHFR, PLK1, BUB1	XBP1, IFI30, RRM2, SLC7A11, BUB1	XBP1, IFI30, RRM2, SLC7A11, BUB1	
KRAS_SIGNALING_UP	LAT2, CD37, HKDC1, ITGA2, VWA5A	PRDM1, ETV4, FUCA1, LAT2, MMP10	FBXO4, EPB41L3, CROT, DNMBP, CCL20	EPB41L3, NAP1L2, GPNMB, TNFAIP3, FBXO4	BTBD3, SATB1, IGFBP3, PIGR, PLEK2
KRAS_SIGNALING_DOWN	PRODH, CYP39A1, GDNF, ADRA2C, NUDT11	CLDN8, MX1, MAGIX, GP1BA, TENM2	FGGY, NUDT11, DLK2, THNSL2, CAPN9	NR4A2, SNCB, EDN2, THNSL2, CYP39A1	ADRA2C, HSD11B2, RYR2, TENT5C, GDNF
ESTROGEN_RESPONSE_LATE	KLF4, WFS1, ASS1, SLC26A2, CISH	ANXA9, ALDH3B1, SLC1A4, RAPGEFL1, CPE	ARL3, ID2, FDFT1, CAV1, CHPT1	CACNA2D2, PTGES, CYP26B1, TMPRSS3, CD9	TMPRSS3, AMFR, EMP2, MICB, KCNK5
ESTROGEN_RESPONSE_EARLY	SLC7A2, KAZN, BAG1, MAST4, SYNGR1	CELSR1, TPD52L1, ELF3, ANXA9, ALDH3B1	MAPT, TBC1D30, TTC39A, WFS1, PODXL	BCL11B, TTC39A, B4GALT1, MAPT, SNX24	MICB, KCNK5, TJP3, DYNLT3, GLA
ANDROGEN_RESPONSE			GPD1L, MAK, IDI1, MAP7, SPCS3	ELL2, TNFAIP8, PIAS1, MAP7, ELOVL5	

3.5 Discussion

The use of tissue engineering techniques to recapitulate specific cell-cell and cell-matrix interactions found within the native tumor microenvironment has demonstrated significant potential in not only enabling clinically translatable drug development, but also identifying novel therapeutic targets (Kim et al., 2019). In this study, a 3D *in vitro* engineered prostate cancer tissue model comprised of prostate cancer cells of varying clinical stages in direct coculture with fibroblasts within a bioinspired, natural-synthetic hybrid matrix was developed. First, the role of fibroblasts and impact of modulating the cancer to stromal cell ratio was elucidated in a highly aggressive, neuroendocrine variant of castration-resistant prostate cancer. Significantly different cellular and whole-tissue features were observed in coculture EPCaTs, both in comparison to the monoculture condition and ratiometrically between coculture conditions. Monoculture CRPC-ne EPCaTs yielded large, circular PC-3 cell colonies and demonstrated significant temporal tissue growth, yet no temporal changes in tissue stiffness were observed. In general, the addition of normal fibroblasts at any ratio resulted in 1) a significantly increased percentage of cells expressing the Ki67 proliferation marker after 15 days of coculture; 2) cell and colony elongation; and 3) significant loss of PF matrix structural integrity resulting in a dramatically decreased tissue stiffness. It is important to note that despite a larger percentage of the cell population displaying a proliferative phenotype, the total number of cells within the coculture EPCaTs temporally decreased; simultaneously, PCa cells were observed to exhibit f-actin morphologies that resemble preliminary features of a migratory phenotype including lamellipodia, filopodia extensions, and early stage invadopodia. Taken together, these results suggest that the EPCaT platform likely supports fibroblast-

driven cell migration through a 3D matrix, thereby recapitulating PCa invasion *in vitro*. Interestingly, EPCaTs fabricated with a 5:1 cancer to stromal cell ratio exhibited uniquely more aggressive behavior than the other cancer-fibroblast coculture EPCaT ratios. Encapsulated cells had already begun to display a more proliferative phenotype than the monoculture condition after 24 hours of *in vitro* coculture and continued to exhibit a higher percentage of proliferative cells over 15 days, while maintaining the 5:1 cancer to stromal cell ratio; additionally, the PC-3 5:1 EPCaTs simultaneously demonstrated temporal tissue growth, large cell colonies, and the greatest degree of cell-mediated degradation and remodeling of the PF matrix.

To further elucidate how fibroblasts contribute to tumorigenic progression, additional investigations employing the 5:1 cancer to stromal ratio within an androgen-dependent engineered prostate cancer tissue model were performed. First, the LNCaP monoculture EPCaTs appropriately exhibited more indolent behavior, in comparison to the CRPC-ne condition. No tissue growth or matrix degradation was noted and yet the encapsulated cells underwent significant colony growth and the number of cells per tissue temporally increased, which was dissimilar to any other condition tested. From this, it can be inferred that the encapsulated cells are able to grow within the PF matrix, but do not exhibit features that align with migratory or invasive behavior. These findings, which constitute *in vitro* recapitulation of clinical differences between ADPC and CRPC, suggest that the PF EPCaT model may enable pathophysiologically-relevant prostate cancer cell behavior in an *in vitro* setting.

In sharp contrast to the monoculture LNCaP ADPC EPCaTs, the inclusion of normal fibroblasts in the ADPC EPCaT model resulted in outcomes more similar to that of

the highly aggressive CRPC-ne EPCaTs. Temporal tissue growth, increased cell proliferation, preservation of the 5:1 cancer to stromal cell ratio throughout long-term coculture, and significant degradation of the PF matrix were all noted. LNCaP 5:1 EPCaTs also exhibited unique behavior wherein large colonies near the edge of the tissue severely degraded the PF matrix and broke apart from the originating EPCaT. Taken together, these findings suggest that in the presence of a small number of fibroblasts both ADPC and CRPC-ne cells assume a more aggressive cell phenotype and begin to reflect primary stages of tumorigenic phenomena, such as invasion, that contribute to a more severe clinical disease state.

Bulk RNAseq analysis of the ADPC and CRPC-ne EPCaT transcriptomes provided critical insight into fibroblast-driven mechanisms impacting the differential cell behavior observed between monoculture and coculture tissues. Whereas many significant, differentially expressed genes were found between LNCaP 5:1 versus LNCaP EPCaTs, surprisingly few were identified among PC-3 5:1 and PC-3 EPCaTs. It is hypothesized that this diminished impact stems from the fact that PC-3 cells already represent a highly aggressive form of PCa and thus, do not have the same potential for an additional heightened response as more indolent cell lines. Hallmark gene set enrichment and gene ontology analysis together afforded a broader understanding of the specific biological processes impacted by fibroblast coculture. Both ADPC and CRPC-ne coculture EPCaTs presented significant enrichment of genes defining or involved in 1) the epithelial to mesenchymal transition; 2) inflammatory response and coagulation; 3) extracellular matrix organization and collagen metabolic processes; 4) response to hypoxia; and 5) genes mediating apoptosis pathways. Importantly, the top specific genes contributing to positive

enrichment of the coagulation gene set included matrix metalloproteinases *MMP1*, *MMP2*, *MMP3*, and *MMP11*, as well as *TIMP1*, *TIMP3, SERPINE1*, and *PLAU*; these genes are likely the main contributors to the enhanced matrix degradation observed in coculture conditions.

The ADPC coculture EPCaTs also uniquely demonstrated enrichment in other gene sets that are understood to be important contributors to tumorigenic progression. These include genes defining or involved in 1) angiogenesis; 2) epithelial cell proliferation; 3) complement system activation; 4) cell-substrate adhesion and migration; 5) IL-6/JAK/STAT3 signaling; 6) KRAS activation; and 7) TNFα signaling via NF-κβ. To provide clinical context for fibroblast-driven changes to the ADPC and CRPC-ne coculture transcriptomes, DEGs from the *in vitro* study were compared to the differential gene expression found in PCa patient primary tumor tissue against patient normal tissue. Interestingly, the ADPC comparison yielded a larger overlap with patient differential gene expression; this, in tandem with the total number of ADPC coculture DEGs, further indicates (Bonollo et al., 2020) that fibroblasts play a role in elevating less aggressive PCa disease states.

Building upon the EPCaT coculture versus monoculture transcriptomic comparisons, differential gene expression in each of the ADPC and CRPC-ne conditions against TCGA patient normal tissue data was additionally investigated; the resultant EPCaT DEGs were then compared to the TCGA primary solid tumor versus normal tissue DEGs to elucidate how well the *in vitro* model mimics patient disease. Interestingly, while the degree of differential expression was significantly different between *in vitro* and patient tumor conditions, nearly 94% of the DEGs exhibited similar directionality to the patient

tumor expression. More simply put, the DEGs identified between the *in vitro* EPCaT model and patient normal tissue were similarly upregulated or downregulated as the patient primary tumor tissue, just to a greater degree. Similar hallmark gene set enrichment was also observed among the ADPC and CRPC-ne EPCaTs and the patient primary tumor dataset. This suggests that the 3D *in vitro* EPCaT model may be an appropriate candidate for further consideration for use in future drug testing studies.

While the general conclusion that fibroblasts significantly contribute to the initiation of tumorigenic phenomena fits well within current literature, a number of this study's outcomes were unexpected and thus, contribute important discussion to the field. First, the consistent, fibroblast-driven degradation of the PF matrix, resulting in a decreased Young's modulus, was in stark contrast to the fibroblast-mediated temporal stiffening observed in other PF-based engineered models comprised of fibroblasts in monoculture (Kesselman et al., 2013) or coculture with breast or colorectal cancer cells (Hassani et al., 2022, Anbiah et al., 2019). In native tumors, fibroblasts, and particularly cancer-associated fibroblasts, are most often associated with contributing to an increased matrix stiffness (Mohammadi and Sahai, 2018, Asif et al., 2021); however, they are additionally responsible for "paving the way" for cancer cell invasion and metastasis via a dynamic exchange between ECM degradation and deposition of aligned matrix fibers (Mohammadi and Sahai, 2018, Kalluri, 2016, Sahai et al., 2020, Asif et al., 2021). Interestingly, the coculture EPCaTs were not observed to deposit an appreciable amount of ECM in tandem with PF matrix degradation despite significant upregulation of a small subset of genes traditionally responsible for ECM production in both ADPC and CRPC-ne coculture EPCaTs, particularly those in the collagen family. A recent study investigating collagen

assemblies in biopsied PCa patient tissue samples via second harmonic generation (SHG) imaging found increased alignment of collagen fibers in higher grade tumors; however, strong collagen signals were not present at the precise tissue locations of malignant growth where the cancerous cells would be proliferating and interacting with a small number of stromal cell types (Ling et al., 2017). Rather, as expected, strong collagen SHG signals were overwhelmingly found in the stromal regions of the tissue; this appeared to be exacerbated in high grade tumors in which cancerous cells had already fused glandular structures and began to invade the stromal tissue. When considering the EPCaT model, several observations in this study seem to more closely replicate the initial interactions between malignant cells and the adjacent stroma, which first results in matrix degradation, rather than mimicking post-glandular and stromal invasion of advanced malignancies, which may be the main contributor to the stiffening of native tumor tissue. Deeper investigation is needed to examine whether the EPCaT model could be a useful tool in mimicking clinically relevant mechanisms responsible for the initiation of invasion and metastasis, including the inclusion of more pathophysiologically relevant cell sources, single cell transcriptomic analyses, and extending the EPCaT model to a microfluidic tumor-on-a-chip platform that enables clear visualization of fibroblast-related changes in cell migration.

The observed cancer-fibroblast ratiometric-driven differences in both cell and engineered tissue behavior was also unexpected and has not been well characterized in an *in vitro* model to date, despite a small number of prostate cancer-fibroblast coculture models having been reported. As previously mentioned, the stromal content of native PCa tumors varies substantially (Boufaied et al., 2019), while the normal prostate and benign

prostatic hyperplasia conditions exhibit epithelial to stromal cell ratios of 2:1 and 5:1 (Shapiro et al., 1992). Reported PCa-fibroblast *in vitro* models employing spheroidal 3D coculturing methodology investigated 1:1 (Eder et al., 2016, Ortiz-Otero et al., 2020, Ojalill et al., 2020, Ishii et al., 2021) and 1:2 (Ojalill et al., 2018) cancer to fibroblast ratios; one 3D study employing a sandwiched, polymerized Matrigel/collagen type-I mixture in a 96-well plate-supported culture method reported a 2:1 cancer to fibroblast ratio (Åkerfelt et al., 2015). Other 3D models employing PCa and fibroblast cocultures have shown fibroblast-mediated regulation of immune cell recruitment (Yu et al., 2021) and PCa organoid formation and branching (Richards et al., 2019); however, in these studies the specific role that the cancer to fibroblast cell ratio may have in driving such observations was outside the scope of work. Interestingly, while all of the above discussed models broadened our understanding of prostate cancer-stromal interactions, none reported investigating the impacts of varying the cell populations at the start of *in vitro* culture or monitoring changes in cell populations over time. Thus, findings that the initial cancer-stromal cell ratio significantly influences cell proliferation, colonization, and matrix degradation, as well as that higher stromal populations are not maintained temporally, initiate an important discussion for the field. Furthermore, while unexpected, results indicating a more aggressive prostate cancer phenotype in the presence of a small number of fibroblasts provides further indication that future investigation is required to understand how fibroblasts contribute to prostate tumorigenic progression. Interestingly, PCa patient tissue samples with a higher number of fibroblasts have been observed to correlate to a higher Gleason score, and thus poor patient outcomes (Blom et al., 2019). While this appears to contradict findings presented herein, it further supports the postulate that the

ADPC and CRPC-ne 5:1 EPCaT coculture models are recapitulating cell-cell and cell-matrix interactions that contribute to progression from a less severe to more severe disease state, which is the point at which there is a dire need for therapeutic intervention. As such, a deeper investigation is warranted to further elucidate and refine the alignment of the EPCaT model with patient disease.

Notably, transcriptomic analyses of 1) EPCaT-mediated cancer-fibroblast interactions and 2) EPCaT relevancy to patient transcriptomes afforded insight into the utility of this model to elucidate potential therapeutic targets. Of highest interest, an approximate five-fold increase in *OR51E2* expression both in ADPC coculture EPCaTs (relative to monoculture EPCaTs) and in the TCGA patient primary tumor tissue (relative to patient tissue normal) was identified. This olfactory receptor gene has recently been found to play a crucial role in prostate cancer progression by facilitating the trans-differentiation of ADPC to both CRPC and CRPC-ne (Abaffy et al., 2018); however, 2D ADPC cell monocultures surprisingly revealed that *OR51E2* overexpression inhibits cell growth and is toxic to PCa cells (Pronin and Slepak, 2021). Simultaneously, a xenograft model of ADPC-fibroblast coculture indicated that fibroblasts contribute to castration resistance, however, specific pathways that may be responsible were not isolated (Thalmann et al., 2010). As such, there exists a crucial need to elucidate the pathway(s) by which *OR51E2* and cancer-fibroblast interaction each stimulate the ADPC to CRPC switch in order to successfully interrupt PCa progression. The finding that 3D engineered tissue ADPC-fibroblast coculture resulted in significant upregulation of *OR51E2* and a more aggressive PCa phenotype as compared to monoculture, provides important context for how fibroblasts and the *OR51E2* gene may together contribute to poor patient outcomes.

A much deeper investigation that extends beyond the scope of this study is required to further elucidate this interaction; however, this finding highlights the potential of the EPCaT model to make substantial future contributions to the PCa therapeutic development field.

Importantly, there are several areas in which ADPC and CRPC-ne model development and characterization can be improved. First, the PC-3 cells included in this study have recently been discovered to represent an even more aggressive neuroendocrine variant of castration-resistant prostate cancer and do not express androgen receptors (Puca et al., 2019). As such, further studies employing a true CRPC model, such as the C4-2 cell line, in addition to the PC-3 and LNCaP cell lines already investigated here, are warranted to gain a more complete understanding of PCa-fibroblast interaction. Another limitation is the use of a normal fibroblast cell line; next steps toward improved clinical relevancy should include examining paired patient-derived prostate cancer-associated fibroblasts and benign normal fibroblasts. Similarly, incorporating other tumor cell types such as macrophages or endothelial cells would also heighten the pathophysiological relevancy of this *in vitro* model.

Next, while the bulk RNAseq analyses performed herein provided critical insight into both fibroblast-mediated differential gene expression and the ability of the EPCaT model to mimic patient disease, single-cell RNAseq at initial and late culture time points would be more appropriate in future studies. Single-cell RNAseq would afford the opportunity to individually isolate coculture-driven changes in cancer cell and fibroblast gene expression and thus, demonstrates a greater potential for novel therapeutic target

identification. This would become even more critical if the EPCaT model were expanded to include a patient-derived fibroblast source and/or additional tumor cell types.

Finally, the TCGA patient cohort employed herein to assess the clinical relevancy of the EPCaT models does not represent the most appropriate disease stage for comparison. The PC-3 and LNCaP cell lines employed in the ADPC and CRPC-ne EPCaT models were both originally isolated from metastatic sites. Conversely, both tumor and normal TCGA patient tissue specimen were collected from the primary tumor site prior to treatment by other modalities, such as androgen depravation therapy which would lead to CRPC. As such, these *in vitro* models aimed to mimic patient conditions that are not present in the TCGA.

3.6 Conclusions

Here, a 3D *in vitro* engineered prostate cancer tissue model comprised of PCa cells of varying disease stages either in monoculture or in direct coculture with normal fibroblasts has been developed and characterized. Three cancer to stromal cell ratios were initially investigated within the EPCaT model to elucidate the role of fibroblasts in a highly aggressive metastatic, neuroendocrine variant of castration-resistant prostate cancer; in general, direct PCa-fibroblast coculture resulted in increased proliferative cell populations and significant remodeling of the PF matrix. Interestingly, this finding was significantly exacerbated at a 5:1 cancer to stromal cell ratio. Building upon this, the identified 5:1 cancer to stromal cell ratio was employed to investigate the role of fibroblasts in a less aggressive, androgen-dependent variant of prostate cancer. Notably, the inclusion of fibroblasts resulted in ADPC cell behavior that was more similar to the aggressive CRPC-ne condition, including increased proliferation and matrix degradation.

Transcriptomic analyses revealed fibroblast-driven enrichment of tumorigenic hallmark gene sets in both CRPC-ne and ADPC EPCaTs, while a comparison to the prostate cancer patient transcriptome revealed that EPCaT models exhibit similar enrichment to clinical primary tumor samples. Overall, these findings suggest that fibroblasts may play an elevated role in less aggressive disease states and likely contribute to the ADPC to CRPC switch. In conclusion, this work serves to 1) substantiate the coculture EPCaT model as a drug development tool that appropriately mimics several key features of the native tumor microenvironment and 2) demonstrate the model's potential for future use in novel therapeutic target identification and drug testing studies. Future studies will include paired, patient-isolated prostate cancer-associated fibroblasts and benign fibroblasts from both recurring and non-recurring patients in place of the normal fibroblast cell line employed herein to augment the pathophysiological relevancy of the EPCaT model.

Chapter 4. Microfluidic Prostate Tumor-on-a-chip Model for *in vitro* Recapitulation of Native Tumor Pathophysiology and Pre-clinical Evaluation of Nano-sized Therapeutic Delivery Systems

4.1 Abstract

This chapter introduces a bioinspired, microfluidic prostate tumor-on-a-chip model that features three-dimensional engineered coculture prostate cancer tissue, surrounded by a fully endothelialized microvascular network design that is based upon and informed by the severely bifurcating and tortuous geometries of vasculature *in vivo*. By recapitulating key features of native prostate tumor pathophysiology, this platform aims to enable more robust, translatable investigations of tumorigenic progression and prediction of therapeutic response. The results included herein serve to first characterize the prostate tumor-on-a-chip model and subsequently probe its ability to identify nanotherapeutic size-based differences in delivery to the engineered tumor tissue. Tumor cell type-dependent differences in "invasion" and "metastasis" to ancillary tumor growth regions on-chip were observed; whereas a large number of prostate cancer cells migrated to various proximal and distal regions on-chip, fibroblasts largely remained near the microvascular network within the primary tumor chamber. Vascular geometry-dependent differential drug perfusion and vascular shear rate impacts on chemotherapeutic response were detected throughout the primary tumor chamber. Some size-based differences in stealth liposomal nanoparticle delivery to the 3D engineered prostate tumor tissue were observed. Importantly, limited liposomal perfusion through an intact endothelium occurred regardless of nanoparticle size; vascular disruption by migrating cancer cells then mimicked an enhanced permeability and retention effect on-chip, by which some

liposomes were able to perfuse into the primary tumor chamber. Conversely, substantial vascular geometry and nanoparticle size-dependent differences in the delivery of super paramagnetic iron oxide nanoparticles to the engineered tumor tissue were identified. Most notably, the prostate tumor-on-a-chip positively identified preferential cellular uptake of a singular super paramagnetic iron oxide nanoparticle size, thus suggesting future potential to identify the most appropriate nanotherapeutic configuration for a specific application.

4.2 Introduction

The highly specific and efficacious delivery of anti-cancer therapeutics directly to tumor cells amidst the unforgiving and severely heterogeneous native tumor microenvironment (TME) remains a persistent challenge facing the oncology community (Roberts, 2020). To combat this, nano-sized drug delivery systems (NDDs) have emerged to not only take advantage of TME-specific vulnerabilities such as the enhanced permeability and retention (EPR) effect arising from "leaky vasculature", but also to enable 1) improved stability, prolonged circulation, and extended-release of anti-cancer therapeutics or other payloads, 2) inclusion of targeting moieties to enrich drug distribution at the tumor sites, and 3) simultaneous delivery of multiple anti-cancer therapeutics, thereby diminishing drug resistance (Navya et al., 2019). While only 15 nanoparticle-based anti-cancer therapeutics have been globally approved for clinical use, close to 75 NDDs-therapeutics have recently been involved in approximately 190 oncology clinical trials in the United States (He et al., 2019, Mundekkad and Cho, 2022); markedly, over 25,000 manuscripts are reported to have been published with the keywords "nanoparticles for cancer", indicating that successful bench-to-bedside clinical translation of NDDs has been quite limited (He et al., 2019). As such, it is critical that robust NDDs-evaluating

technologies that closely mimic the patient tumor condition are also rapidly introduced to carefully assess therapeutic efficacy during the pre-clinical phase of development. This chapter reports the establishment of a three-dimensional (3D) microfluidic prostate tumor-on-a-chip model that is pointedly engineered to integrate several key characteristics of native tumor pathophysiology, thereby providing a more rigorous platform for the evaluation of anti-cancer nanotherapeutic response.

Similar to many solid adenocarcinomas, prostate cancer (PCa) exhibits a high degree of intratumoral heterogeneity in the extent of tumor vascularization and angiogenesis, populations of tumor-supporting stromal and immune cell types and their resultant secretory factors (chemokines, cytokines, enzymes, etc.), and the extracellular matrix (ECM) microarchitectural structure of the tumor mass (Bahmad et al., 2021). In turn, this complex environment drives a number of phenomena that contribute to tumorigenic progression including the formation of biophysical and chemical gradients across the tumor mass, the initiation of invasion and metastasis, and the development of therapeutic resistance or disease recurrence (Quail and Joyce, 2013). Importantly, accurate recapitulation of these key attributes of the native TME by *in vitro* therapeutic testing models used in the pre-clinical stage of development is crucial for more accurate prediction of clinical NDDs performance. Whereas a small number of TME characteristics can be mimicked *in vitro* by two-dimensional (2D) or 3D cancer models, both are limited in their ability to incorporate multiple human tumor cell types, monitor cell invasion and metastasis, and induce vascular geometry-dependent gradients in media or therapeutic availability (Kim et al., 2019, Trujillo-de Santiago et al., 2019). Microfluidic tumor-on-a-chip models boast the potential to overcome these limitations of conventional culture

methods to provide robust information regarding cell and therapeutic behavior under physiological flow conditions (Trujillo-de Santiago et al., 2019, Kim et al., 2019), while also addressing many difficulties associated with *in vivo* animal studies such as accessibility for imaging and data collection, mismatched species-driven variability, and cost (Van Norman, 2019).

Through intentional design choices, the 3D microfluidic prostate tumor-on-a-chip model reported herein aims to recapitulate interactions between multiple tumor cell types, monitor for cell "invasion" and "metastasis", mimic pathophysiological flow conditions including the presence of "leaky vasculature", and achieve differential therapeutic gradients. Computed tomography (CT) images of mouse vasculature (Rosano et al., 2009, Prabhakarpandian et al., 2015) were employed to inform a microvascular channel design that closely mimics the tortuous geometries and severe bifurcations of native tumor vasculature; this, in turn, exposes different regions of the prostate tumor-on-a-chip model to varying shear rates (Pradhan et al., 2018). Importantly, the microvascular channels are lined with a lumenized human umbilical vein endothelial cell (HUVEC) endothelium, thereby providing a biomimetic barrier to intra- and extravasation. The microvascular network also features an engineered "leaky" interstitium which facilitates fluidic exchange between chip regions and affords micropores that migratory cells must navigate to reach the microvascular channels, circulate, and "metastasize" on-chip. Bounded by the microvascular network, a 3D primary tumor chamber (PTC) houses the previously established (Habbit et al., 2022a, Habbit et al., 2022b) engineered prostate cancer tissue (EPCaT) comprised of a coculture of castration-resistant PCa and fibroblast cells encapsulated within the natural-synthetic hybrid poly(ethylene glycol)-fibrinogen (PF)

biomaterial. Finally, initially empty secondary and tertiary tumor chambers provide the opportunity to monitor for on-chip PCa and fibroblast cell migration.

Notably, the prostate tumor-on-a-chip model is maintained under *in vitro* flow culture conditions for over 14 days, thereby enabling long-term evaluation of cell behavior and therapeutic response. Here, the on-chip migration patterns of PCa versus fibroblast cells against a lumenized endothelium were demonstrated, the vascular geometry-driven drug perfusion gradient across the EPCaT-laden PTC was elucidated, a shear rate-dependent EPCaT response to an intravenously-administered chemotherapeutic was assessed, and finally, the prostate tumor-on-a-chip model was employed in an investigation of NDDs size-based differences in therapeutic delivery on-chip using both liposomal nanoparticles and superparamagnetic iron oxide nanoparticles (SPIONs). Overall, the findings included herein demonstrate the future utility of the prostate tumor-on-a-chip model in both disease progression studies and in the pre-clinical development and testing of NDDs anti-cancer therapeutics.

4.3 Materials and Methods

All chemicals were acquired from Sigma-Aldrich (St. Louis, MO) unless stated otherwise.

4.3.1 Microfluidic Chip Device Fabrication

The microfluidic tumor-on-a-chip devices employed in this investigation were fabricated via silicon etching as previously described (Pradhan et al., 2018). Briefly, the tumor-on-a-chip design (including microvascular channels, leaky interstitium, primary tumor chamber, and ancillary tumor chambers) was translated to a high-resolution photomask (Advanced Reproduction Corporation, North Andover, MA), which was subsequently employed to pattern the photoresist on silicon wafers. Polydimethylsiloxane

(PDMS) (SYLGARD 184 Elastomer Kit, Dow Chemical Company, Midland, MI) was added over the resultant master mold to produce the patterned PDMS devices. Inlet and outlet ports were added using a 1.5 mm biopsy punch and the central tumor port (CTP) was added using a 30 gauge needle. Finally, the patterned PDMS devices were bonded to a glass slide. Throughout all studies, Tygon tubing (0.06" outer diameter, 0.02" inner diameter) was employed in the inlet, outlet, and central tumor ports to facilitate fluidic interfacing.

4.3.2 PEGDA Synthesis and Characterization

Poly(ethylene glycol)-diacrylate (PEGDA) was synthesized in-house according to an established protocol (DeLong et al., 2005). Briefly, 10 kDa molecular weight poly(ethylene glycol) (PEG) was reacted with acryloyl chloride at a 1:4 molar ratio in anhydrous dichloromethane with triethylamine at a 1:2 molar ratio; the reaction was allowed to proceed overnight at 25 ºC. Phase separation with 2M potassium carbonate was then employed to purify the resultant PEGDA; the organic phase, containing PEGDA, was dried using anhydrous magnesium sulfate and subsequently filtered. The PEGDA was precipitated using diethyl ether, filtered again, and finally dried overnight under vacuum at 25 ºC. Synthesized PEGDA was stored at -20 ºC and ^{1}H NMR was performed to characterize the degree of acrylation achieved during synthesis.

4.3.3 PF Synthesis and Characterization

PF was also synthesized in-house according to an established protocol (Almany and Seliktar, 2005). To begin, bovine fibrinogen was dissolved in an 8 M urea, 10 mM phosphate buffered saline (PBS) solution to a final concentration of 7 mg/mL. Tris (2-carboxyethyl) phosphine hydrochloride (TCEP-HCl) was subsequently added at a 1.5:1

TCEP to fibrinogen cysteine molar ratio. Upon adjusting the fibrinogen solution pH to 8.0, PEGDA dissolved in urea-PBS (280 mg/mL) was slowly added to the reaction vessel; the ensuing reaction progressed for 3 hours under dark conditions at 25 ºC. In order to stop the reaction and initiate product precipitation, acetone was added at a 4:1 acetone to reaction solution volumetric ratio. The precipitate product was collected, separated from the liquid phase via centrifugation, and redissolved in urea-PBS at a final concentration of 2.6 mL buffer per gram of precipitate product. This product solution was finally dialyzed against 1L PBS three times over a 24-hour period under dark conditions at 4 ºC. PF was collected and stored at -80 ºC for future use. A standard Pierce™ BCA Protein Assay Kit (Thermo Fisher Scientific, Rockford, IL) was employed to quantify the PF product protein concentration; PF protein concentrations ranging from 10 – 12 mg/mL were employed in all prostate tumor-on-a-chip investigations.

4.3.4 Cell Culture and Maintenance

PC-3 cells (ATCC, Manassas, VA) were cultured in F-12K culture media (Corning, Corning, NY) supplemented with 10% (v/v) fetal bovine serum (FBS) (Atlanta Biologicals, Flowery Branch, GA) and 1% (v/v) Pen-Strep (GE Healthcare Biosciences, Pittsburgh, PA). BJ-5ta human immortalized fibroblasts (ATCC, Manassas, VA) were cultured in 4 parts of DMEM (Lonza, Walkersville, MD) containing 4 mM L-glutamine, 4.5 g/L glucose, and 1.5 g/L sodium bicarbonate, and 1 part of Medium 199 (Lonza, Walkersville, MD) supplemented with 0.01 mg/mL hygromycin B (MilliporeSigma, Burlington, MA), and 10% (v/v) FBS. HUVECs were cultured in EGM™-2 Endothelial Cell Growth Medium-2 Bulletkit™ (Lonza, Walkersville, MD). All cells and prostate tumor-on-a-chips were maintained in a humidified atmosphere with 5% CO_2 at 37 ºC. Culture media was

replenished twice or thrice weekly; 0.25% trypsin/2.21 mM EDTA (Corning, Corning, NY) was employed to dissociate all cells from the tissue-culture flask surface.

4.3.5 Endothelium Formation On-chip

The microfluidic prostate tumor-on-a-chip culture timeline (Fig. 46) begins on Day -2/3 with endothelial cell seeding. To prepare the tumor-on-a-chip device for cell culture, PBS was added through the inlet port and the chip was degassed at 8 psi for approximately one hour or until no bubbles were visible. A gelatin-based coating solution (Cell Biologics Inc., Chicago, IL) was then added and incubated for one hour to support cell adhesion to the PDMS. Meanwhile, HUVECs were enzymatically dissociated from 2D culture and resuspended in media. After washing out the excess gelatin-based coating solution, HUVECs were manually seeded through the inlet port; seeding was stopped when an appropriate density of HUVECs were observed at all regions of the microvascular network. The seeded HUVECs were then permitted to adhere to the gelatin coated PDMS microvascular channel walls before initiation of flow conditions via incubation at 37 ºC for approximately 4 hours. Once all of the HUVECs were properly adhered, *in vitro* flow culture conditions were initiated using a programmable syringe pump (Harvard Apparatus, Holliston, MA) set to cycle between flow at 0.1 µL/min for four hours and a four-hour delay for 24 hours. HUVEC media, syringes, and Tygon tubing were replaced every day. A fully lumenized endothelium was usually formed after approximately 48 – 72 hours of *in vitro* flow conditions.

4.3.6 Engineered Prostate Cancer Tissue Encapsulation On-chip

Upon the formation of a fully lumenized endothelium, the 3D engineered prostate cancer tissue was directly encapsulated on-chip within the primary tumor chamber on

Day 0. To begin, the PF hydrogel precursor solution was prepared by augmenting the synthesized PF with 1.5% (v/v) triethanolamine (TEOA), 37 mM 1-vinyl-2-pyrrolidinone (NVP), and 0.1 mM eosin Y. For some studies, additional PEGDA (250 mg/mL in PBS) was also added at volumetric ratios of 96:4 (1% w/v), 92:8 (2% w/v), or 88:12 (3% w/v) to modulate the EPCaT matrix properties. Next, PC-3 and BJ-5ta cells were enzymatically dissociated from the tissue culture flasks, counted using a hemocytometer with 0.4% trypan blue (Lonza, Walkersville, MD), and resuspended in the PF precursor solution at a cancer to fibroblast cell ratio of 5:1 and a concentration of 40 x 10^6 cells/mL or 60 x 10^6 cells/mL. Using a syringe affixed with Tygon tubing, the cell-laden PF solution was directly added to the PTC via the CTP until cells were seen in all regions of the PTC; importantly, PBS was simultaneously flowed through the microvascular network to ensure no tumor cells or biomaterial were present within the microvascular network before photocrosslinking. The PTC-EPCaT was photocrosslinked under visible light using a custom-built LED device for two minutes. Finally, *in vitro* flow culture conditions were again initiated using a programmable syringe pump set to cycle between flow at 0.1 μL/min for four hours and a four-hour delay for 24 hours. Culture media, syringes, and Tygon tubing were replaced every day for 14 days of culture.

4.3.7 Endothelium Immunostaining and Fluorescence Microscopy

The HUVEC endothelium cell morphology on Day 0 of prostate tumor-on-a-chip culture was visualized at bifurcating regions of the microvascular network by immunostaining and fluorescence microscopy. The anti-von Willebrand Factor (VWF) primary antibody (Abcam Inc., Cambridge, MA) at a 1:200 dilution was employed with the Goat anti-Rabbit Alexa Fluor™ 488 (Rb488) secondary antibody (Invitrogen,

Waltham, MA) at a 1:200 dilution to positively label endothelial cells. Alexa Fluor™ 568 phalloidin (Thermo Fisher Scientific, Rockford, IL) at a 1:100 dilution was used to positively label F-actin filaments. The H33342 fluorochrome (MilliporeSigma, Burlington, MA) at a 1:50 dilution was used to positively label intranuclear DNA. To prepare the prostate tumor-on-a-chip microvascular networks for immunostaining, a PBS wash was performed, and HUVECs were fixed with 4% paraformaldehyde (PFA) (Electron Microscopy Sciences, Hatfield, PA) for 10 minutes at 25 ºC. Cell permeabilization was performed using 0.5% Triton-X for 10 minutes at 25 ºC and blocking was performed using 3% FBS in PBS overnight at 4 ºC. The anti-VWF primary was then added on-chip for 90 minutes at 25 ºC and followed by a PBS wash. Next, the phalloidin/H33342/Rb488 solution was added for three hours at 25 ºC and again, followed by a PBS wash. Fluorescence microscopy was immediately performed using an inverted Nikon Eclipse Ti microscope fitted with an Andor Luca S camera and Prior light source. Image processing was performed utilizing ImageJ software, version 1.52c.

4.3.8 Tumor Cell Type-dependent Migration Investigation

Fluorescent cell type-dependent labeling was employed to positively identify migration patterns of PCa and fibroblast cells throughout 14 days of *in vitro* flow culture. PC-3 cells labeled with green fluorescent protein (GFP) and luciferase (PC-3-GFP/Luc) were kindly provided by Dr. Robert D. “Rusty” Arnold (Auburn University, Auburn, AL). The Qtracker™ 655 Cell Labeling Kit (Invitrogen, Waltham, MA) was employed to label BJ-5ta fibroblasts. PC-3-GFP/Luc cells and BJ-5ta-Qtracker cells were encapsulated within the PTC (40 x 10^6 cells/mL, PF matrix), as described above. Stitched phase contrast and fluorescent images of the entire tumor-on-a-chip design were acquired at 20X

magnification daily using an inverted Nikon Eclipse Ti microscope fitted with an Andor Luca S camera and Prior light source. At the end of the evaluation period, the total number of PC-3-GFP/Luc and BJ-5ta-Qtracker cells located within the secondary and tertiary tumor chambers were each individually counted; initial counts were made manually utilizing ImageJ software and compared to the Find Maxima function. Once the Find Maxima function was validated, it was carefully employed for subsequent replicates.

4.3.9 Characterization of Primary Tumor Chamber Perfusion

To visualize the drug perfusion gradient across the EPCaT-laden PTC (60 x 10^6 cells/mL, PF, PF+1%PEGDA, PF+2%PEGDA, and PF+3%PEGDA matrices), the TRITC-dextran probe molecule (average molecular weight 4.4 kDa, 5 mg/mL concentration) was constantly perfused through the microvascular network at a flow rate of 40 μL/hour for up to 130 minutes or until complete perfusion of the PTC was achieved. Fluorescent images were taken at timed intervals using an inverted Nikon Eclipse Ti microscope fitted with an Andor Luca S camera and Prior light source. Image J software was subsequently employed for image analysis. To generate heat maps indicating TRITC-dextran delivery across the PTC, a log transformation of each raw image pixel value was performed, and the "physics" look-up tables (LUTs) were subsequently applied. To quantify the fluorescence intensity at varying regions within the PTC, linear regions of interest (ROIs) were drawn on raw images and the plot profile was analyzed. All fluorescence intensity values were normalized to that of TRITC-dextran in the inlet channel; as such, a relative fluorescence intensity value equal to one indicates complete perfusion at that location.

4.3.10 Chemotherapeutic Drug Testing and Viability Assessment

Vascular shear rate-dependent chemotherapeutic response was evaluated by perfusing 10 μM doxorubicin (in dimethyl sulfoxide (DMSO)/DMEM media) through the microvascular network at 20 μL/hour for 24 hours at 37 ºC and subsequently assessing the PTC-EPCaT viability (60 x 10^6 cells/mL, PF+1%PEGDA matrix). Control chips were perfused with normal culture media. After doxorubicin perfusion, chips were washed with PBS and cell viability was immediately assessed using a LIVE/DEAD™ (Invitrogen, Waltham, MA) mammalian cell cytotoxicity kit to label live and dead cells and H33342 to label all cellular nuclei. Fluorescent imaging was performed using an inverted Nikon Eclipse Ti microscope fitted with an Andor Luca S camera and Prior light source. ImageJ software was subsequently employed for image analysis. To quantify doxorubicin-mediated cell death, cell viability at six ROIs within the PTC were evaluated (three exposed to high vascular shear rates and three exposed to low vascular shear rates). The total number of nuclei and the total number of dead cells were manually counted at each ROI; the viability from each of the three locations was averaged to yield one high shear rate value and one low shear rate value per chip.

4.3.11 Liposomal NDDs Evaluation On-chip

To evaluate a liposomal NDDs against the prostate tumor-on-a-chip platform, 10mM DSPC:Chol:mPEG-2000-DSPE stealth liposomes loaded with DiI at 0.1% (w/v) were kindly provided by Dr. Robert D. “Rusty” Arnold (Auburn University, Auburn, AL) at two sizes: 100 nm and 220 nm. The liposomes were then perfused through the microvascular network at 40 μL/hour for up to 12 hours and liposomal delivery to the PTC EPCaT (60 x 10^6 cells/mL, PF matrix) was monitored via fluorescence microscopy at timed

intervals using an inverted Nikon Eclipse Ti microscope fitted with an Andor Luca S camera and Prior light source. Image J software was subsequently employed for image analysis. To generate heat maps indicating liposomal delivery across the PTC, a log transformation of each raw image pixel value was performed, and the "physics" LUTs were subsequently applied. To quantify the fluorescence intensity at varying regions within the PTC, linear ROIs were drawn on raw images and the plot profile was analyzed. All fluorescence intensity values were normalized to that of the liposomes in the inlet channel on a size-specific basis; as such, a relative fluorescence intensity value equal to one indicates complete perfusion at that location.

4.3.12 SPION NDDs Evaluation On-chip

To evaluate a SPION NDDs against the prostate tumor-on-a-chip platform, three sizes of PEGylated SPIONs (47.3±0.7 nm, 77.9±1.7 nm, and 112.3±1.3 nm) labeled with Cy5 were kindly provided by Dr. Allan E. David (Auburn University, Auburn, AL) at a concentration of 0.33 mg Fe/mL. The SPIONs were then perfused through the microvascular network at 40 μL/hour for up to 6 hours and SPION delivery to the PTC EPCaT (60 x 10^6 cells/mL, PF matrix) was monitored via fluorescence microscopy at timed intervals using an inverted Nikon Eclipse Ti microscope fitted with an Andor Luca S camera and Prior light source. Image J software was subsequently employed for image analysis. To generate heat maps indicating SPION delivery across the PTC, a log transformation of each raw image pixel value was performed, and the "physics" LUTs were subsequently applied. To quantify the fluorescence intensity at varying regions within the PTC, linear ROIs were drawn on raw images and the plot profile was analyzed. All fluorescence intensity values were normalized to that of the SPIONs in the inlet channel

on a size-specific basis; as such, a relative fluorescence intensity value equal to one indicates complete perfusion at that location.

4.3.13 Enhanced Darkfield Hyperspectral Microscopy

EDHM is specifically designed for imaging and analysis of a wide range of materials and biological samples *in situ*. There are some distinct advantages inherent in the design and engineering of this system. Specifically, it can enable the imaging of nanoscale sample elements based on their scattering properties. These sample elements are not required to be treated in any manner before imaging, as is required with other established techniques such as fluorescence microscopy or electron microscopy. The system can also support the imaging of live biological samples.

The system utilizes a tungsten halogen light (Dolan Jenner, Boxborough, MA) as a source of illumination which generates a spectral output from 400 nm to 2,200 nm. This light source has a variable power control output from 0 – 150 watts. For this experiment, the light source was set to the full 150-watt output. Light from this light source was directed to the microscope via a liquid light guide (Newport Inc., Newport, CA). This light guide transmits wavelengths from 420 nm – 2,200 nm.

The light guide connects directly to the enhanced darkfield illuminator system which mounts onto the condenser mount of the research grade optical microscope. It consists of an annular cardioid oil condenser, which produces highly collimated light at oblique angles with a numerical aperture of 1.2 – 1.4 NA. Additionally, this enhanced darkfield illuminator contains collimating lenses. When the light guide is precisely connected to the enhanced darkfield illuminator, these collimating lenses serve to modify the geometry of the source light to closely match the geometry of the system's cardioid oil

condenser. These collimating lenses also perform the function of focusing the light onto the condenser which serves to permanently refine and fix Koehler illumination of the light onto the condenser. This then enables the highly oblique darkfield illumination to then be focused onto the precise focal plane of the sample without losing the integrity of the Koehler illumination. This focusing of the light onto the sample is often times referred to as critical illumination.

This darkfield illumination process outlined above serves to provide enhanced contrast and 10 times higher signal-to-noise ratio compared to conventional darkfield optics. This indirect oblique illumination upon interaction with the sample collects the reflected or elastically scattered light from the sample, which permits distinguishable visualization of objects with similar refractive indexes as the background.

This light scatter from the sample is then collected by a 10X or 40X objective (Olympus Inc., Tokyo, Japan). The image formed from the objective is projected onto a visible and near-infrared (VNIR) diffraction grating spectrograph (Specim, Oulu, Finland). This diffraction grating is a transmission-based grating that separates the light into distinct wavelengths from 400 nm – 1,000 nm at high spectral resolution (~2 nm). This spectrally resolved light is then projected through a 30 μm slit onto the pixels of a charge-coupled device (CCD) video camera (PCO, Kelheim, Germany). This camera then sends the data to a highly custom version of ENVI 4.8 hyperspectral image capture analysis software.

The hyperspectral image is captured in a pixel row by pixel row line scan or pushbroom method. To accomplish this, an automated translational stage is utilized (Prior Scientific Instruments Ltd, Cambridge, UK). This stage provides for 10 nm step resolution. This stage and the camera communicate with the hyperspectral image capture software to

move the stage at precise distances to capture an image (of light projected onto the spectrograph slit). The hyperspectral image is then built, pixel row by pixel row.

After capture of the hyperspectral image, image analysis is conducted using a customized version of ENVI 4.8 hyperspectral image analysis software (Harris Geospatial Solutions, Inc., Herndon, VA). Each pixel of the hyperspectral image contains the optical spectral response from 400 nm – 1,000 nm of that pixel's spatial area at 2 nm of spectral resolution. Image analysis for this experiment consisted of two primary methods. The first was to collect large areas of spectrum from the hyperspectral images of the 47.3±0.7 nm and 77.9±1.7 nm prostate tumor-on-a-chip samples. To spectrally map Fe_2O_3, thousands of individual pixel level spectrum was captured as a spectral library from Fe_2O_3 exposed cells. These spectral libraries were then compared to all pixels in each negative control image in a process known as "Filter Spectral Library." This process ensures that mapping occurs in the areas containing Fe_2O_3 with no false positives. Then, to spectrally map the Fe_2O_3 in the cells, a spectral mapping algorithm known as "Spectral Angle Mapper" (SAM) was utilized. SAM is a powerful algorithm utilized to determine the spectral resemblance between two spectral profiles and to match the pixels to reference spectrum.

4.3.14 Statistical Methods

GraphPad Prism 8.0 (GraphPad Software, San Diego, CA) was employed for all statistical analysis and figure preparation performed herein. Whereas T-tests were performed to compare the means of two groups, one- or two-way ANOVA followed by the Tukey *post hoc* test were performed to compare the means of more than two groups with normal distribution. Alternatively, the Kruskal-Wallis and Dunn's multiple comparisons *post hoc* test or Friedman and Dunn's multiple comparisons *post hoc* test were performed

in the event of non-normal distribution for non-matched and matched data, respectively. A p value of ≤ 0.05 was considered statistically significant unless otherwise stated; * indicates statistical significance with $p \leq 0.05$, ** indicates statistical significance with $p \leq 0.01$, *** indicates statistical significance with $p \leq 0.001$, and **** indicates statistical significance with $p \leq 0.0001$. Unless otherwise stated, error bars indicate standard deviation.

4.4 Results

4.4.1 *Prostate tumor-on-a-chip model design recapitulates key features of tumor pathophysiology unachievable by standard 2D or 3D cell culture*

The microfluidic prostate tumor-on-a-chip model design was created via the amalgamation of an endothelialized tumor-mimetic microvascular network with the previously established three-dimensional engineered prostate tumor tissue (Habbit et al., 2022a). Figure 46 and Figure 47 illustrate key tumor-on-a-chip model design elements to orient the reader and augment understanding of the ensuing results. Briefly, these design elements include 1) a tortuous network of microvascular channels (height = 100 μm, width = 100 μm) derived from CT images of mouse vasculature and lined with a HUVEC endothelium, 2) a primary tumor chamber housing the 3D EPCaT (approximately 1.5 mm^3) comprised of a coculture of prostate cancer and fibroblast cells encapsulated within the natural-synthetic hybrid PF biomaterial, 3) secondary and tertiary 3D tumor chambers initially left empty to monitor cell migration throughout long-term culture, and 4) an interstitium (termed “vascular gap”, width = 100 μm) between the microvascular network and each tumor chamber to mimic the “leaky” vasculature observed in native tumors.

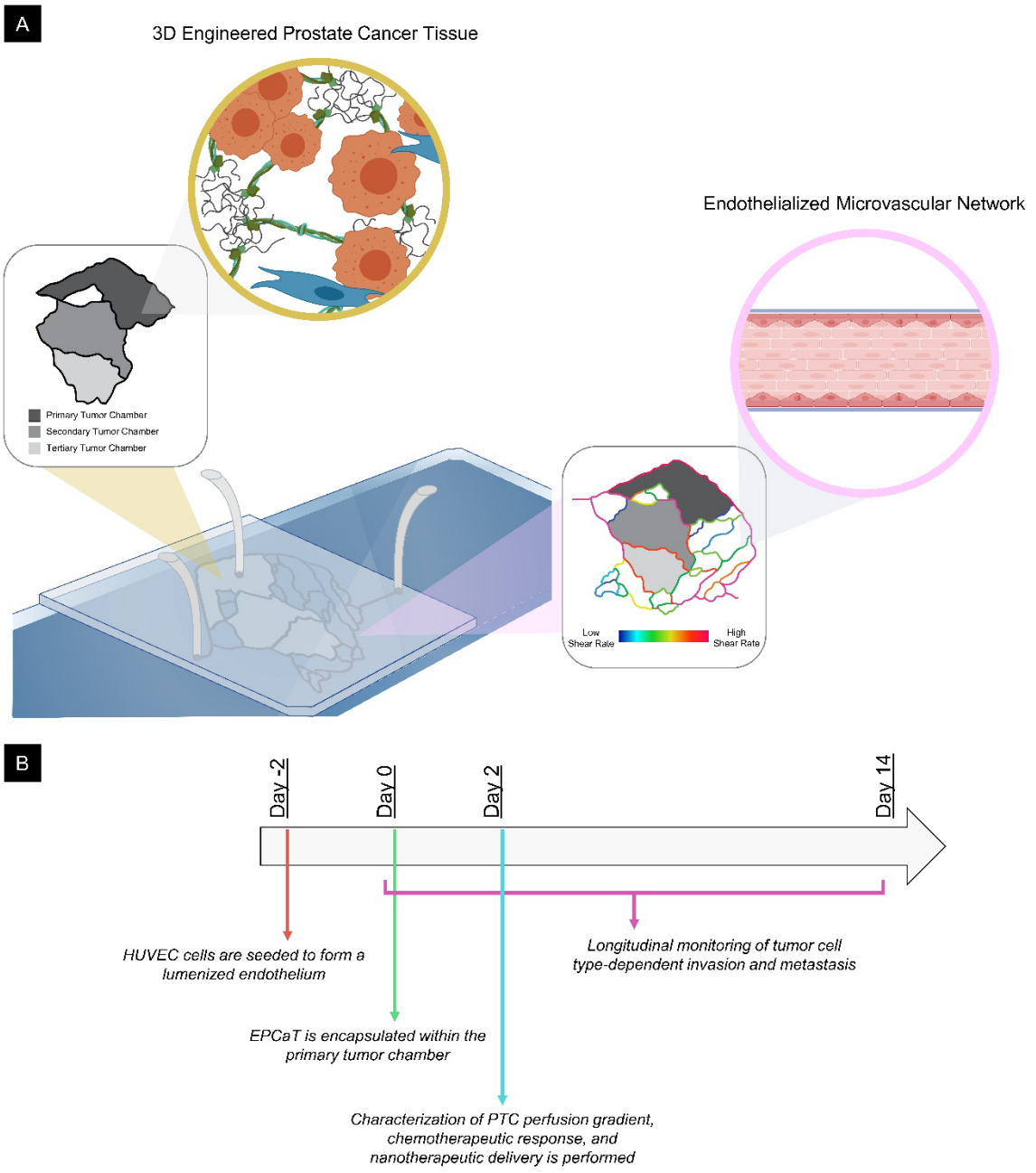

Figure 46: The prostate tumor-on-a-chip microphysiological system integrates the previously established EPCaT model with a tortuous microvascular network to more accurately mimic native tumor pathophysiology.

A) Illustration of the prostate tumor-on-a-chip device. B) Timeline illustrating prostate tumor-on-a-chip formation and analysis.

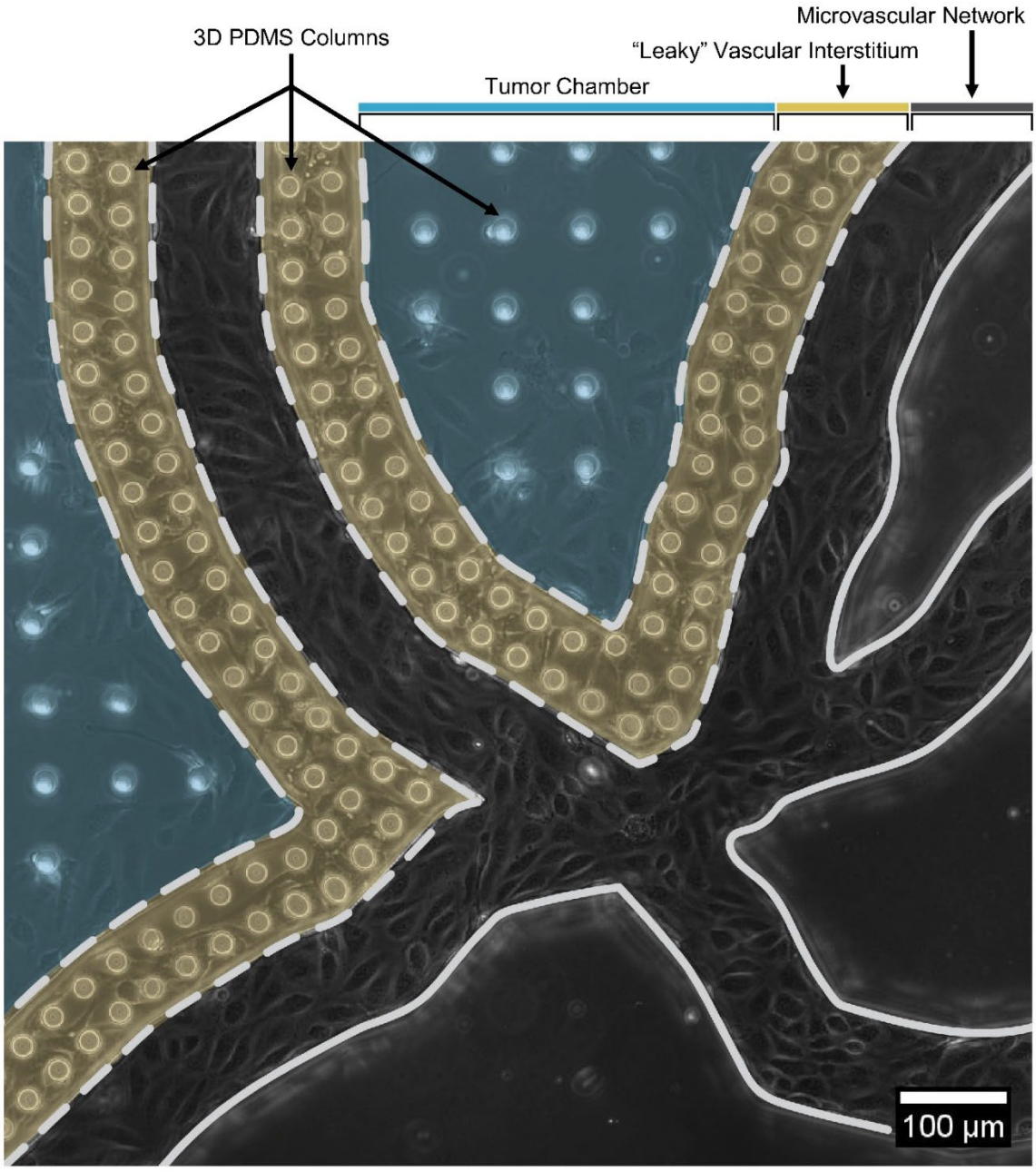

Figure 47: Prostate tumor-on-a-chip map illustrates key design features.

It is also important to note that PDMS columns are incorporated both into the tumor chambers (25 μm diameter, 50 μm spacing between columns) and the vascular interstitium (20 μm diameter, 20 μm spacing between columns) to facilitate the 3D structure of the prostate tumor-on-a-chip platform.

4.4.2 *Prostate tumor-on-a-chip model enables in vitro visualization of cancer cell migration against a lumenized endothelium*

Invasion of nearby organs and the metastatic dissemination of tumor cells to distal regions of the body remains a driving factor of poor clinical outcomes; key steps in the metastatic cascade include successful tumor cell entry into the site-of-origin vasculature (intravasation) and subsequent exiting of the vasculature (extravasation) at potential metastatic sites. To begin to mimic *in vitro* the intra- and extravasation phenomena *in vivo*, a fully lumenized HUVEC endothelium was established within the microvascular network prior to engineered prostate cancer tissue encapsulation within the primary tumor chamber (Fig. 46B). Upon permitting the seeded HUVECs to adhere to the gelatin-coated microvascular channels, flow conditions were initiated via the perfusion of media through the inlet port. After approximately 48-72 hours, the HUVECs exhibited an appropriate cobblestone morphology amidst the severe bifurcations of the microvascular network (Fig. 48A,B); positive immunostaining for the von Willebrand factor endothelial cell marker was also observed (Fig. 48B). At this point, the EPCaT was directly encapsulated on-chip within the primary tumor chamber and maintained *in vitro* under flow conditions for 14 days. Throughout long-term culture, the HUVEC endothelium appeared to fully lumenize (Fig. 48A); interestingly, after seven days of dynamic flow, the intact

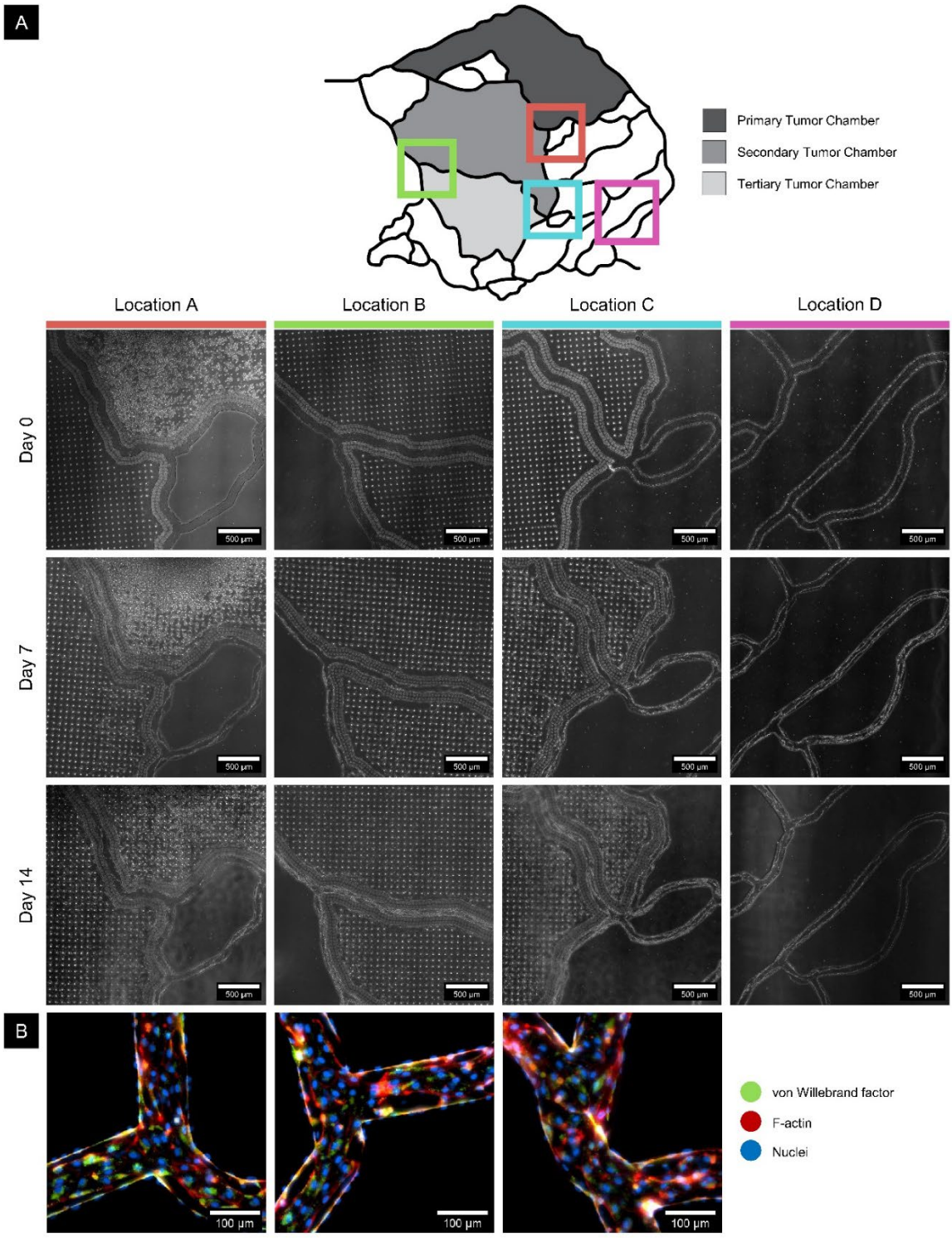

Figure 48: Long-term prostate tumor-on-a-chip culture revealed tumor cell migration to ancillary tumor chambers against a lumenized HUVEC endothelium.

Figure 48 caption continued: A) Longitudinal phase contrast imaging of a variety of locations within the prostate tumor-on-a-chip model. B) Immunostaining of the HUVEC endothelium on Day 0 (F-actin filaments are labeled red, cell nuclei are labeled blue, and VWF is labeled green).

endothelium began to release from the PDMS walls at channel locations with mild to severe angularity (Fig. 48A), thus indicating maturation and robust cell-cell junctions.

PCa and fibroblast cells encapsulated within the primary tumor chamber also exhibited temporal changes throughout long-term culture. Cell proliferation and migration were appreciable within the primary tumor chamber and most notably, cell "invasion" and "metastasis" to the secondary and tertiary tumor chambers were observed (Fig. 48A). This indicates that both intra- and extravasation through the HUVEC endothelium has occurred. In order to elucidate cell type-dependent differences in on-chip tumor dissemination, PC-3-GFP/Luc PCa cells and Qtracker-labeled BJ-5ta fibroblasts were employed in EPCaT encapsulation.

Interestingly, fibroblasts accumulated near the edge of the PTC but were not observed outside of the primary tumor chamber in large numbers over 14 days of *in vitro* flow culture; less than five fibroblasts were found in the secondary and tertiary tumor chambers combined at each time point assessed (Fig. 49A, n = three prostate tumor-on-a-chips). Conversely, PCa cells began to spread to ancillary tumor chambers after only 24 hours and continued to migrate through the PF biomaterial towards and proliferate near the PTC-surrounding vascular channels throughout two weeks of flow-based culture (Fig. 49A). Quantification of the total number of PCa cells in the secondary and tertiary

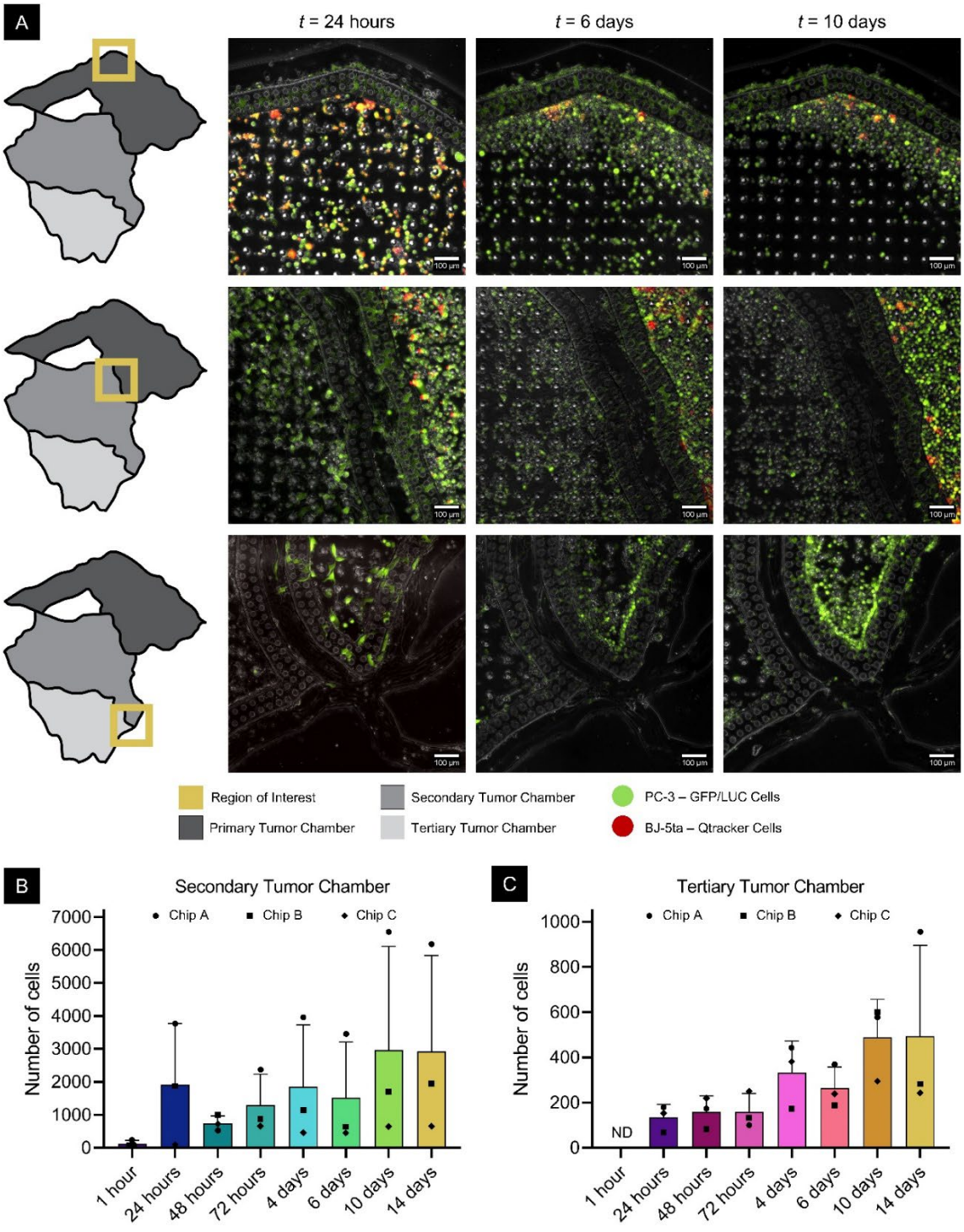

Figure 49: Tumor cell type-differences in "invasion" and "metastasis" were detectable using the prostate tumor-on-a-chip microphysiological system.

Figure 49 caption continued: A) Longitudinal fluorescent and phase contrast imaging overlays illustrating cell migration throughout the prostate tumor-on-a-chip platform (PC-3-GFP/Luc prostate cancer cells are labeled green and BJ-5ta-Qtracker fibroblasts are labeled red). B,C) Temporal quantification of the number of migratory PC-3-GFP/Luc cells in the secondary and tertiary tumor chambers (n = 3 prostate tumor-on-a-chips per time point, ND indicates not detected).

tumor chambers revealed very dynamic temporal cellular behavior as well as substantial chip-to-chip variability, particularly in the secondary tumor chamber (Fig. 49B,C, n = three prostate tumor-on-a-chips). The total number of PCa cells in the secondary tumor chamber ranged from several hundred to thousands of cells at each time point, whereas the total number of PCa cells in the tertiary tumor chamber remained in the hundreds (Fig. 49 B,C, n = three prostate tumor-on-a-chips). Markedly, the number of cells within either tumor chamber did not always follow a continuously increasing trend, indicating that cells within the ancillary tumor chambers at a particular time point may or may not elect to remain in that "metastatic" environment and begin proliferating.

4.4.3 *Vascular geometry-driven differential drug distribution is achieved within the EPCaT-laden primary tumor chamber*

As introduced herein, a major challenge facing cancer treatment is adequate, targeted therapeutic delivery to the neoplastic cells; however, the incomplete and "leaky" vascularization of native solid tumors plays a substantial role in complicating this challenge and often results in highly heterogeneous drug distribution across the tumor mass. As previously reported (Pradhan et al., 2018), the tortuosity of the tumor-on-a-chip microvascular network design exposes the primary tumor chamber to varying shear rates,

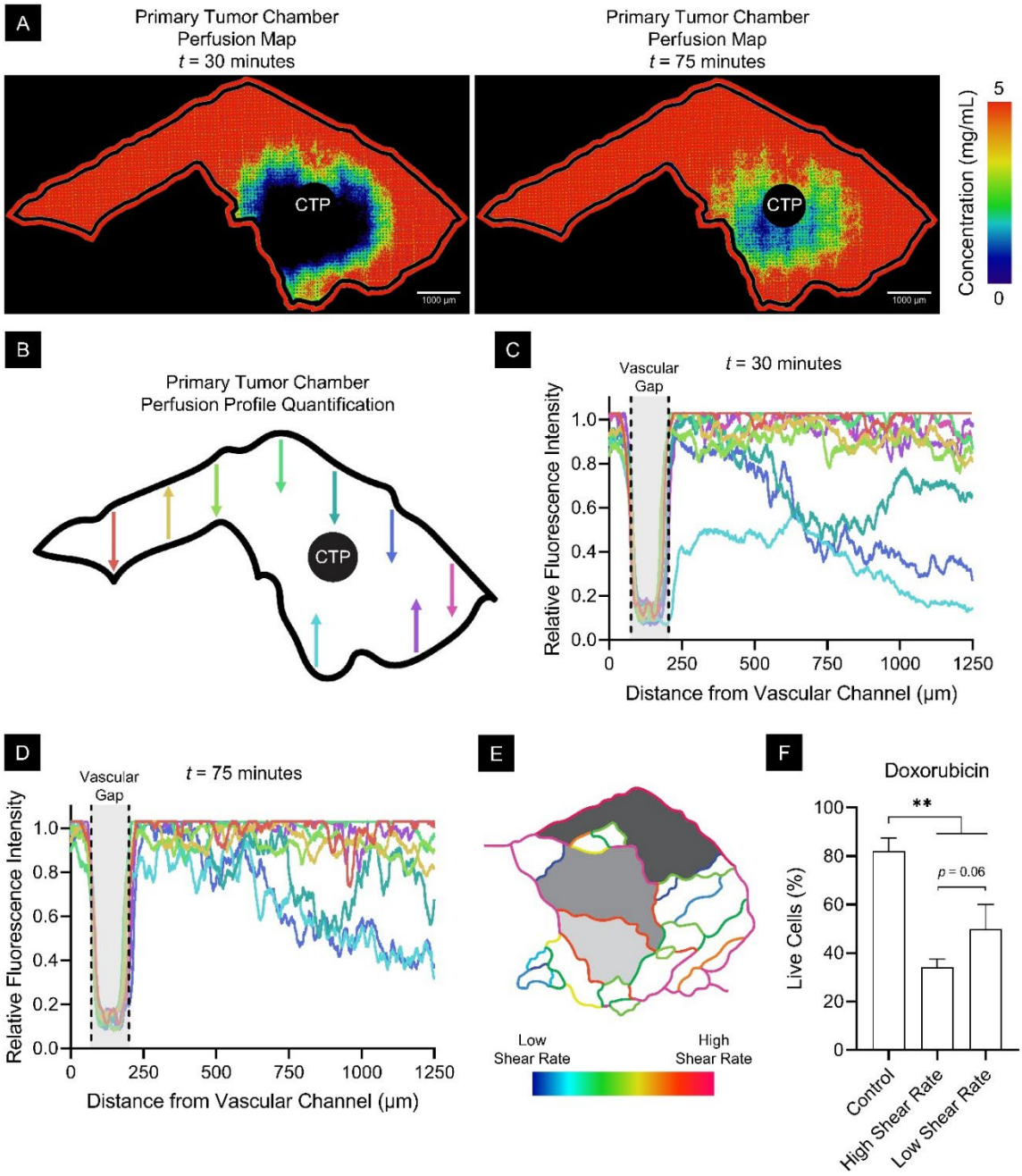

Figure 50: Perfusion of a fluorescent probe molecule revealed vascular geometry-dependent differential perfusion of the primary tumor chamber; vascular shear rate-driven impacts on chemotherapeutic response were also detected.

Figure 50 caption continued: A) Primary tumor chamber TRITC-dextran perfusion heat maps. B) TRITC-dextran perfusion profile quantification map. C,D) TRITC-dextran perfusion profiles at multiple locations on-chip (n = 1 prostate tumor-on-a-chip). E) Illustration of varying shear rates on-chip. F) Quantification of EPCaT viability post-doxorubicin exposure (n = 3 prostate tumor-on-a-chips, with 3 values averaged per chip per condition) (CTP denotes central tumor port).

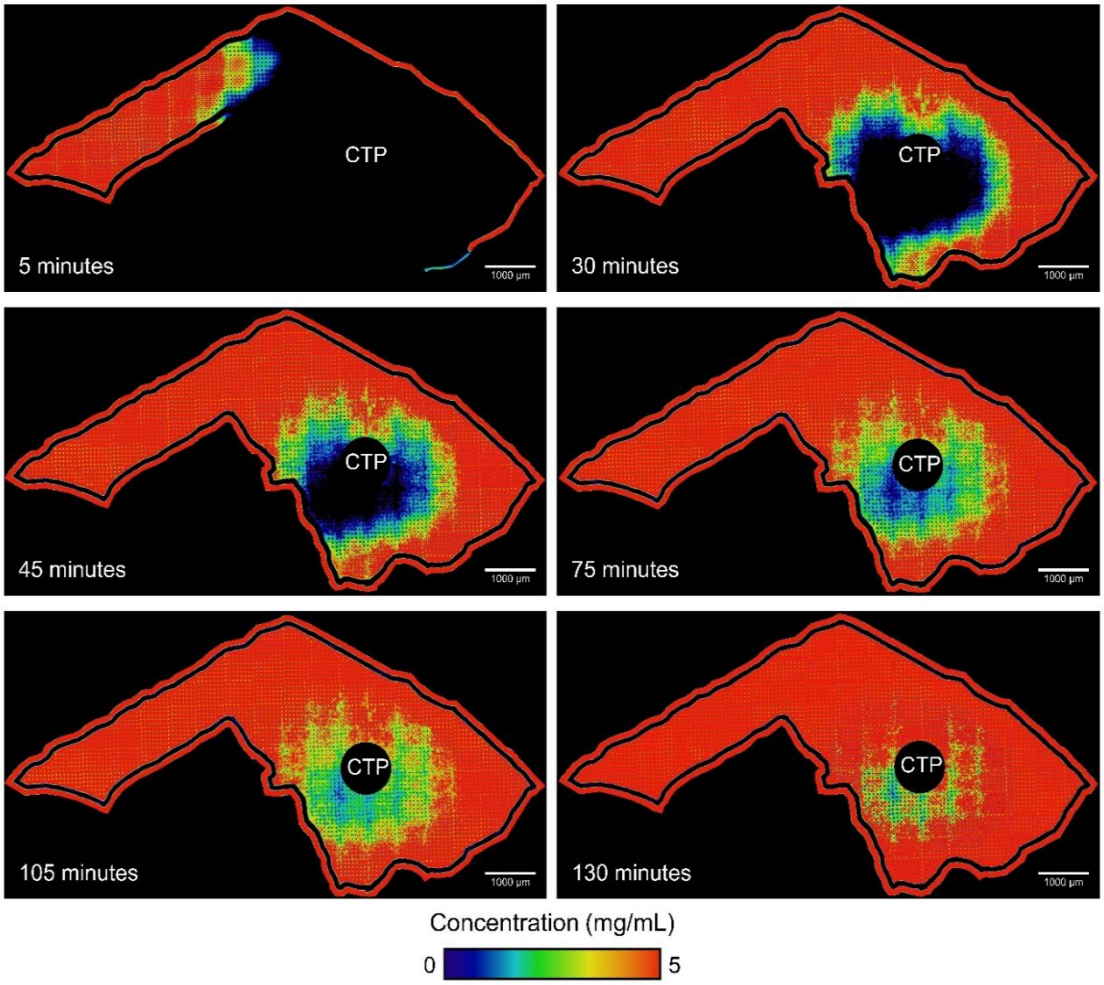

Figure 51: Temporal changes in TRITC-dextran perfusion into the EPCaT-laden primary tumor chamber under continuous flow.

(CTP denotes central tumor port).

ranging from zero to 50 reciprocal seconds. To visualize the resultant perfusion gradient into the EPCaT-laden primary tumor chamber, the TRITC-dextran fluorescent probe molecule was continuously perfused through the inlet port; recurrent fluorescent imaging and *post hoc* processing enabled the generation of temporal heat maps illustrating differential probe molecule concentration spatially throughout the PTC (Fig. 50A). This temporally dynamic perfusion gradient is also appreciable in Figure 51.

Subsequent quantification of the relative fluorescence intensity, normalized to the inlet channel, at varying PTC locations confirmed vascular geometry-driven differences in TRITC-dextran distribution (Fig. 50B-D). Regions of the primary tumor chamber most proximal to the inlet channel were well-perfused at early time points, as compared to distal regions and the immediate area surrounding the central tumor port, in particular (Fig. 50B-D). Complete perfusion of the PTC was achieved after approximately 130 minutes. Interestingly, modifying the mechanical stiffness of the PF biomaterial employed in EPCaT encapsulation through the addition of 1%, 2%, and 3% excess PEGDA (w/v), resulted in substantial changes to the perfusion gradient (Figs. 52-55). An increase in EPCaT matrix stiffness yielded much more rapid perfusion of the PTC, likely due to increased pore size (Pradhan et al., 2017b); the most-stiff PF+3%PEGDA EPCaT matrix was completely perfused after only 45 minutes (Fig. 52,55), whereas PF+1%PEGDA and PF+2%PEGDA matrices were completely perfused after 115 minutes (Figs. 52-54).

In order to evaluate how the differential perfusion gradient within the EPCaT-laden PTC translates to an observable, differential response to therapeutics, doxorubicin (a common, intravenously administered chemotherapeutic) was perfused through the microvascular network. Cell viability within the PTC was subsequently assessed at and

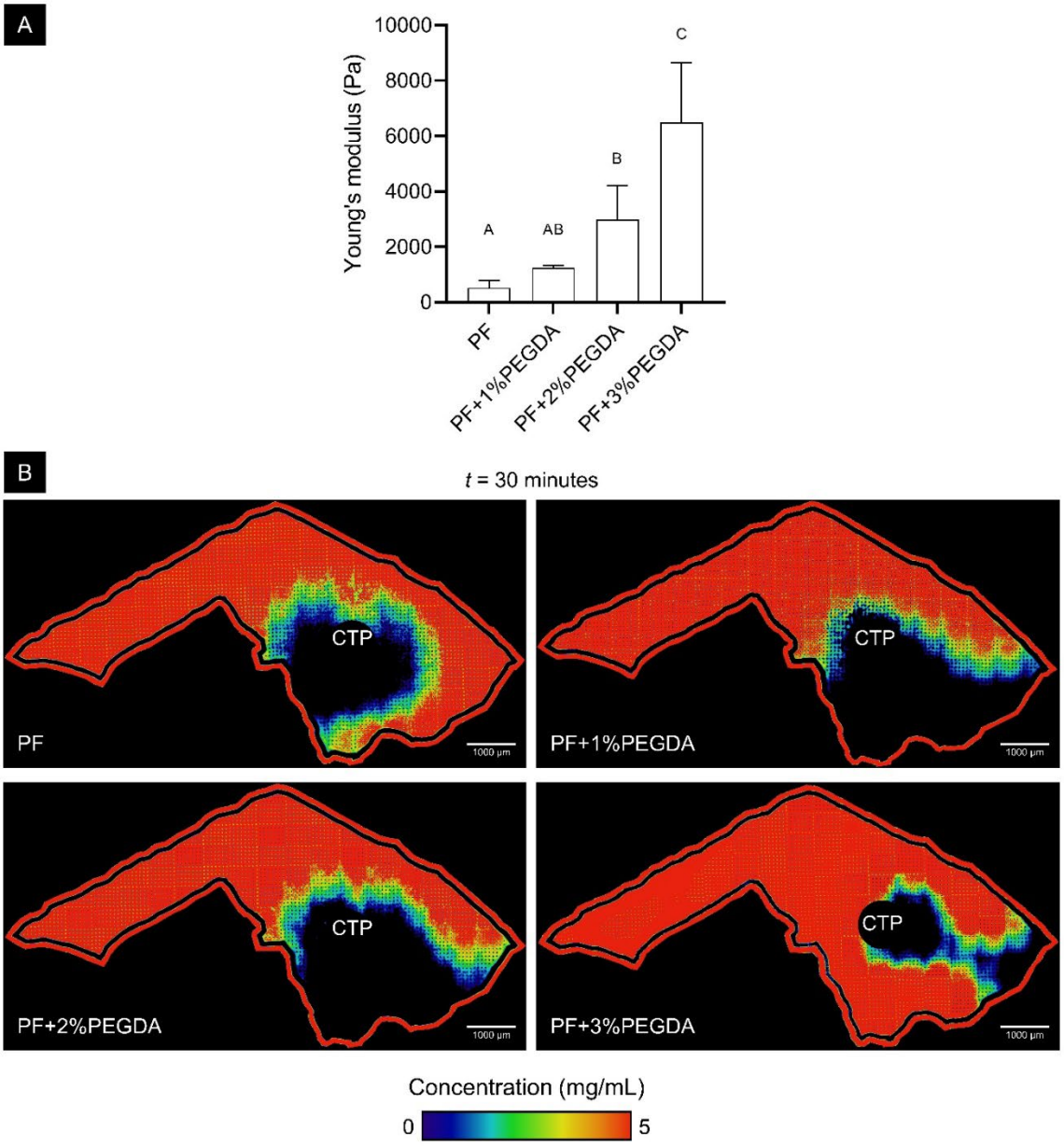

Figure 52: Modulating the EPCaT matrix stiffness within the primary tumor chamber resulted in differential perfusion gradients.

A) Quantification of initial EPCaT stiffness when modulated with excess PEGDA (n = 6 EPCaTs). B) Matrix stiffness-driven variability in TRITC-dextran perfusion within the primary tumor chamber (CTP denotes central tumor port).

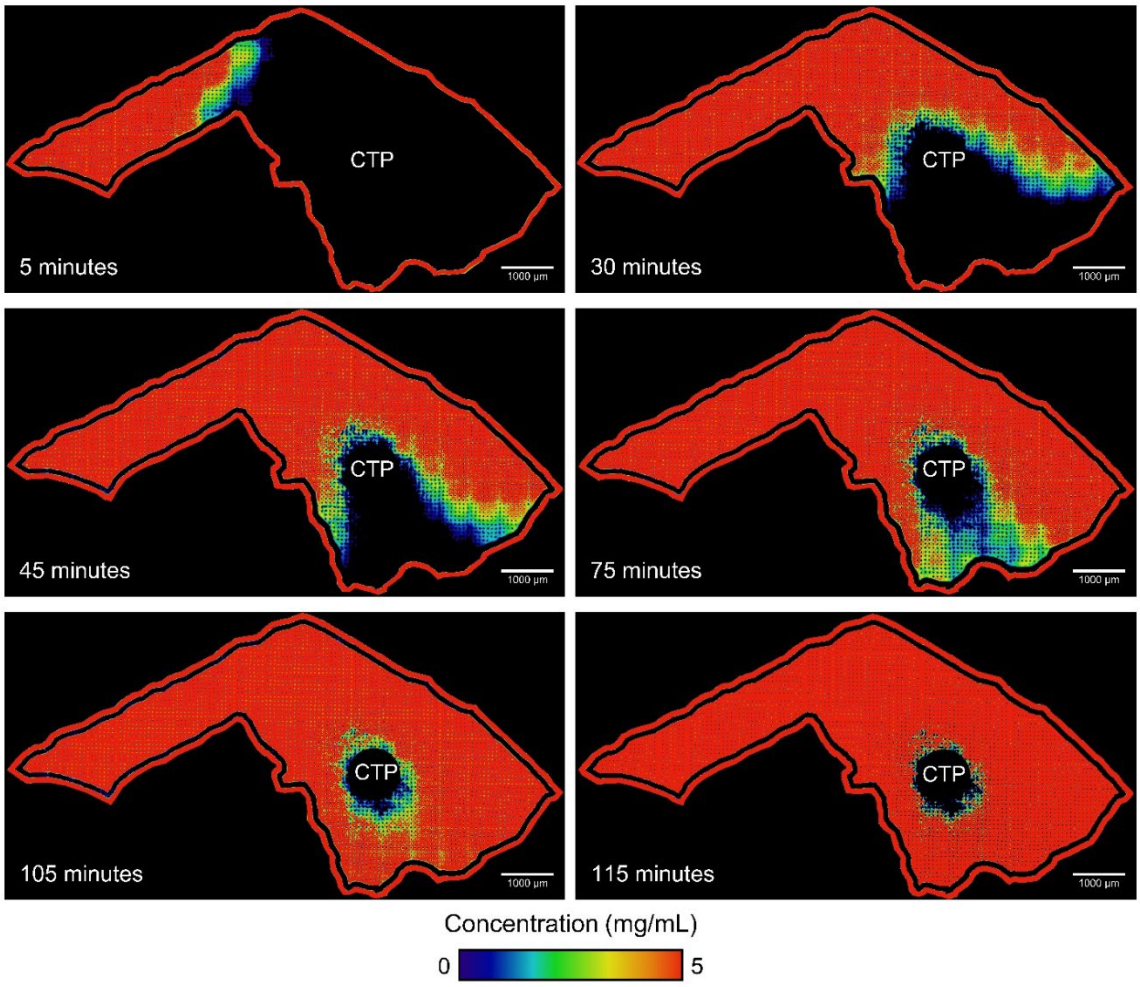

Figure 53: Temporal changes in TRITC-dextran perfusion into the PF+1%PEGDA EPCaT-laden primary tumor chamber under continuous flow.

(CTP denotes central tumor port).

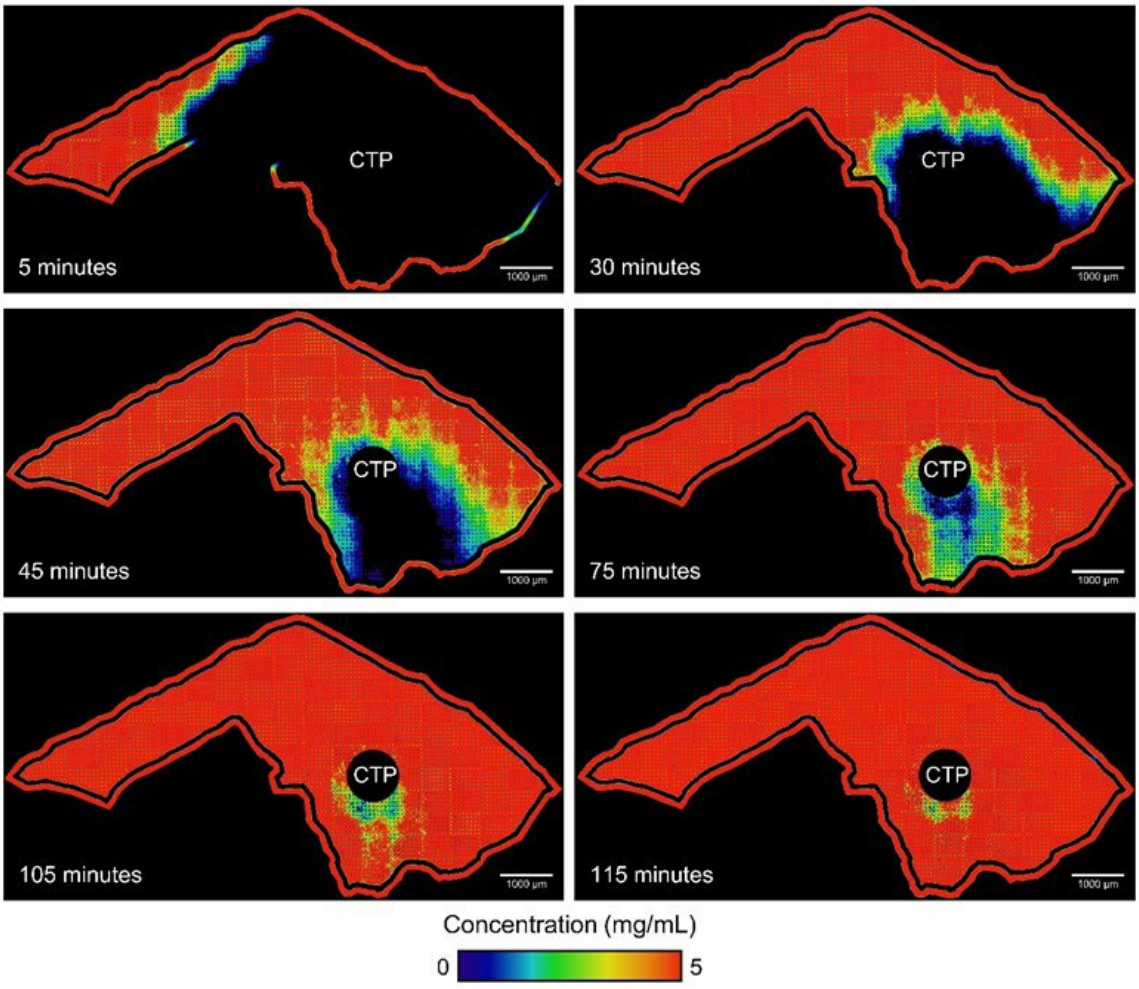

Figure 54: Temporal changes in TRITC-dextran perfusion into the PF+2%PEGDA EPCaT-laden primary tumor chamber under continuous flow.

(CTP denotes central tumor port).

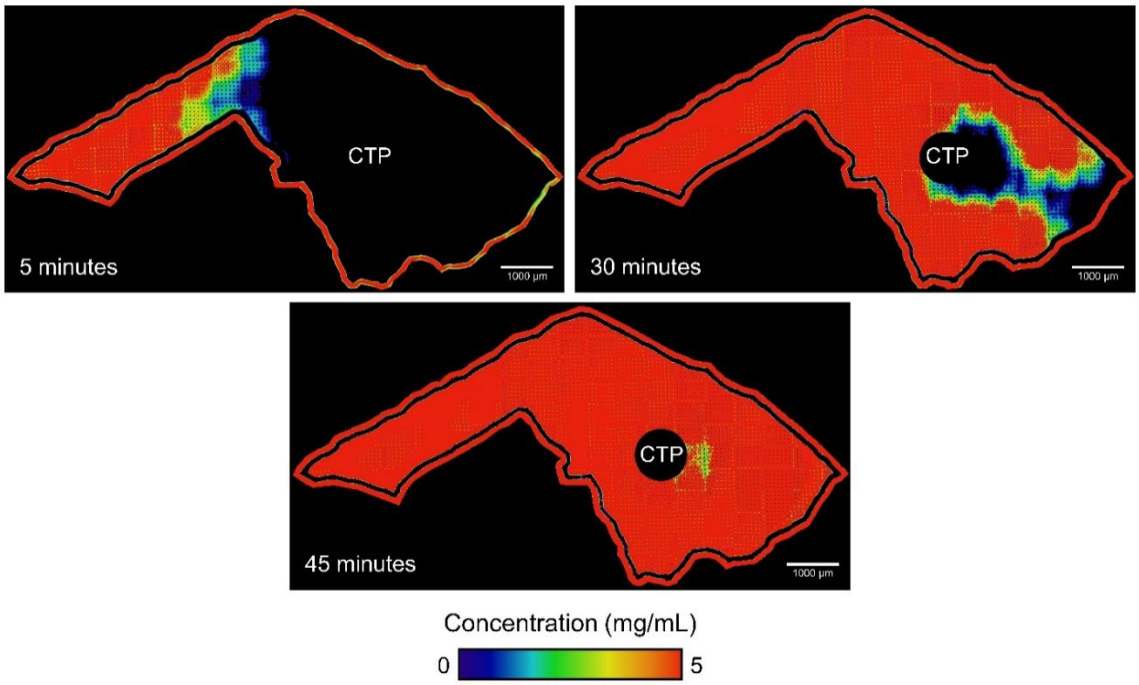

Figure 55: Temporal changes in TRITC-dextran perfusion into the PF+3%PEGDA EPCaT-laden primary tumor chamber under continuous flow.

(CTP denotes central tumor port).

compared between regions exposed to high shear rates and regions exposed to low shear rates (Fig. 50E). A significant increase in cell death, as compared to the control viability, was observed in response to doxorubicin at both high and low shear rate regions (Fig. 50F, n = three prostate tumor-on-a-chips, with three values averaged per chip per condition, $p \leq 0.01$). Those regions exposed to higher vascular shear rates tended to exhibit a lower percentage of viable cells than those regions exposed to lower shear rates, which also exhibited more chip-to-chip variability. Though a significant difference in drug response was not found specifically between the selected regions used for analysis, it is clear that spatially differential drug response is achievable and observable using the prostate tumor-on-a-chip model (Fig. 50F, n = three prostate tumor-on-a-chips, with three values averaged per chip per condition, $p = 0.06$).

4.4.4 *Size-based differences in liposomal nanoparticle delivery were observed using the prostate tumor-on-a-chip model*

Liposomal nanoparticle therapeutic carriers for anti-cancer therapeutics are both highly researched and clinically implemented (Taléns-Visconti et al., 2022); as such, it is imperative that pre-clinical cancer models demonstrate proven utility in evaluating liposomal delivery and efficacy. While a number of liposomal nanoparticle parameters can be tuned to improve therapeutic performance (including the inclusion of hydrophilic polymer moieties, controlled release mechanisms, targeting ligand surface modifications, etc.) (Sercombe et al., 2015), size-based differences in liposomal delivery were first elected to be evaluated against the prostate tumor-on-a-chip platform, given the heavy reliance on tumor EPR effects for appropriate intratumoral liposome delivery. DSPC:CHOL:mPEG2000-DSPE stealth liposomes were separately sized at 100 nm and 220 nm and fluorescently labeled with DiI to enable visualization throughout prostate tumor-on-a-chip perfusion. Similar to the TRITC-dextran probe molecule study, recurrent fluorescent imaging and *post hoc* image processing were performed to generate heat maps illustrating 100 nm versus 220 nm liposomal distribution within the primary tumor chamber. Figures 56 and 57 illuminate temporal shifts in the perfusion gradient for 100 nm and 220 nm liposomes, respectively. Markedly, quite limited liposomal delivery is observed within the PTC, even after 12 hours of constant perfusion; this observation is in stark contrast to the TRITC-dextran probe molecule perfusion gradient. Quantification of the relative fluorescence intensity, individually normalized to the inlet channel for each liposome size, at varying PTC locations not only exposed expected vascular geometry-

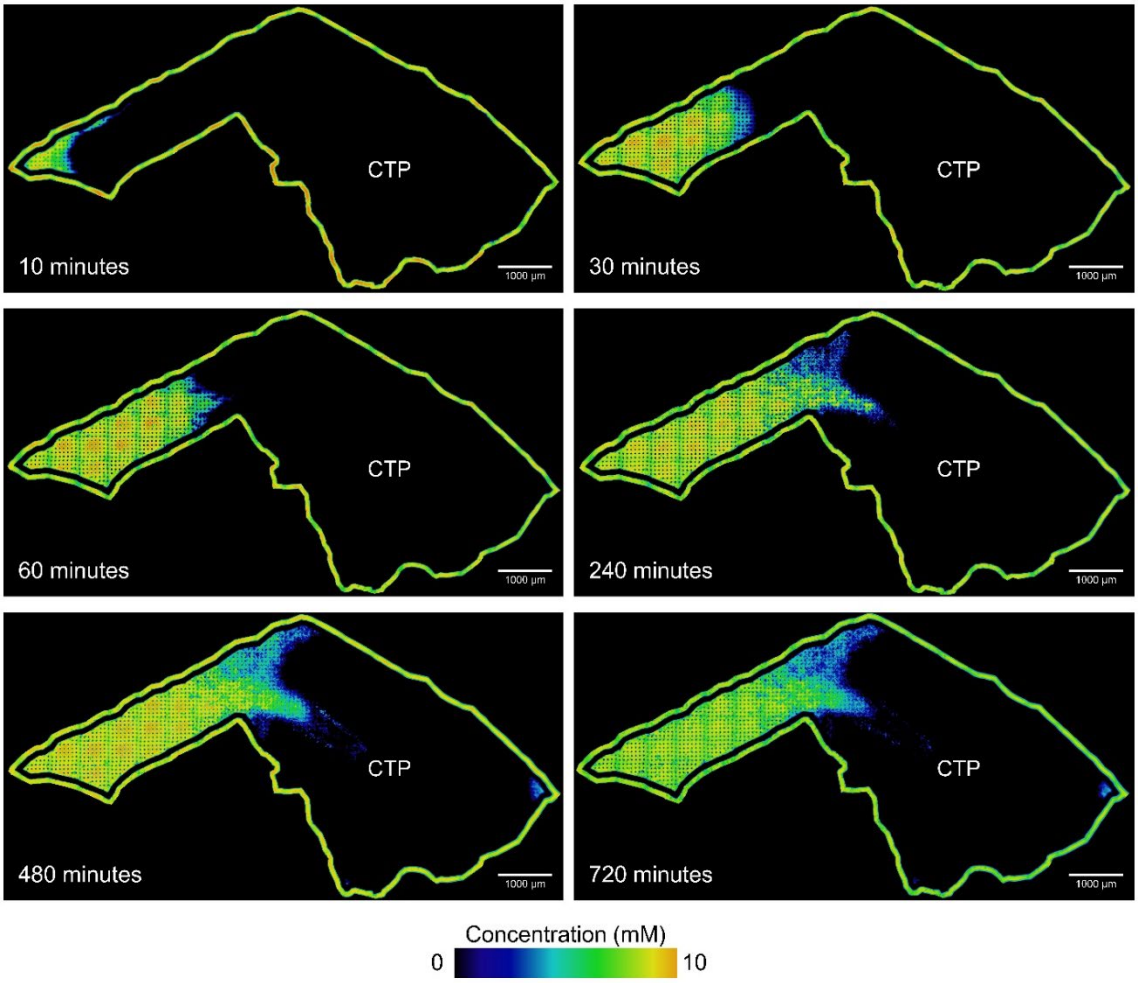

Figure 56: Temporal changes in 100 nm stealth liposome perfusion into the EPCaT-laden primary tumor chamber.

(CTP denotes central tumor port).

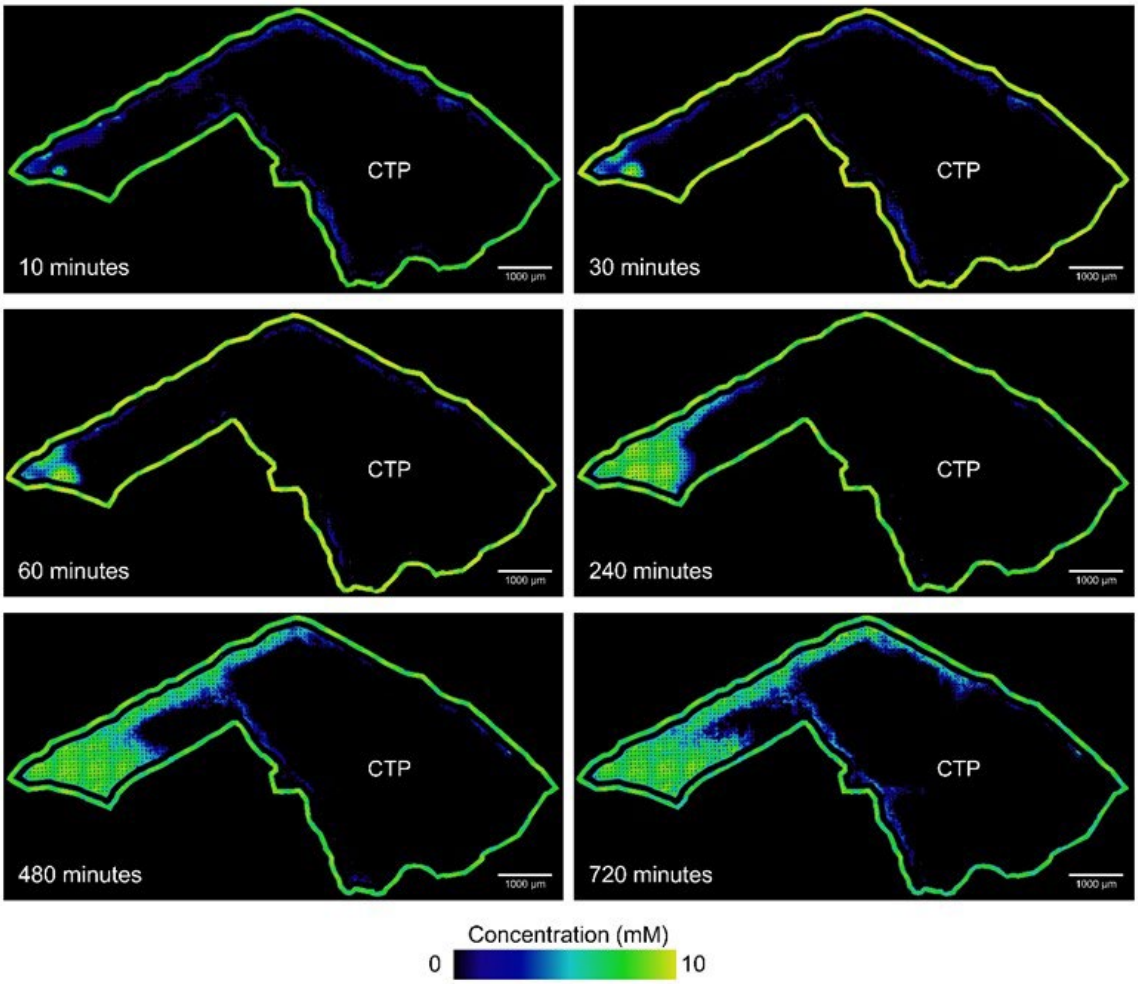

Figure 57: Temporal changes in 220 nm stealth liposome perfusion into the EPCaT-laden primary tumor chamber.

(CTP denotes central tumor port).

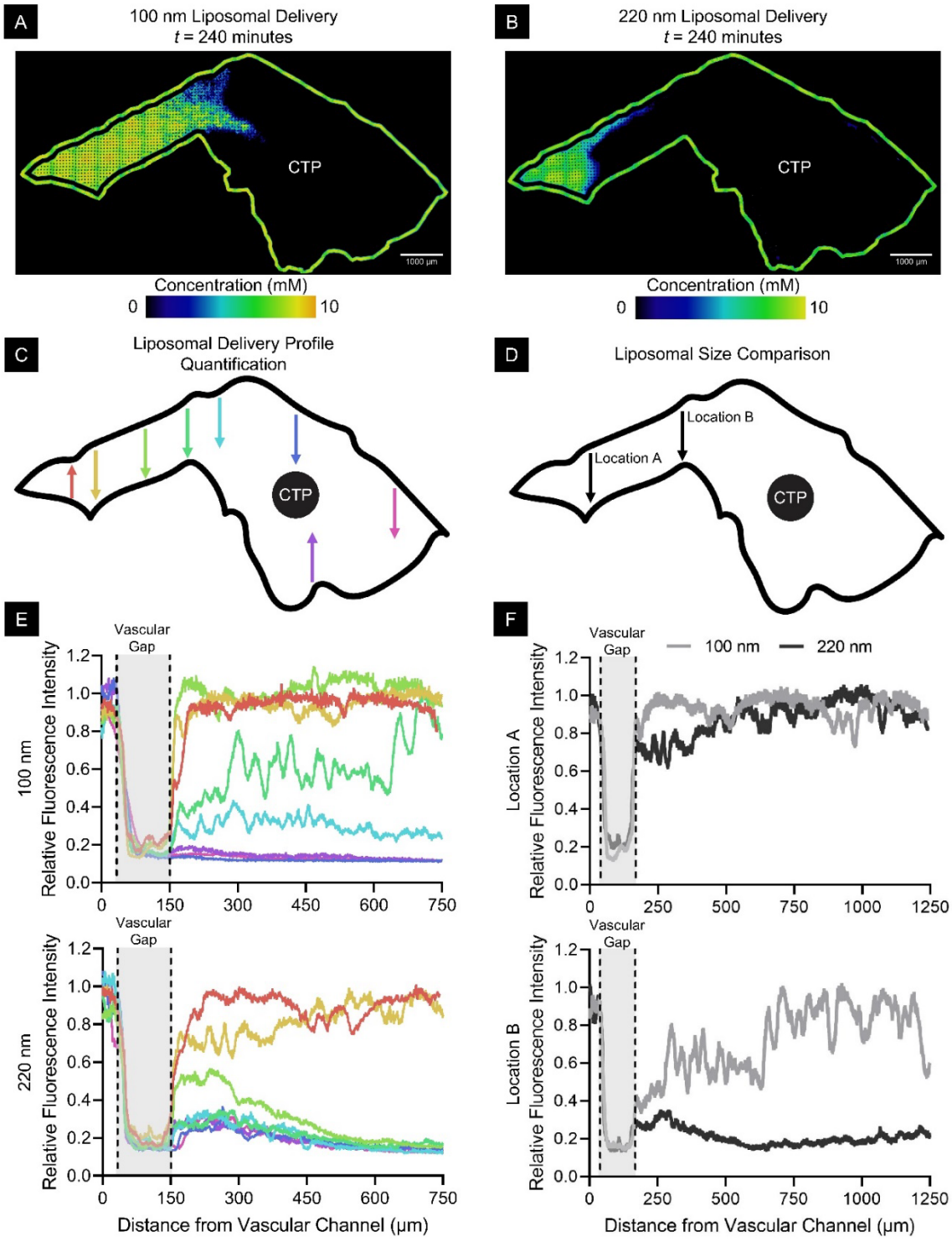

Figure 58: Stealth liposome delivery through the HUVEC endothelium to the EPCaT-laden PTC was limited, although some vascular geometry-dependent and liposome size-based differences in perfusion were detectable on-chip.

Figure 58 caption continued: A,B) 100 nm and 220 nm stealth liposome delivery heatmaps after 4 hours of perfusion. C) Liposomal delivery profile quantification map. D) Map illustrating selected PTC locations for direct 100 nm versus 220 nm delivery comparison. E) Liposomal delivery profiles at varying locations on-chip after 4 hours of perfusion. F) Direct liposome size comparison at two locations on-chip after 4 hours of perfusion (CTP denotes central tumor port).

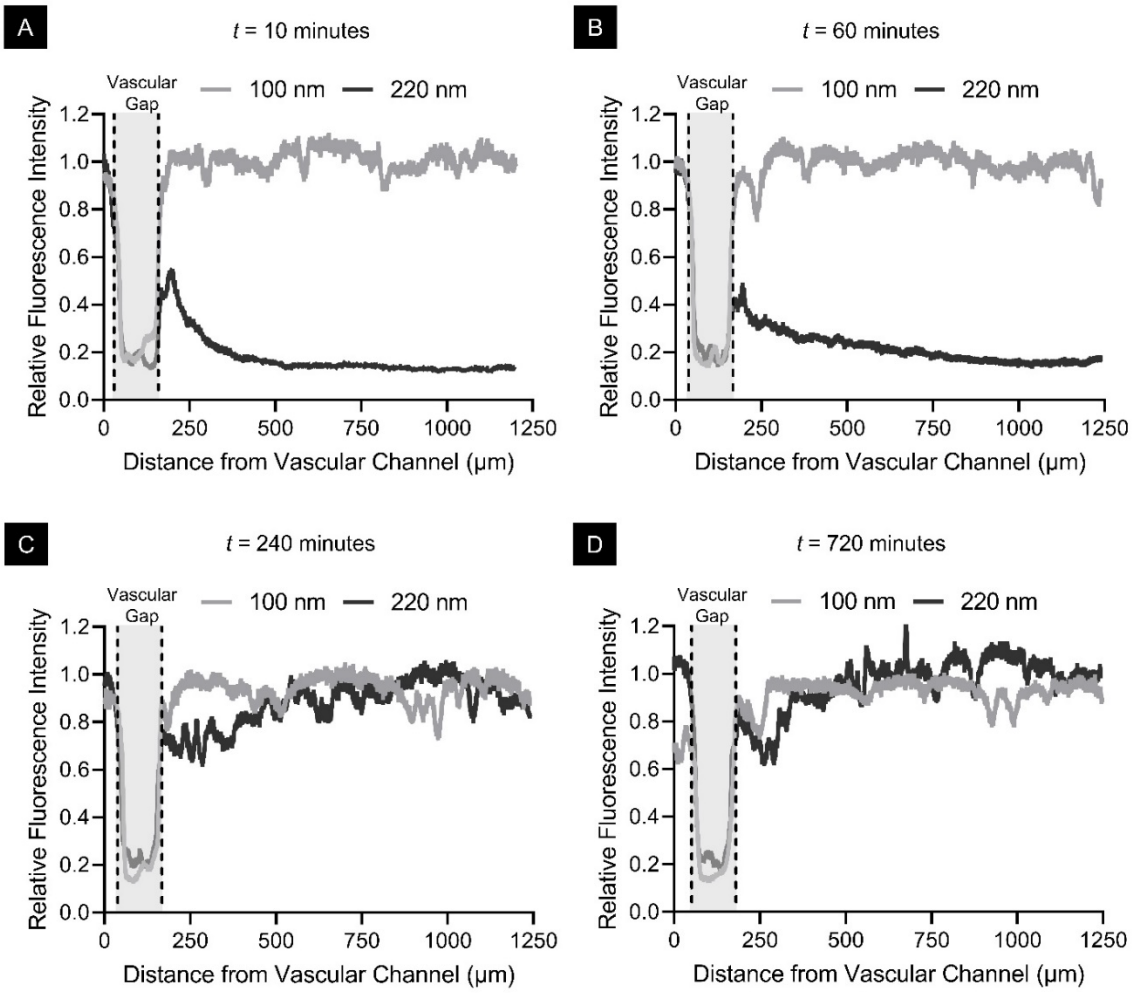

Figure 59: Temporal 100 nm versus 200 nm liposomal delivery profiles at Location A throughout twelve hours of perfusion.

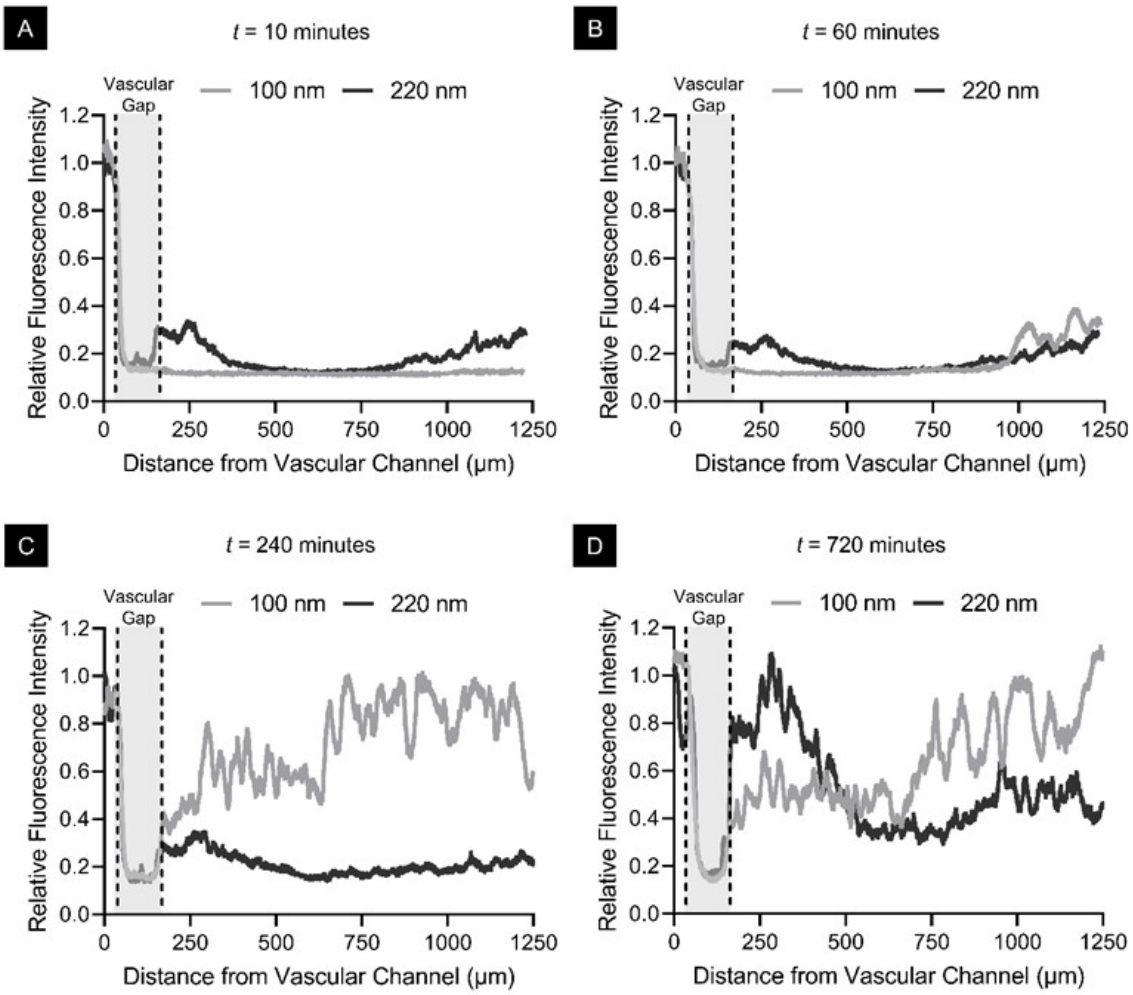

Figure 60: Temporal 100 nm versus 200 nm liposomal delivery profiles at Location B throughout twelve hours of perfusion.

driven differences in liposome distribution, but also verified very minimal perfusion throughout the majority of the chamber (Fig. 58A,B,C,E).

Liposomal delivery to the EPCaT appeared to be even more limited for the larger 220 nm sized liposomes. To directly compare size-based differences in perfusion profiles, two locations were selected within the primary tumor chamber: “Location A” at closest proximity to the inlet vasculature and “Location B” at moderate proximity to the inlet vasculature (Fig. 58D,F). Substantial differences in initial liposomal delivery at Location A

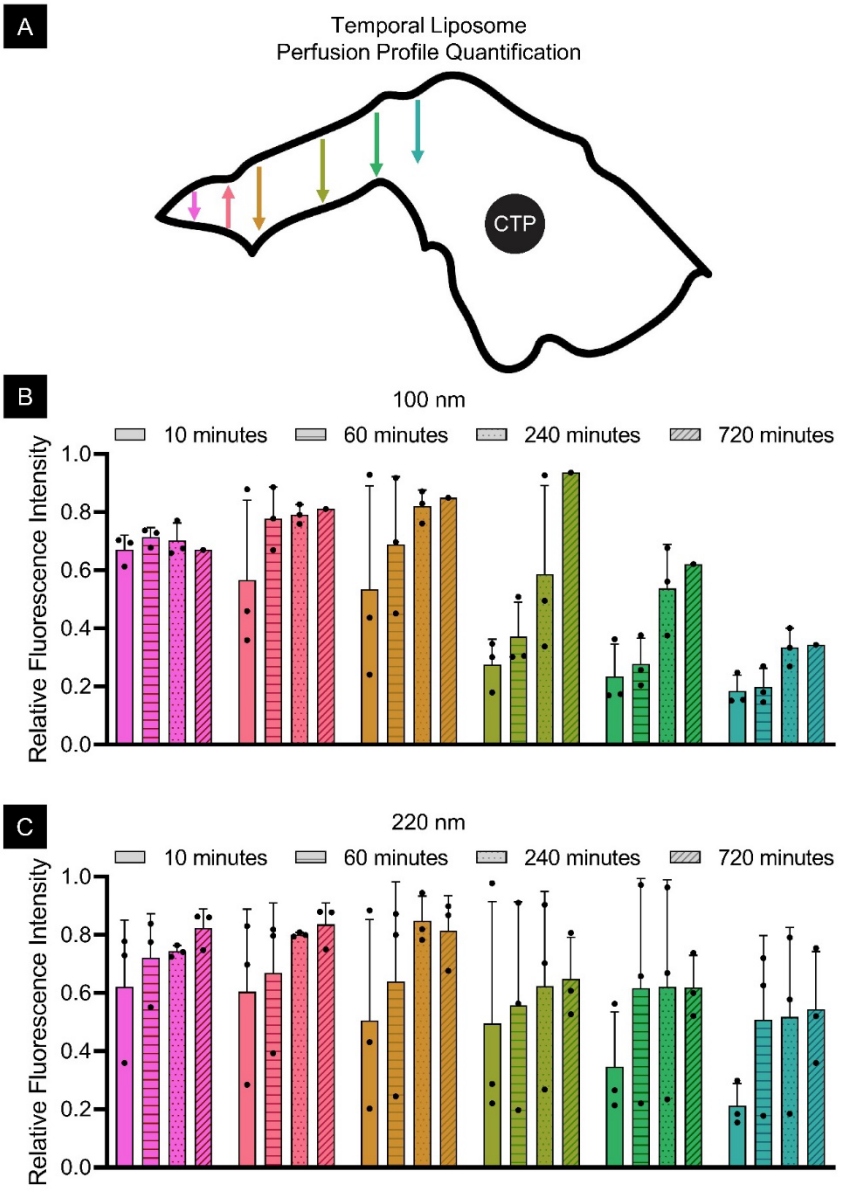

Figure 61: Chip-to-chip variability in temporal liposomal delivery at varying locations within the primary tumor chamber.

A) Liposome delivery profile quantification map. B) Temporal 100 nm stealth liposome delivery (n = 3 prostate tumor-on-a-chips for all time points except 720 minutes). C) Temporal 220 nm stealth liposome delivery (n = 3 prostate tumor-on-a-chips) (CTP denotes central tumor port, error bars indicate standard deviation).

were observed; whereas 100 nm liposomes completely perfused this region of the PTC after only 10 minutes, baseline 220 nm liposomal delivery was not observed until after approximately 240 minutes (Fig. 58F,59, baseline relative fluorescence intensity = one). Conversely, neither the 100 nm nor the 220 nm liposomes perfused Location B until approximately 240 minutes, at which point some delivery of 100 nm liposomes was detected (Fig. 58F,60). Complete liposomal delivery at Location B did not occur for either liposome configuration throughout 12 hours of perfusion (Fig. 59,60). Interestingly some chip-to-chip variability in liposomal delivery was noted at regions of the primary tumor chamber that are exposed to high vascular shear rates and were shown to be well-perfused by the TRITC-dextran probe molecule, particularly for the 220 nm liposomes (Fig. 61, n = 3 prostate tumor-on-a-chips).

4.4.5 *Prostate tumor-on-a-chip model identified size-based differences in SPION delivery and cellular uptake*

To further explore size-based differences in nanoparticle therapeutic delivery against the prostate tumor-on-a-chip model, now using a solid nanoparticle configuration, three sizes of PEGylated SPIONs (47.3±0.7 nm, 77.9±1.7 nm, and 112.3±1.3 nm) were selected and individually perfused through the microvascular network. Once again, recurrent fluorescent imaging, *post hoc* image processing, and quantification of relative fluorescence intensity (individually normalized to the inlet for each SPION size) were performed to generate heat maps and plot profiles illustrating SPION distribution within the primary tumor chamber. As expected, vascular geometry-dependent differences in perfusion were observed for all SPION sizes at initial time points (up to 30 minutes) in which regions of the PTC proximal to the inlet port experienced more rapid SPION

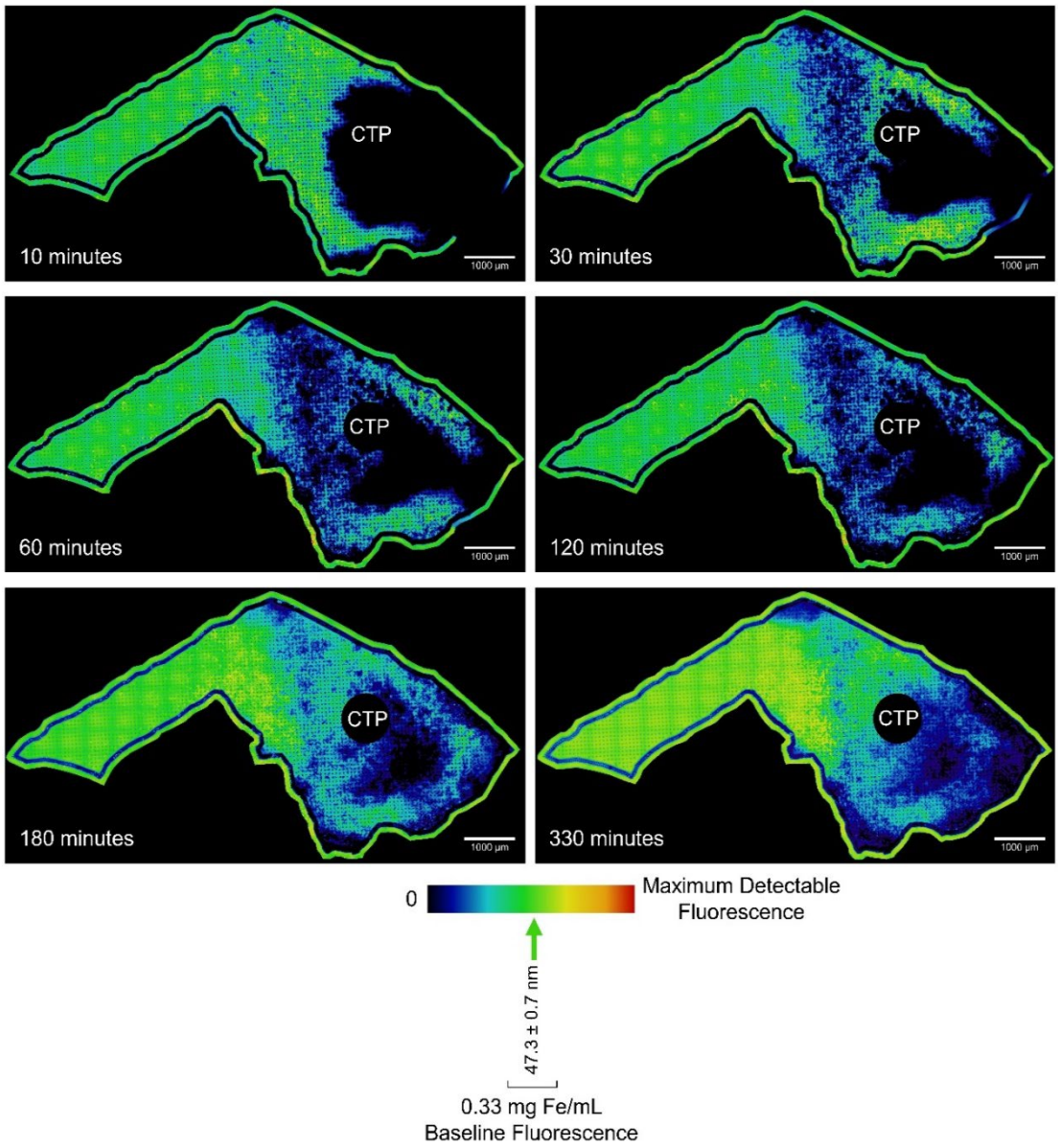

Figure 62: Temporal changes in 47.3±0.7 nm SPION perfusion into the EPCaT-laden primary tumor chamber.

(CTP denotes central tumor port).

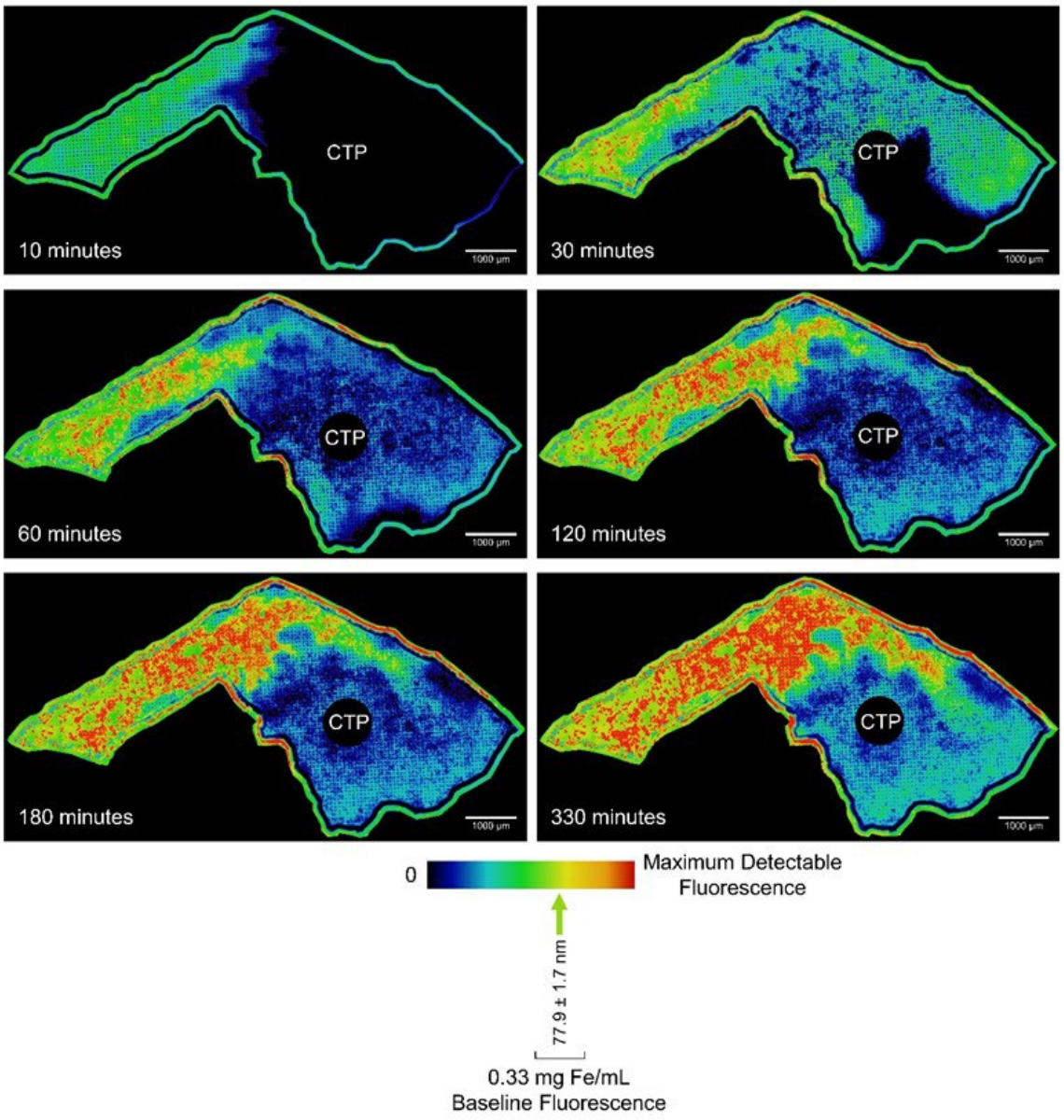

Figure 63: Temporal changes in 77.9±1.7 nm SPION perfusion into the EPCaT-laden primary tumor chamber.

(CTP denotes central tumor port).

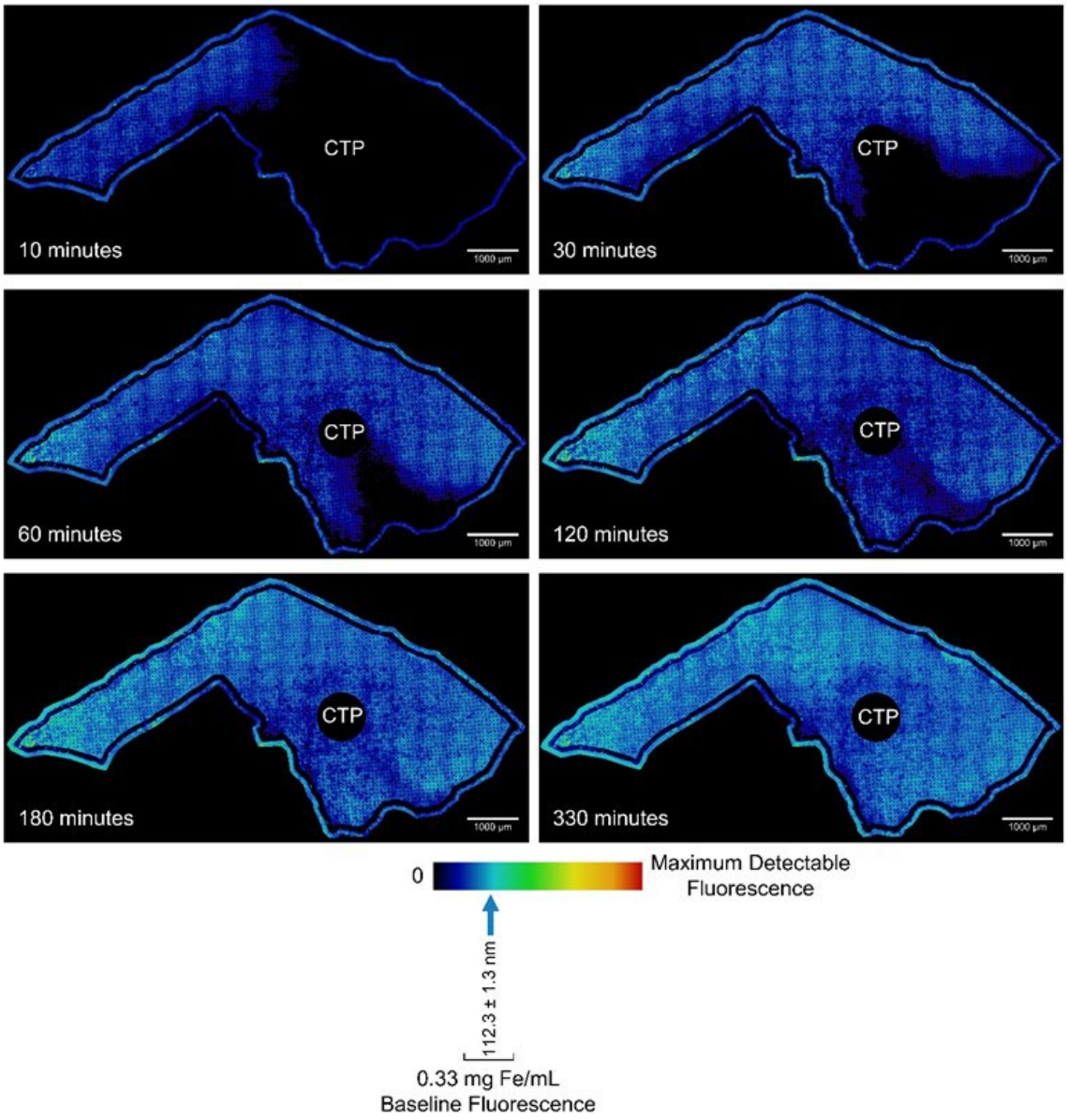

Figure 64: Temporal changes in 112.3±1.3 nm SPION perfusion into the EPCaT-laden primary tumor chamber.

(CTP denotes central tumor port).

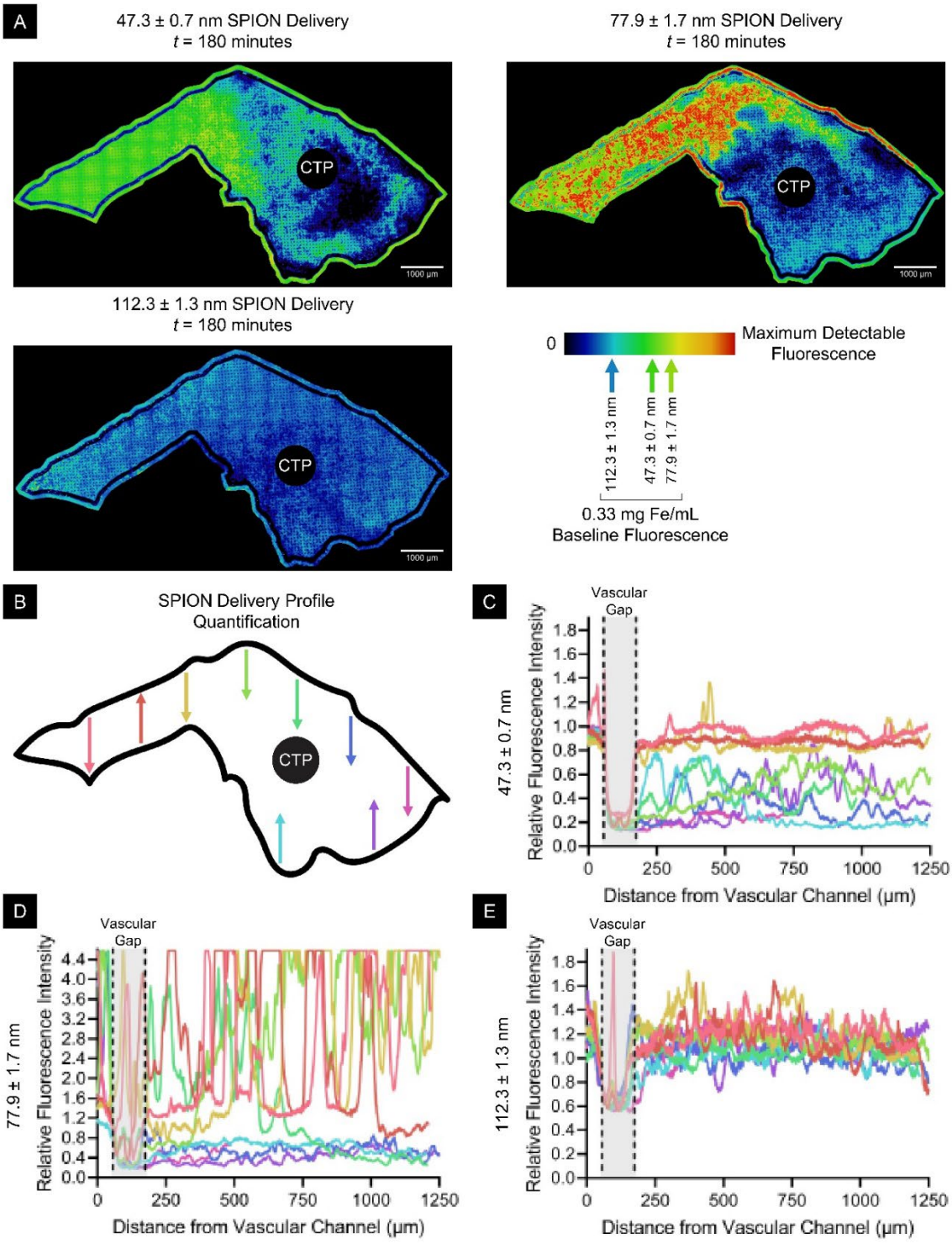

Figure 65: Vascular geometry-dependent differential SPION delivery to the EPCaT-laden primary tumor chamber was achieved on-chip.

Figure 65 caption continued: A) SPION delivery heatmaps after 3 hours of perfusion. B) SPION delivery profile quantification map. C) 47.3±0.7 nm SPION delivery profiles at varying locations on-chip after 3 hours of perfusion. D) 77.9±1.7 nm SPION delivery profiles at varying locations on-chip after 3 hours of perfusion. E) 112.3±1.3 nm SPION delivery profiles at varying locations on-chip after 3 hours of perfusion (CTP denotes central tumor port).

delivery than those distal or near the central tumor port (Figs. 62-65). Both 47.3±0.7 nm and 77.9±1.7 nm SPIONs continued to exhibit considerable temporal and spatial heterogeneity in nanoparticle distribution throughout 330 minutes of perfusion (Figs. 62,63,65); however, upon complete perfusion of the PTC at the 120-minute time point, the larger 112.3±1.3 nm SPIONs continued to exhibit very uniform nanoparticle distribution for the duration of the study (Fig. 64, 65E). Most notably, the 77.9±1.7 nm SPIONs presented punctate nanoparticle accumulation that met or exceeded the maximum detectable fluorescence of the microscope at time points as early as 30 minutes (Fig. 63, 65D). This continued throughout the duration of the study and interestingly, the incidence of accumulated fluorescence followed a similar pattern to the initial perfusion profile seen moving across the PTC, where regions proximal to the inlet port exhibited accumulation earlier than those distal. This translated to a significant temporal increase in the average fluorescence intensity at various locations on-chip, whereas the smallest and largest SPIONs demonstrated much more temporally uniform intensities (Fig. 66). It is also important to note that decreased chip-to-chip variability was observed in SPION delivery, as compared to liposomal delivery (Fig. 66).

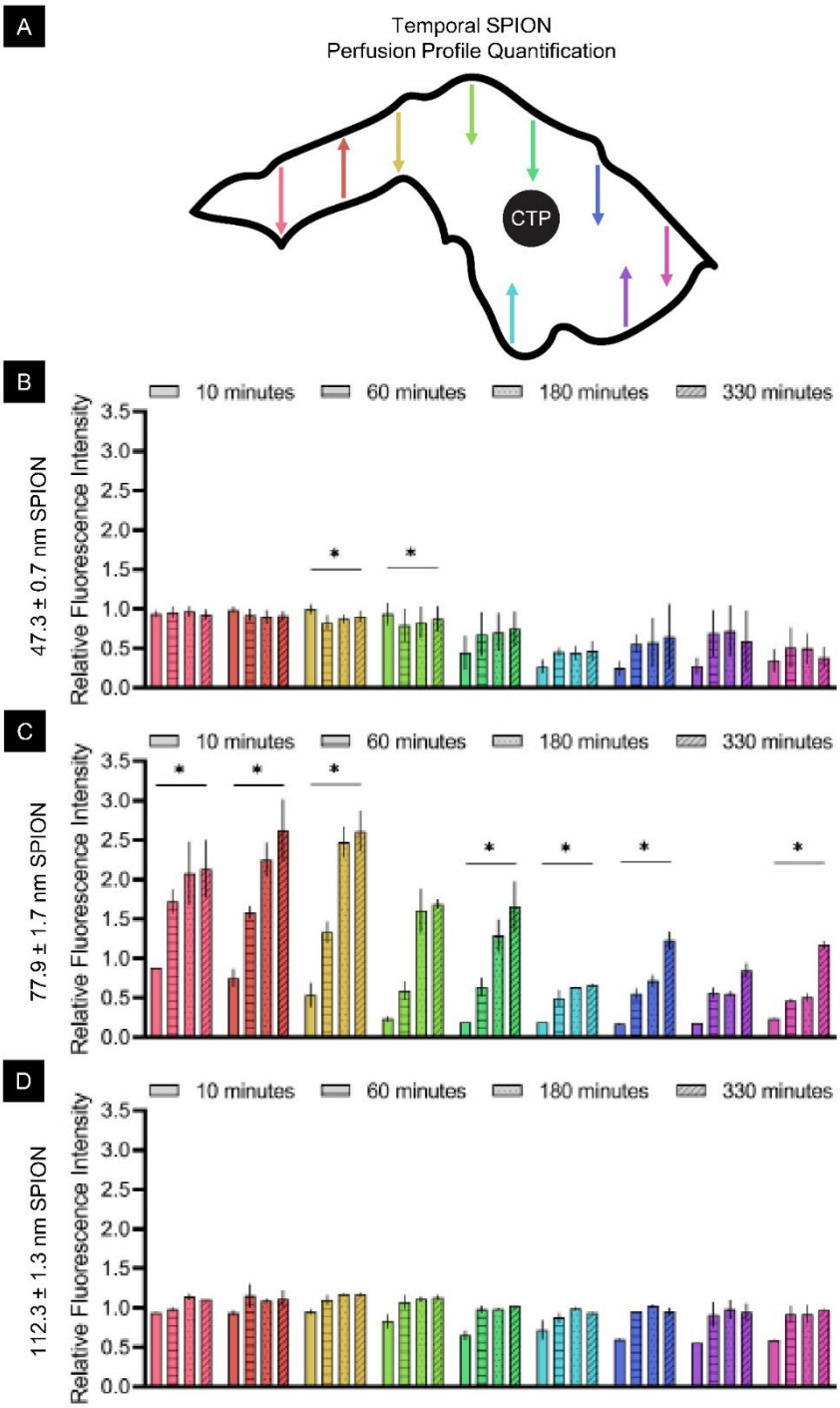

Figure 66: Significant changes in temporal SPION delivery at varying locations within the primary tumor chamber.

A) SPION delivery profile quantification map. B-D) Temporal SPION delivery (n = 2 prostate tumor-on-a-chips per size, CTP denotes central tumor port, error bars indicate range).

Increasingly distinct size-based differences in SPION delivery between each nanoparticle configuration tested were observed with increased perfusion time. To directly compare 47.3±0.7 nm versus 77.9±1.7 nm versus 112.3±1.3 nm SPIONs, two locations were selected within the primary tumor chamber: “Location A” at close proximity to the inlet vasculature and “Location B” at distal proximity to the inlet, but near the CTP (Fig. 67A). After 60 minutes of perfusion at Location A, the largest 112.3±1.3 nm and smallest 47.3±0.7 nm SPIONs exhibited very similar perfusion profiles; however, the medium-sized 77.9±1.7 nm SPIONs clearly began to illustrate accumulation, thus resulting in substantially higher relative fluorescence intensity across the PTC (Fig. 67C). This trend was also observed at the end time point of the study (Fig. 67C). Conversely, after 60 minutes at the more poorly perfused Location B, baseline delivery of the largest 112.3±1.3 nm SPIONs was observed (baseline relative fluorescence intensity = one), while very little delivery of the 47.3±0.7 nm or 77.9±1.7 nm had occurred (Fig. 67D). Interestingly, after 330 minutes of perfusion at Location B, delivery of the smallest 47.3±0.7 nm SPIONs remained nearly undetectable, preliminary accumulation of the medium 77.9±1.7 nm was evident, and baseline delivery of the largest 112.3±1.3 nm SPIONs remained unchanged from the early timepoints (Fig. 67D).

The significant accumulation of 77.9±1.7 nm SPIONs was fairly unexpected; however, when overlaying a phase contrast image of the primary tumor chamber taken prior to SPION perfusion with a fluorescent image of the ending SPION distribution, it is evident that accumulation is occurring at the location of prostate cancer cell colonies within the EPCaT, thus suggesting cell uptake (Fig. 67B). To begin to better understand this finding, the 77.9±1.7 nm SPION-perfused prostate tumor-on-a-chips were subjected to

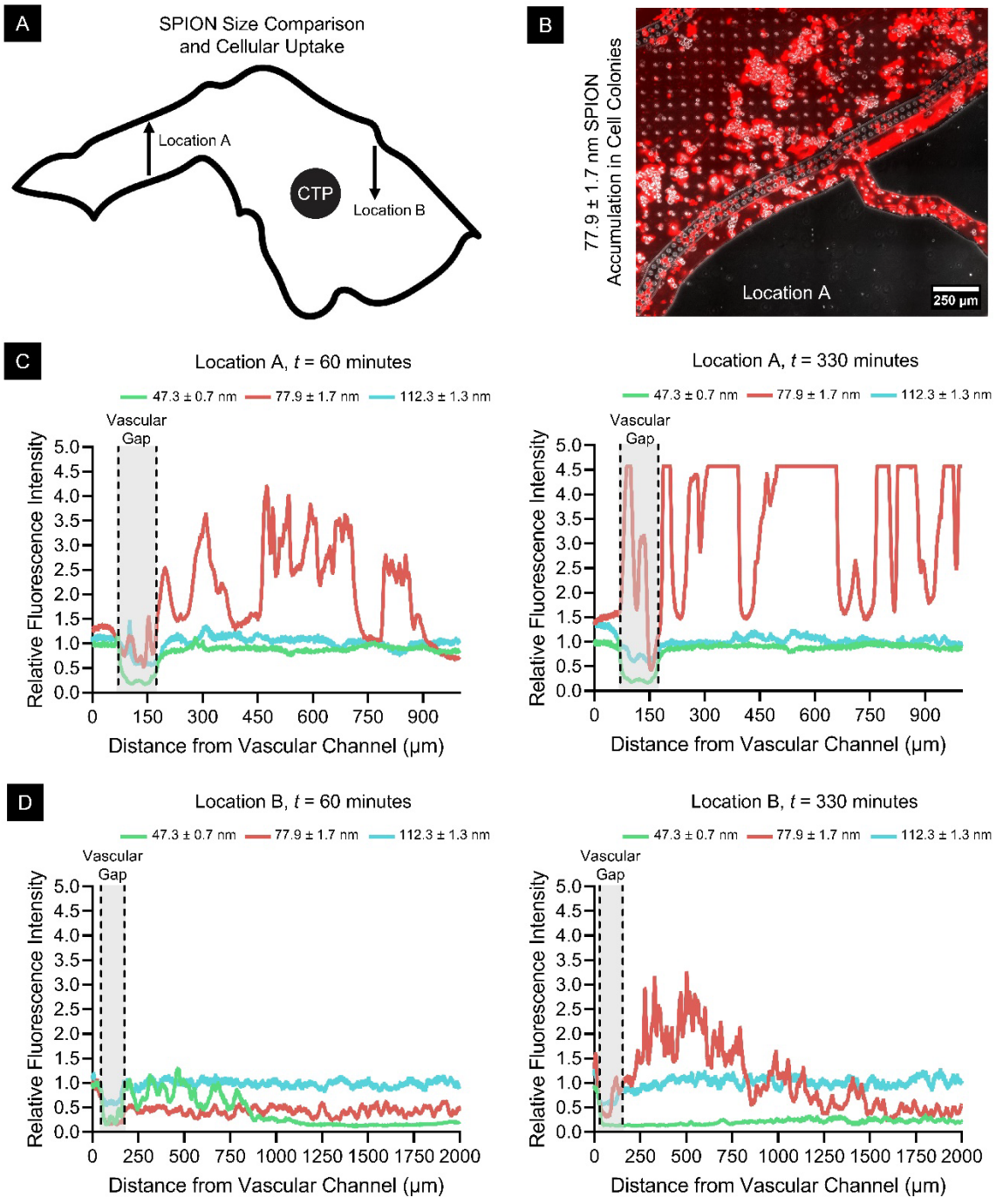

Figure 67: Significant size-based differences in SPION delivery and uptake were elucidated using the prostate tumor-on-a-chip platform.

Figure 67 caption continued: A) Map illustrating selected PTC locations for direct SPION delivery comparison. B) Overlay of phase contrast PTC image prior to 77.9±1.7 nm SPION perfusion and Cy5 fluorescent image post-perfusion. C) Direct comparison of SPION size-based delivery at Location A at two time points. D) Direct comparison of SPION size-based delivery at Location B at two time points (CTP denotes central tumor port).

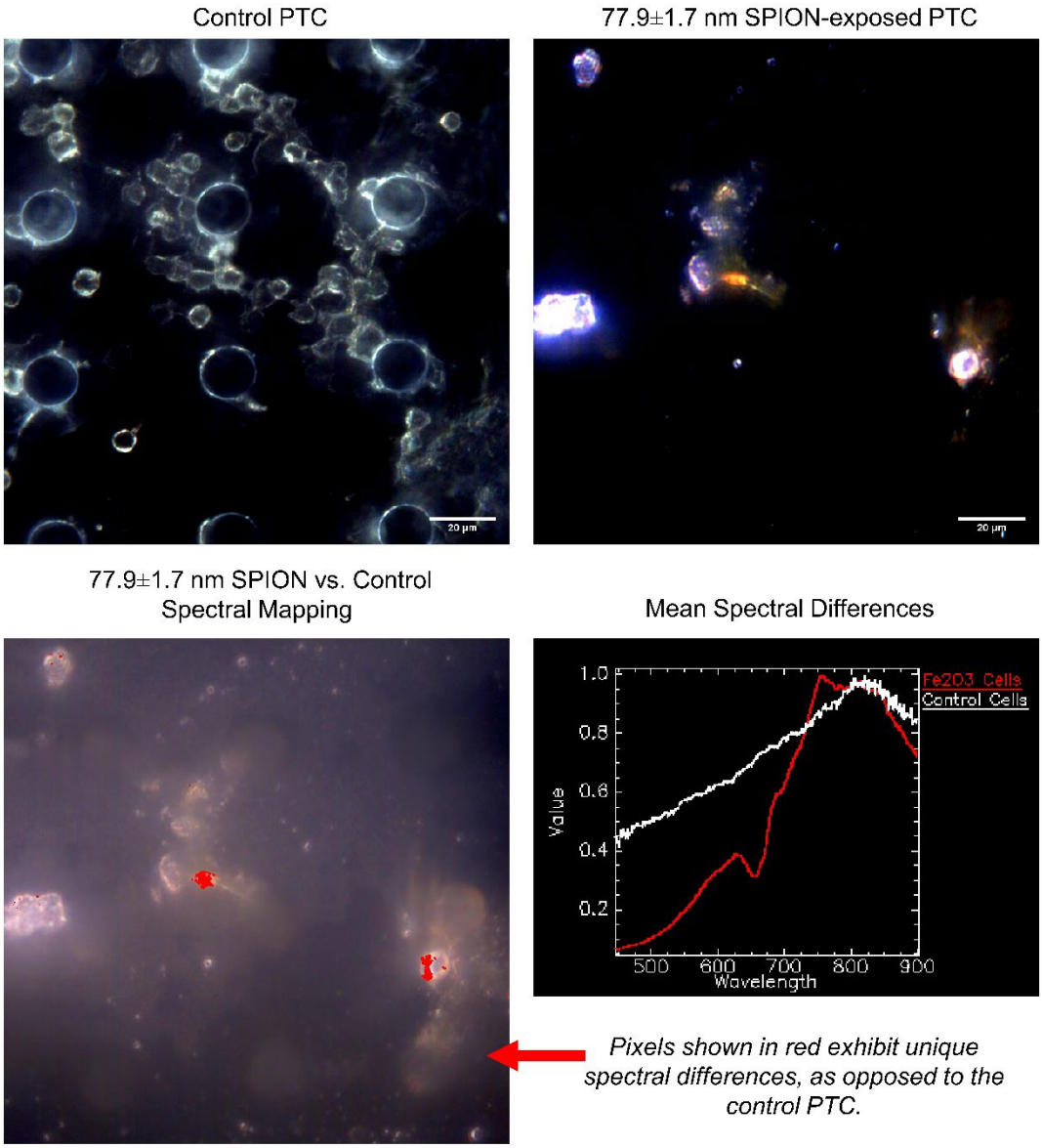

Figure 68: Enhanced darkfield hyperspectral microscopy confirmed cellular uptake of 77.9±1.7 nm SPIONs using the prostate tumor-on-a-chip microphysiological system.

EDHM, thereby evaluating spectral differences between control chips and chips exposed to the 77.9±1.7 nm SPIONs. Notably, spectral mapping revealed very high levels of iron oxide within multiple cells in the primary tumor chamber (Fig. 68); thereby confirming positive uptake of 77.9±1.7 nm SPIONs.

4.5 Discussion

As novel anti-cancer NDDs are rapidly developed to precisely target and treat tumors, it is imperative that paralleled advancements in pre-clinical therapeutic testing platforms are also made in order to facilitate and expedite rigorous translation to the clinic. Building upon the previously established 3D engineered prostate cancer tissue models (Habbit et al., 2022a, Habbit et al., 2022b), the microfluidic prostate tumor-on-a-chip introduced herein augments EPCaT pathophysiology by incorporating additional TME elements including 1) dynamic flow conditions within a tortuously-patterned endothelium, 2) opportunities for on-chip invasion and migration that require both intra- and extravasation, and 3) vascular geometry-dependent differential therapeutic delivery to the 3D engineered tumor tissue. Taken together, the results of this investigation serve to demonstrate the potential broad utility of the prostate tumor-on-a-chip platform for application in studying PCa tumorigenic progression and developing anti-cancer therapeutics and treatment strategies, all in a more patient disease-mimetic manner.

Under flow conditions, endothelial cells seeded within the prostate tumor-on-a-chip microvascular channels formed a complete, lumenized endothelium; concomitantly, PCa cells initially encapsulated within the primary tumor chamber began migration to the secondary and tertiary tumor chambers. This suggests the appropriate recapitulation of some endothelial-cancer-fibroblast cell-cell interactions observed in the native TME

(Sznurkowska and Aceto, 2022, Bonollo et al., 2020). Interestingly, fibroblasts were not observed in large numbers outside of the PTC throughout long-term *in vitro* flow culture; however, fibroblasts did appear to preferentially accumulate near the microvascular network. It is hypothesized that fibroblasts are aptly facilitating PCa cell intravasation and may be circulating alongside the cancer cells but are not proliferating at the "metastatic" sites.

The perfusion of a fluorescent probe molecule through the prostate tumor-on-a-chip microvascular network confirmed vascular-geometry and shear rate-dependent differential perfusion gradients into the EPCaT-laden PTC, similar to what is observed in tumors *in vivo* (Saggar et al., 2013). Moderate translation of this differential perfusion gradient into differential shear rate-dependent chemotherapeutic response was observed, although a statistically significant difference in post-doxorubicin exposure viability between high and low vascular shear-rate PTC regions was not found. This is likely due to slight chip-to-chip variability in EPCaT cell density and distribution at each location. Notably, the perfusion of both liposomal and SPION NDDs through the vascular network and into the EPCaT-laden PTC followed a similar pattern to the fluorescent probe molecule, albeit to different extents and at different timing, wherein those regions most proximal to the inlet port or exposed to high vascular shear rates were perfused sooner than those regions distal to the inlet and immediately surrounding the central tumor port.

Liposomal perfusion of the PTC EPCaT was severely limited in comparison to both the TRITC-dextran probe molecule and the SPION NDDs. After twelve hours of continuous perfusion, the majority of the PTC had experienced little to no liposome delivery, regardless of size; however, the 220 nm liposomes exhibited substantially less

overall perfusion than the 100 nm liposomes. It is important to restate here that most NDDs rely to some extent on the EPR effect of tumors for targeted delivery to diseased tissue; "leaky vasculature" pore sizes *in vivo* range from 100 nm to 780 nm, whereas intact cell-cell vascular junctions are < 6 nm (Drummond et al., 1999). Additionally, liposomal NDDs between 100 nm – 200 nm demonstrated substantially higher tumor delivery *in vivo* than liposomes smaller than 50 nm or larger than 300 nm (Zhang et al., 2021). As such, the limited liposomal delivery observed herein is not only indicative of a mostly intact, yet slightly compromised HUVEC endothelium, but also introduces the idea that the prostate tumor-on-a-chip model could be particularly useful in the development of combinatorial therapies employing vascular disrupting agents (VDAs) in tandem with liposomal or other NDDs to improve accumulation at tumor sites (Smolarczyk et al., 2021, Liu et al., 2018b).

Notably, significant size-based differences in SPION perfusion and uptake were observed using the prostate tumor-on-a-chip platform. It is important to note that the selected SPION sizes (47.3±0.7 nm, 77.9±1.7 nm, and 112.3±1.3 nm) span the reported optimal range for therapeutic applications; in general, nanoparticles less than 10 nm in size are removed via renal clearance, while those greater than approximately 200 nm in size cannot be internalized into cells via endocytic pathways and are instead consumed by phagocytic cells (Zhang et al., 2021, Sousa de Almeida et al., 2021). For SPIONs specifically, a range of approximately 10 nm – 100 nm is thought to be optimal for therapeutic applications (Wahajuddin and Arora, 2012). Interestingly, the smallest SPION size tested here consistently demonstrated vascular geometry-dependent differential delivery throughout the EPCaT-laden PTC, whereas the largest SPION size consistently demonstrated relatively uniform delivery. Most notably, the middle SPION size of

77.9±1.7 nm not only exhibited vascular geometry-dependent delivery, but also consistently underwent substantial cellular uptake, as confirmed by EDHM, in a similar pattern to the perfusion profile. While elucidating the mechanisms behind such drastic, size-driven differences in SPION perfusion outcomes on-chip requires a much deeper investigation that is outside the scope of this particular study, it is important to note that the microfluidic tumor-on-a-chip platform demonstrated a great degree of potential in identifying an optimal NDDs formulation.

While a number of microfluidic technologies exist for the detection of PCa (Sheng and Jia, 2022, Bernstein et al., 2021); only two very simplistic PCa chip models have been reported. In 2005, Farokhzad, et. al. developed a microfluidic device that is positioned over a previously cultured 2D layer of patterned PCa cells to investigate cell interaction with PEGylated poly(lactic acid) nanoparticles (Farokhzad et al., 2005). More recently, Bischel, et. al. reported a microfluidic coculture device in which osteoblasts are cultured on the side of a channel, coated with a layer of collagen, and overlayed with a small number of PCa cells to monitor invasion (Bischel et al., 2014). While each of the devices generated interesting and focused findings to answer a specific question asked in the investigation, they offer very little utility to other researchers or companies as a broad testing platform to investigate PCa progression or therapeutic efficacy. Therein lies a significant contribution of the prostate tumor-on-a-chip platform to the field of pre-clinical anti-PCa therapeutic development.

While the prostate tumor-on-a-chip model presents several distinct advantages over conventional 2D or 3D *in vitro* PCa models, as previously introduced, several limitations to the platform and gaps in characterization do exist. First, a trade-off for increasing the

pathophysiological complexity is increased variability between individual prostate tumor-on-a-chip replicates. This chip-to-chip variability was observable both in the temporal migration of prostate cancer cells to the secondary and tertiary tumor chambers, as well as in the average relative fluorescence intensity of NDDs at specific locations within the PTC. While the prostate tumor-on-a-chip formation process provides tight control over initial EPCaT cell density at the point of encapsulation, there is little to no control over the precise location of each cell or cell cluster at the point of photocrosslinking. Throughout long term *in vitro* flow culture, the encapsulated prostate cancer and fibroblast cells will proliferate, migrate, and colonize independently; as such, measurements taken at the exact same location (using landmark PDMS features of the microvascular network and tumor chamber designs) on three different chips will have slight inherent differences. For example, the plot profile quantification performed herein illustrating relative fluorescence intensity versus distance from the microvascular channels may vary between replicates due to variable positioning of cell colonies, migratory cells blocking the vasculature, etc. It is also important to note that as prostate cancer cells migrate on-chip and disrupt those endothelial cell junctions immediately surrounding the PTC, continuous flow conditions further dislocate the endothelium, particularly at areas of high vascular shear rate such as the top edge of the PTC; however, this cell-mediated vascular disruption is observed to occur at slightly different locations and to slightly different extents between tumor-on-a-chip replicates. Interestingly, this in turn results in the PTC-housed EPCaT experiencing an EPR-mimetic effect to different degrees, similar to the patient-to-patient intertumoral heterogeneity observed clinically (Wu, 2021, Janku, 2014). In future applications of the prostate tumor-on-a-chip model in disease progression or therapeutic development, this

phenomena could be desirable or undesirable depending upon the goals of the study; as such, careful experimental design choices must be made while considering chip-to-chip variability.

Another limitation of the prostate tumor-on-a-chip model is that migratory cells are confined to 2D growth within the secondary and tertiary tumor chambers as there is no biomaterial matrix present to support 3D growth. Furthermore, upon extravasation at or near the ancillary tumor chamber sites, migratory cells are not required to invade tissue or remodel ECM to initiate the "metastatic" site; this is not fully replicative of the post-extravasation microenvironment observed in tumors *in vivo* (Chen et al., 2013). As such, the terms "invasion" and "metastasis" used to describe the migration and movement of cancer and fibroblast cells on-chip are applied generously. Extending the prostate tumor-on-a-chip design to include additional biomaterial-laden tumor chambers at substantially more distal locations to the PTC would more appropriately warrant the use of such terminology.

Next, it is important to note that the vascular geometry-dependent therapeutic perfusion gradient throughout the EPCaT-laden PTC is also apparent when flowing other compounds through the microvascular network. Unfortunately, this renders complete immunohistochemical analysis of the full primary tumor chamber quite difficult as both immunolabeling and staining reagents experience similarly limited perfusion. A number of attempts have been made to overcome this limitation including reverse flow through the microvascular network, removal of the photocrosslinked central tumor port, and inserting a needle through the top PDMS layer of the PTC; however, none of these methods were completely successful. Lastly, whereas the prostate tumor-on-a-chip can be readily

analyzed through several microscopy techniques, cell retrieval and subsequent analysis is more difficult. Bulk tumor-on-a-chip cell populations can be washed out of the chip and collected, but it is not yet possible to preferentially retrieve only those cells that have migrated out of the primary tumor chamber. Efforts to enable this are ongoing.

Looking towards future applications of the prostate tumor-on-a-chip model, a strong advantage of this design remains the ease of fluidic interfacing with other organ-on-a-chip platforms. This would not only enable simultaneous investigation of anti-cancer therapeutic efficacy alongside organ-specific toxicity but would also introduce the opportunity to monitor organ-specific metastasis and subsequently decode the "seed and soil" relationships between circulating tumor cells and metastatic growth (Zhang et al., 2017, Liu et al., 2017).

4.6 Conclusions

Through the amalgamation of key attributes of prostate cancer pathophysiology, the prostate tumor-on-a-chip introduced in this chapter augments the previously established coculture EPCaT model by incorporating 1) dynamic flow conditions through an endothelialized, tortuous microvascular network design that was informed by vasculature patterns *in vivo*, 2) the opportunity to monitor for tumor cell type-dependent invasion of and metastasis to ancillary tumor regions, and 3) differential therapeutic and NDDs delivery to the 3D engineered prostate cancer tissue. Throughout long-term culture, fibroblasts were observed to preferentially assemble within the primary tumor chamber in close proximity to the microvascular channels; conversely, prostate cancer cells intravasated through the lumenized endothelial barrier and migrated on-chip to the secondary and tertiary tumor chamber regions. Vascular geometry-dependent differential

drug perfusion into the EPCaT-laden primary tumor chamber was illustrated first through the use of a fluorescent probe molecule and subsequently using both stealth liposomal and PEGylated SPION nano-sized drug delivery systems. Importantly, size-based differences in nanoparticle delivery to and cellular uptake within the primary tumor chamber were observed using both platforms, thereby indicating the ability of the prostate tumor-on-a-chip model to preferentially identify an optimal therapeutic configuration on an application-by-application basis. In total, this work represents a much-needed advancement in our pre-clinical therapeutic development toolkit and serves to demonstrate the potential utility of this model in future NDDs development efforts.

Summary and Future Directions

The bioinspired microphysiological systems introduced herein each build off of one another while aiming to recapitulate specific aspects of prostatic tumor pathophysiology. The 3D engineered prostate cancer tissue model was first introduced in Chapter 2 and originally featured a coculture of castration-resistant prostate cancer cells and fibroblasts within a PF biomaterial matrix. Following an in-depth characterization of the vast tissue stiffness range observed in tumors *in vivo*, the EPCaT PF matrix was modified via the addition of excess PEGDA in varying amounts to provide tunable biomechanical cues to the encapsulated cells. As anticipated, an increased matrix stiffness was associated with differential cell behavior and enrichment of tumorigenic gene sets; however, the inclusion of fibroblasts surprisingly resulted in severe cell-mediated matrix degradation throughout long-term culture, which was in stark contrast to the fibroblast-mediated stiffening observed in colorectal and breast cancer.

Digging deeper into this unexpected finding, Chapter 3 extends the engineered prostate cancer tissue model to elucidate the role of fibroblasts in multiple clinical stages of prostate cancer by incorporating varied cancer to stromal cell ratios. In general, direct prostate cancer-fibroblast coculture resulted in increased proliferative cell populations, significant remodeling of the PF matrix, and enrichment of tumorigenic hallmark gene sets. Importantly, the engineered prostate cancer tissues were also revealed to exhibit similar hallmark gene set enrichment to patient primary tumor samples, thereby suggesting some level of clinical relevancy.

Chapter 4 then incorporates the engineered prostate cancer tissue model into a microfluidic prostate tumor-on-a-chip platform and augments the pathophysiological

relevancy through the inclusion of additional tumor cell types, dynamic flow conditions, differential therapeutic exposure, and opportunities for “invasion” and “metastasis”. Notably, tumor cell type-dependent differences in cell migration and size-based differences in nanotherapeutic delivery and cellular uptake were observed using the prostate tumor-on-a-chip model.

In total, the findings delineated in this dissertation suggest that these microphysiological systems boast substantial potential for future applications in mechanistic disease progression studies and clinically translatable pharmacological testing. It is important to note, however, that several steps can be taken to improve the pathophysiological and clinical relevancy of these microphysiological systems, many of which are individually delineated in the discussion section of each chapter. One common route to improvement is the inclusion of more clinically relevant cell sources, particularly patient-derived prostate cancer-associated fibroblasts. Through an ongoing collaboration with the University of Texas MD Anderson Cancer Center, it is recommended that paired cancer-associated and benign fibroblasts be harvested from recurring and non-recurring patient tumors post-radical prostatectomy and subsequently incorporated into the engineered prostate cancer tissues in place of the normal fibroblast cell line used herein. Concurrent employment of single-cell transcriptomic analyses, alongside the experimental techniques included in this dissertation, would additionally afford more robust evaluation of the role of fibroblasts in driving prostate cancer progression, as well as the utility of these microphysiological systems in mechanistic disease progression studies.

References

ABAFFY, T., BAIN, J. R., MUEHLBAUER, M. J., SPASOJEVIC, I., LODHA, S., BRUGUERA, E., O'NEAL, S. K., KIM, S. Y. & MATSUNAMI, H. 2018. A Testosterone Metabolite 19-Hydroxyandrostenedione Induces Neuroendocrine Trans-Differentiation of Prostate Cancer Cells via an Ectopic Olfactory Receptor. *Frontiers in Oncology,* 8.

ÅKERFELT, M., BAYRAMOGLU, N., ROBINSON, S., TORISEVA, M., SCHUKOV, H.-P., HÄRMÄ, V., VIRTANEN, J., SORMUNEN, R., KAAKINEN, M., KANNALA, J., EKLUND, L., HEIKKILÄ, J. & NEES, M. 2015. Automated tracking of tumor-stroma morphology in microtissues identifies functional targets within the tumor microenvironment for therapeutic intervention. *Oncotarget,* 6**,** 30035-30056.

ALEMANY-RIBES, M. & SEMINO, C. E. 2014. Bioengineering 3D environments for cancer models. *Advanced Drug Delivery Reviews,* 79-80**,** 40-49.

ALKASALIAS, T., MOYANO-GALCERAN, L., ARSENIAN-HENRIKSSON, M. & LEHTI, K. 2018. Fibroblasts in the Tumor Microenvironment: Shield or Spear? *International journal of molecular sciences,* 19**,** 1532.

ALMANY, L. & SELIKTAR, D. 2005. Biosynthetic hydrogel scaffolds made from fibrinogen and polyethylene glycol for 3D cell cultures. *Biomaterials,* 26**,** 2467-2477.

ALONSO-NOCELO, M., RAIMONDO, T. M., VINING, K. H., LÓPEZ-LÓPEZ, R., DE LA FUENTE, M. & MOONEY, D. J. 2018. Matrix stiffness and tumor-associated macrophages modulate epithelial to mesenchymal transition of human adenocarcinoma cells. *Biofabrication,* 10**,** 035004.

AMERICAN CANCER SOCIETY. 2018. *Early History of Cancer* [Online]. Available: https://www.cancer.org/cancer/cancer-basics/history-of-cancer/what-is-cancer.html [Accessed April 25 2018].

ANBARASAN, T., WEI, C., BAMBER, J. C., BARR, R. G. & NABI, G. 2021. Characterisation of Prostate Lesions Using Transrectal Shear Wave Elastography (SWE) Ultrasound Imaging: A Systematic Review. *Cancers,* 13**,** 122.

ANBIAH, B., HASSANI, I., HABBIT, N., JASPER, L., RAMSAY, D., PRABHAKARPANDIAN, B., ARNOLD, R. & LIPKE, E. 2019. Abstract 999: In vivo breast tumor stiffness and vascular drug delivery recapitulated in a microfluidic tumor-on-a-chip. *Cancer Research,* 79**,** 999-999.

ASIF, P. J., LONGOBARDI, C., HAHNE, M. & MEDEMA, J. P. 2021. The Role of Cancer-Associated Fibroblasts in Cancer Invasion and Metastasis. *Cancers,* 13.

AW YONG, K. M., SUN, Y., MERAJVER, S. D. & FU, J. 2017. Mechanotransduction-Induced Reversible Phenotypic Switching in Prostate Cancer Cells. *Biophysical Journal,* 112**,** 1236-1245.

BACCELLI, I., SCHNEEWEISS, A., RIETHDORF, S., STENZINGER, A., SCHILLERT, A., VOGEL, V., KLEIN, C., SAINI, M., BÄUERLE, T., WALLWIENER, M., HOLLAND-LETZ, T., HÖFNER, T., SPRICK, M., SCHARPFF, M., MARMÉ, F., SINN, H. P., PANTEL, K., WEICHERT, W. & TRUMPP, A. 2013. Identification of a population of blood circulating tumor cells

from breast cancer patients that initiates metastasis in a xenograft assay. *Nature Biotechnology,* 31**,** 539.

BÄCKER, A., GÖPPERT, B., STURM, S., ABAFFY, P., SOLLICH, T. & GRUHL, F. J. 2016. Impact of adjustable cryogel properties on the performance of prostate cancer cells in 3D. *SpringerPlus,* 5**,** 902-902.

BAHMAD, H. F., JALLOUL, M., AZAR, J., MOUBARAK, M. M., SAMAD, T. A., MUKHERJI, D., AL-SAYEGH, M. & ABOU-KHEIR, W. 2021. Tumor Microenvironment in Prostate Cancer: Toward Identification of Novel Molecular Biomarkers for Diagnosis, Prognosis, and Therapy Development. *Frontiers in Genetics,* 12.

BALANI, S., NGUYEN, L. V. & EAVES, C. J. 2017. Modeling the process of human tumorigenesis. *Nature Communications,* 8**,** 15422.

BERNSTEIN, D. E., PIEDAD, J., HEMSWORTH, L., WEST, A., JOHNSTON, I. D., DIMOV, N., INAL, J. M. & VASDEV, N. 2021. Prostate cancer and microfluids. *Urologic Oncology: Seminars and Original Investigations,* 39**,** 455-470.

BIOTECHNOLOGY INNOVATION ORGANIZATION 2016. Clinical Development Success Rates 2006-2015. *BIO Industry Analysis.*

BISCHEL, L. L., CASAVANT, B. P., YOUNG, P. A., ELICEIRI, K. W., BASU, H. S. & BEEBE, D. J. 2014. A microfluidic coculture and multiphoton FAD analysis assay provides insight into the influence of the bone microenvironment on prostate cancer cells. *Integr Biol (Camb),* 6**,** 627-635.

BLOM, S., ERICKSON, A., ÖSTMAN, A., RANNIKKO, A., MIRTTI, T., KALLIONIEMI, O. & PELLINEN, T. 2019. Fibroblast as a critical stromal cell type determining prognosis in prostate cancer. *The Prostate,* 79**,** 1505-1513.

BONOLLO, F., THALMANN, G. N., KRUITHOF-DE JULIO, M. & KARKAMPOUNA, S. 2020. The Role of Cancer-Associated Fibroblasts in Prostate Cancer Tumorigenesis. *Cancers,* 12**,** 1887.

BOUFAIED, N., TAKHAR, M., NASH, C., ERHO, N., BISMAR, T. A., DAVICIONI, E. & THOMSON, A. A. 2019. Development of a predictive model for stromal content in prostate cancer samples to improve signature performance. *The Journal of pathology,* 249**,** 411-424.

BRANNEN, A., EGGERT, M., NAHRENDORF, M., ARNOLD, R. & PANIZZI, P. 2018. Correlation of 360-degree Surface Mapping In Vivo Bioluminescence with Multi-Spectral Optoacoustic Tomography in Human Xenograft Tumor Models. *Scientific Reports,* 8**,** 3321.

BRESLIN, S. & O'DRISCOLL, L. 2016. The relevance of using 3D cell cultures, in addition to 2D monolayer cultures, when evaluating breast cancer drug sensitivity and resistance. *Oncotarget,* 7**,** 45745-45756.

BUDCZIES, J., VON WINTERFELD, M., KLAUSCHEN, F., BOCKMAYR, M., LENNERZ, J. K., DENKERT, C., WOLF, T., WARTH, A., DIETEL, M., ANAGNOSTOPOULOS, I., WEICHERT, W., WITTSCHIEBER, D. & STENZINGER, A. 2015. The landscape of metastatic progression patterns across major human cancers. *Oncotarget,* 6**,** 570-583.

BURRELL, R. A., MCGRANAHAN, N., BARTEK, J. & SWANTON, C. 2013. The causes and consequences of genetic heterogeneity in cancer evolution. *Nature,* 501**,** 338.

CAIRNS, R., PAPANDREOU, I. & DENKO, N. 2006. Overcoming physiologic barriers to cancer treatment by molecularly targeting the tumor microenvironment. *Mol Cancer Res,* 4**,** 61-70.

CALIARI, S. R. & BURDICK, J. A. 2016. A Practical Guide to Hydrogels for Cell Culture. *Nature methods,* 13**,** 405-414.

CAVO, M., FATO, M., PEÑUELA, L., BELTRAME, F., RAITERI, R. & SCAGLIONE, S. 2016. Microenvironment complexity and matrix stiffness regulate breast cancer cell activity in a 3D in vitro model. *Scientific Reports,* 6**,** 35367.

CHAU, Y., LUO, Y., CHEUNG, A. C. Y., NAGAI, Y., ZHANG, S., KOBLER, J. B., ZEITELS, S. M. & LANGER, R. 2008. Incorporation of a matrix metalloproteinase-sensitive substrate into self-assembling peptides – A model for biofunctional scaffolds. *Biomaterials,* 29**,** 1713-1719.

CHAUHAN, V. P., STYLIANOPOULOS, T., BOUCHER, Y. & JAIN, R. K. 2011. Delivery of Molecular and Nanoscale Medicine to Tumors: Transport Barriers and Strategies. *Annual Review of Chemical and Biomolecular Engineering,* 2**,** 281-298.

CHEN, M. B., WHISLER, J. A., JEON, J. S. & KAMM, R. D. 2013. Mechanisms of tumor cell extravasation in an in vitro microvascular network platform. *Integr Biol (Camb),* 5**,** 1262-71.

CHEUNG, P. F. Y., YIP, C. W., NG, L. W. C., LO, K. W., CHOW, C., CHAN, K. F., CHEUNG, T. T. & CHEUNG, S. T. 2016. Comprehensive characterization of the patient-derived xenograft and the paralleled primary hepatocellular carcinoma cell line. *Cancer Cell International,* 16**,** 41.

CHIM, L. K. & MIKOS, A. G. 2018. Biomechanical forces in tissue engineered tumor models. *Current opinion in biomedical engineering,* 6**,** 42-50.

CHOI, S. Y. C., LIN, D., GOUT, P. W., COLLINS, C. C., XU, Y. & WANG, Y. 2014. Lessons from patient-derived xenografts for better in vitro modeling of human cancer. *Advanced Drug Delivery Reviews,* 79-80**,** 222-237.

CHWALEK, K., TSURKAN, M. V., FREUDENBERG, U. & WERNER, C. 2014. Glycosaminoglycan-based hydrogels to modulate heterocellular communication in in vitro angiogenesis models. *Scientific Reports,* 4**,** 4414.

COLAPRICO, A., SILVA, T. C., OLSEN, C., GAROFANO, L., CAVA, C., GAROLINI, D., SABEDOT, T. S., MALTA, T. M., PAGNOTTA, S. M., CASTIGLIONI, I., CECCARELLI, M., BONTEMPI, G. & NOUSHMEHR, H. 2015. TCGAbiolinks: an R/Bioconductor package for integrative analysis of TCGA data. *Nucleic Acids Research,* 44**,** e71-e71.

CORREAS, J.-M., TISSIER, A.-M., KHAIROUNE, A., VASSILIU, V., MÉJEAN, A., HÉLÉNON, O., MEMO, R. & BARR, R. G. 2014. Prostate Cancer: Diagnostic Performance of Real-time Shear-Wave Elastography. *Radiology,* 275**,** 280-289.

CORREAS, J. M., TISSIER, A. M., KHAIROUNE, A., KHOURY, G., EISS, D. & HÉLÉNON, O. 2013. Ultrasound elastography of the prostate: State of the art. *Diagnostic and Interventional Imaging,* 94**,** 551-560.

DAMHOFER, H., EBBING, E. A., STEINS, A., WELLING, L., TOL, J. A., KRISHNADATH, K. K., VAN LEUSDEN, T., VAN DE VIJVER, M. J., BESSELINK, M. G., BUSCH, O. R., HENEGOUWEN, M. I. V. B., VAN DELDEN, O., MEIJER, S. L., DIJK, F., MEDEMA, J. P., VAN LAARHOVEN, H. W. & BIJLSMA, M. F. 2015. Establishment of patient-derived xenograft models

and cell lines for malignancies of the upper gastrointestinal tract. *Journal of Translational Medicine,* 13**,** 115.

DANIEL, V. C., MARCHIONNI, L., HIERMAN, J. S., RHODES, J. T., DEVEREUX, W. L., RUDIN, C. M., YUNG, R., PARMIGIANI, G., DORSCH, M., PEACOCK, C. D. & WATKINS, D. N. 2009. A primary xenograft model of small-cell lung cancer reveals irreversible changes in gene expression imposed by culture in vitro. *Cancer Res,* 69**,** 3364-73.

DAS, V., BRUZZESE, F., KONEČNÝ, P., IANNELLI, F., BUDILLON, A. & HAJDÚCH, M. 2015. Pathophysiologically relevant in vitro tumor models for drug screening. *Drug Discovery Today,* 20**,** 848-855.

DELONG, S. A., MOON, J. J. & WEST, J. L. 2005. Covalently immobilized gradients of bFGF on hydrogel scaffolds for directed cell migration. *Biomaterials,* 26**,** 3227-34.

DENAYER, T., STÖHR, T. & VAN ROY, M. 2014. Animal models in translational medicine: Validation and prediction. *New Horizons in Translational Medicine,* 2**,** 5-11.

DEVILLE, S. S. & CORDES, N. 2019. The Extracellular, Cellular, and Nuclear Stiffness, a Trinity in the Cancer Resistome—A Review. *Frontiers in Oncology,* 9.

DIKOVSKY, D., BIANCO-PELED, H. & SELIKTAR, D. 2006. The effect of structural alterations of PEG-fibrinogen hydrogel scaffolds on 3-D cellular morphology and cellular migration. *Biomaterials,* 27**,** 1496-1506.

DINGLI, D., CHALUB, F. A. C. C., SANTOS, F. C., VAN SEGBROECK, S. & PACHECO, J. M. 2009. Cancer phenotype as the outcome of an evolutionary game between normal and malignant cells. *British Journal of Cancer,* 101**,** 1130-1136.

DRUMMOND, D. C., MEYER, O., HONG, K., KIRPOTIN, D. B. & PAPAHADJOPOULOS, D. 1999. Optimizing Liposomes for Delivery of Chemotherapeutic Agents to Solid Tumors. *Pharmacological Reviews,* 51**,** 691.

DUVAL, K., GROVER, H., HAN, L.-H., MOU, Y., PEGORARO, A. F., FREDBERG, J. & CHEN, Z. 2017. Modeling Physiological Events in 2D vs. 3D Cell Culture. *Physiology,* 32**,** 266-277.

EDER, T., WEBER, A., NEUWIRT, H., GRÜNBACHER, G., PLONER, C., KLOCKER, H., SAMPSON, N. & EDER, I. E. 2016. Cancer-Associated Fibroblasts Modify the Response of Prostate Cancer Cells to Androgen and Anti-Androgens in Three-Dimensional Spheroid Culture. *International journal of molecular sciences,* 17**,** 1458.

EMON, B., BAUER, J., JAIN, Y., JUNG, B. & SAIF, T. 2018. Biophysics of Tumor Microenvironment and Cancer Metastasis - A Mini Review. *Computational and Structural Biotechnology Journal,* 16**,** 279-287.

FAROKHZAD, O. C., KHADEMHOSSEINI, A., JON, S., HERMMANN, A., CHENG, J., CHIN, C., KISELYUK, A., TEPLY, B., ENG, G. & LANGER, R. 2005. Microfluidic System for Studying the Interaction of Nanoparticles and Microparticles with Cells. *Analytical Chemistry,* 77**,** 5453-5459.

FISHER, S. A., ANANDAKUMARAN, P. N., OWEN, S. C. & SHOICHET, M. S. 2015. Tuning the Microenvironment: Click-Crosslinked Hyaluronic Acid-Based Hydrogels Provide a Platform for Studying Breast Cancer Cell Invasion. *Advanced Functional Materials,* 25**,** 7163-7172.

GILL, B. J. & WEST, J. L. 2014. Modeling the tumor extracellular matrix: Tissue engineering tools repurposed towards new frontiers in cancer biology. *Journal of Biomechanics,* 47**,** 1969-1978.

GILLET, J.-P., VARMA, S. & GOTTESMAN, M. M. 2013. The Clinical Relevance of Cancer Cell Lines. *JNCI Journal of the National Cancer Institute,* 105**,** 452-458.

GKRETSI, V. & STYLIANOPOULOS, T. 2018. Cell Adhesion and Matrix Stiffness: Coordinating Cancer Cell Invasion and Metastasis. *Frontiers in Oncology,* 8.

GURSKI, L. A., XU, X., LABRADA, L. N., NGUYEN, N. T., XIAO, L., VAN GOLEN, K. L., JIA, X. & FARACH-CARSON, M. C. 2012. Hyaluronan (HA) interacting proteins RHAMM and hyaluronidase impact prostate cancer cell behavior and invadopodia formation in 3D HA-based hydrogels. *PLoS One,* 7**,** e50075.

HABBIT, N. L. 2018. *Tissue Engineered Cancer Models for in vitro Recapitulation of the Native Tumor Microenvironment.* Master of Science Auburn University

HABBIT, N. L., ANBIAH, B., ANDERSON, L., SURESH, J., HASSANI, I., EGGERT, M., BRANNEN, A., DAVIS, J., TIAN, Y., PRABHAKARPANDIAN, B., PANIZZI, P., ARNOLD, R. D. & LIPKE, E. A. 2022a. Tunable three-dimensional engineered prostate cancer tissues for in vitro recapitulation of heterogeneous in vivo prostate tumor stiffness. *Acta Biomaterialia*.

HABBIT, N. L., ANBIAH, B., SURESH, J., TIAN, Y., ANDERSON, L. S., DAVIES, M. L., HASSANI, I., GHOSH, T. M., PRABHAKARPANDIAN, B., ARNOLD, R. D. & LIPKE, E. A. 2022b. Abstract 3856: Elucidating the role of fibroblasts in CRPC and ADPC progression using 3D engineered prostate cancer tissues. *Cancer Research,* 82**,** 3856-3856.

HANAHAN, D. & WEINBERG, R. A. 2000. The Hallmarks of Cancer. *Cell,* 100**,** 57-70.

HANAHAN, D. & WEINBERG, ROBERT A. 2011. Hallmarks of Cancer: The Next Generation. *Cell,* 144**,** 646-674.

HANDORF, A. M., ZHOU, Y., HALANSKI, M. A. & LI, W.-J. 2015. Tissue Stiffness Dictates Development, Homeostasis, and Disease Progression. *Organogenesis,* 11**,** 1-15.

HASSANI, I., ANBIAH, B., KUHLERS, P. C., HABBIT, N. L., AHMED, B., HESLIN, M. J., MOBLEY, J. A., GREENE, M. W. & LIPKE, E. 2022. Engineered colorectal cancer tissue recapitulates key attributes of a patient-derived xenograft tumor line. *Biofabrication*.

HE, H., LIU, L., MORIN, E. E., LIU, M. & SCHWENDEMAN, A. 2019. Survey of Clinical Translation of Cancer Nanomedicines-Lessons Learned from Successes and Failures. *Acc Chem Res,* 52**,** 2445-2461.

HEBERLE, H., MEIRELLES, G. V., DA SILVA, F. R., TELLES, G. P. & MINGHIM, R. 2015. InteractiVenn: a web-based tool for the analysis of sets through Venn diagrams. *BMC Bioinformatics,* 16**,** 169.

HEERBOTH, S., HOUSMAN, G., LEARY, M., LONGACRE, M., BYLER, S., LAPINSKA, K., WILLBANKS, A. & SARKAR, S. 2015. EMT and tumor metastasis. *Clinical and Translational Medicine,* 4**,** 6.

HOYT, K., CASTANEDA, B., ZHANG, M., NIGWEKAR, P., DI SANT'AGNESE, P. A., JOSEPH, J. V., STRANG, J., RUBENS, D. J. & PARKER, K. J. 2008. Tissue elasticity properties as biomarkers for prostate cancer. *Cancer biomarkers : section A of Disease markers,* 4**,** 213-225.

IACOPINO, F., ANGELUCCI, C. & SICA, G. 2012. Interactions between normal human fibroblasts and human prostate cancer cells in a co-culture system. *Anticancer Res,* 32**,** 1579-88.

IMAMURA, Y., MUKOHARA, T., SHIMONO, Y., FUNAKOSHI, Y., CHAYAHARA, N., TOYODA, M., KIYOTA, N., TAKAO, S., KONO, S., NAKATSURA, T. & MINAMI, H. 2015. Comparison of 2D- and 3D-culture models as drug-testing platforms in breast cancer. *Oncol Rep,* 33**,** 1837-43.

INTERNATIONAL AGENCY FOR RESEARCH ON CANCER 2014. World Cancer Report. *In:* BERNARD W. STEWART, C. P. W. (ed.). World Health Organization

IPPOLITO, L., MORANDI, A., TADDEI, M. L., PARRI, M., COMITO, G., ISCARO, A., RASPOLLINI, M. R., MAGHERINI, F., RAPIZZI, E., MASQUELIER, J., MUCCIOLI, G. G., SONVEAUX, P., CHIARUGI, P. & GIANNONI, E. 2019. Cancer-associated fibroblasts promote prostate cancer malignancy via metabolic rewiring and mitochondrial transfer. *Oncogene,* 38**,** 5339-5355.

ISHII, K., NAKAGAWA, Y., MATSUDA, C., KATOH, D., ICHISHI, M., SHIRAI, T., HIROKAWA, Y., FUJIWARA, M., SUGIMURA, Y. & WATANABE, M. 2021. Heterogeneous induction of an invasive phenotype in prostate cancer cells by coculturing with patient-derived fibroblasts. *Journal of Cellular Biochemistry,* 122**,** 679-688.

JABBARI, E., SARVESTANI, S. K., DANESHIAN, L. & MOEINZADEH, S. 2015. Optimum 3D Matrix Stiffness for Maintenance of Cancer Stem Cells Is Dependent on Tissue Origin of Cancer Cells. *PLOS ONE,* 10**,** e0132377.

JANG, J., RATH, O., SCHUELER, J., SUNG, H. H., JEON, H. G., JEONG, B. C., SEO, S. I., JEON, S. S., LEE, H. M., CHOI, H.-Y., KWON, G.-Y., PARK, W. Y., LEE, J. & PARK, S. H. 2017. Development of Novel Patient-Derived Preclinical Models from Malignant Effusions in Patients with Tyrosine Kinase Inhibitor–Resistant Clear Cell Renal Cell Carcinoma. *Translational Oncology,* 10**,** 304-310.

JANKU, F. 2014. Tumor heterogeneity in the clinic: is it a real problem? *Ther Adv Med Oncol,* 6**,** 43-51.

JHA, K. K., BANGA, S., PALEJWALA, V. & OZER, H. L. 1998. SV40-Mediated Immortalization. *Experimental Cell Research,* 245**,** 1-7.

JI, Y., RUAN, L., REN, W., DUN, G., LIU, J., ZHANG, Y. & WAN, Q. 2019. Stiffness of prostate gland measured by transrectal real-time shear wave elastography for detection of prostate cancer: a feasibility study. *The British journal of radiology,* 92**,** 20180970-20180970.

JUNTTILA, M. R. & DE SAUVAGE, F. J. 2013. Influence of tumour micro-environment heterogeneity on therapeutic response. *Nature,* 501**,** 346.

JUSTUS, C. R., DONG, L. & YANG, L. V. 2013. Acidic tumor microenvironment and pH-sensing G protein-coupled receptors. *Front Physiol,* 4**,** 354.

KALLI, M. & STYLIANOPOULOS, T. 2018. Defining the Role of Solid Stress and Matrix Stiffness in Cancer Cell Proliferation and Metastasis. *Front Oncol,* 8**,** 55.

KALLURI, R. 2016. The biology and function of fibroblasts in cancer. *Nature Reviews Cancer,* 16**,** 582-598.

KALLURI, R. & WEINBERG, R. A. 2009. The basics of epithelial-mesenchymal transition. *The Journal of Clinical Investigation,* 119**,** 1420-1428.

KANG, J. Y., EGGERT, M., MOULI, S., ALJUFFALI, I., FU, X., NIE, B., SHEIL, A., WADDEY, K., OLDHAM, C. D., MAY, S. W., AMIN, R. & ARNOLD, R. D. 2015. Pharmacokinetics, Antitumor and Cardioprotective Effects of Liposome-Encapsulated Phenylaminoethyl Selenide in Human Prostate Cancer Rodent Models. *Pharmaceutical Research,* 32**,** 852-862.

KAPAŁCZYŃSKA, M., KOLENDA, T., PRZYBYŁA, W., ZAJĄCZKOWSKA, M., TERESIAK, A., FILAS, V., IBBS, M., BLIŹNIAK, R., ŁUCZEWSKI, Ł. & LAMPERSKA, K. 2018. 2D and 3D cell cultures - a comparison of different types of cancer cell cultures. *Archives of medical science : AMS,* 14**,** 910-919.

KATT, M. E., PLACONE, A. L., WONG, A. D., XU, Z. S. & SEARSON, P. C. 2016. In Vitro Tumor Models: Advantages, Disadvantages, Variables, and Selecting the Right Platform. *Front Bioeng Biotechnol,* 4**,** 12.

KAUR, G. & DUFOUR, J. M. 2012. Cell lines: Valuable tools or useless artifacts. *Spermatogenesis,* 2**,** 1-5.

KERSTEN, K., DE VISSER, K. E., VAN MILTENBURG, M. H. & JONKERS, J. 2017. Genetically engineered mouse models in oncology research and cancer medicine. *EMBO Molecular Medicine,* 9**,** 137-153.

KESSELMAN, D., KOSSOVER, O., MIRONI-HARPAZ, I. & SELIKTAR, D. 2013. Time-dependent cellular morphogenesis and matrix stiffening in proteolytically responsive hydrogels. *Acta Biomaterialia,* 9**,** 7630-7639.

KIM, H. N., HABBIT, N. L., SU, C.-Y., CHOI, N., AHN, E. H., LIPKE, E. A. & KIM, D.-H. 2019. Microphysiological Systems as Enabling Tools for Modeling Complexity in the Tumor Microenvironment and Accelerating Cancer Drug Development. *Advanced Functional Materials,* 29**,** 1807553.

KRANING-RUSH, C. M. & REINHART-KING, C. A. 2012. Controlling matrix stiffness and topography for the study of tumor cell migration. *Cell adhesion & migration,* 6**,** 274-279.

LAM, C. R. I., WONG, H. K., NAI, S., CHUA, C. K., TAN, N. S. & TAN, L. P. 2014. A 3D Biomimetic Model of Tissue Stiffness Interface for Cancer Drug Testing. *Molecular Pharmaceutics,* 11**,** 2016-2021.

LANGHANS, S. A. 2018. Three-Dimensional in Vitro Cell Culture Models in Drug Discovery and Drug Repositioning. *Frontiers in Pharmacology,* 9.

LARSSON, J. 2020. eulerr: Area-Proportional Euler and Venn Diagrams with Ellipses. *R package version 6.1.0.*

LEE, K. M., CHOI, K. H. & OUELLETTE, M. M. 2004. Use of exogenous hTERT to immortalize primary human cells. *Cytotechnology,* 45**,** 33-38.

LEIGHT, J. L., DRAIN, A. P. & WEAVER, V. M. 2017. Extracellular Matrix Remodeling and Stiffening Modulate Tumor Phenotype and Treatment Response. *Annual Review of Cancer Biology,* 1**,** 313-334.

LEVENTAL, I., GEORGES, P. C. & JANMEY, P. A. 2007. Soft biological materials and their impact on cell function. *Soft Matter,* 3**,** 299-306.

LEVENTAL, K. R., YU, H., KASS, L., LAKINS, J. N., EGEBLAD, M., ERLER, J. T., FONG, S. F. T., CSISZAR, K., GIACCIA, A., WENINGER, W., YAMAUCHI, M., GASSER, D. L. & WEAVER, V. M. 2009. Matrix crosslinking forces tumor progression by enhancing integrin signaling. *Cell,* 139**,** 891-906.

LEVESQUE, C. & NELSON, P. S. 2018. Cellular Constituents of the Prostate Stroma: Key Contributors to Prostate Cancer Progression and Therapy Resistance. *Cold Spring Harb Perspect Med,* 8.

LIBERZON, A., BIRGER, C., THORVALDSDÓTTIR, H., GHANDI, M., MESIROV, J. P. & TAMAYO, P. 2015. The Molecular Signatures Database (MSigDB) hallmark gene set collection. *Cell systems,* 1**,** 417-425.

LIN, D., WYATT, A. W., XUE, H., WANG, Y., DONG, X., HAEGERT, A., WU, R., BRAHMBHATT, S., MO, F., JONG, L., BELL, R. H., ANDERSON, S., HURTADO-COLL, A., FAZLI, L., SHARMA, M., BELTRAN, H., RUBIN, M., COX, M., GOUT, P. W., MORRIS, J., GOLDENBERG, L., VOLIK, S. V., GLEAVE, M. E., COLLINS, C. C. & WANG, Y. 2014. High fidelity patient-derived xenografts for accelerating prostate cancer discovery and drug development. *Cancer Res,* 74**,** 1272-83.

LING, Y., LI, C., FENG, K., PALMER, S., APPLETON, P. L., LANG, S., MCGLOIN, D., HUANG, Z. & NABI, G. 2017. Second harmonic generation (SHG) imaging of cancer heterogeneity in ultrasound guided biopsies of prostate in men suspected with prostate cancer. *Journal of Biophotonics,* 10**,** 911-918.

LINXWEILER, J., HAJILI, T., KÖRBEL, C., BERCHEM, C., ZEUSCHNER, P., MÜLLER, A., STÖCKLE, M., MENGER, M. D., JUNKER, K. & SAAR, M. 2020. Cancer-associated fibroblasts stimulate primary tumor growth and metastatic spread in an orthotopic prostate cancer xenograft model. *Scientific Reports,* 10**,** 12575.

LIU, J., DANG, H. & WANG, X. W. 2018a. The significance of intertumor and intratumor heterogeneity in liver cancer. *Experimental &Amp; Molecular Medicine,* 50**,** e416.

LIU, Q., ZHANG, H., JIANG, X., QIAN, C., LIU, Z. & LUO, D. 2017. Factors involved in cancer metastasis: a better understanding to "seed and soil" hypothesis. *Molecular Cancer,* 16**,** 176.

LIU, Y., KIM, Y. J., SIRIWON, N., ROHRS, J. A., YU, Z. & WANGA, P. 2018b. Combination drug delivery via multilamellar vesicles enables targeting of tumor cells and tumor vasculature. *Biotechnology and Bioengineering,* 115**,** 1403-1415.

LIU, Z. & VUNJAK-NOVAKOVIC, G. 2016. Modeling tumor microenvironments using custom-designed biomaterial scaffolds. *Current opinion in chemical engineering,* 11**,** 94-105.

LOVE, M. I., HUBER, W. & ANDERS, S. 2014. Moderated estimation of fold change and dispersion for RNA-seq data with DESeq2. *Genome Biology,* 15**,** 550.

LYSSIOTIS, C. A. & KIMMELMAN, A. C. 2017. Metabolic Interactions in the Tumor Microenvironment. *Trends in Cell Biology,* 27**,** 863-875.

MAHAL, B. A., BUTLER, S., FRANCO, I., SPRATT, D. E., REBBECK, T. R., D'AMICO, A. V. & NGUYEN, P. L. 2019. Use of Active Surveillance or Watchful Waiting for Low-Risk Prostate Cancer and Management Trends Across Risk Groups in the United States, 2010-2015. *JAMA,* 321**,** 704-706.

MALANDRINO, A., MAK, M., KAMM, R. D. & MOEENDARBARY, E. 2018. Complex mechanics of the heterogeneous extracellular matrix in cancer. *Extreme Mechanics Letters,* 21**,** 25-34.

MARTIN, T. A., YE, L., SANDERS, A. J., LANE, J. & JIANG, W. G. 2013. Cancer Invasion and Metastasis: Molecular and Cellular Perspective. *In:* JANDIAL, R. (ed.) *Metastatic Cancer: Clinical and Biological Perspectives* Landes Bioscience.

MATTE, B. F., KUMAR, A., PLACONE, J. K., ZANELLA, V. G., MARTINS, M. D., ENGLER, A. J. & LAMERS, M. L. 2019. Matrix stiffness mechanically conditions EMT and migratory behavior of oral squamous cell carcinoma. *Journal of Cell Science,* 132**,** jcs224360.

MATTERN, J., BAK, M., HAHN, E. W. & VOLM, M. 1988. Human tumor xenografts as model for drug testing. *Cancer Metastasis Rev,* 7**,** 263-84.

MEHTA, G., HSIAO, A. Y., INGRAM, M., LUKER, G. D. & TAKAYAMA, S. 2012. Opportunities and Challenges for use of Tumor Spheroids as Models to Test Drug Delivery and Efficacy. *Journal of controlled release : official journal of the Controlled Release Society,* 164**,** 192-204.

MILOTTI, E., VYSHEMIRSKY, V., SEGA, M. & CHIGNOLA, R. 2012. Interplay between distribution of live cells and growth dynamics of solid tumours. *Scientific Reports,* 2**,** 990.

MINCHINTON, A. I. & TANNOCK, I. F. 2006. Drug penetration in solid tumours. *Nat Rev Cancer,* 6**,** 583-92.

MITRA, A. K., KUMAR, H., RAMAKRISHNAN, V., CHEN, L., BAUGHN, L., KUMAR, S., RAJKUMAR, S. V. & VAN NESS, B. G. 2020. In vitro and ex vivo gene expression profiling reveals differential kinetic response of HSPs and UPR genes is associated with PI resistance in multiple myeloma. *Blood cancer journal,* 10**,** 78-78.

MOAZZEM HOSSAIN, M., WANG, X., BERGAN, R. C. & JIN, J. P. 2014. Diminished expression of h2-calponin in prostate cancer cells promotes cell proliferation, migration and the dependence of cell adhesion on substrate stiffness. *FEBS Open Bio,* 4**,** 627-636.

MOHAMMADI, H. & SAHAI, E. 2018. Mechanisms and impact of altered tumour mechanics. *Nature Cell Biology,* 20**,** 766-774.

MUNDEKKAD, D. & CHO, W. C. 2022. Nanoparticles in Clinical Translation for Cancer Therapy. *Int J Mol Sci,* 23.

MYUNGJIN LEE, J., MHAWECH-FAUCEGLIA, P., LEE, N., CRISTINA PARSANIAN, L., GAIL LIN, Y., ANDREW GAYTHER, S. & LAWRENSON, K. 2013. A three-dimensional microenvironment alters protein expression and chemosensitivity of epithelial ovarian cancer cells in vitro. *Laboratory Investigation,* 93**,** 528.

NATIONAL CANCER INSTITUTE. *Cancer Stat Facts: Prostate Cancer* [Online]. NIH [Accessed September 20 2020].

NATIONAL CANCER INSTITUTE. 2020. *Cancer Statistics* [Online]. National Cancer Institute Available: https://www.cancer.gov/about-cancer/understanding/statistics [Accessed October 21 2022].

NATIONAL INSTITUTE OF BIOMEDICAL IMAGING AND BIOENGINEERING. 2018. *Tissue Engineering and Regenerative Medicine* [Online]. National Institute of Health. Available: https://www.nibib.nih.gov/science-education/science-topics/tissue-engineering-and-regenerative-medicine [Accessed April 26 2018].

NAVYA, P. N., KAPHLE, A., SRINIVAS, S. P., BHARGAVA, S. K., ROTELLO, V. M. & DAIMA, H. K. 2019. Current trends and challenges in cancer management and therapy using designer nanomaterials. *Nano Convergence,* 6**,** 23.

NEUWIRT, H., BOUCHAL, J., KHARAISHVILI, G., PLONER, C., JÖHRER, K., PITTERL, F., WEBER, A., KLOCKER, H. & EDER, I. E. 2020. Cancer-associated fibroblasts promote prostate tumor growth and progression through upregulation of cholesterol and steroid biosynthesis. *Cell communication and signaling : CCS,* 18**,** 11-11.

OJALILL, M., RAPPU, P., SILJAMÄKI, E., TAIMEN, P., BOSTRÖM, P. & HEINO, J. 2018. The composition of prostate core matrisome in vivo and in vitro unveiled by mass spectrometric analysis. *The Prostate,* 78**,** 583-594.

OJALILL, M., VIRTANEN, N., RAPPU, P., SILJAMÄKI, E., TAIMEN, P. & HEINO, J. 2020. Interaction between prostate cancer cells and prostate fibroblasts promotes accumulation and proteolytic processing of basement membrane proteins. *The Prostate,* 80**,** 715-726.

ORTIZ-OTERO, N., CLINCH, A. B., HOPE, J., WANG, W., REINHART-KING, C. A. & KING, M. R. 2020. Cancer associated fibroblasts confer shear resistance to circulating tumor cells during prostate cancer metastatic progression. *Oncotarget,* 11**,** 1037-1050.

OUDIN, M. J. & WEAVER, V. M. 2016. Physical and Chemical Gradients in the Tumor Microenvironment Regulate Tumor Cell Invasion, Migration, and Metastasis. *Cold Spring Harbor Symposia on Quantitative Biology,* 81**,** 189-205.

PARK, K. M., LEWIS, D. & GERECHT, S. 2017. Bioinspired Hydrogels to Engineer Cancer Microenvironments. *Annual Review of Biomedical Engineering,* 19**,** 109-133.

PEYTON, S. R., KIM, P. D., GHAJAR, C. M., SELIKTAR, D. & PUTNAM, A. J. 2008. The effects of matrix stiffness and RhoA on the phenotypic plasticity of smooth muscle cells in a 3-D biosynthetic hydrogel system. *Biomaterials,* 29**,** 2597-2607.

PHARMACEUTICAL RESEARCH AND MANUFACTURERS OF AMERICA 2007. Drug Discovery and Development.

POLZER, B. & KLEIN, C. A. 2013. Metastasis Awakening: The challenges of targeting minimal residual cancer. *Nature Medicine,* 19**,** 274.

PRABHAKARPANDIAN, B., SHEN, M. C., NICHOLS, J. B., GARSON, C. J., MILLS, I. R., MATAR, M. M., FEWELL, J. G. & PANT, K. 2015. Synthetic tumor networks for screening drug delivery systems. *J Control Release,* 201**,** 49-55.

PRADHAN, S., CHAUDHURY, C. S. & LIPKE, E. A. 2014. Dual-Phase, Surface Tension-Based Fabrication Method for Generation of Tumor Millibeads. *Langmuir,* 30**,** 3817-3825.

PRADHAN, S., CLARY, J. M., SELIKTAR, D. & LIPKE, E. A. 2017a. A three-dimensional spheroidal cancer model based on PEG-fibrinogen hydrogel microspheres. *Biomaterials,* 115**,** 141-154.

PRADHAN, S., HASSANI, I., SEETO, W. J. & LIPKE, E. A. 2017b. PEG-fibrinogen hydrogels for three-dimensional breast cancer cell culture. *J Biomed Mater Res A,* 105**,** 236-252.

PRADHAN, S., SMITH, A. M., GARSON, C. J., HASSANI, I., SEETO, W. J., PANT, K., ARNOLD, R. D., PRABHAKARPANDIAN, B. & LIPKE, E. A. 2018. A

Microvascularized Tumor-mimetic Platform for Assessing Anti-cancer Drug Efficacy. *Scientific Reports,* 8**,** 3171.

PRATT, S. J. P., LEE, R. M. & MARTIN, S. S. 2020. The Mechanical Microenvironment in Breast Cancer. *Cancers,* 12**,** 1452.

PRAUZNER-BECHCICKI, S., RACZKOWSKA, J., MADEJ, E., PABIJAN, J., LUKES, J., SEPITKA, J., RYSZ, J., AWSIUK, K., BERNASIK, A., BUDKOWSKI, A. & LEKKA, M. 2015. PDMS substrate stiffness affects the morphology and growth profiles of cancerous prostate and melanoma cells. *Journal of the Mechanical Behavior of Biomedical Materials,* 41**,** 13-22.

PRONIN, A. & SLEPAK, V. 2021. Ectopically expressed olfactory receptors OR51E1 and OR51E2 suppress proliferation and promote cell death in a prostate cancer cell line. *Journal of Biological Chemistry,* 296**,** 100475.

PROVENZANO, P. P., INMAN, D. R., ELICEIRI, K. W., KNITTEL, J. G., YAN, L., RUEDEN, C. T., WHITE, J. G. & KEELY, P. J. 2008. Collagen density promotes mammary tumor initiation and progression. *BMC Med,* 6**,** 11.

PUCA, L., VLACHOSTERGIOS, P. J. & BELTRAN, H. 2019. Neuroendocrine Differentiation in Prostate Cancer: Emerging Biology, Models, and Therapies. *Cold Spring Harbor perspectives in medicine,* 9**,** a030593.

QUAIL, D. F. & JOYCE, J. A. 2013. Microenvironmental regulation of tumor progression and metastasis. *Nature medicine,* 19**,** 1423-1437.

RICHARDS, Z., MCCRAY, T., MARSILI, J., ZENNER, M. L., MANLUCU, J. T., GARCIA, J., KAJDACSY-BALLA, A., MURRAY, M., VOISINE, C., MURPHY, A. B., ABDULKADIR, S. A., PRINS, G. S. & NONN, L. 2019. Prostate Stroma Increases the Viability and Maintains the Branching Phenotype of Human Prostate Organoids. *iScience,* 12**,** 304-317.

ROBERTS, K. 2020. We're asking scientists to tackle 9 of the toughest challenges in cancer research Available from: https://news.cancerresearchuk.org/2020/10/14/were-asking-scientists-to-tackle-9-of-the-toughest-challenges-in-cancer-research/ 2022].

ROSANO, J. M., TOUSI, N., SCOTT, R. C., KRYNSKA, B., RIZZO, V., PRABHAKARPANDIAN, B., PANT, K., SUNDARAM, S. & KIANI, M. F. 2009. A physiologically realistic in vitro model of microvascular networks. *Biomed Microdevices,* 11**,** 1051-7.

ROTH, A. 2021. Human microphysiological systems for drug development. *Science,* 373**,** 1304-1306.

RUOSLAHTI, E. 1996. RGD AND OTHER RECOGNITION SEQUENCES FOR INTEGRINS. *Annual Review of Cell and Developmental Biology,* 12**,** 697-715.

SAGGAR, J. K., YU, M., TAN, Q. & TANNOCK, I. F. 2013. The tumor microenvironment and strategies to improve drug distribution. *Front Oncol,* 3**,** 154.

SAHAI, E., ASTSATUROV, I., CUKIERMAN, E., DENARDO, D. G., EGEBLAD, M., EVANS, R. M., FEARON, D., GRETEN, F. R., HINGORANI, S. R., HUNTER, T., HYNES, R. O., JAIN, R. K., JANOWITZ, T., JORGENSEN, C., KIMMELMAN, A. C., KOLONIN, M. G., MAKI, R. G., POWERS, R. S., PURÉ, E., RAMIREZ, D. C., SCHERZ-SHOUVAL, R., SHERMAN, M. H., STEWART, S., TLSTY, T. D., TUVESON, D. A., WATT, F. M., WEAVER, V., WEERARATNA, A. T. & WERB, Z. 2020. A framework for advancing our

understanding of cancer-associated fibroblasts. *Nature Reviews Cancer,* 20**,** 174-186.

SAYOLS, S. 2020. rrvgo: a Bioconductor package to reduce and visualize Gene Ontology terms.

SEO, B. R., BHARDWAJ, P., CHOI, S., GONZALEZ, J., ANDRESEN EGUILUZ, R. C., WANG, K., MOHANAN, S., MORRIS, P. G., DU, B., ZHOU, X. K., VAHDAT, L. T., VERMA, A., ELEMENTO, O., HUDIS, C. A., WILLIAMS, R. M., GOURDON, D., DANNENBERG, A. J. & FISCHBACH, C. 2015. Obesity-dependent changes in interstitial ECM mechanics promote breast tumorigenesis. *Science translational medicine,* 7**,** 301ra130-301ra130.

SERCOMBE, L., VEERATI, T., MOHEIMANI, F., WU, S. Y., SOOD, A. K. & HUA, S. 2015. Advances and Challenges of Liposome Assisted Drug Delivery. *Front Pharmacol,* 6**,** 286.

SHAPIRO, E., BECICH MICHAEL, J., HARTANTO, V. & LEPOR, H. 1992. The Relative Proportion of Stromal and Epithelial Hyperplasia is Related to the Development of Symptomatic Benign Prostate Hyperplasia. *Journal of Urology,* 147**,** 1293-1297.

SHARMA, S. V., HABER, D. A. & SETTLEMAN, J. 2010. Cell line-based platforms to evaluate the therapeutic efficacy of candidate anticancer agents. *Nature Reviews Cancer,* 10**,** 241.

SHEN, Y.-I., ABACI, H. E., KRUPSKI, Y., WENG, L.-C., BURDICK, J. A. & GERECHT, S. 2014. Hyaluronic acid hydrogel stiffness and oxygen tension affect cancer cell fate and endothelial sprouting. *Biomaterials Science,* 2**,** 655-665.

SHENG, F. & JIA, R.-P. 2022. The design basis and application in urology of the tumor-on-a-chip platform. *Urologic Oncology: Seminars and Original Investigations,* 40**,** 331-342.

SIEH, S., TAUBENBERGER, A. V., RIZZI, S. C., SADOWSKI, M., LEHMAN, M. L., ROCKSTROH, A., AN, J., CLEMENTS, J. A., NELSON, C. C. & HUTMACHER, D. W. 2012. Phenotypic characterization of prostate cancer LNCaP cells cultured within a bioengineered microenvironment. *PLoS One,* 7**,** e40217.

SIMPSON-HAIDARIS, P. J. & RYBARCZYK, B. 2001. Tumors and fibrinogen. The role of fibrinogen as an extracellular matrix protein. *Ann N Y Acad Sci,* 936**,** 406-25.

SINGH, V. P., PRATAP, K., SINHA, J., DESIRAJU, K., BAHAL, D. & KUKRETI, R. 2016. Critical evaluation of challenges and future use of animals in experimentation for biomedical research. *International Journal of Immunopathology and Pharmacology,* 29**,** 551-561.

SIOLAS, D. & HANNON, G. J. 2013. Patient-derived tumor xenografts: transforming clinical samples into mouse models. *Cancer Res,* 73**,** 5315-9.

SMOLARCZYK, R., CZAPLA, J., JAROSZ-BIEJ, M., CZERWINSKI, K. & CICHOŃ, T. 2021. Vascular disrupting agents in cancer therapy. *European Journal of Pharmacology,* 891**,** 173692.

SOUSA DE ALMEIDA, M., SUSNIK, E., DRASLER, B., TALADRIZ-BLANCO, P., PETRI-FINK, A. & ROTHEN-RUTISHAUSER, B. 2021. Understanding nanoparticle endocytosis to improve targeting strategies in nanomedicine. *Chem Soc Rev,* 50**,** 5397-5434.

STEWART, D. A., COOPER, C. R. & SIKES, R. A. 2004. Changes in extracellular matrix (ECM) and ECM-associated proteins in the metastatic progression of prostate cancer. *Reproductive biology and endocrinology : RB&E,* 2**,** 2-2.

SUNG, H., FERLAY, J., SIEGEL, R. L., LAVERSANNE, M., SOERJOMATARAM, I., JEMAL, A. & BRAY, F. 2021. Global Cancer Statistics 2020: GLOBOCAN Estimates of Incidence and Mortality Worldwide for 36 Cancers in 185 Countries. *CA: A Cancer Journal for Clinicians,* 71**,** 209-249.

SZNURKOWSKA, M. K. & ACETO, N. 2022. The gate to metastasis: key players in cancer cell intravasation. *The FEBS Journal,* 289**,** 4336-4354.

TALÉNS-VISCONTI, R., DÍEZ-SALES, O., DE JULIÁN-ORTIZ, J. V. & NÁCHER, A. 2022. Nanoliposomes in Cancer Therapy: Marketed Products and Current Clinical Trials. *Int J Mol Sci,* 23.

TAM, N. W., CHUNG, D., BALDWIN, S. J., SIMMONS, J. R., XU, L., RAINEY, J. K., DELLAIRE, G. & FRAMPTON, J. P. 2020. Material properties of disulfide-crosslinked hyaluronic acid hydrogels influence prostate cancer cell growth and metabolism. *Journal of Materials Chemistry B,* 8**,** 9718-9733.

THALMANN, G. N., RHEE, H., SIKES, R. A., PATHAK, S., MULTANI, A., ZHAU, H. E., MARSHALL, F. F. & CHUNG, L. W. K. 2010. Human prostate fibroblasts induce growth and confer castration resistance and metastatic potential in LNCaP Cells. *European urology,* 58**,** 162-171.

TRUJILLO-DE SANTIAGO, G., FLORES-GARZA, B. G., TAVARES-NEGRETE, J. A., LARA-MAYORGA, I. M., GONZÁLEZ-GAMBOA, I., ZHANG, Y. S., ROJAS-MARTÍNEZ, A., ORTIZ-LÓPEZ, R. & ÁLVAREZ, M. M. 2019. The Tumor-on-Chip: Recent Advances in the Development of Microfluidic Systems to Recapitulate the Physiology of Solid Tumors. *Materials (Basel),* 12.

US FOOD & DRUG ADMINISTRATION. 2018. *The Drug Development Process* [Online]. Available: https://www.fda.gov/ForPatients/Approvals/Drugs/default.htm [Accessed April 30 2018].

VAN NORMAN, G. A. 2019. Limitations of Animal Studies for Predicting Toxicity in Clinical Trials: Is it Time to Rethink Our Current Approach? *JACC Basic Transl Sci,* 4**,** 845-854.

VOGELSTEIN, B. & KINZLER, K. W. 2004. Cancer genes and the pathways they control. *Nature Medicine,* 10**,** 789.

WAHAJUDDIN & ARORA, S. 2012. Superparamagnetic iron oxide nanoparticles: magnetic nanoplatforms as drug carriers. *Int J Nanomedicine,* 7**,** 3445-71.

WANG, Y., YAO, B., LI, H., ZHANG, Y., GAO, H., GAO, Y., PENG, R. & TANG, J. 2017. Assessment of Tumor Stiffness With Shear Wave Elastography in a Human Prostate Cancer Xenograft Implantation Model. *Journal of Ultrasound in Medicine,* 36**,** 955-963.

WEI, S. C., FATTET, L., TSAI, J. H., GUO, Y., PAI, V. H., MAJESKI, H. E., CHEN, A. C., SAH, R. L., TAYLOR, S. S., ENGLER, A. J. & YANG, J. 2015. Matrix stiffness drives epithelial–mesenchymal transition and tumour metastasis through a TWIST1–G3BP2 mechanotransduction pathway. *Nature Cell Biology,* 17**,** 678-688.

WEI, S. C. & YANG, J. 2016. Forcing through Tumor Metastasis: The Interplay between Tissue Rigidity and Epithelial-Mesenchymal Transition. *Trends in cell biology,* 26**,** 111-120.

WEIGEL, T., SCHINKEL, G. & LENDLEIN, A. 2006. Design and preparation of polymeric scaffolds for tissue engineering. *Expert Review of Medical Devices,* 3**,** 835-851.

WHITESIDE, T. L. 2008. The tumor microenvironment and its role in promoting tumor growth. *Oncogene,* 27**,** 5904.

WONG, C. H., SIAH, K. W. & LO, A. W. 2018. Estimation of clinical trial success rates and related parameters. *Biostatistics***,** kxx069-kxx069.

WU, J. 2021. The Enhanced Permeability and Retention (EPR) Effect: The Significance of the Concept and Methods to Enhance Its Application. *J Pers Med,* 11.

XU, K., GANAPATHY, K., ANDL, T., WANG, Z., COPLAND, J. A., CHAKRABARTI, R. & FLORCZYK, S. J. 2019. 3D porous chitosan-alginate scaffold stiffness promotes differential responses in prostate cancer cell lines. *Biomaterials,* 217**,** 119311.

XU, X., GURSKI, L. A., ZHANG, C., HARRINGTON, D. A., FARACH-CARSON, M. C. & JIA, X. 2012. Recreating the tumor microenvironment in a bilayer, hyaluronic acid hydrogel construct for the growth of prostate cancer spheroids. *Biomaterials,* 33**,** 9049-9060.

YANG, L. V. 2017. Tumor Microenvironment and Metabolism. *International Journal of Molecular Sciences,* 18**,** 2729.

YANG, X., SARVESTANI, S. K., MOEINZADEH, S., HE, X. & JABBARI, E. 2013. Three-Dimensional-Engineered Matrix to Study Cancer Stem Cells and Tumorsphere Formation: Effect of Matrix Modulus. *Tissue Engineering Part A,* 19**,** 669-684.

YU, G. 2020. Gene Ontology Semantic Similarity Analysis Using GOSemSim. *Methods Mol Biol,* 2117**,** 207-215.

YU, G., LI, F., QIN, Y., BO, X., WU, Y. & WANG, S. 2010. GOSemSim: an R package for measuring semantic similarity among GO terms and gene products. *Bioinformatics,* 26**,** 976-8.

YU, G., WANG, L.-G., HAN, Y. & HE, Q.-Y. 2012. clusterProfiler: an R package for comparing biological themes among gene clusters. *Omics : a journal of integrative biology,* 16**,** 284-287.

YU, J., PIAZZA, A., SPARKS, S., HIND, L. E., NILES, D. J., INGRAM, P. N., HUANG, W., RICKE, W. A., JARRARD, D. F., HUTTENLOCHER, A., BASU, H. & BEEBE, D. J. 2021. A reconfigurable microscale assay enables insights into cancer-associated fibroblast modulation of immune cell recruitment. *Integrative Biology,* 13**,** 87-97.

YU, X. & MACHESKY, L. M. 2012. Cells assemble invadopodia-like structures and invade into matrigel in a matrix metalloprotease dependent manner in the circular invasion assay. *PLoS One,* 7**,** e30605.

ZHANG, M., GAO, S., YANG, D., FANG, Y., LIN, X., JIN, X., LIU, Y., LIU, X., SU, K. & SHI, K. 2021. Influencing factors and strategies of enhancing nanoparticles into tumors in vivo. *Acta Pharmaceutica Sinica B,* 11**,** 2265-2285.

ZHANG, X., CLAERHOUT, S., PRAT, A., DOBROLECKI, L. E., PETROVIC, I., LAI, Q., LANDIS, M. D., WIECHMANN, L., SCHIFF, R., GIULIANO, M., WONG, H., FUQUA, S. W., CONTRERAS, A., GUTIERREZ, C., HUANG, J., MAO, S., PAVLICK, A. C., FROEHLICH, A. M., WU, M. F., TSIMELZON, A., HILSENBECK, S. G., CHEN, E. S., ZULOAGA, P., SHAW, C. A., RIMAWI, M. F., PEROU, C. M., MILLS, G. B., CHANG, J. C. & LEWIS, M. T. 2013. A renewable tissue resource of phenotypically stable, biologically and ethnically diverse, patient-derived human breast cancer xenograft models. *Cancer Res,* 73**,** 4885-97.

ZHANG, X. & LONG, Q. 2017. Elevated serum plasma fibrinogen is associated with advanced tumor stage and poor survival in hepatocellular carcinoma patients. *Medicine,* 96.

ZHANG, Y. S., ZHANG, Y.-N. & ZHANG, W. 2017. Cancer-on-a-chip systems at the frontier of nanomedicine. *Drug Discovery Today,* 22**,** 1392-1399.

ZHOU, R., FENG, Y., YE, J., HAN, Z., LIANG, Y., CHEN, Q., XU, X., HUANG, Y., JIA, Z. & ZHONG, W. 2021. Prediction of Biochemical Recurrence-Free Survival of Prostate Cancer Patients Leveraging Multiple Gene Expression Profiles in Tumor Microenvironment. *Frontiers in Oncology,* 11.